TIME-DEPENDENT BEHAVIOR OF VERTICALLY-LOADED PILED RAFT FOUNDATION MODELS SUPPORTED BY JACKED-IN PILES ON SATURATED CLAYEY GROUND

Dissertation

TIME-DEPENDENT BEHAVIOR OF VERTICALLY-LOADED PILED RAFT FOUNDATION MODELS SUPPORTED BY JACKED-IN PILES ON SATURATED CLAYEY GROUND

Graduate School of
Natural Science & Technology
Kanazawa University

Division of Environmental Design

Student ID No.: 1724052014
Name: Hoang Thi Lua
Chief advisor: Prof. Tatsunori Matsumoto
Date of Submission: September, 2020

Abstract

In recent years, heavy structures such as high-rise buildings have become increasingly common requirements in urban areas and especially in megacities. This has led to increasing demands for geotechnical engineers to use piled raft foundations (PRFs) as an effective solution for both economy and safety, this being because the raft and the piles share the load.

With the wide distribution of clayey soil over the world, including Japan, Vietnam, or Thailand, the need arises to understand the time-dependent behavior of PRFs when applying this type of foundation on clay. This is because the stresses and strains in clayey ground change for a long time after the construction work because of ground consolidation. For such understanding, this study aims to investigate the long-term behavior of vertically loaded PRF models on saturated clay, using small scale physical modeling and numerical modeling.

For the experiments, the model ground was prepared by consolidating a slurry clayey mixture. The consistent condition of the model ground is kept in all the experiments and confirmed by a series of cone penetration tests, T-bar tests, and unconfined compression tests. The CU triaxial test is also carried out to study ground behavior. The model foundations comprised a square raft and a group of small piles with different pile spacings or different pile numbers. Besides, the load tests on individual piles, pile groups, and unpiled raft were also conducted for comparison purposes. In long-term load tests of PRFs, the applied load was increased in multiple steps until the foundation settlement exceeded 10% of the raft width. Each load step was maintained for a sufficient period to observe the long-term behavior of the foundation. The applied load, the PRF deformation, the axial forces along the piles, the pore water pressure (PWP), and the earth pressure beneath the raft base were measured. The results show that the foundation settlement increased rapidly in the short period of load-increasing, and then slowed down and was nearly proportional to the dissipation rate of PWP beneath the raft base in the primary consolidation period. The foundation continued to settle during the secondary consolidation period because of ground creep. The pile load increased with elapsed time in the primary consolidation period because of the corresponding increase of effective ground stresses, due to the consolidation process. The location of the piles influenced the change of pile resistances as well as axial load distribution along the piles. The load sharing between raft and piles, and the load sharing between piles changed with the magnitude of the applied load, the time, and the pile arrangement. It is interesting that in the secondary consolidation period, the load sharing between raft and piles was unstable under the small applied loads but stable at the large applied loads. The experimental study involved small-scale experiments; however, it

emphasized the importance of considering the interaction among the piles, the raft, the ground, and the PWP.

The numerical analyses of PRFs using a three-dimensional finite element program PLAXIS 3D were conducted following the procedure of model tests, and the analysis results were compared with the experimental results. To select an appropriate soil constitutive model for the analyses as well as determine proper soil parameters for the model, the simulations of element tests, such as oedometer and CU triaxial tests, were conducted first. Then a constitutive model, called "soft soil creep model", was employed to simulate the behaviors of PRF models on clay ground with soil parameters basically obtained from the element tests. The foundation structures were modeled by elastic materials. The effect of the pile jacking process on the ground stresses was simulated by the cylindrical expansion of pile using volume expansion of pile volume elements. The calculated (predicted) results showed good agreements with the experimental results in terms of the time-dependent settlement trend and the tendency of load sharing between raft and piles with time. Moreover, the trends of changes of pile load with time, load sharing between piles with magnitudes of applied load, and behavior of excess pore water pressure beneath the raft base were also well simulated. The results indicate that FEM analysis with well-determined soil parameters will be a promising design procedure for piled raft foundations on clay ground.

In further studies, the behavior of PRFs will be studied in more details using FEM analysis to investigate more deeply the resistance mechanisms of PRFs under different foundation configurations and different load types, and the recommendations for the application of results in the practical design of PRF on clayey ground will be made.

Acknowledgments

The journey to this dissertation is one of the most meaningful and unforgettable periods in my life. I have gained a lot of things from this journey, and I would like to express my gratitude to professors, friends, family, and colleagues who have made it possible for me.

First and foremost, I would like to express my gratitude to the respected professor Tatsunori Matsumoto who has spent countless time supervising me since the start of my research path. It has been a great honor to study with you, professor. I am not always a positive person, I often got depressed and kept silent when I was in difficult situations in research but you did not let me down, you inspired and encouraged me to look at positives, and guided me through problems. I have learned from you not only geotechnical knowledge but also how to write and present a paper. Thanks for the plenty of valuable discussions, comments, and corrections on my works, especially on my papers. Thank you so much for giving me the chance to pursue this research with you, with your profound knowledge. This dissertation could not be completed without your enthusiastic dedication.

I would like to appreciate Mr. Dao Xuan Khang, a Master's student in the Laboratory of Geotechnical Engineering at Kanazawa University, for his considerable help with the experimental work; Mr. Shinya Shimono, a technician in the Faculty of Geosciences and Civil Engineering at Kanazawa University, for his excellent technical support. The experiments were complicated and took a lot of time, I wouldn't have been able to do such experiments without your help.

This thesis is completed also thanks to Assoc. Prof. Shun-ichi Kobayashi, he gave me kind advice and valuable discussions for my research.

I would like to thank the jury members for insightful feedback and constructive comments.

I am indebted to the Vietnamese government who financially supported both tuition fees and living expenses for my three-year doctoral course in Japan. The financial supports of Kanazawa University is also appreciated.

I would like to thank the guidance of the Geotechnical Engineering division and Thuyloi University, especially prof. Trinh Minh Thu, so I decided to begin my Ph.D. course.

At the beginning of my Ph.D. journey in an oversea country, everything was so new and challenging for me, and Kongpop Watcharasawe, a special friend, came at the right time to share experiences and help me. Thank you so much, I am lucky to have a friend like you.

During years away from home, new friends have come and colored my Ph.D. life. Special appreciations are given for Yukio Abe-san, you have helped and treated me like your children. With Hai, thanks very much for sharing with me many thoughts in life, for spending

your time to listen to my miscellaneous stories. I also want to give my thanks for Thien-Thao, Thiem-Dan, Nga-Sao, Hue-Tung, Nham-Hoa, Ha, Thuy, Hang, Tuan, Mi-san, Yamakuri, Diah, Amna, Wentao, and many others, thanks to you guys, I have had memorable moments in beautiful Japan. I am very glad to meet you and grateful for the precious times.

Lastly but never enough, my deepest thanks are for my beloved husband, lovely daughter, my parents, my mother in law, my sisters, and my other family members. They love me unconditionally, give me energy and motivation to complete this thesis.

HOANG THI LUA
Kanazawa University
September 2020

Contents

List of Figures

Chapter 2:

Chapter 3:

Chapter 4:

List of Tables

Chapter 3:

Chapter 4:

List of notations

B_r = raft width;

C_C = compression index;

C_{cs} = creep settlement index;

C_S = swelling index;

c_k = change of permeability;

c_u = undrained shear strength;

c_v = consolidation coefficient;

c' = effective cohesion;

D = pile diameter;

$d_{T\text{-}bar}$ = T-bar cylinder diameter;

D_r = relative density;

e = void ratio;

e_0 = initial void ratio;

E_p = Young's modulus of pile;

E_r = Young's modulus of raft;

EA = axial stiffness;

EI = bending stiffness;

F_S = safety factor;

G_s = shear modulus of soil;

H = drainage distance;

k = permeability;

K_{rs} = raft - soil stiffness ratio;

L = pile length;

L_r = raft length;

$L_{T\text{-}bar}$ = T-bar cylinder length

LL = liquid limit;

M = stress ratio at the failure;

N_{kt} = cone resistance factor;

$N_{T\text{-}bar}$ = T-bar resistance factor;

P_0 = design load;

P_1 = load carried by the raft corresponding to acceptable design settlement;

P = applied load;

P_p = load carried by piles;

$P_{PG,\ ult}$ = ultimate capacity of pile group;

P_r = load carried by raft;

P_{su} = pile ultimate shaft capacity;

P_w = uplift force;

PL = plastic limit;

p = mean normal total stress;

p' = mean effective stress;

Q = column load;

Q' = reduced column load;

Q_r = load supported by raft;

Q_{pr} = total load applied on piled raft;

q = deviatoric stress;

$q_{cone\ tip}$ = cone tip resistance;

$q_{T\text{-}bar}$ = stress acting on T-bar cylinder;

q_u = unconfined compression strength;

R_{inter} = strength reduction factor;

s = center-to-center pile spacing;

S_a = acceptable design settlement;

S_0 = total settlement;

t = time;

t_r = raft thickness;

T_v = time factor;

u = excess pore water pressure;

w = settlement;

z = depth coordinate;

ΔP = increment of applied load;

ΔP_p = increment of pile load;

ΔP_r = increment of raft load;

ΔP_w = increment of uplift force;

Δw = increment of settlement;

α_r = load sharing ratio between raft and total applied load;

γ_{unsat} = unsaturated unit weight;

γ_{sat} = saturated unit weight;

γ_{water} = unit weight of water;

ε_a = axial strain;

ε_v = volume strain;

ν_p = Poisson’s ratio of pile;

ν_s = Poisson’s ratio of soil;

ν_{ur} = Poisson's ratio for unloading/reloading;

ρ_s = density of soil particle;

ρ_{sat} = Saturated density;

σ_t = tensile strength;

σ_v = vertical stress;

σ_{vo} = total overburden stress;

ϕ' = friction angle;

Chapter 1
Introduction

1.1 Motivation of the study

In recent years, heavy structures such as high-rise buildings have become increasingly common requirements in urban areas and especially in megacities. This has led to increasing demands for geotechnical engineers to use piled raft foundations (PRFs) as an effective solution for both economy and safety, this being because the raft and the piles share the load.

However, although PRFs offer these benefits, PRF design, especially their design on clayey ground, remains challenging.

Many cases have been reported of piled foundations located on clayey ground. Field measurement data have shown that the foundations begin to settle in the construction period and continue doing so long after the full construction load is achieved (Hooper 1973; EI-Mossallamy 2002; Sales, Small, and Poulos 2010; Tang, Pei, and Zhao 2014). This may be due to (i) the dissipation of excess pore water pressure (PWP), which is generated in the construction period, with elapsed time in the primary consolidation period, and (ii) the creep settlement in the secondary consolidation period. The dissipation of excess PWP changes the effective stresses in the ground, causes deformation, and changes the load sharing between the raft and the piles in the case of a PRF. Therefore, when designing a PRF on clay, we must understand how the PRF behaves throughout its entire service life, including the construction and primary and secondary consolidation periods.

The behavior of PRF on clay has been investigated for several decades. A large number of researches on immediate (short-term) behavior of PRFs (behavior of PRFs until the end of the full-load construction) have been published, e.g. Cooke (1986); Yamashita, Kakurai, and Yamada (1994); Horikoshi (1995); Horikoshi and Randolph (1996); Horikoshi and Randolph (1998); Horikoshi et al. (1999); deSanctis and Mandolini (2006); Lee, Kim, and Jeong (2010); Roy, Chattopadhyay, and Sahu (2011); Cho et al. (2012); Karim, AL-Qaissy, and Hameedi (2013); Roshan and Shooshpasha (2014); Thoidingjam, Prasad, and Devi (2016); Mandal and Sengupta (2017); Thoidingjam and Devi (2017); Mali and Singh (2018); Rodríguez, Cunha, and Caicedo (2018). In the above researches, the behavior of PRs in clay has investigated detailed in many aspects by different methods, included numerical study, experimental study, and field measurement.

Some studies have pay attention to the time-dependent behavior of PRFs on clay. Field observations of the performance of PRF were carried out by Hooper (1973); Russo and

Viggiani (1995); and Tang, Pei, and Zhao (2014). In some other studies, numerical methods were employed to investigate the long-term behavior of PRF, e.g. Small and Liu (2008); Fattah, AI-Mosawi, and AI-Zayadi (2013, 2014); and Cui, Luan, and Zhao (2009).

In general, there have been relatively few studies, especially experimental ones, of the long-term behavior of PRFs on clay. Therefore, one of the difficulties of the design of PRFs on clay is the lack of reliable information for predicting the settlement and for estimating the behavior of such foundations for their entire service life.

With the desire to expand the PRF application on clay, especially in Southeast Asia and East Asia countries where the clay ground is thick and common, this research aims to investigate the fundamental mechanisms of the long-term behavior of vertically loaded PRFs on saturated clay using both small-scale physical modeling and numerical method.

1.2 Scope of the study

The main objectives of this research are as follows:

1. Investigate the long-term behavior of vertically loaded PRFs supported by jacked-in piles on saturated clay through a series of experiments. In each experiment, focuses are placed on the PRF settlement, the load sharing between the raft and the piles, the axial forces distributed along the piles, the changes of PWP at the raft base, and the changes of soil strength beneath the raft base. The behaviors of PRFs were obtained for the full experimental duration (including the load-increasing period, the primary consolidation period, and the secondary consolidation period) for different PRF cases. A series of tests were performed with different pile numbers or different pile spacing to obtain the long-term behavior of PRFs with different pile arrangements.

2. The jacked-in piles were used for the PRF, static load tests of individual piles and pile group were conducted before conducting the static load tests of piled rafts, therefore, the effect of the jacking process on the pile resistance, the influence of pile interaction on pile resistance, the behavior of pile group supported by jacked-in piles in clay are also other objectives of this research.

3. Numerical analyses of the experiments were carried out. The three dimensional FEM software, PLAXIS 3D, was adopted to analyze the behavior of the model foundations supported by jacked-in piles to confirm the experimental results and to obtain more deeply the mechanisms of the long-term behavior of the PRFs on clay.

1.3 Thesis structure

The thesis consists of the following chapters:

Chapter 1 is the introduction chapter of this thesis

Chapter 2 is the literature review chapter. In this chapter, the previous researches related to PRFs on clay ground are briefly reported.

Chapter 3 presents the experimental study on behaviors of PRFs. For the description of the experiments in this chapter, the techniques used for the present work are described in detail. Also outlined in this chapter are soil investigation techniques and their results. The experimental results are presented and discussed in detail. The foundation settlement and the pile response in both the load-increasing period and consolidation periods are primary concerns. The importance of considering the interaction among the piles, the raft, the ground, and the PWP are emphasized. Furthermore, the results of soil investigation are discussed together with the results of load tests of PRF to clarify the consolidation effect on the ground strength. The comparisons of performances of PRFs with different pile arrangements are made.

Chapter 4 presents the numerical analyses of the experiments. The finite element program, PLAXIS 3D, is used to simulate the load tests on the foundation models. The influence of the jacking process on pile behavior is modeled by the volume expansion method. The simulations of laboratory soil tests such as the oedometer test and triaxial test are also conducted to select an appropriate soil model and to estimate the soil parameters.

In chapter 5, the conclusions derived from the present work are summarized. Recommendations for further study are also suggested.

References for chapter 1

Cho, J., Lee, J.H., Jeong, S., Lee, J., 2012. The settlement behavior of piled raft in clay soils. Ocean Eng. 53, 153–163. https://doi.org/10.1016/j.oceaneng.2012.06.003

Cooke, R.W., 1986. Piled raft foundations on stiff clays—a contribution to design philosophy. Géotechnique 36(2), 169–203. https://doi.org/10.1680/geot.1986.36.2.169

Cui, C.Y., Luan, M.T., Zhao, Y.H., 2009. Time-dependent behavior of piled-raft on soil foundation with reference to creep and consolidation. Electron. J. Geotech. Eng. 14 A, 1–14.

de Sanctis, L., Mandolini, A., 2006. Bearing capacity of piled rafts on soft clay soils. J. Geotech. Geoenviron. Eng. 132(12), 1600–1610. https://doi.org/10.1061/(ASCE)1090-0241(2006)132:12(1600)

EI-Mossallamy, Y., 2002. Innovative Application of Piled Raft Foundation in Stiff and Soft Subsoil. Proc. of International Deep Foundations Congress, 426-440. https://doi.org/10.1061/40601(256)31

Fattah, M.Y., Al-Mosawi, M.J., Al-Zayadi, A.A.O., 2013. Time dependent behavior of piled raft foundation in clayey soil. Geomech. Eng. 5, 17–36. https://doi.org/10.12989/gae.2013.5.1.017

Fattah, M.Y., Al-Mosawi, M. J., Al-Zayadi, A. A. O., 2014. Contribution to Long Term Performance of Piled Raft Foundation in Clayey Soil. International Journal of Civil Engineering and Technology 5(7), 130–148.

Hooper, J.A., 1973. Observations on the behaviour of a piled-raft foundation on london clay. Proceedings of the Institution of Civil Engineers 55(4), 855–877. https://doi.org/10.1680/iicep.1973.4144

Horikoshi, K. (1995). Optimum Design of Piled Raft Foundations. PhD thesis, The University of Western Australia, Perth, W.A., Australia.

Horikoshi, K., Randolph, M.F., 1996. Centrifuge modelling of piled raft foundations on clay. Géotechnique 46(4), 741–752. https://doi.org/10.1680/geot.1996.46.4.741

Horikoshi, K. and Randolph, M.F. 1998. “A Contribution to Optimum Design of Piled Rafts”. *Geotechnique* 48, no. 3 (June): 301-317. https://doi.org/10.1680/geot.1998.48.3.301

Horikoshi, K., Randolph, M.F., 1999. Estimation of overall settlement of piled rafts. Soils and Foundations 39(2), 59-68. https://doi.org/10.3208/sandf.39.2_59

Karim, H.H., Al-qaissy, M.R., Hameedi, M.K., 2013. Numerical Analysis of Piled Raft Foundation on Clayey Soil. Eng. & Tech. Journal 31(7), 1297–1312.

Lee, J.H., Kim, Y., Jeong, S., 2010. Three-dimensional analysis of bearing behavior of piled raft on soft clay. Comput. Geotech. 37(1–2), 103–114.

https://doi.org/10.1016/j.compgeo.2009.07.009

Mali, S., Singh, B., 2018. Behavior of large piled-raft foundation on clay soil. Ocean Eng. 149, 205–216. https://doi.org/10.1016/j.oceaneng.2017.12.029

Mandal, S., Sengupta, S., 2017. Experimental Investigation of Eccentrically Loaded Piled Raft Resting on Soft Cohesive Soil. Indian Geotech. J. 47(3), 314–325. https://doi.org/10.1007/s40098-017-0235-9

Rodriguez, E., Cunha, R. P., Caicedo, B., 2018. Behaviour of piled raft foundation systems in soft soil with consolidation process. Proc. of the 9th Int. Conf. on Physical Modelling in Geotechnics 2(21), 1407–1411.

Roshan, A., Shooshpasha, I., 2014. Numerical analysis of piled raft foundations in soft clay. Electron. J. Geotech. Eng. 19 S, 4541–4554.

Roy, S., Chattopadhyay, B. C., Sahu, R. B., 2011. Piled-Raft Foundation on Consolidating Soft Soil. Proc. of Indian Geotechnical Conference (Kochi, December 15-17), 879–882.

Sales, M.M., Small, J.C., Poulos, H.G., 2010. Compensated piled rafts in clayey soils: Behaviour, measurements, and predictions. Can. Geotech. J. 47(3), 327–345. https://doi.org/10.1139/T09-106

Small, J.C., Liu, H.L.S., 2008. Time-settlement behaviour of piled raft foundations using infinite elements. Comput. Geotech. 35(2), 187–195. https://doi.org/10.1016/j.compgeo.2007.04.004

Tang, Y.J., Pei, J., Zhao, X.H., 2014. Design and measurement of piled-raft foundations. Proc. Inst. Civ. Eng. Geotech. Eng. 167(5), 461–475. https://doi.org/10.1680/geng.13.00004

Thoidingjam, D., Prasad, D. S. V, Devi, D.K.R., 2016. Effect Of Number Of Pile In Pile-Raft System In Organic Clay. IOSR J. Mech. Civ. Eng. 13(4), 83–88. https://doi.org/10.9790/1684-1304078388

Thoidingjam, D., Devi, K.R., 2017. Behavior of Pile Raft Foundation in Organic Clay. Indian J. Sci. Technol. 10(31), 1–4. https://doi.org/10.17485/ijst/2017/v10i31/113867

Russo, G., Viggiani, C., 1995. Long Term Monitoring of a Pile Foundation. Proc. FMGM 95-4th International Symposium, Bergamo, Italy, 283–290.

Yamashita, K., Kakurai, M., Yamada, T., 1994. Investigation of a Piled Raft Foundation on Stiff Clay. Proc. XIII CIMSTF, New Delhi, India, 543–546.

Chapter 2

Literature review

2.1 Introduction

The behavior of PRFs has been investigated for several decades. A humorous number of researches related to the behavior of PRF has been conducted; among these researches, a major number of publications related to the behavior of PRFs on sandy ground although rather few papers have dealt with the behavior of PRF on clayey ground. This chapter reviews briefly the merits of the previous researches on PRF, in which, the primary concern is placed on the research of PRF on cohesive ground. The literature survey on PRF on clay is classified into immediate behavior (short-term behavior) and time-dependent behavior (long-term behavior). Analytical techniques, experimental techniques, as well as reports on field observations are reviewed.

2.2 Overview of piled raft foundation

2.2.1 Concept of piled raft foundation

In the traditional approach, there are two types of foundation usually used: (i) shallow foundation (raft/ cap foundation) of which the raft guarantees a sufficient safety margin against bearing capacity failure and contemporarily experiences settlements under working loads, this foundation is usually used to support light structure; (ii) pile group foundation of which the piles are designed to support 100 % of the applied load and the contact between raft and soil is neglected, this foundation is usually used to support heavy structure. However, when designing a piled foundation, the group of piles is always surmounted by a cap connecting piles' heads. If this cap is in direct contact with the ground, it will contribute to carrying a portion of the applied loads. In the latter case, the full system involving piles, cap, and soil constitutes a mixed foundation system and is generally referred in literature to as a "piled raft foundation" (Mandolini, Laora, and Iodice 2017). Fig. 2.1 shows the definition of different foundation systems. In the figure, the load sharing ratio α_r is defined as the ratio of the proportion of load supported by the raft Q_r and the total applied load Q_{pr}. Of course, when the raft supports 100 % applied load (the case of shallow foundation), α_r = 1, and oppositely when the piles support 100 % applied load (the case of pile group

foundation, and the raft is not contacted to the ground surface), $\alpha_r = 0$. For the case of piled raft foundation, $0 < \alpha_r < 1$.

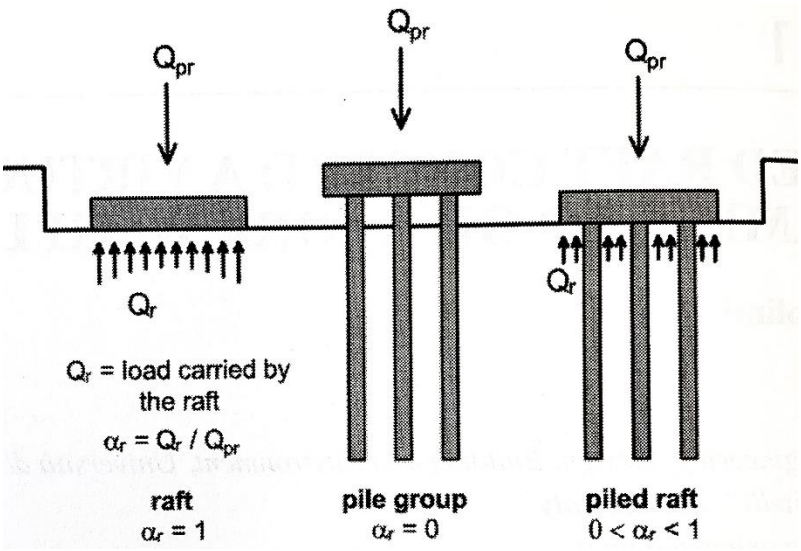

Fig. 2.1. Definition of different foundation systems (Mandolini, Laora, and Iodice 2017).

2.2.2 Design methods for piled raft foundation

The design tools for piled raft foundations indicated in previous researches range from simplified calculation to complex numerical analyses and simple analyses. According to Poulos (1997), the analysis methods of piled raft foundations can be classified into the following categories:

1. Simplified calculation methods (e.g. equivalent raft/ pier method);
2. Approximation computer-based methods (e.g. plate on springs approach);
3. More rigorous computer-based methods (e.g. boundary element methods, three-dimensional finite element analysis).

Simplified approaches involve simplifications concerning the modeling of the soil profile and loading conditions on the raft. Poulos and Davis (1980) presented a hand calculation method for constructing the overall load-settlement curve to failure. The elastic solution is used to the initial stiffness of the piled raft, the stiffness of the raft alone, and the ultimate capacities of the piles and raft. This method results in a trilinear load-settlement relationship (Fig. 2.2) and the flexibility of the raft is not considered. Randolph (1994) developed a simple approximate equation for the stiffness of a piled raft system and the load-sharing between the piles and the raft, and this method suited to the conventional design with the linear behavior of foundation (Fig. 2.3). Poulos (2001) presented the extension of the method proposed by Poulos and Davis (1980) using the simple method of estimating the load sharing between the raft and the piles outlined by Randolph (1994) to estimate the load-settlement behavior. In general, these simple approaches provide the bi-linear load-

settlement relationship for the piled raft and the load sharing between pile group and raft under the following assumption: (i) piles and raft behave as linearly elastic systems until failure; (ii) the raft is rigid and subjected to a vertical central load, hence only a uniform vertical displacement can occur.

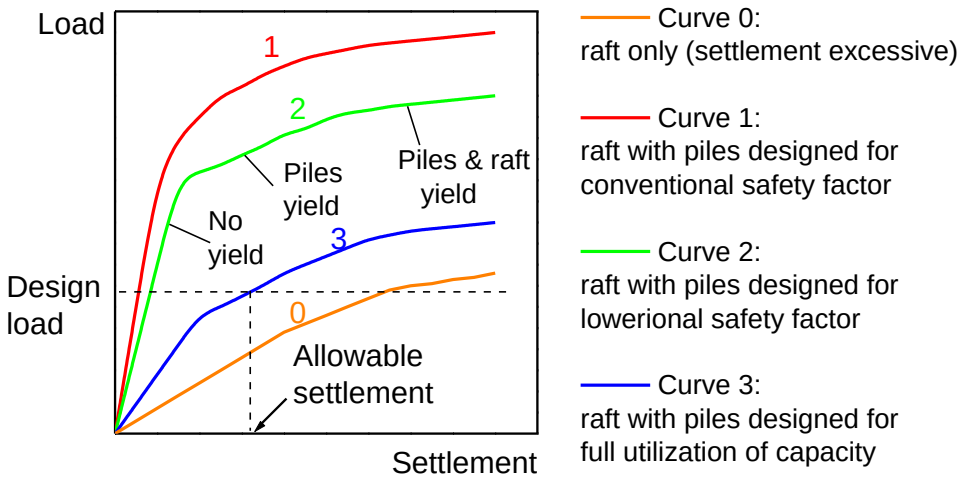

Fig. 2.2. Typical load-settlement curves for piled rafts (Poulos and Davis 1980).

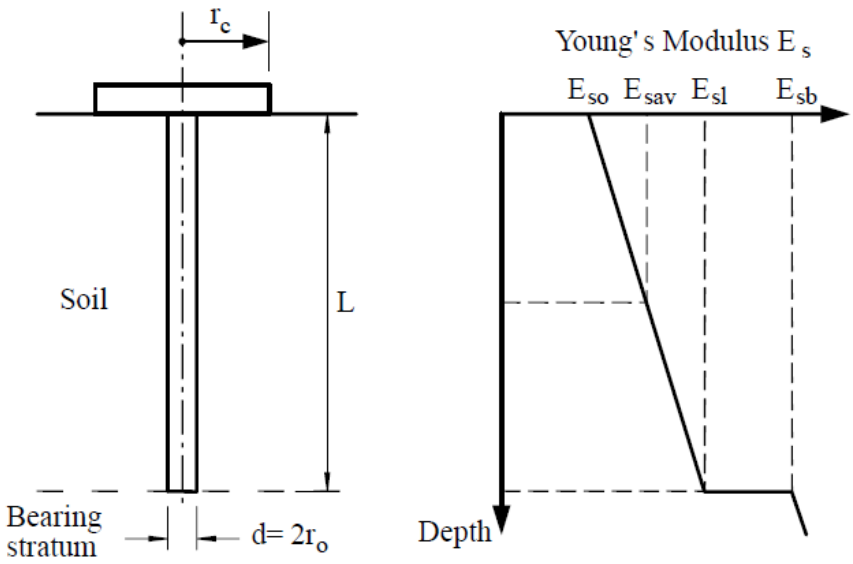

Fig. 2.3. Simplified representation of piled raft unit (Randolph, 1994).

Burland (1995) introduced the following simplified process of design when piles are designed as settlement reducers:

- Estimate the total long-term load-settlement relationship for the raft without piles (see Fig. 2.4). The design load P_0 gives a total settlement S_0.

- Assess an acceptable design settlement S_a, which should include a margin of safety.
- P_1 is the load carried by the raft corresponding to S_a.
- The load excess P_0- P_1 is assumed to be carried by settlement-reducing piles. The shaft resistance of these piles will be fully mobilized and therefore no factor of safety is applied. Burland suggested a mobilization factor of about 0.9 for ultimate shaft capacity, P_{su}.
- If the total load on the piled raft exceeds P_{su}, the piled raft may be analyzed as a raft (Fig. 2.4(c)).
- The bending moment in the raft can be obtained by analyzing the piled raft as a raft subjected to the reduced Q_r= Q- 0.9 P_{su}.

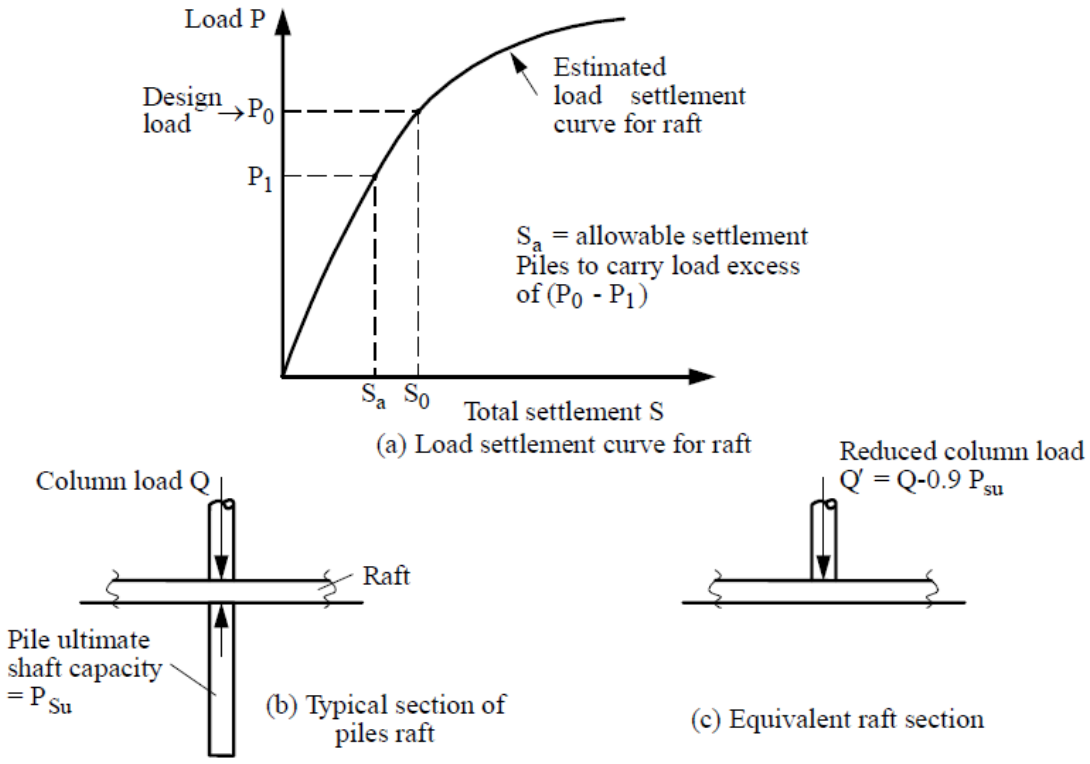

Fig. 2.4. Simplified design concept (Burland, 1995).

For approximate computer-based analyses:

The methods employing a strip on springs was presented by Poulos (1991) in which a section of the raft is represented by a strip, and the supporting piles by springs.

Methods employing a plate on springs were presented early by Hongladaromp et al (1973), Brown et al (1975) in which the raft is presented by an elastic plate, while the piles are modeled as springs supporting the plate. Clancy and Randolph (1993) adopted a refined approach in which each pile is modeled as a series of rod finite elements while the raft is

analyzed via two-dimensional thin-plate finite elements. Parametric studies were conducted to investigate the effect of raft stiffness, pile spacing, pile length, and pile stiffness. A similar type of analysis has been outlined by Franke et al. (1994), Yamashita et al. (1993).

More rigorous numerical methods: Complex numerical analyses such as boundary element methods, combining boundary element and finite element analysis, or three-dimensional finite element analysis have been developed to analyze the behavior of piled raft foundations in comprehensive conditions.

Russo (1998) using FEM developed an approximate method for the analysis piled raft foundations subjected to vertical load. The raft is modeled as a thin plate, the piles and soil are modeled as linear or non-linear interacting springs using the superposition factors. A computer program NARA (Non-linear Analysis of Piled RAfts) was created. The results predicted by NARA were compared with the measured data and those calculated by Poulos (1994).

Kitiyodom and Matsumoto (2002 and 2003) presented an approximate method for the analysis of piled raft foundations. The analysis approach is similar to those used by O'Neill et al. (1977), Chow (1987), and Clancy and Randolph (1993), however, two additional soil springs in the horizontal plane are attached at each node of the piles and the raft to take into account the bending of the piles, the lateral soil resistance to the piles, and the shear resistance between the raft base and the soil surface (Fig. 2.5). This approach could solve the behavior of piled foundations having batter piles. The raft is modeled as the plate elements and the piles are modeled as beam elements using FEM. The numerical procedure is implemented via a computer program PRAB (Piled Raft Analysis with Batter piles).

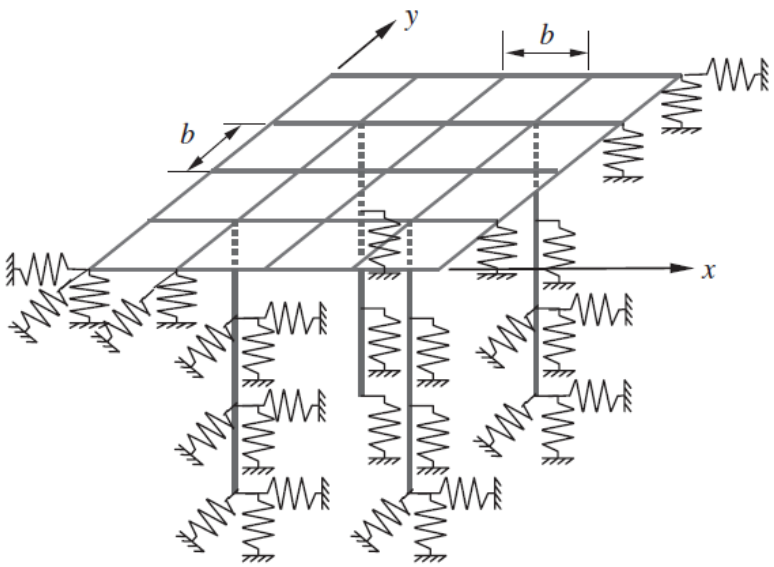

Fig. 2.5. Plate-beam-spring modeling of a piled raft foundation (Kitiyodom and Matsumoto, 2002).

More rigorous approaches for the analysis of piled raft foundations, especially the combining boundary element and finite element analysis and three-dimensional finite element analysis, based on numerical analysis methods are presented in the parts of numerical study in section 2.3.

2.3 Previous research of piled raft foundation on clay

2.3.1 Research on immediate behavior of piled raft foundation

2.3.1.1. Experimental study

Various methods have been used in previous investigations to study the short-term behavior of PRFs on the clayey ground until the end of the construction period. Regarding experiments, Cooke (1986) carried out a series of small-scale model tests on unpiled rafts, free-standing piles, and piled rafts of various sizes on homogeneous stiff clay to assess how the number of piles and their spacing affected the behavior of foundations when they were subjected to loads with the same safety factor. Cooke (1986) pointed out that the load sharing in a PRF depends on (i) the magnitude of the applied load and (ii) the stiffness of the structure–foundation system. Regarding the effect of pile length, Cooke (1986) found that, when the ratio of pile length to raft breadth was less than 2, the settlement reduction may be between 1/3 and 1/2 of the unpiled raft settlement under the same applied load. He suggested that to obtain the maximum benefit from piles included for reducing settlement, the piles should be long relative to the breadth of the foundation. Regarding the effect of pile spacing, Cooke (1986) found that (i) at pile spacings that are closer than the critical spacing at which block behavior of free-standing groups occurs, piled rafts and free-standing groups of the same size have similar ultimate bearing capacities and similar immediate settlements at working loads. (ii) At pile spacings that are wider than the critical spacing, the ultimate bearing capacity of a pile group can be increased significantly by a raft formed on the clay surface.

Horikoshi (1995) and Horikoshi and Randolph (1996) used centrifuge modeling to investigate (i) the role of a small centered pile group in reducing the differential settlement of the piled raft foundation and (ii) the load transferred to these center piles; they suggested that even a small pile group could reduce the differential raft settlement significantly despite rather low loads being transferred to the piles, and they indicated that under the maximum load of PRFs, the load carried by the piles is smaller than the pile capacity estimated from load tests on single (capped) piles. Also, they found from the test results that the proportion

of the pile load decreased with increasing the total applied load, however, there was no evidence of any marked increases in the differential settlement at high load level.

Dey and Ghosh (2016) studied the effect of pile number, pile length, pile diameter, and raft thickness on the behavior of vertically loaded piled raft foundations on cohesive soil through a series of laboratory model tests. From experimental results, they found that the foundation settlement decreased with increasing pile number, pile length, pile diameter, and raft thickness. The pile act as settlement reducers, however, the use of a large group of piles is not always beneficial from both economical and settlement point of view. They also concluded that for the combined pile-raft foundation systems, the design is based on a specified maximum allowable settlement. Similarly, Thoidingjam, Prasad, and Devi (2016) and Thoidingjam and Devi (2017) conducted laboratory piled raft model tests to exam the influence of raft thickness and pile number on the behavior of pile-raft systems in organic clay and reported similar results.

Recently, some other experimental studies were conducted to investigate how foundation configurations, the structural load properties, and the underground water level affect the load sharing and settlement of PRFs on clay (Roy, Chattopadhyay, and Sahu 2011; Mandal and Sengupta 2017; Rodríguez, Cunha, and Caicedo 2018).

2.3.1.2. Numerical study

De Sanctis and Mandolini (2006) evaluated the bearing capacity of vertically loaded piled rafts from the separate ultimate capacities of the raft and the pile group by using a three-dimensional finite-element program (the FE code ABAQUS). The analysis was conducted on different foundation systems (including circular footing and one pile, unpiled rafts, pile group, and piled raft) resting on clay in undrained conditions. In the analysis, De Sanctis and Mandolini (2006) used the elastoplastic soil model with a Tresca yield surface. From the FE analysis, they found that the proportion of the total load, carried by the piles at failure state, is nearly constant and equal about to unity, with the piles beneath the raft achieving the same capacity as for a free-standing pile group. By contrast, the proportion of the load taken by the raft at failure is typically less than unity, depending on the pile layout and geometry. They also suggested that the estimated safety factor of the complete foundation by merely multiplying the sum of the safety factors of the separate components for an overall multiplier ranging between 0.8 and 1. The safety factor of a piled raft is slightly lower than the sum of the two safety factors of the unpiled raft and the pure pile group.

Lee, Kim, and Jeong (2010) used a 3D finite element method to study the bearing behavior of a piled raft on soft clay. A series of vertically loaded foundation models with various pile lengths, pile configurations, and a square raft were analyses. In the analyses,

Lee, Kim, and Jeong (2010) paid attention to the pile-soil slip interface, on relatively stiff soil properties, and loading types also. They pointed out form analysis results that the average settlements were larger when the slip interface was used, the pile load distributions depended on pile spacing and slippage at the pile-soil interface. For both stiff and soft ground, the piled raft coefficient was highly dependent on both pile arrangement and loading properties as the piled raft coefficient decreased with increasing pile spacing and increasing load level. Regarding bearing behavior (see Fig. 2.6), at the settlement level of 0.35 % raft width, the safety factor of a piled raft was about 4-8 on soft clay and about 4 on stiff clay.

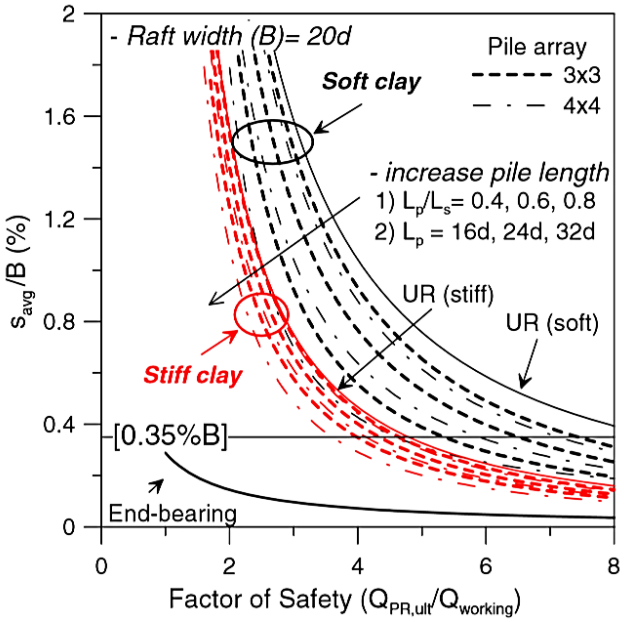

Fig. 2.6. Average settlement ratios with overall factor of safety (Lee, Kim, and Jeong 2010).

Cho et al. (2012) investigated the settlement behavior of a square piled raft on clay through a three-dimensional finite element program (ABAQUS) with an emphasis on quantifying the reduction of the average and differential settlements in soft and stiff clayey ground. In the analysis, the effect of pile-soil slip interface, loading types, and foundation configurations were considered. In terms of average settlement, Cho et al. (2012) suggested that average settlement could be reduced effectively with wider pile spacing with the same pile number. In addition, the pile efficiency was maximized when the applied load on the piled raft was similar to the ultimate capacity of the corresponding pile group. In terms of differential settlement, Cho et al. (2012) pointed out that the centered piles helped to reduce differential settlement effectively, however, the required pile installation area for minimizing differential settlement depended on pile number, pile size, and load level (see Fig. 2.8). In terms of soil type, Cho et al. (2012) showed that for minimizing differential settlement, the

required pile installation area is slightly larger in case of soft clay, compared to that of stiff clay in the same pile array (see Figs. 2.7 and 2.8).

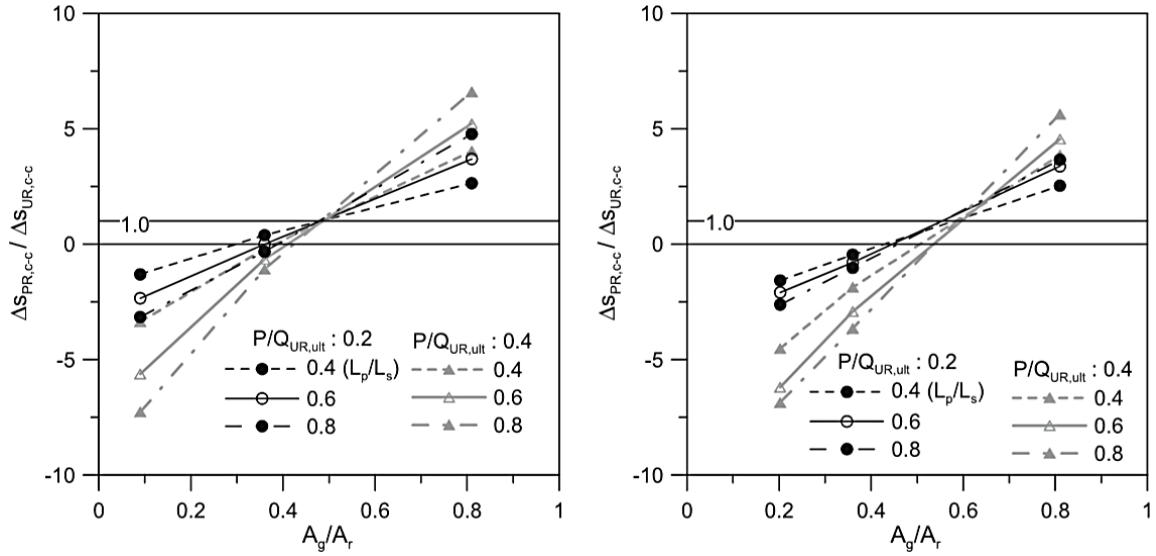

(a) (b)

Fig. 2.7. Normalized differential settlements with pile group-raft raft area ratio (soft clay): (a) 3×3 array; (b) 4×4 array (Cho et al. 2012).

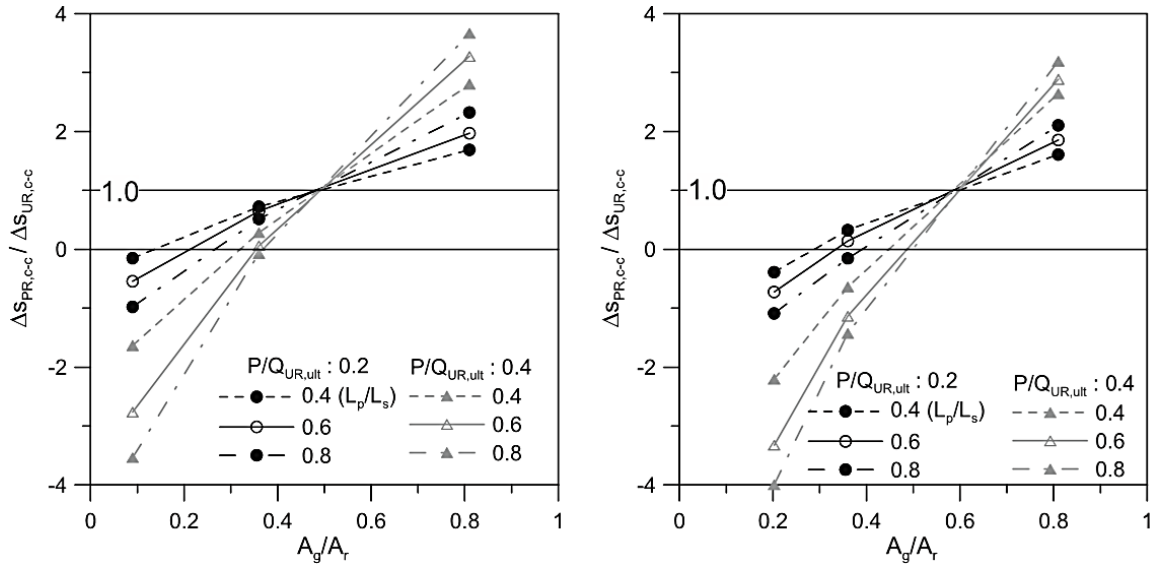

(a) (b)

Fig. 2.8. Normalized differential settlements with pile group-raft raft area ratio (stiff clay): (a) 3×3 array; (b) 4×4 array (Cho et al. 2012).

Bisht and Singh (2012) used geotechnical finite element software, Plaxis 2D, to model a series of piled raft foundations with the same length and width of rafts but the difference in raft thicknesses, pile lengths, pile spacings, and pile numbers. They modeled

the foundations by a linearly elastic material and the single-layer highly cohesive ground soil by elastic-perfectly plastic material with Mohr-Coulomb yield criteria. The water table was very deep and the undrained condition was assumed (total stress analysis). They found from the FEM results show that the raft thickness did not have a pronounced effect on the overall settlement but it did minimize the differential settlement. However, at the higher thickness, they found that the overall and differential settlement was the same and the thick raft, therefore, was not recommended (from an economic point of view). The overall settlement of long piles was smaller than short piles but pile length did not have any significant effect on the differential settlement. Pile spacing has a major influence on both the overall and the differential settlement. Both the settlements increased with increasing pile spacing, and greater influence was observed in the case of center-edge differential settlement as the pile spacing increased from 3*D* to 6*D*. The use of a large group of piles is not always beneficial from both economical and settlement point of view. The overall settlement decreases with the increase in the number of piles but the differential settlement does not change in a similar trend. The differential settlement is less when a small group of the pile was placed at the center of the raft.

By a numerical method, Karim, AL-Qaissy, and Hameedi (2013) modeled a series of piled rafts through a computer program (Plaxis 3D Foundation V 1.1) to evaluate the effect of parameter on the load-settlement behavior of foundations. In the analysis, the soft clay ground was modeled by the Mohr-Coulomb model. The results from Plaxis analyses show that the pile number affected to the average load carried by the piles. The pile spacing influenced directly to the pile interaction. The proportion of pile load in a piled raft decreased moderately when the spacing between piles increased from 3 to 10 times of pile diameter. In comparison to a corresponding shallow foundation (piled raft foundation), the piled raft reduced foundation settlement significantly.

Roshan and Shooshpasha (2014) also investigated the influence of various factors such as raft thickness, pile length, pile spacing, and pile number on the behavior of piled raft foundation on soft clay by using the finite element software, Plaxis 3D Foundation. In their research, the Mohr-Coulomb Elasto-Plastic medium model was employed to model ground soil, and Linear Isotropic was selected for raft and piles. Roshan and Shooshpasha (2014) pointed out from Plaxis results that the increase of raft thickness helped to reduce both average settlement and differential settlement (Fig. 2.9), however, it is more effective on reducing the differential settlement than on reducing the average settlement. Furthermore, when the raft thickness increased to a reference value (2.5 m in their study), the effect in differential settlement and total settlement reduction were basically optimal. When the raft thickness was over the reference value, the effect in differential settlement and total

settlement reduction did not increase significantly. Both the raft stiffness and pile stiffness had an important role in determining the total and differential settlement of the foundation. Roshan and Shooshpasha (2014) also found out that the differential settlement decreased with the increase of pile length, however, when the increase of pile length reached a reference value (20 m in their study), the effect of increasing pile length on reducing differential settlement was basically reached optimum efficiency (Fig. 2.10).

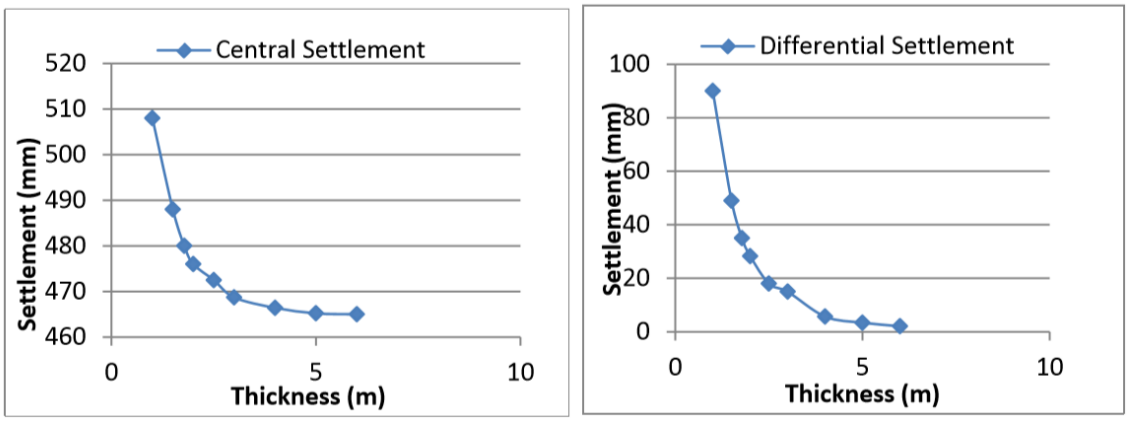

Fig. 2.9. Plots of central and differential settlement against thickness of raft (Roshan and Shooshpasha (2014)).

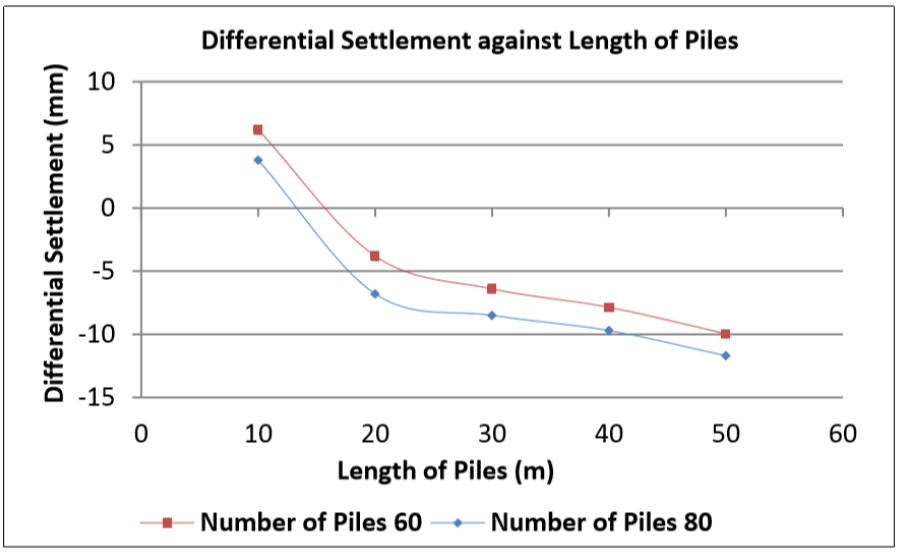

Fig. 2.10. Variation of differential settlement with pile length (Pile spacing 3.0 m) (Roshan and Shooshpasha (2014)).

Mali and Singh (2018) study the effect of different parameters on the behavior of large piled-raft foundation on a clay soil through PLAXIS 3D software. In the study, they focused on the effect of pile size, pile spacing, and raft-soil stiffness on the foundation settlement, the load-sharing, bending moments, and shear force. Mali and Singh (2018)

found that both average settlement ratio and differential settlement ratio decreased effectively when increasing the pile spacing up to 5-6 times of the pile diameter, but increased gradually thereafter (when increasing the pile spacing over 5-6 times of the pile diameter). They pointed out that raft with smaller raft-soil stiffness ratio and larger pile group to raft width ratio observed to be effective in decreasing the average settlement ratio. The load shared by the piles decreased with the increase in pile spacing meanwhile it increased with the increase in pile length. The bending moment was affected marginally when raft-soil stiffness increases more than 0.09. The shear force increases as the raft-soil stiffness ratio increase. At any raft-soil stiffness ratio, shear force at the edge pile is noted to be minimal, compared to inside piles. The maximum bending moment and maximum shear force in the raft increases when the raft-soil stiffness ratio increases.

Finally, there have been some numerical studies on other aspects of piled raft foundation behavior on clay (Poulos, Small, and Chow 2011; Reul and Randolph 2003; Reul 2004; Liang, Chen and Han 2009; Tran, Kimura, and Boonyatee 2012; Wulandari and Tjandra 2015; Sinha and Hanna 2017; Wood and Karstunen 2017; Watcharasawe, Kitiyodom, and Jongpradist 2015)

2.3.1.3. Field observation

Regarding field measurements, Yamashita, Kakurai, and Yamada (1994) observed the behavior of the PRF of a five-story building on stiff clay in Urawa City. The average contact pressure of the building was 84 kPa with the local maximum contact pressure of 101 kPa. Yamashita, Kakurai, and Yamada (1994) measured the building settlement, the axial forces on twelve piles, the earth contact pressure, and pore water pressure beneath the raft base for whole the construction time of 300 days. They reported that the proportion of the load carried by the piles to the building load on the tributary area was 49% at the end of the construction, with settlements amounting to 10–20 mm.

2.3.2. Research on long-term behavior of piled raft foundations

2.3.2.1. Numerical study

Small and Liu (2008) used three-dimensional finite element analysis to estimate the consolidation rate of piled rafts and to calculate the development of the magnitude of differential deflections as well as associated moments in the raft with time. In their study, they used 8-noded isoparametric shell elements to combine the raft stiffness with the soil stiffness. The soil was treated as a poroelastic material and modeled by three-dimensional

finite elements in the region of interest, but infinite consolidation elements were used to model the lateral boundaries. Small and Liu (2008) focused on the consolidation aspect, but not on the creep settlements. For estimating the consolidation rate for the piled rafts, the simple technique of treating the foundation as an equivalent block having the same size in the plan as the raft was using in their analyses. Small and Liu (2008) found that their method could reproduce the excess pore pressures beneath a surface raft, and could estimate consolidation rates for piled rafts. Also found from the analytic solution, the behavior of full-scale structures could be modeled. The time-dependent moments in the raft may also be calculated.

Fattah, AI-Mosawi, and AI-Zayadi (2013) used ABAQUS computer program, a finite element tool, to investigate the consolidation settlement of piled rafts on clayey grounds, detect the excess pore water pressure dissipation, and effect of the consolidation process on the bearing capacity of five piled raft foundations with different configurations. Fattah, AI-Mosawi, and AI-Zayadi (2013) modeled the soil by the modified Drucker-Prager constitutive model. They pointed out from the FEM results that the time-dependent behavior of soil under the consolidation process had obvious effects on the pile-raft-soil interaction system. The time variation characteristics of excess pore pressure in the soil were associated intimately with the raft dimensions. They suggested that the excess pore water pressure dissipation had a considerable effect on the final foundation settlement, and enough attention should be paid to the settlement change with time.

Fattah, AI-Mosawi, and AI-Zayadi (2014) continued to study time-dependent behavior of piled raft foundations on saturated clay, using the same method as they did in 2013 (Fattah, AI-Mosawi, and AI-Zayadi 2013). However, in this research, they placed the focus on the effects of raft thickness, pile length, pile diameter, and pile-soil stiffness ratio. The influence of a granular cushion with different thicknesses between the raft base and the clay ground was also studied. They showed from numerical results that the load distribution between piles became more uniform with the increase of raft thickness. For a high stiffness raft, the pile may share the same loads. The increments of pile diameter led to the decrement of pore water pressure beneath the raft base, reducing the settlement, changing the shape of moment distribution in the raft, and also increasing the load carried by the piles. The load taken by the piles firstly increased with increasing relative pile-soil stiffness (from 100 to 1000 in their study), after that, the pile load remained unchanged for higher values of pile-soil stiffness. They also found that the center piles carried higher loads than the other piles at small values of pile-soil stiffness, but all piles approximately share the same proportions of load at a higher value of pile-soil stiffness. The granular cushion help to enhance the raft bearing capacity and reduce both the total settlement and differential settlement.

Cui, Luan, and Zhao (2009) used a fully coupled finite-element method of consolidation with an elasto-viscoplastic soil model to analyze the time-dependent effects of soil deformation on the interaction behavior of piled raft. They found that the increased rate of pore-water pressure resulting from the coupled viscous and Mandel-Cryer effects is identical to the decrease rate of pore-water pressure due to drainage, the pore-water pressures will gain their peak. The higher the modified creep index and the lower permeability, the more considerable the delay of the pore-water dissipation. For the time-dependent deformation behavior of raft, they pointed out that the raft differential settlements increased with time and approached to a certain value later. For the time-dependent pile behavior (Fig. 2.11), they presented that the axial deformations of center piles decreased at the beginning period and increased afterward, by contrast, the axial deformations of the edge piles increased monotonically with time. They explained that the varying pile deformation characteristics were related to both the time factor and the distribution of pore water pressure beneath the piled raft foundation. The soils adjoining the center piles were affected more considerably by both the coupled viscous and Mandel-Cryer effects, therefore, the soil effective stresses at raft center area decreased at the beginning period and then increased. They also showed the corresponding axial forces along an edge pile (Fig. 2.12). In general, they noted that it is necessary to include the creep behavior of clay to analyze piled raft behavior on soft clay accurately.

Watcharasawe, Kitiyodom, and Jongpradist (2017) investigated the consolidation effect on load sharing behaviors of high-rise and low-rise buildings supported by piled raft foundations on soft soil in the north of Bangkok, Thailand. The finite element program PLAXIS 3D was employed for the study. The soil was modeled by Mohr-Coulomb model and Hardening Soil Model with small strain. Watcharasawe, Kitiyodom, and Jongpradist (2017) pointed out that the consolidation had a strong influence on the load carried by piles on Bangkok soil. The load carried by piles increased by up to 12 % for the case of low-rise buildings and 6 % for the case of high-rise buildings. The increment of consolidation settlement had a significant influence on the increment of the load sharing ratio. They suggest that the consolidation effect should be considered when designing a PRF system on Bangkok subsoil.

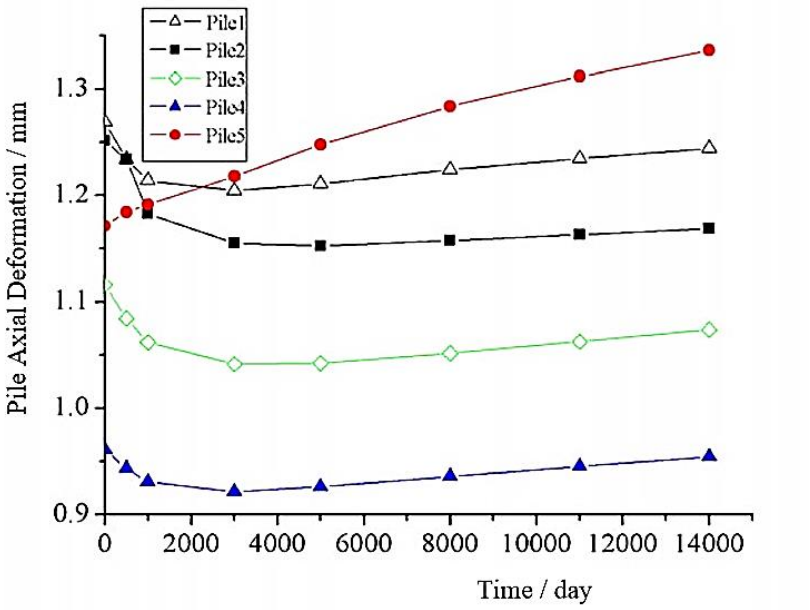

Fig. 2.11. Variation of axial deformations of piles with time (Cui, Luan, and Zhao 2009).

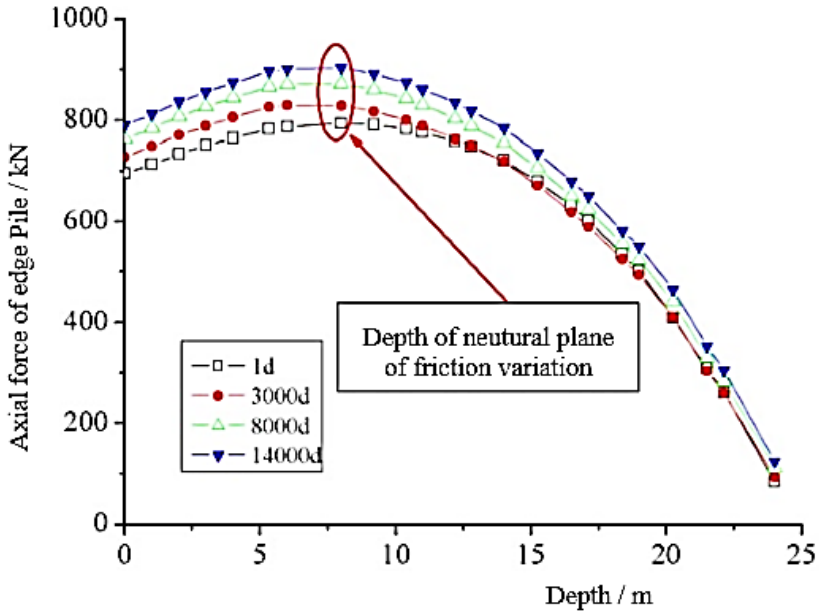

Fig. 2.12. Variation of axial forces of edge pile along depth at different times (Cui, Luan, and Zhao 2009).

2.3.2.2. Field observation

Hooper (1973) combined field observations and a numerical method to analyze the load sharing and settlement with time of a PRF supporting a 90-m-high building on London clay. From the field observations, Hooper (1973) reported that the PRF settlement rate far exceeded what might be expected based on the laboratory values of the coefficient of

consolidation, and it took only 6 years from the start of construction to complete the primary consolidation settlement. At any stage of the construction, the load sharing between the raft and the piles depended on the ratio of uplift force to vertical structural load. At the completed structure, the ratio of uplift force to vertical structural load is about 0.3, and the piles carried approximately the same load. From the results of both field measurements and numerics, Hooper (1973) indicated that during the consolidation process, the load carried by the piles increased and the raft contact pressures decreased from those at the start of the consolidation process, however, the raft will probably be carrying a significant proportion of the applied load.

Yamashita and Kakurai (1991) observed the settlement of a piled raft foundation with large pile spacing of 8.4 - 22 times the pile diameter on layered ground, in which, the ground soil composed of diluvial over consolidation clay and sand. The Observations were made for the foundation settlement, the contact pressure between the raft base and the soil, and the load transferred to piles at different locations on the foundation plan from the beginning of construction until almost 4 years after the completion of the construction. Yamashita and Kakurai (1991) reported that the pile load continued growing after the completion of the building for 1 year. After that, the axial forces had converged to almost fixed values. At the time of building completion, the piles carried about 51% of the building load on the tributary area and the foundation settlement was around 1 cm. The corresponding proportion of load carried by the piles increased to 56% at the time of one year after the completion of the construction.

Russo and Viggiani (1995) monitored the load sharing between the raft and the piles and the load distribution among different piles at the Garigliano Bridge in Italy; they reported that while the applied load did not increase, the total load taken by the piles did increase, in which the load taken by the inner piles increased and correspondingly that taken by the peripheral piles of the group decreased.

Yamashita et al. (2011) by monitoring full-scale measurements investigated the settlement behavior and the load sharing between the rafts and the piles of five case histories of piled raft foundations in Japan. The field measurements were conducted from the beginning of the construction stage to 17 to 60 months after the end of the construction stage. It was indicated from the measured results that piled rafts worked more effectively at a pile spacing ratio, S/D, larger than six, in which the raft can carry at least 30% the effective load of the structure.

In a more recent study using field observations, Tang, Pei, and Zhao (2014) analyzed long-term data on three piled raft foundations supported three multi-story residential buildings to propose an improved design method that has the potential to reduce construction

costs. From the measured results, they found no fixed value for the ratio between the pile load and the soil (raft) load and that the ground pressures, pile loads, and settlements varied with the pile arrangement, time, and external loads. Tang, Pei, and Zhao (2014) suggested that pile spacing and safety factors of the pile, particularly pile spacing, were the key parameters for the load sharing between the raft and the piles. In the study cases, when pile spacing was greater than five times of pile diameter, the pile bearing capacity could be mobilized, and the exceeding loads (exceed the pile bearing capacity) can be carried by the soil (raft).

2.3.2.3. Experimental study

At present, in the author's knowledge, there is no experimental study on the long-term behavior of piled raft foundation on clay.

2.4. Summary chapter 2

In this chapter, previous research works on piled raft foundations on clay have been reviewed briefly. From the literature review, numerous studies have investigated many aspects of the immediate (short-term) behavior of piled raft foundations on clay. However, there have been relatively few studies, especially experimental ones, of the long-term behavior of piled raft foundations on clay. Therefore, one of the difficulties of the current design of PRFs on clay is the lack of reliable information for predicting the long-term settlement and for estimating the long-term behavior of such foundations for their entire service life.

In practical design procedures for piled raft foundations, the application of numerical methods in the calculation is indispensable, especially the finite element method with computer programs. To have high reliability in calculated results, it is required to validate the calculation results to the corresponding results of the loading tests. The full-scale loading tests or the large-scale loading tests at the construction fields are considered as the most reliable tests for the validation of the design method. However, the large-scale loading tests with the field structure measurements are difficult to implement because they are costly and require a lot of time, construction equipment, measurement devices, and labor. Otherwise, the full-scale loading tests were only conducted during and after the completion of the construction stage. One feasible approach for the validation is conducting the comparisons between the simulated results and the measured results of the small-scale loading tests. If the calculated results are satisfied with the experimental results, the calculation method then could be applied approximately to analyze the corresponding full-scale load tests.

Therefore, the main aim of this research is to use small-scale physical modeling to investigate the fundamental mechanisms of the long-term behavior of a series of vertically loaded piled raft foundation models on saturated clay. After that, the simulations of the experiments were conducted and the calculated results were compared with the experimental results. The findings are derived and the feasibility of the design method is confirmed through the experimental and the calculated results.

References for chapter 2

Alnuaim, A.M., El Naggar, M.H., El Naggar, H., 2018. Performance of micropiled rafts in clay: Numerical investigation. Comput. Geotech. 99, 42–54. https://doi.org/10.1016/j.compgeo.2018.02.020

Bisht, R.S., Singh, B., 2012. Study on behaviour of piled raft foundation by numerical modelling. Proceeding of SAITM Research Symposium on Engineering Advancements, 27th–28th April, Off Chandrika Kumaratunga Mawatha Malabe, Sri Lanka, 23–26.

Brown, P.T., Wiesner, T.J., 1975. The behavior of uniformly loaded piled strip footings. Soils and Foundations 15, 13-21.

Brown, P.T., Poulos, H.G., Wiesner, T.J., 1975. Piled raft foundation design. In: Proc. Symp. On Raft Foundation, Perth, CSIRO, 13-21.

Burland, J.B., 1995. Piles as settlement reducers. In: Proc. of 19th National Italian Geotechnical Conference, Pavia, 21-34.

Cho, J., Lee, J.H., Jeong, S., Lee, J., 2012. The settlement behavior of piled raft in clay soils. Ocean Eng. 53, 153–163. https://doi.org/10.1016/j.oceaneng.2012.06.003

Chow, Y.K., 1987. Three-dimensional analysis of pile group. Journal of Geotechnical Engineering ASCE 113(6), 637-651.

Clancy, P., Randolph, M.F., 1993. Analysis and design of piled raft foundations. International Journal for Numerical and Analytical Methods in Geomechanics 17(12), 849-869.

Cooke, R.W., 1986. Piled raft foundations on stiff clays—a contribution to design philosophy. Géotechnique 36(2), 169–203. https://doi.org/10.1680/geot.1986.36.2.169

Cui, C.Y., Luan, M.T., Zhao, Y.H., 2009. Time-dependent behavior of piled-raft on soil foundation with reference to creep and consolidation. Electron. J. Geotech. Eng. 14 A, c

de Sanctis, L., Mandolini, A., 2006. Bearing capacity of piled rafts on soft clay soils. J. Geotech. Geoenviron. Eng. 132(12), 1600–1610. https://doi.org/10.1061/(ASCE)1090-0241(2006)132:12(1600)

Dey, R., Ghosh, A., 2016. Experimental investigation on behavior of pile-raft foundation. Proc. Indian geotechnical society, Kolkata chapter, Geotechnics for infrastructure development, 11th-12th March, Kolkata, West Bengal, India,

EI-Mossallamy, Y., 2002. Innovative Application of Piled Raft Foundation in Stiff and Soft Subsoil. Proc. of International Deep Foundations Congress, 426-440. https://doi.org/10.1061/40601(256)31

Fattah, M.Y., Al-Mosawi, M.J., Al-Zayadi, A.A.O., 2013. Time dependent behavior of piled

raft foundation in clayey soil. Geomech. Eng. 5, 17–36. https://doi.org/10.12989/gae.2013.5.1.017

Fattah, M.Y., Al-Mosawi, M. J., Al-Zayadi, A. A. O., 2014. Contribution to Long Term Performance of Piled Raft Foundation in Clayey Soil. International Journal of Civil Engineering and Technology 5(7), 130–148.

Franke, E., Lutz, B., El-Mossallamy, Y., 1994. Measurements and numerical modeling of high-rise building foundations on Frankfurt clay. In: Proc. Vertical and horizontal deformations of foundations and embankments, ASCE Geotechnical Special Publication 40, 1325-1336.

Hongladaromp, T., Chen, N.J., Lee, S.L., 1973. Load distributions in rectangular footings on piles. Geotech. Eng. 4(2), 77-90.

Hooper, J.A., 1973. Observations on the behaviour of a piled-raft foundation on london clay. Proceedings of the Institution of Civil Engineers 55(4), 855–877. https://doi.org/10.1680/iicep.1973.4144

Horikoshi, K., 1995. Optimum design of piled raft foundations. Dissertation, The Universtiy of Western Australia, W.A., Australia.

Horikoshi, K., Randolph, M.F., 1996. Centrifuge modelling of piled raft foundations on clay. Géotechnique 46(4), 741–752. https://doi.org/10.1680/geot.1996.46.4.741

Karim, H.H., Al-qaissy, M.R., Hameedi, M.K., 2013. Numerical Analysis of Piled Raft Foundation on Clayey Soil. Eng. & Tech. Journal 31(7), 1297–1312.

Kitiyodom, P., Matsumoto, T., 2002. A simplified analysis method for piled raft and pile group foundations with batter piles. International Journal of Numerical and Analytical methods in Geomechanics 26, 1349-1369.

Kitiyodom, P., Matsumoto, T., 2003. A simplified analysis method for piled raft foundations in non-homogeneous soils. International Journal of Numerical and Analytical methods in Geomechanics 27, 85-109.

Lee, J.H., Kim, Y., Jeong, S., 2010. Three-dimensional analysis of bearing behavior of piled raft on soft clay. Comput. Geotech. 37(1–2), 103–114. https://doi.org/10.1016/j.compgeo.2009.07.009

Liang, F., Chen, L., Han, J., 2009. Integral equation method for analysis of piled rafts with dissimilar piles under vertical loading. Comput. Geotech. 36, 419–426. https://doi.org/10.1016/j.compgeo.2008.08.007

Mali, S., Singh, B., 2018. Behavior of large piled-raft foundation on clay soil. Ocean Eng. 149, 205–216. https://doi.org/10.1016/j.oceaneng.2017.12.029

Mandal, S., Sengupta, S., 2017. Experimental Investigation of Eccentrically Loaded Piled Raft Resting on Soft Cohesive Soil. Indian Geotech. J. 47(3), 314–325.

https://doi.org/10.1007/s40098-017-0235-9

Mandolini, A., Laora, R. D., Iodice, C., 2017. Piled raft concept: A virtuous example to get more with less. In: Der-Wen Chang, Tatsunori Matsumoto, and Deepankar Choudhury (eds) Design and Analysis of Piled Raft Foundations, Tamkang University press, 3-14.

O'Neill, M.W., Ghazzaly, O.I., Ha, B., 1977. Analysis of three-dimensional pile groups with non-linear soil response and pile-soil-pile interaction. In: Proc. 9th Annual Offshore Tech. Conf., Houston, Texas, 245-256.

Poulos, H.G., Davis, E.H., 1980. Pile foundation analysis and design. New York, John Wiley and Sons.

Poulos, H.G., 1991. Analysis of piled strip foundations. Comp. Methods and Advances in Geomechs., Ed. G. Beer, J.R. Booker, J.P. Carter, A.A., Balkema, Rotterdam 1, 183-191.

Poulos, H.G., 1994. An approximate numerical analysis of pile-raft interaction. International Journal for Numerical and Analytical Methods in Geomechanics18, 73-92.

Poulos, H.G., Small, J.C., Ta, L.D., Sinha, J., Chen, L., 1997. Comparison of some methods for analysis of piled rafts. In Proc. of int. conf. 14th Soil Mechanic Foundation Engineering, Hamburg 2, 1119-1124.

Poulos, H.G., 2001. Piled raft foundations - design and applications. Géotechnique 51(2), 95-113.

Poulos, H.G., Small, J.C., Chow, H., 2011. Piled raft foundations for tall buildings. Geotech. Eng. J. of the SEAGS&AGSSEA 42(2), 78–84.

Randolph, M.F., 1994. Design methods for pile groups and piled rafts. In Proc. of int. conf. 12th Soil Mechanic Foundation Engineering, New Delhi 5, 61-82.

Reul, O., Randolph, M.F., 2003. Piled rafts in overconsolidated clay: Comparison of in situ measurements and numerical analyses. Géotechnique 53(3), 301–315. https://doi.org/10.1680/geot.2003.53.3.301

Reul, O., 2004. Numerical study of the bearing behavior of piled rafts. International Journal of Geomechanics 4(2), 59–68. https://doi.org/10.1061/(ASCE)1532-3641(2004)4:2(59)

Rodriguez, E., Cunha, R. P., Caicedo, B., 2018. Behaviour of piled raft foundation systems in soft soil with consolidation process. Proc. of the 9th Int. Conf. on Physical Modelling in Geotechnics 2(21), 1407–1411.

Roshan, A., Shooshpasha, I., 2014. Numerical analysis of piled raft foundations in soft clay. Electron. J. Geotech. Eng. 19 S, 4541–4554.

Roy, S., Chattopadhyay, B. C., Sahu, R. B., 2011. Piled-Raft Foundation on Consolidating Soft Soil. Proc. of Indian Geotechnical Conference (Kochi, December 15-17), 879–882.

Russo, G., Viggiani, C., 1995. Long Term Monitoring of a Pile Foundation. Proc. FMGM

95-4th International Symposium, Bergamo, Italy, 283–290.

Russo, G., Viggiani, C., 1998. Factors controlling soil-structure interaction for piled rafts. In: Proc. International Conference on Soil-Structure Interaction in Urban Civil Engineering, Darmstadt University of Technology, 297-321, DOI: 10.13140/2.1.4035.7125

Sales, M.M., Small, J.C., Poulos, H.G., 2010. Compensated piled rafts in clayey soils: Behaviour, measurements, and predictions. Can. Geotech. J. 47(3), 327–345. https://doi.org/10.1139/T09-106

Sinha, A., Hanna, A.M., 2017. 3D numerical model for piled raft foundation. Int. J. Geomech. 17, 1–9. https://doi.org/10.1061/(ASCE)GM.1943-5622.0000674

Small, J.C., Liu, H.L.S., 2008. Time-settlement behaviour of piled raft foundations using infinite elements. Comput. Geotech. 35(2), 187–195. https://doi.org/10.1016/j.compgeo.2007.04.004

Tang, Y.J., Pei, J., Zhao, X.H., 2014. Design and measurement of piled-raft foundations. Proc. Inst. Civ. Eng. Geotech. Eng. 167(5), 461–475. https://doi.org/10.1680/geng.13.00004

Thoidingjam, D., Prasad, D. S. V, Devi, D.K.R., 2016. Effect Of Number Of Pile In Pile-Raft System In Organic Clay. IOSR J. Mech. Civ. Eng. 13(4), 83–88. https://doi.org/10.9790/1684-1304078388

Thoidingjam, D., Devi, K.R., 2017. Behavior of Pile Raft Foundation in Organic Clay. Indian J. Sci. Technol. 10(31), 1–4. https://doi.org/10.17485/ijst/2017/v10i31/113867

Tran, T. Van, Kimura, M., Boonyatee, T., 2012. 3D FE Analysis of Effect of Ground Subsidence and Piled Spacing on Ultimate Bearing Capacity of Piled Raft and Axial Force of Piles in Piled Raft. Open J. Civ. Eng. 02, 206–213. https://doi.org/10.4236/ojce.2012.24027

Watcharasawe, K., Kitiyodom, P., Jongpradist, P., 2015. Numerical analyses of piled raft foundation in soft soil using 3D-FEM. Geotech. Eng. 46, 109–116.

Watcharasawe, K., Kitiyodom, P., Jongpradist, P., 2017. 3-D numerical analysis of consolidation effect on piled raft foundation in Bangkok subsoil condition. Int. J. GEOMATE 12, 105–111. https://doi.org/10.21660/2017.31.6529

Wood, T., Karstunen, M., 2017. Modelling the creep of deep foundations in soft Gothenburg clays. Eur. J. Environ. Civ. Eng. 8189, 1–19. https://doi.org/10.1080/19648189.2017.1344146

Wulandari, P.S., Tjandra, D., 2015. Analysis of piled raft foundation on soft soil using PLAXIS 2D. Procedia Eng. 125, 363–367. https://doi.org/10.1016/j.proeng.2015.11.083

Yamashita, K. and Kakurai, M., 1991. Settlement behavior of the raft foundation with friction piles, Proc. 4th Int. Conf. on Piling and Deep Foundations, 461-466.

Yamashita, K., Kakurai, M., Yamada, T., Kuwabara, F., 1993. Settlement behavior of five-storey building on a piled raft foundation. In: Proc. 2nd Int. Geotechnical Seminar on Deep Foundations on Bored and Auger Piles, Ghent University, Belgium. Edited by WF Van Impe. AA Balkema, Rotterdam, The Netherlands, 351-356.

Yamashita, K., Kakurai, M., Yamada, T., 1994. Investigation of a Piled Raft Foundation on Stiff Clay. Proc. XIII CIMSTF, New Delhi, India, 543–546.

Yamashita, K., Yamada, T., Hamada, J., 2011. Investigation of settlement and load sharing on piled rafts by monitoring full-scale structures. Soils Found. 51, 513–532. https://doi.org/10.3208/sandf.51.513

Chapter 3

Experimental study on the behavior of piled raft foundations supported by jacked-in piles on saturated clayey ground

3.1 Introduction

In this chapter, the long-term behavior of unpiled raft and piled rafts were investigated through a series of physical model tests. Vertical static load tests were applied to the foundation models on a saturated clayey ground model in the 1-g field. The time-dependent behavior of piled rafts was investigated on many aspects with much emphasis on the foundation settlement, the pile responses, and the change of soil stiffness under different magnitudes of the applied load, concerning the change of excess pore water pressure with time.

In total, five main tests were performed to examine the behavior of unpiled raft and piled rafts. Excepting to unpiled raft, four other tests allowed two model foundations, pile group, and piled raft, to be carried out and compared, in which the main focus was placed on the piled raft. Also, the load tests on single piles (SPs) and each pile in pile foundation were conducted.

It should be noted that the small-sized experiments were carried out in the 1-g field. The models designed for the present work were not intended to simulate the behavior of a specific prototype foundation but to investigate the fundamental mechanisms of the foundations. Furthermore, the results from the physical model tests are interpreted to investigate the validity of the existing numerical approaches.

3.2 Description of the experiments

3.2.1 Model foundation

3.2.1.1 Model pile

The model piles used in the present study were solid bars of acrylonitrile butadiene styrene (ABS bars) of diameter D = 10 mm and length L = 150 mm (see Fig. 3.1). The ABS material

was selected to model piles because they have reasonable Young's modulus when the piles are tested in the soft to medium-stiff saturated clay. If the harder materials such as aluminum or steel are used, the pile deformations during the tests will be too small to measure. The Young's modulus E_p and Poisson's ratio ν_p of the model piles were 2920 N/mm^2 and 0.406, respectively (Table 3.1).

(a) a model pile after attaching strain gages

(b) model piles after covering silicone

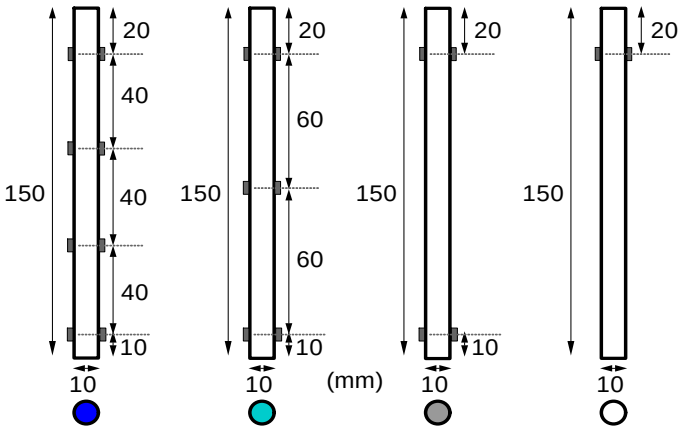

(c) four types of model pile with different levels of strain gages

Fig. 3.1. Model piles and locations of strain gages.

Table 3.1. Properties of the model piles.

Parameter	Value
Diameter, D (mm)	10.0
Length from raft base, L (mm)	150
Young's modulus, E_p (N/mm^2)	2920
Poisson's ratio, ν_p	0.406

To measure the axial force along each pile, strain gages (SGs) were attached on both the left and right sides of the pile shaft at different levels, as shown in Fig. 3.1. To eliminate the effect of temperature on the experimental results, cross gages were used at each location. After the SGs were attached to the pile shaft (Fig. 3.1(a)), the pile will be covered with silicone to protect SGs when working in saturated soil. The wires of SGs were also protected in silicone tubing to avoid damages when subjected to shear forces from the clay and raft. Fig. 3.1(b) shows the photo of piles after the piles were covered with silicone and the wires were protected by the silicone tube.

In the pile- group and piled-raft conditions, the load carried by each pile was obtained from the strain measured near the pile head. Four types of piles (with different levels of SGs) were used for the model foundations as shown in Fig. 3.1(c). Depend on the pile number in each experiment, the number of piles of each type was selected.

3.2.1.2 Model raft

The model raft was a square aluminum plate of thickness t = 12 mm and width $B_r = L_r$ = 125 mm (Fig. 3.2). Properties of the model raft are presented in Table 3.2.

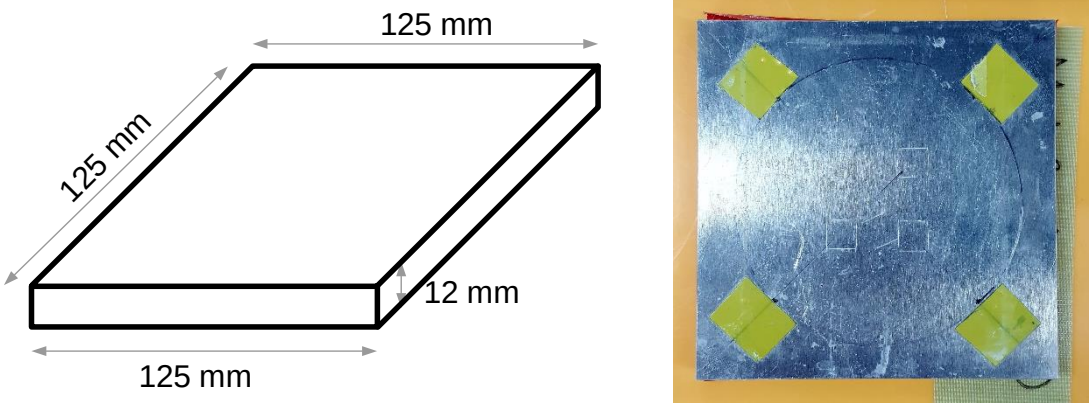

(a) Dimension of model raft (b) A photo of model raft

Fig. 3.2. Model raft.

Table 3.2. Properties of the model raft.

Parameter	Value
Raft width, $L_r = B_r$ (mm)	125
Raft thickness, t_r (mm)	12
Young's modulus, E_p (N/mm^2)	69×10^6 kPa
Poisson's ratio, ν_p	0.35

The raft – soil stiffness ratio K_{rs} for a rectangular raft was calculated, using equation proposed by Brown (1975), namely

$$K_{rs} = \frac{(1-\nu_s)\times E_r}{2G_s} \times \frac{4B_r}{3\pi L_r} \times \left(\frac{t}{L_r}\right)^3 \quad (3\text{-}1)$$

where G_s is shear modulus of the soil, taken as 267 kPa (the highest value obtained from axial stress-strain relationships of UCTs); and ν_s was Poisson's ratio of the soil, taken as 0.5 (an assumed value for saturated clay under undrained condition).

The value K_{rs} = 27 was obtained for the case of raft and soil in this study. When K_{rs} is larger than 1, the raft is considered as a rigid plate (Brown, 1975).

3.2.1.3 Test series

In this research, five main long-term tests on five foundation models were conducted for this study, included:

1) Unpiled raft (UR);
2) 4-pile pile foundation with center-to-center pile spacing of 6 times of pile diameter (4P-6*D*);
3) 4-pile pile foundation with center-to-center pile spacing of 3 times of pile diameter (4P-3*D*);
4) 9-pile pile foundation with center-to-center pile spacing of 3 times of pile diameter (9P-3*D*);
5) 16-pile pile foundation with center-to-center pile spacing of 3 times of pile diameter (16P-3*D*).

Furthermore, one test on single piles (SP) and an unpiled raft (UR*) was carried out in short-term conditions, before the five main tests, in order to roughly estimate the bearing capacity of each element and to determine the magnitude of the loads which will be applied on the piled raft foundations. Table 3.3 shows the list of the model foundations and test series in this study.

Fig. 3.3(a) shows the foundation model for the case of the short-term tests on single pile and unpiled raft and Fig. 3.3(b)-(f) respectively show the foundation models for the five main long-term tests on piled raft foundations as mentioned above.

Table 3.3 shows the test series which were carried out on each model ground. Basically, the procedure for each series was as follows: The pile was firstly jacked into the ground one by one (PPT), then, the static load test of each pile was carried out (SLTSP for single piles in test no. 1/ SLTIP for piles in foundations in test no. 3, 4, 5, & 6). Next, the static load test of the pile group was conducted (SLTPG) after the completion of the SLTIP. The raft was

then set on the pile heads and the static load test of pile raft in long-term condition was carried out (SLTPR). For the cases of unpiled rafts in test no. 1 & 2, the static load test of the unpiled raft was conducted separately with the SLTSPs. The details of the test procedures are presented in section 3.2.4.

Table 3.3. Model foundations and test series.

Test no.	Model foundation descriptions	Load tests conducted in short term condition	Load test conducted in long term condition	Notation of model foundation
1	Single piles and unpiled raft	PPT, SLTSP, SLTUR*	None	SPs & UR*
2	Unpiled raft	None	SLTUR	UR
3	4-pile pile foundation with center-to-center pile spacing of 6 times of pile diameter	PPT, SLTIP, SLTPG	SLTPR	4P-6*D*
4	4-pile pile foundation with center-to-center pile spacing of 3 times of pile diameter	PPT, SLTIP, SLTPG	SLTPR	4P-3*D*
5	9-pile pile foundation with center-to-center pile spacing of 6 times of pile diameter	PPT, SLTIP, SLTPG	SLTPR	9P-3*D*
6	16-pile pile foundation with center-to-center pile spacing of 6 times of pile diameter	PPT, SLTIP, SLTPG	SLTPR	16P-3*D*

Note, PPT: Pile penetration test
SLTSP: Static load test of single pile
SLTUR*, SLTUR: Static load test of unpiled raft
SLTIP: Static load test of each (individual) pile after the installation of all piles in the case of pile foundation.
SLTPG: Static load tests of pile group
SLTPR: Static load tests of pile raft

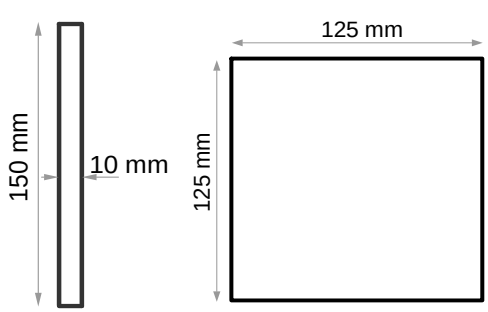

(a) SP & UR* (short term)

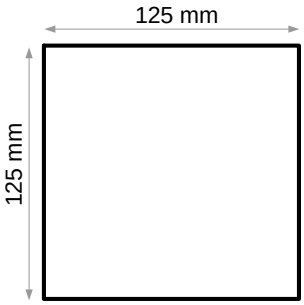

(b) UR

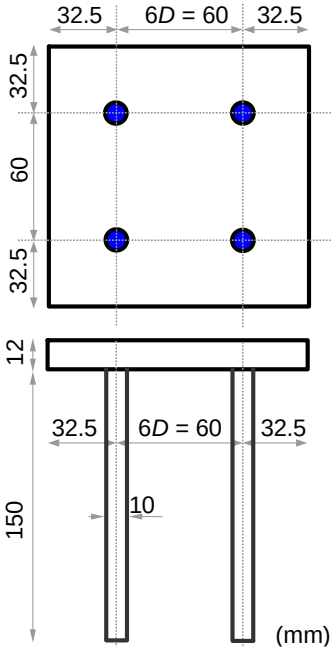

(c) 4P-6*D*

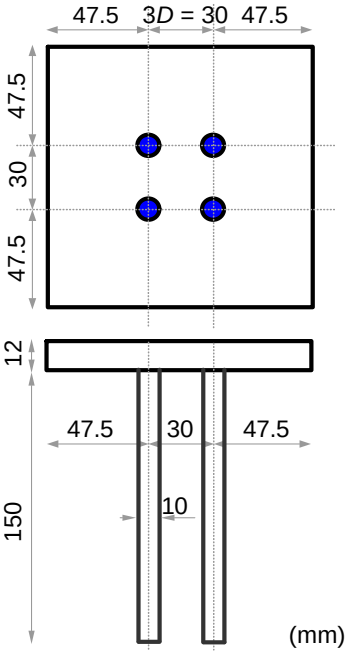

(d) 4P-3*D*

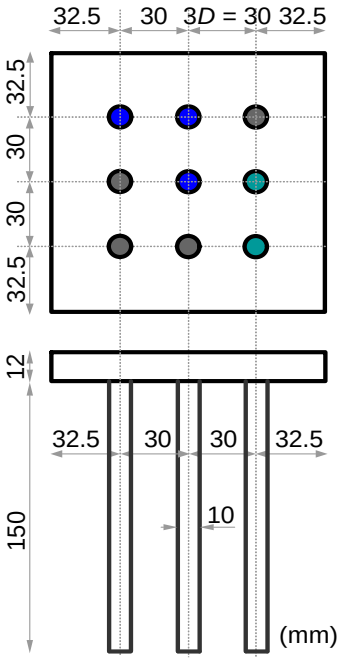

(e) 9P-3*D*

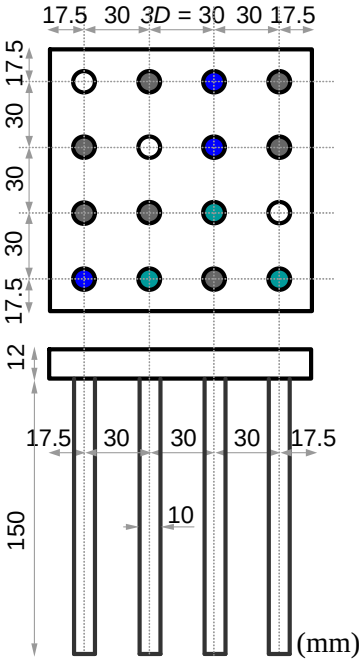

(f) 16P-3*D*

Fig. 3.3. Model foundations.

3.2.2 Model ground

3.2.2.1 Soil preparations

Commercially available Kasaoka clay powder, silica sand #6, and silica sand #3 were used for the experiments, of which silica sand #3 was used for drainage layers and the two other soils were used for the "clay ground". Firstly, the laboratory soil tests such as oedometer, liquid limit, and plasticity limit were conducted to obtain the properties of the pure Kasaoka clay. Results of the laboratory tests indicated that Kasaoka clay is a high-plasticity clay (with liquid limit *LL* of 62% and plasticity index *PI* of 34%), and it requires a considerable time for primary consolidation periods. To reduce the consolidation time, a mixture of Kasaoka clay and silica sand #6 was used instead of the pure Kasaoka clay. Mixtures of Kasaoka clay (powder) and silica sand were considered at several different dry mass ratios. Some laboratory tests were conducted to obtain properties of each mixture to ensure that the mixture used for the model ground was clayey soil, and also the consolidation time of the corresponding model ground was reduced effectively. The dry mass ratio of 1:1 between Kasaoka clay powder and silica sand #6 was finally selected for the mixture using for all model grounds (this mixture being referred to as K50S50). Properties of K50S50 are shown in section 3.2.2.2.

Clay ground was prepared in a cylindrical chamber of inner height 420 mm and inner diameter 420 mm (Fig. 3.4). A drainage line with a valve was connected to the bottom of the chamber, and with the valve either open or closed, the bottom surface of the model ground was either drained or undrained, respectively.

The model ground was prepared as follows. First, for the bottom drainage layer, silica sand #3 was poured into the chamber and was compacted in the saturated condition until it reached a high relative density D_r of around 81% and a thickness of 50 mm (Fig. 3.4(a)). This drainage layer was deemed to be a stiff layer. Then, to keep this layer saturated, a sheet of drainage paper was set above it and the bottom drain valve was closed. Next, in a rectangular basin, Kasaoka clay powder and silica sand #6 were mixed in a dry mass ratio of 1:1. Water was then added to the K50S50 to obtain soil slurry with a water content *w* of 1.3 times the liquid limit *LL* (*LL* = 33.9%, obtained from Atterberg liquid limit test). This soil slurry was poured into the soil chamber to an initial thickness of 370 mm (Fig. 3.5(a)). The soil was then left to consolidate under its self-weight for 2 days (Fig. 3.5(b)), after which a surface layer of silica sand #6 of thickness 10 mm was placed on the clay to provide the top drainage layer. Drainage paper was set between the K50S50 and the top drainage layer to prevent soil particles from moving between the layers, and another piece of drainage paper was set on the top surface of the top sand drainage layer (Fig. 3.5.(c)).

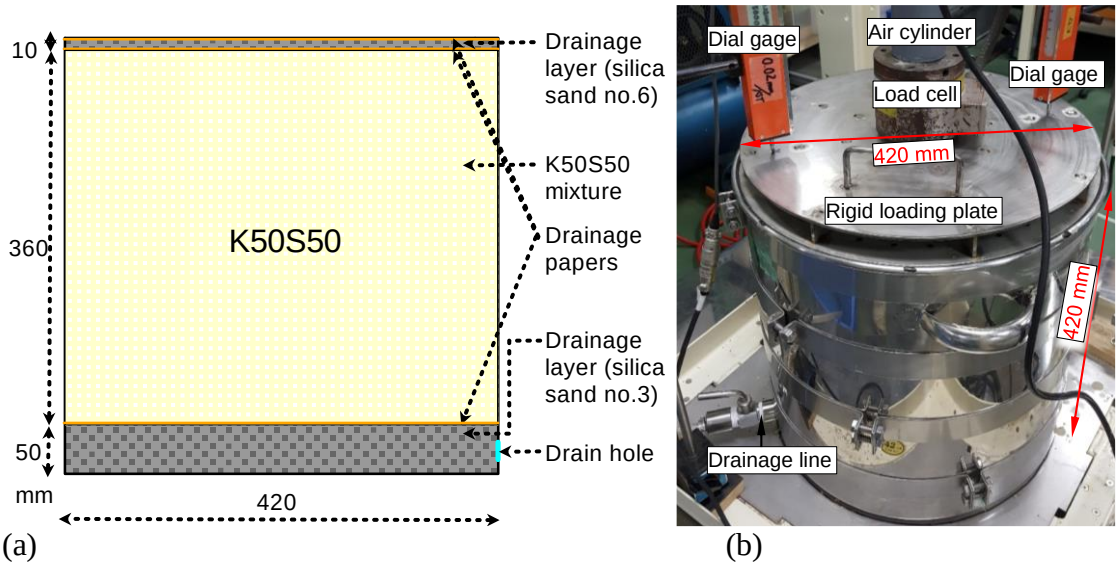

(a) (b)

Fig. 3.4. Set-up of model ground preparation: (a) longitudinal cross-sectional view before applying consolidation pressure; (b) set-up of an experiment during consolidation stage.

To apply a consolidation pressure, a rigid circular loading plate was placed on the top drainage layer. An air cylinder was used to apply the vertical load on the loading plate in a load-controlled manner through a 20,000-N load cell. Two dial gages with a travel of 100 mm were set on the surface of the loading plate to measure the settlement of the ground during the consolidation period. The settlement and the applied load were monitored throughout the consolidation period. Fig. 3.4(b) shows the set-up of devices for the consolidation stage of an experiment. Next, the vertical load on the loading plate was increased to consolidate the soil one-dimensionally in several steps up to a vertical stress σ_v of 100 kPa (Fig. 3.5(d)). Each load step was maintained until the degree of consolidation reached 90% as estimated from Terzaghi's one-dimensional consolidation theory. The final load step was held for an additional week to obtain a higher degree of consolidation. Finally, the consolidation pressure was removed (Fig. 3.5(e)), and the ground was allowed to undergo swelling for 10 days (Fig. 3.5(f)). It should be noted that during the consolidation and swelling processes, the bottom drainage line was opened so that water could seep through both the top and bottom surfaces to reduce the consolidation time. Fig. 3.6(a) and (b) show the time-settlement curves of the final consolidation step (σ_v was increased from 70 to 100 kPa) and the swelling process, respectively, of a model ground. The total settlement of the ground was 79 mm at the end of the final consolidation step, including a self-weight settlement of around 10 mm. The final height of the model ground after the swelling process was 294 mm.

(a) (b) (c)

(d) (e) (f)

Fig. 3.5. Procedure of model ground preparation: (a) filling soil slurry into soil chamber; (b) waiting to consolidation under self-weight; (c) preparing for applying consolidation pressure; (d) consolidation process under uniform pressure; (e) removing consolidation pressure after completing consolidation stage under vertical pressure of 100 kPa; (f) heaving stage.

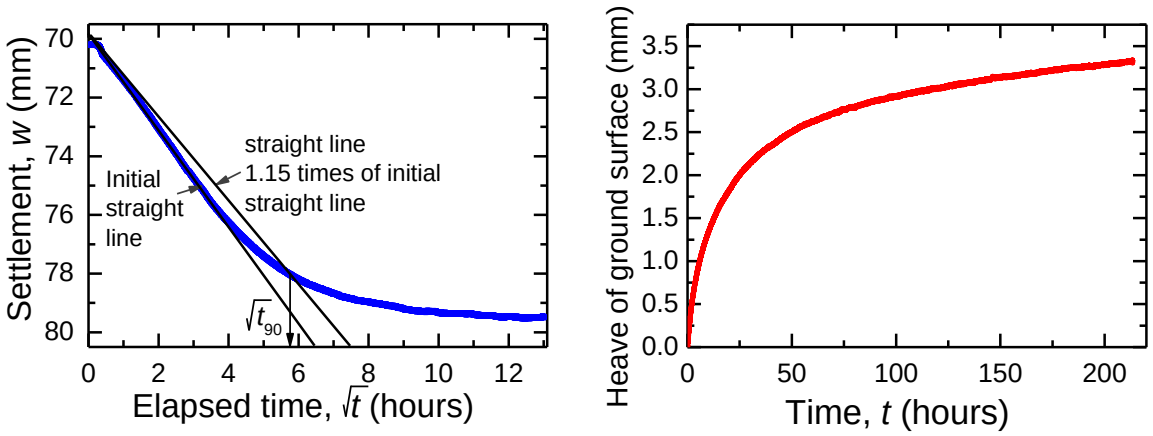

(a) (b)

Fig. 3.6. Time–settlement relationships while preparing a model ground: (a) primary consolidation stage in final load step; (b) ground heaving after removing consolidation pressure.

3.2.2.2 Soil property investigation

a. Laboratory soil tests before model ground preparation

Before preparing the first model ground, a series of laboratory soil tests such as oedometer, Atterberg limits, density of soil particles, particle size distribution were carried out, following the JGS laboratory testing standards of geomaterials (2015). The detail of the oedometer test was shown below, for the other tests, only the results were shown.

Oedometer test: An oedometer test was carried out using the slurry soil (K50S50) with $w = 1.3LL$ (the same soil slurry that was prepared for the model ground as mentioned above). First, the consolidation pressure σ_v was increased in eight steps up to σ_v = 300 kPa (Fig. 3.7(a)), whereupon it was decreased from 300 kPa to 5 kPa in six steps. The consolidation pressure was then increased again in multiple steps to exceeding 300 kPa, reaching 1257 kPa at the final step; this pressure was maintained for around 6,000 hours (250 days) to measure the creep behavior of the soil for a very long time. Fig. 3.7 shows the results of the oedometer test. In Fig. 3.7(a), the relationship between σ_v and the void ratio e is plotted. From the test results, the compression index C_C and the swelling index C_S of the soil are 0.291 and 0.055, respectively. Fig. 3.7(b) shows the relationship between the vertical strain ε_v and the elapsed time t in the final load step. At the constant vertical stress of 1257 kPa, a creep index C_B of 0.00176 was obtained. Fig. 3.7(c) shows the change of permeability k with void ratio e. The permeability k changed more significantly when e > 0.6, the permeability index c_k obtained at this stage was 0.425. When e < 0.6, the change of k was smaller and c_k of 0.117 obtained for this stage was also smaller.

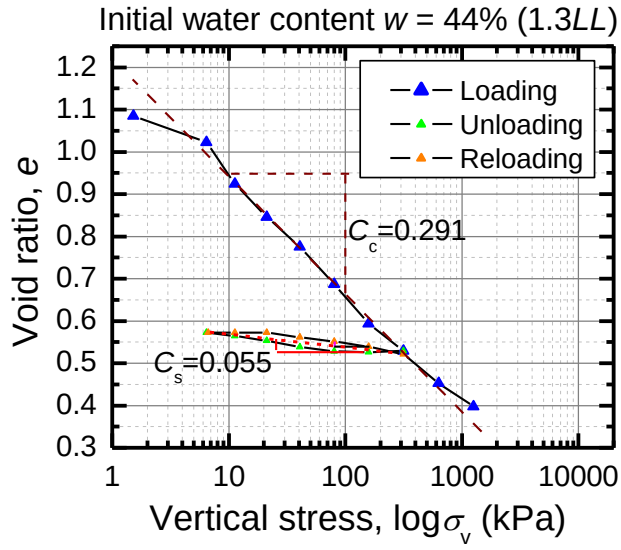

(a)

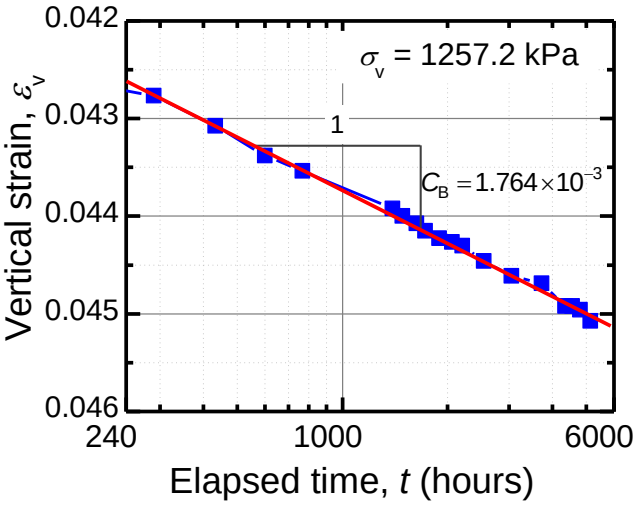

(b)

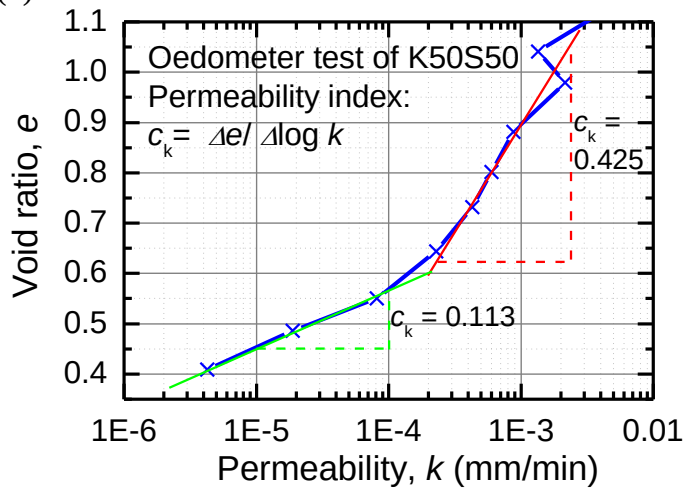

(c)

Fig. 3.7. Results of oedometer test of model ground soil: (a) final void ratio vs. effective stress; (b) secondary creep strain vs. elapsed time of final load step; (c) change of permeability with void ratio.

Result of particle size distribution test: Fig. 3.8 shows the particle size distribution of K50S50. The size of particles distributed in a wide range. The particle size at 10%, 30%, and 60% passing by mass was 0.001 (D_{10}), 0.006 (D_{30}), and 0.15 (D_{60}), respectively.

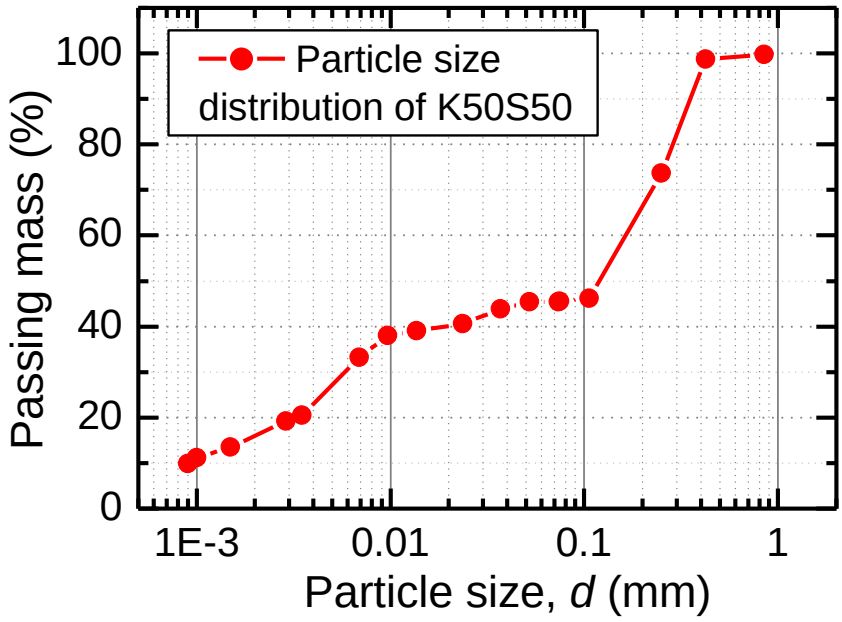

Fig. 3.8. Particle size distribution of K50S50.

Results of other laboratory tests: the results of the other laboratory soil tests such as Atterberg limit tests and density of soil particles as well as the results of the oedometer test are summarized in Table 3.4.

Table 3.4. Properties of model ground soil (referred to as K50S50).

Parameter	Value
Density of soil particle, ρ_s (Mg/m^3)	2.653
Saturated density[a], ρ_{sat} (Mg /m^3)	1.98
Plastic limit, *PL* (%)	13.6
Liquid limit, *LL* (%)	33.9
Plastic index, *PI* (%)	20.3
Compression index, C_c	0.291
Swelling index, C_s	0.055
Water content[a], *w* (%)	26.2
Permeability[a], *k* (mm/min)	0.00038
Void ratio[a], *e*	0.703

Note: [a]after the consolidation with vertical pressure of 100 kPa

Soil classification: Fig. 3.9. presents the location of currently studied soil K50S50 on the Plasticity chart (chart from ASTM standard D 2487-93). As shown by the chart, the studied soil K50S50 is classified as low-plasticity clay.

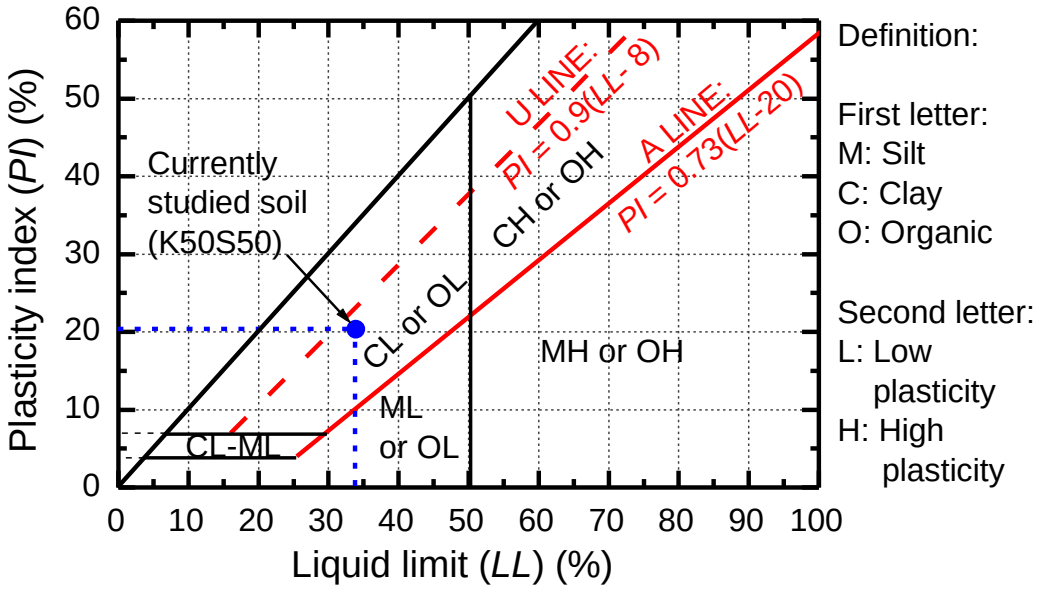

Fig. 3.9. Description of plasticity index of K50S50 on Plasticity chart (ASTM standard D 2487-93).

b. Consolidated-undrained triaxial compression (CU) test

After the completion of the load test on a piled raft, soil specimens were sampled from the model ground using a thin-walled tube of diameter 100 mm and height 150 mm. The location of the soil sample was selected far from the loading area to obtain the mechanical properties of the original ground and to investigate the behavior of the K50S50 clay without the effect of load test on the foundation. The soil sample was trimmed immediately after sampling to obtain a cylindrical specimen of diameter 50 mm and a height of 100 mm. The soil specimen was consolidated under the final isotropic stress of 100 kPa before the axial compression stage. Figs. 3.10(a) and (b) show the results of volume change vs. elapse time during the consolidation stage and excess pore water pressure change vs. elapse time during the consolidation stage, respectively.

For the test results of the axial compression stage, axial strain ε_a vs. deviatoric stress q, and mean normal stress p' vs. q, are shown in Fig 3.10(c) and Fig. 3.10(d), respectively. It is seen from Fig. 3.10(c) that at the initial compression stage ($\varepsilon_a < 1$ %), the stiffness increases sharply and non-linearly with increasing ε_a. After that, the increase of the stiffness slows

down and reaches the residual state of 105 kPa at ε_a of around 7.5 %. It was estimated from the experimental results that the peak internal friction angle, ϕ_p', is 36.9 degrees while the residual internal friction angle, ϕ_r', is around 35.1 degrees. The undrained Poisson's ratio ν_s was around 0.5, estimated from the CU test. In the cyclic loads were applied, the deviatoric stress at residual state did not increase.

Besides the main purpose of investigating soil properties, the results of the above laboratory soil tests are also used to validate the soil constitutive model for the numerical study in the next chapter.

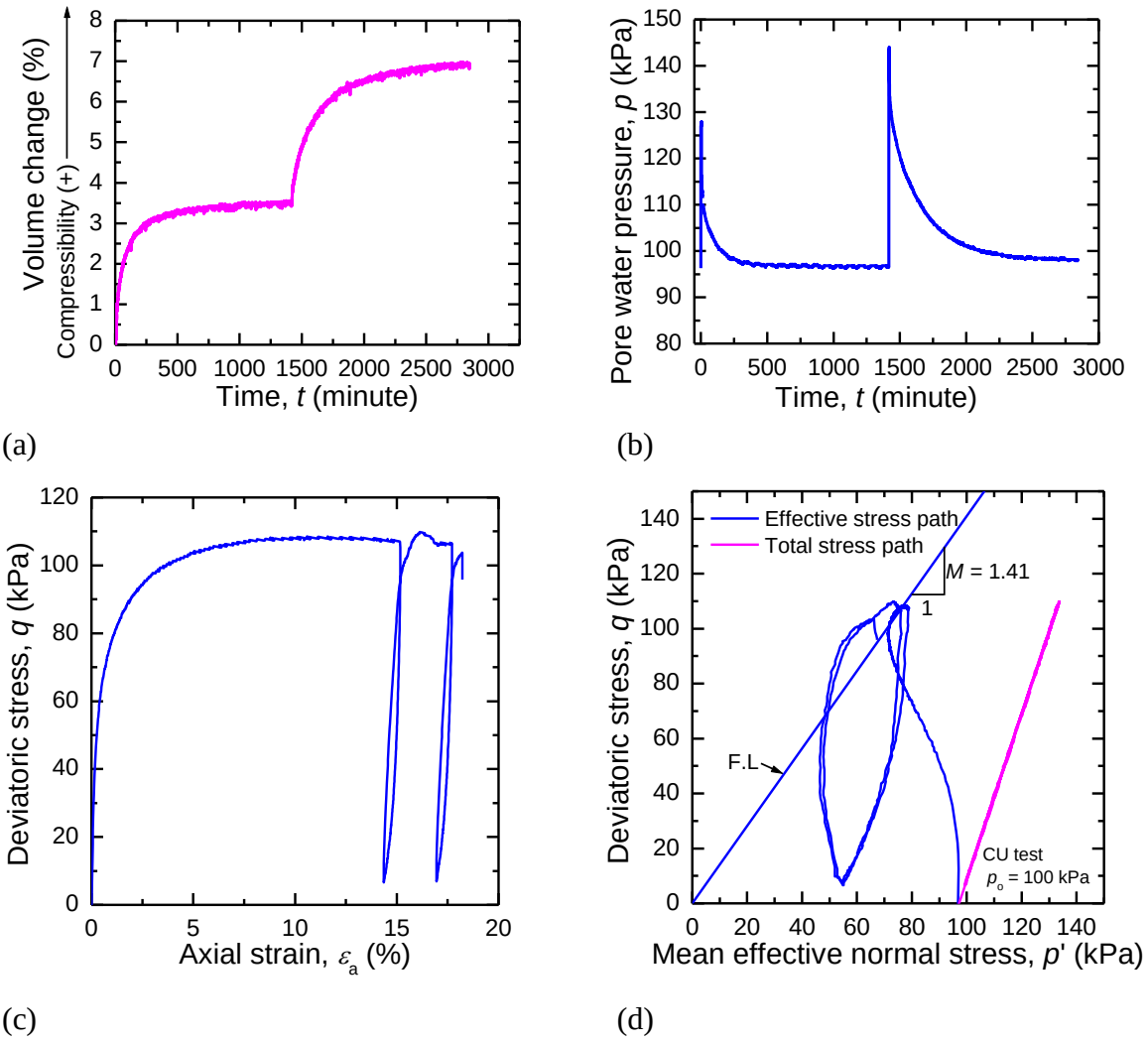

Fig. 3.10. Results of CU test of model ground soil: (a) volume change vs. elapse time during consolidation stage; (b) excess pore water pressure change vs. elapse time during consolidation stage; (c) deviatoric stress vs. axial strain during axial compression stage; (d) deviatoric stress vs. mean normal stress during axial compression stage.

3.2.2.3 Estimation of soil strength

To obtain the strength profiles of the model ground before and after the load test, cone penetration tests (CPTs), T-bar tests (TBTs), and unconfined compression tests (UCTs) were carried out immediately upon completion of the load test on the model foundation in each model ground. The soil at the corresponding locations of the soil tests was also measured water content, to investigate the relationship between soil strength and water content.

Fig. 3.11 shows the locations of the three types of soil tests in each model ground. In the figure, the name of the model ground is the same with the name of the model foundation which was tested on it, as mentioned above in section 3.2.1.3.

a. T-bar penetration test

The T-bar cylinder had a diameter $d_{\text{T-bar}}$ of 7 mm and a length $L_{\text{T-bar}}$ of 35 mm. Strain gages (SGs) were attached on the T-bar rod just above the T-bar cylinder to measure the net force P acting on the T-bar cylinder. The T-bar was pushed into the ground at a constant rate of 2 mm/s, and the undrained shear strength c_{u} was deduced from the average stress $q_{\text{T-bar}}$ acting on the T-bar cylinder using an empirical equation proposed by Low et al. (2010), namely

$$c_{\text{u}} = q_{\text{T-bar}} / N_{\text{T-bar}} = P / (d_{\text{T-bar}} L_{\text{T-bar}} N_{\text{T-bar}}) \quad (3\text{-}2)$$

where $N_{\text{T-bar}}$ is the resistance factor for the T-bar.

In estimating the soil strength, the $N_{\text{T-bar}}$ value was taken based on the suggestion by Low et al. (2010), who used a worldwide high-quality database of lightly over-consolidated clays to evaluate cone and T-bar resistance factors for the estimation of intact and remolded undrained shear strength from the penetration resistance of each device. The range between 8.5 and 12.5 for the $N_{\text{T-bar}}$ value with an average $N_{\text{T-bar}}$ value of 10.5 was obtained from the analysis results. The $N_{\text{T-bar}}$ value of 10.5, therefore, was used to estimate undrained shear strength c_{u} from T-bar tests in this research.

In all the model ground, the locations of two or three T-bar tests were selected far from the loading area to estimate the undrained shear strength of the model grounds without the effect of the loading tests. Additionally, the T-bar tests were also conducted at the loading area (included beneath the raft center and the raft edge) in the model grounds of the 4th-7th test to obtain the undrained shear strength of the model grounds with the effect of the loading tests. Fig. 3.11 shows the detailed locations of T-bar tests for each model ground.

The results of c_{u} estimated from T-bar tests were shown and discussed together with the c_{u} results estimated from other methods in section *e* of this chapter.

b. Cone penetration test

CPTs were carried out using a cone of diameter 20 mm and apex angle 60°. Just above the cone, SGs were attached on the cone rod to measure the net cone tip resistance $q_{\text{cone tip}}$. During the tests, the cone was penetrated at a constant high rate of 2 mm/s. The undrained shear strength c_u was deduced from the measured cone tip resistance $q_{\text{cone tip}}$ using an empirical equation proposed by Low et al. (2010), namely

$$c_u = (q_{\text{cone tip}} - \sigma_{vo}) / N_{kt} \tag{3-3}$$

where σ_{vo} is the total overburden stress (obtained by integrating γ_{bulk} with depth, γ_{bulk} is the total unit weight of the model ground soil) and N_{kt} is the cone resistance factor.

Similar to T-bars, in estimating the soil strength, the N_{kt} value was taken based on the suggestion by Low et al. (2010). The range between 10 and 14 for the N_{kt} value with an average $N_{\text{T-bar}}$ value of 12 was obtained from the analysis results. The N_{kt} value of 12, therefore, was used to estimate undrained shear strength c_u from CPTs in this research.

Excepting the model ground of 4P-3*D*, two CPTs were carried out in each model ground at the locations far from the loading area to estimate c_u without the effect of load tests. To investigate the effect of the loading test on the ground strength, in the model ground of SPs and UR (short term), 9P-3*D*, and 16P-3*D*, the CPTs were also carried out at the raft base edge areas. For the case of UR, one CPT was carried out at the raft base center area.

The results of c_u estimated from CPTs were shown and discussed together with the c_u results estimated from other methods in section *e* of this chapter.

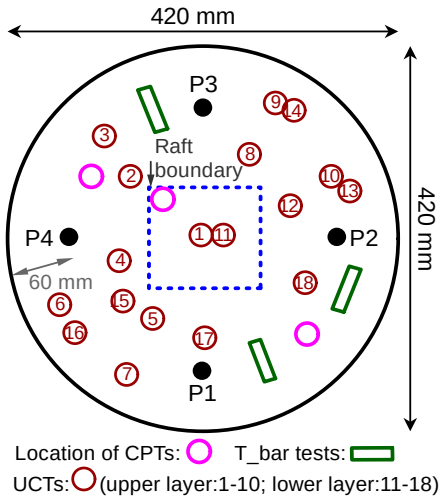

(a) SPs & UR* (short term)

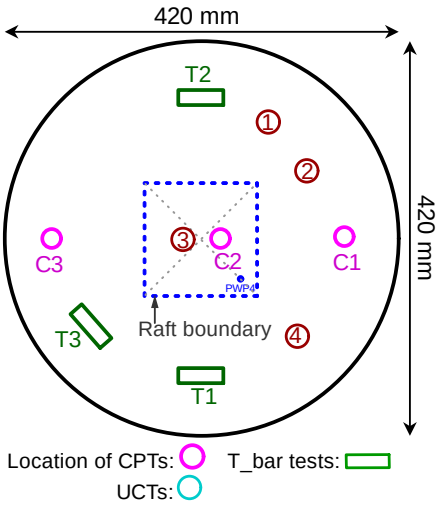

(b) UR

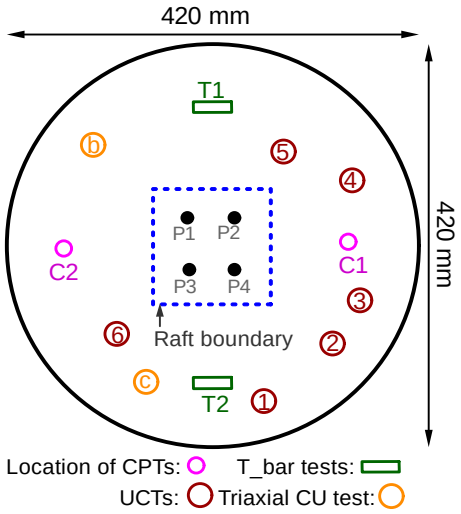

(c) 4P-6*D*

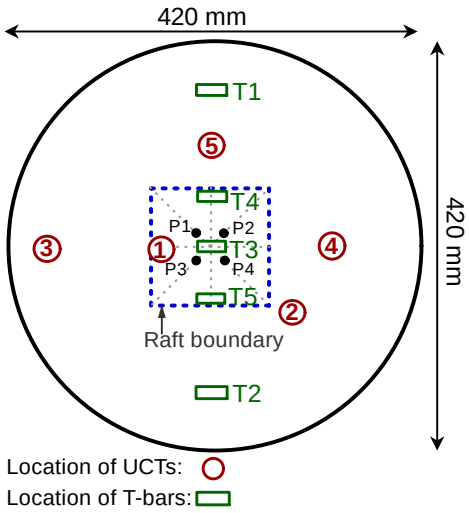

(d) 4P-3*D*

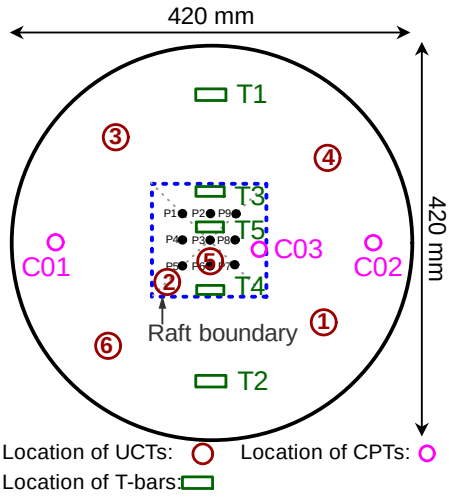

(e) 9P-3*D*

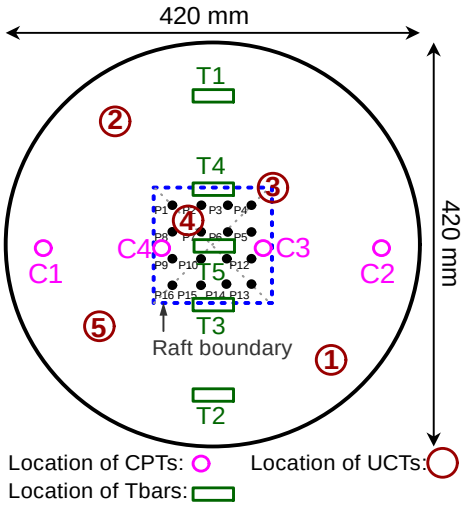

(f) 16P-3*D*

Fig. 3.11. Location of soil tests (CPTs, T-bars, and UCTs) for each model ground.

c. Unconfined compression test

For the UCTs, soil specimens were sampled from different depths in each model ground using a thin-walled tube of diameter 65 mm. The specimen locations were selected at, near, and far from the loading area (see Fig.3.11) to obtain the undrained shear strength of the model grounds with and without the effect of the loading tests. Each soil sample was trimmed immediately after sampling to obtain a cylindrical specimen of diameter 35 mm and a height of around 75 mm. The undrained shear strength c_u was estimated from the unconfined compression strength q_u as $c_u = q_u /2$.

The results of c_u estimated from UCTs were shown and discussed together with the c_u results estimated from other methods in section *e* of this chapter.

d. Changing of water content

The water content of each UCT sample was measured to study the relationship between the undrained shear strength and the saturated water content (or the bulk density).

Table 3.5 presents the distribution of water content for all the six model grounds. In the table, the average depth of each soil sample and the corresponding undrained shear strength c_u obtained from UCT were described. The notice of sample location was also described in the table if the sample was beneath the loading areas. The remained samples without notice of location were sampled at the locations far from the loading areas.

It is clear from Table 3.5 that the water contents of samples at deeper depths were slightly lower than those at a shallower depths. The water content of samples beneath the edge of the loading areas in the long-term load test was smaller and the water content of samples beneath the center of the loading areas (raft base) in the long-term load test was the smallest, in comparison with the water content of samples far from the loading areas. In the long-term load test of PRs, the final load of the PR was higher with a larger pile number. The results of the water contents show that, after the load test, the higher level of load, the lower water content beneath the pile tips were obtained. Basically, the UCT sample with smaller water content showed larger undrained shear strength.

Table 3.5. Water content of UCT samples for six model grounds.

(a) SP & UR (short term)

UCT sam. no.	Average depth, *z* (mm)	Water content, *w* (%)	c_u (kPa)	Notice	UCT sample no.	Average depth, *z* (mm)	Water content, *w* (%)	c_u (kPa)	Notice
1	100	25.05	18.15	Raft center	10	100	24.89	16.70	
2	100	27.22	10.70	Raft edge	11	100	25.22	13.60	Raft center
3	100	25.43	13.50		12	200	24.62	13.00	Raft edge
4	100	25.92	13.60	Raft edge	13	200	24.70	15.40	
5	100	26.56	10.00	Raft edge	14	200	24.46	20.00	
6	100	25.92	15.40		15	200	24.59	20.10	Raft edge
7	100	25.45	16.10	Raft edge	16	200	24.58	21.00	
8	100	25.91	11.30		17	200	24.78	18.70	Raft edge
9	100	25.14	17.80		18	200	24.29	20.80	

Table 3.6. Water content of UCT samples for six model grounds. (continued)

(b) UR

UCT sam. no.	Average depth, z (mm)	Water content, w (%)	c_u (kPa)	Notice	UCT sample no.	Average depth, z (mm)	Water content, w (%)	c_u (kPa)	Notice
1	100	26.08	16.33		3	100	24.53	22.31	Raft center
2	100	26.01	15.82		4	200	25.87	18.23	

(c) 4P-PF-6D

UCT sam. no.	Average depth, z (mm)	Water content, w (%)	c_u (kPa)	Notice	UCT sample no.	Average depth, z (mm)	Water content, w (%)	c_u (kPa)	Notice
1	100	26.13	16.98		4	220	26.27	18.30	
2	100	26.46	15.66		5	220	26.01	20.60	
3	130	26.44	17.45		6	220	25.96	18.40	

(d) 4P-PF-3D

UCT sam. no.	Average depth, z (mm)	Water content, w (%)	c_u (kPa)	Notice	UCT sample no.	Average depth, z (mm)	Water content, w (%)	c_u (kPa)	Notice
1	140	25.79	22.30	Raft edge	4	220	26.07	20.90	
2	140	26.06	20.60	Raft edge	5	220	25.85	20.70	
3	140	24.64	17.20						

(e) 9P-PF-3D

UCT sam. no.	Average depth, z (mm)	Water content, w (%)	c_u (kPa)	Notice	UCT sample no.	Average depth, z (mm)	Water content, w (%)	c_u (kPa)	Notice
1	120	25.82	19.30		4	230	25.07	23.85	
2	120	24.48	18.10	Raft edge	5	230	24.15	28.70	Raft center
3	120	25.84	16.10		6	230	25.07	22.25	

Table 3.5. Water content of UCT samples for six model grounds (continued).

(f) 16P-PF-3D

UCT sam. no.	Average depth, z (mm)	Water content, w (%)	c_u (kPa)	Notice	UCT sample no.	Average depth, z (mm)	Water content, w (%)	c_u (kPa)	Notice
1	120	25.99	14.60		4	230	22.76	30.30	Raft center
2	120	25.95	14.06		5	230	24.83	23.90	
3	120	25.78	16.60	Raft edge					

e. Comparison and discussion of soil strength

The distributions of undrained shear strengths c_u with depths of all model grounds obtained from the 3 methods (T-bar tests, CPTs, and UCTs) are shown in Fig. 3.12 (a)-(f), including the c_u with and without the effect of loading test.

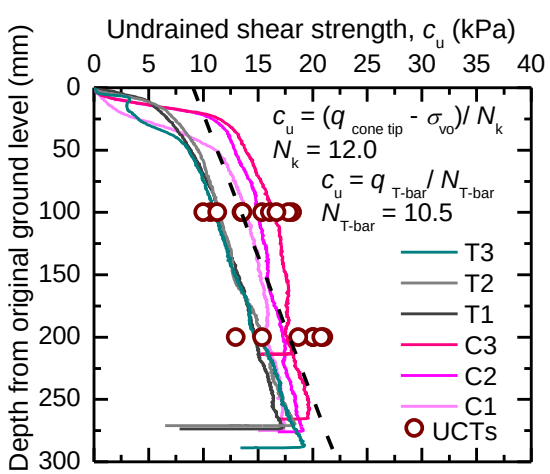

(a) SPs & UR*

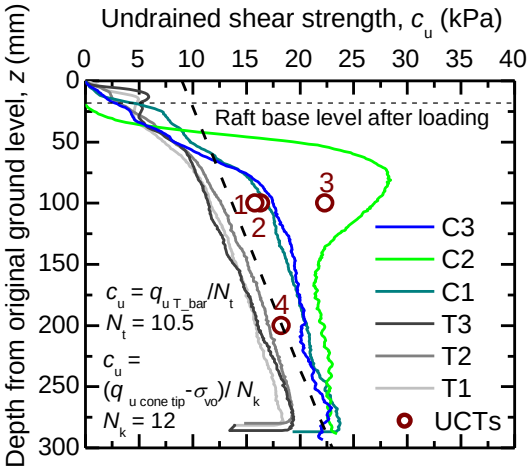

(b) UR

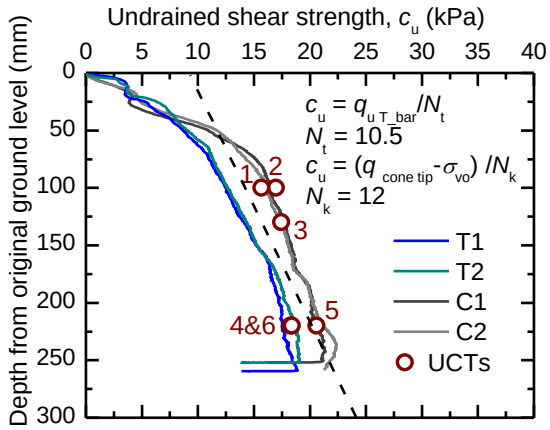

(c) 4P-6*D*

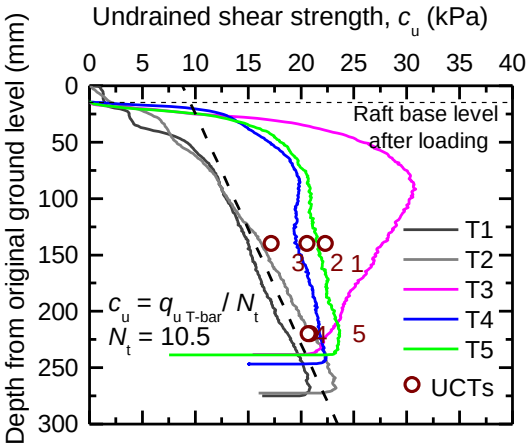

(d) 4P-3*D*

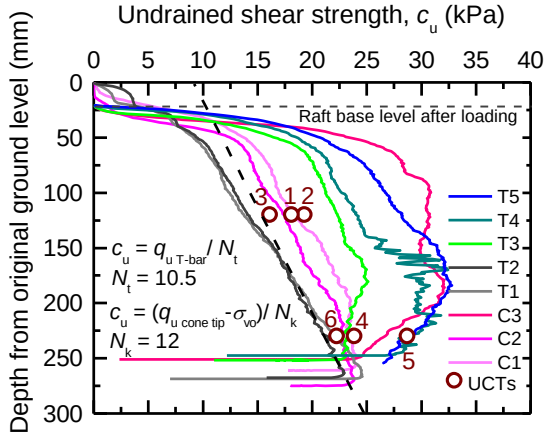

(e) 9P-3*D*

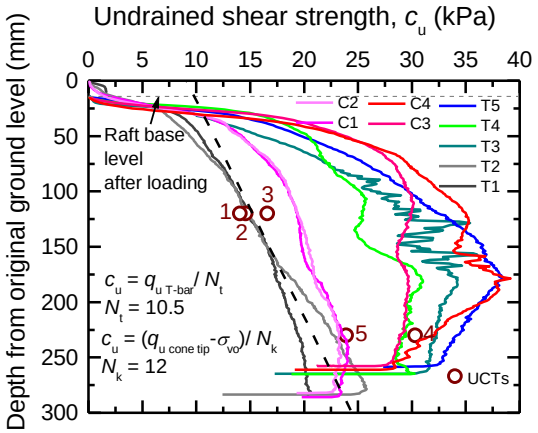

(f) 16P-3*D*

Fig. 3.12. Distributions of undrained shear strength with depth for each model ground.

It is noticed from Fig. 3.12 that the foundations settled by more than 10% of raft width (0.1*B*) upon completion of the load tests, therefore, the profiles for c_u in the loading area begin at the depth of the raft base after loading. Fig. 3.13 shows the sum of c_u without the effect of the loading test (c_u of the original ground) obtained from the three different methods for all model grounds. It is clear from Fig. 3.13 that the c_u profiles estimated for all the model grounds were very consistent. This indicates that the soil strengths for all the model ground were the same. To compare the soil strength between results of T-bar tests and CPTs, in all model grounds, the c_u estimated from T-bar tests was just slightly smaller than the c_u estimated from CPTs at the middle depths of the model grounds. The soil strengths that were obtained directly from the UCTs show very good agreements with the c_u estimated from CPTs and also good agreements with the c_u estimated from T-bars. In general, the c_u of the original model grounds was varied with depth *z* and was described well by the following equation

$$c_u\ [\text{kPa}] = 9\ [\text{kPa}] + z\ [\text{mm}] \times 0.05\ [\text{kPa/mm}] \tag{3-4}$$

except at shallow depths.

The distributions of undrained shear strengths c_u with depth beneath the raft base edge (loading area) are shown in Fig. 3.14. The Eq. (3-4) was also presented in the figure. The detailed discussion about the changes of c_u after loading will be made with the discussion of experimental results in section 3.3. The followings are the general comments on the changes of c_u after loading. Fig. 3.14 show that, for the case of the unpiled raft (short-term behavior), the distribution of soil strength beneath the raft base edge after loading was quite consistent with the soil strength of the original model ground (presented by Eq. (3-4)). This indicates that the loading of the unpiled raft in short-term condition did not have a significant effect on the undrained shear strength of the model ground. For the cases of long-term load tests (4P-3*D*, 9P-3*D*, and 16P-3*D*), the soil strengths beneath the raft base edge after loading became larger than that of the original model ground. The long-term load test with larger applied load shows a larger increment of soil strength, in comparison with the original state.

The distributions of undrained shear strengths c_u with depth beneath the raft base center (loading area) are shown on Fig. 3.15. The Eq. (3-4) was also presented in the figure. Similar to the case of the changes of c_u beneath the raft edges, the detailed discussion about the changes of c_u after loading will be made with the discussion of experimental results in section 3.3. In general, for each experiment, the soil strengths beneath the raft base center after long-term loading became larger than that of the raft base edge, and much larger than that of the

original model ground (Eq. (3-4)). The long-term load test with larger applied load shows a larger increment of soil strength, and the depth affected by that test was also deeper.

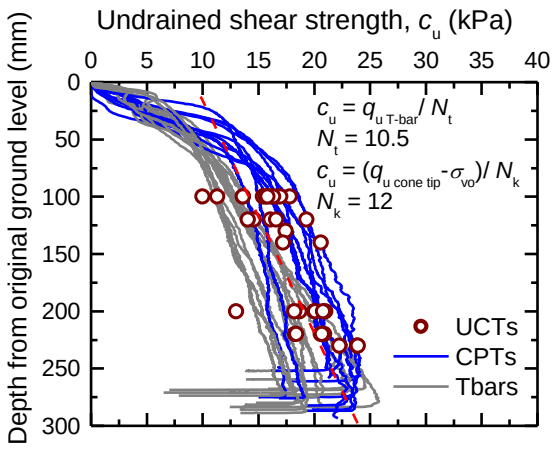

Fig. 3.13. Distributions of undrained shear strength with depth at original state of all model grounds.

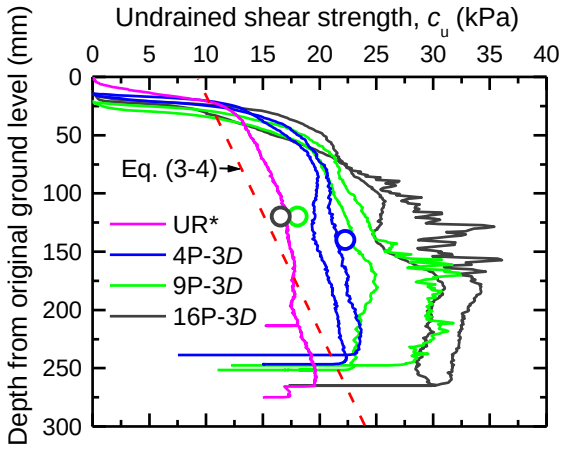

Fig. 3.14. Distributions of undrained shear strength with depth beneath raft edge after loading.

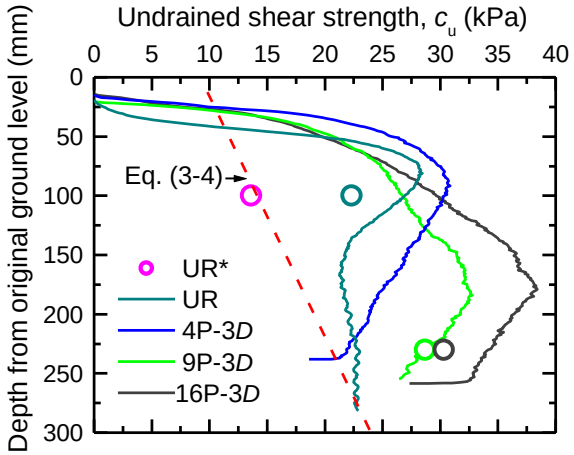

Fig. 3.15. Distributions of undrained shear strength with depth beneath raft center after loading.

3.2.3. Test devices and instrumentation

3.2.3.1 Applied load

For the processes of short term loading tests, which include pile penetration, the static load test of single pile SLTSP/ individual pile SLTIP, static load test of unpiled raft SLTUR*, and static load test of pile group SLTPG, a jack with a travel of 1000 mm was used to apply load. The displacement rate of the jack could be set in a wide range: a high rate of 1 mm/s was set for the pile penetration process, whereas a low rate of 0.1 mm/s was set for the SLTSPs, SLTIPs, SLTUR*, and SLTPG. To measure the applied load during the above short term load tests, a load cell with a capacity of 5000 N (LC1) was employed. One end of the load cell was connected to the jack through a threaded joint and the other one was connected to the pile head through a screw in PPT or pile head/ raft surface through a supporting plate (see Fig. 3.16).

For the long-term loading tests, an air pressure cylinder was employed to apply constant vertical load on each model foundation in a load-controlled manner. The applied load was measured by a load cell with a capacity of 20,000 N (LC2) and that was set between the air cylinder and the top surface of the raft (see Fig. 3.16).

3.2.3.2 Axial forces along pile

The axial forces along piles were measured through strain gages (SGs) attached on both the left and right sides of the pile shaft at different levels, as described in section 3.2.1.1 and shown in Fig. 3.1(c). It should be noted again that in the PG and PR conditions, the load carried by each pile was obtained from the strain measured near the pile head.

3.2.3.3 Settlement

In the jacking processes, the pile-head settlement was measured by an encoder (ENC) with a precision of 0.01 mm and a travel of 440 mm. This ENC was also used for all static load tests in both short term and long term conditions.

Furthermore, for the static load tests in the short term conditions, the foundation settlement was also measured by one dial gage with a precision of 0.001 mm and a travel of 50 mm. For the long term static load tests of foundations, the foundation settlements were measured by four dial gages DG1–DG4 with the same precision of 0.001 mm and the same travel of 50 mm. The four DGs were set on the four symmetric corners of the rigid plate fixed to the raft surface, as shown in Fig. 3.16. The foundation settlement was taken as the average settlement measured from the four dial gages.

One dial gage DG5 was set on the ground surface with a distance of 30 mm from the

raft edge to measure the heaving/ settling of the ground during the long term load tests of 4P-3*D*, 9P-3*D*, and 16P-3*D*.

3.2.3.4 Pore water pressure and earth pressure

The pore water pressures PWPs beneath the raft base were measured by two PWP transducers (PWP1 and PWP2) with the same capacity of 200 kPa and two PWP transducers (PWP3 and PWP4) with the same capacity of 100 kPa. The earth pressures (EPs) were measured at the raft base by an earth pressure cell (EP1) with a capacity of 196 kPa and an earth pressure cell (EP2) with a capacity of 500 kPa.

The measured devices were set up varying according to each experiment. Table 3.6 shows the list of measuring devices and the load tests of which the devices were employed. The locations of these devices during experiments were shown in Fig. 3.17.

During the experiments, all the measured signals from the above devices were recorded using a computerized data acquisition system.

Table 3.7. Measuring devices for experiments.

Device	Capacity	Calibration factor (Solutions)	Application cases
LC1	5000 N	0.8196 N/ μST	PPT, SLTSP, SLTUR*, SLTIP, SLTPG
LC2	20000 N	4.9890 N/ μST	SLTUR, SLTPR
PWP1	100 kPa	0.00278 kPa/ μST	SLTUR, SLTPR
PWP2	100 kPa	0.00283 kPa/ μST	SLTUR, SLTPR
PWP3	200 kPa	0.08615 kPa/ μST	SLTUR, SLTPR
PWP4	200 kPa	0.07368 kPa/ μST	SLTUR, SLTPR
ENC1	440 mm	0.10000 mm/ μST	PPT, SLTSP, SLTUR*, SLTIP, SLTPG, SLTUR, SLTPR
DG1-DG4	50 mm	0.01000 mm/ μST	SLTSP, SLTUR*, SLTIP, SLTPG, SLTUR, SLTPR
DG5	30 mm	0.00675 mm/ μST	SLTPR (in cases: 4P-3*D*, 9P-3*D*, and 16P-3*D*)
EP1	196 kPa	0.03920 kPa/ μST	SLTUR, SLTPR
EP2	500 kPa	0.09335 kPa/ μST	SLTUR, SLTPR

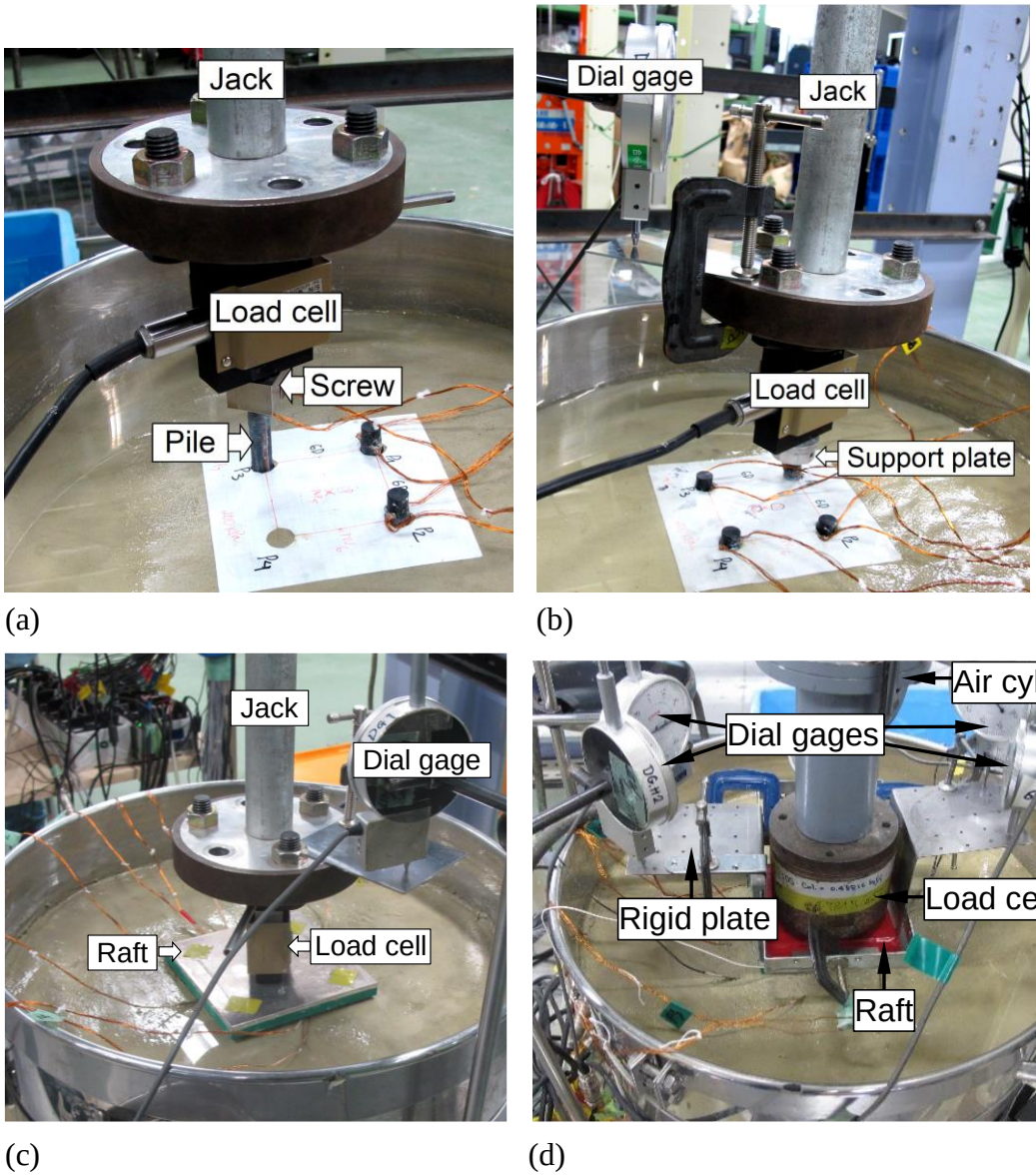

Fig. 3.16. Set up measuring devices for the load tests: (a) PPT; (b) SLTSP/ SLTIP; (c) SLTUR*/ SLTPG; (d) SLTUR/ SLTPR.

3.2.4. Test procedure

Prior to the load tests of the pile foundations, vertical load tests of SPs and the UR* in short term condition were conducted to obtain the bearing capacity of each element and to determine the magnitude of the vertical loads to be applied to the PRF

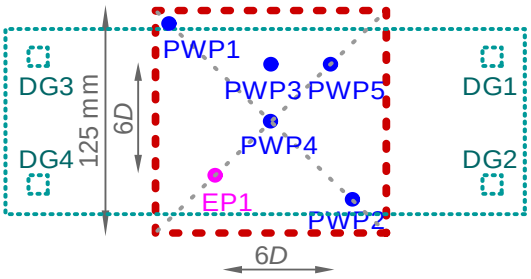

(a)

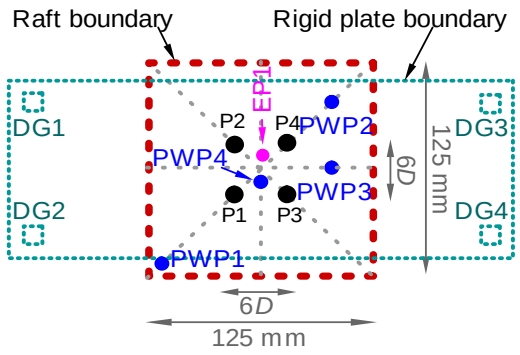

(b)

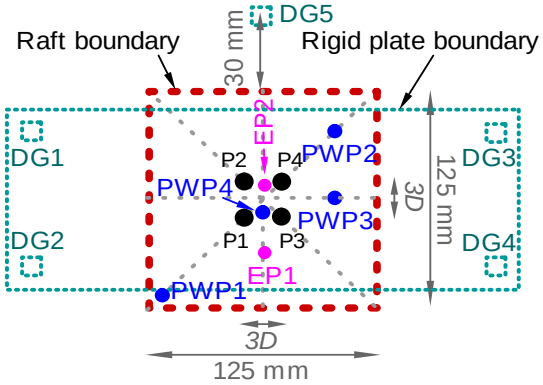

(c)

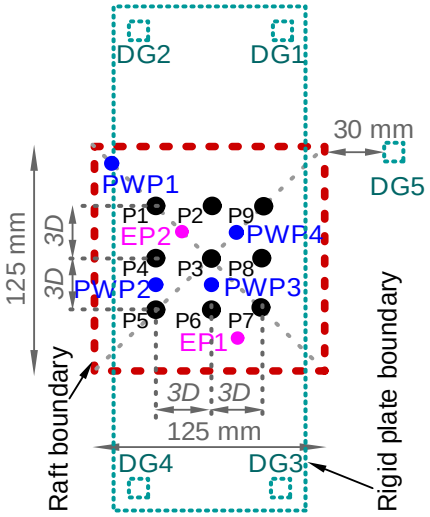

(d)

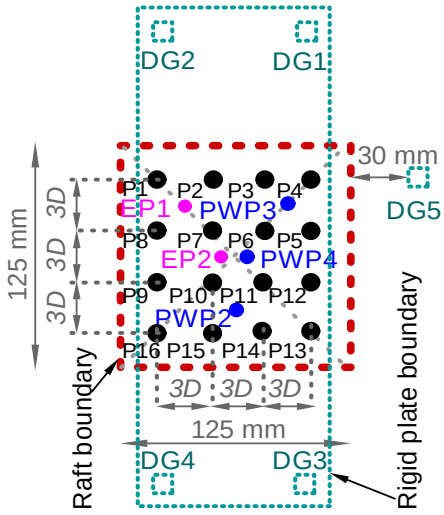

(e)

Fig. 3.17. Locations of measuring devices for the long term load tests: (a) UR; (b) 4P-6*D*; (c) 4P-3*D*; (d) 9P-3*D*; (e) 16P-3*D*.

3.2.4.1 Load test of single pile and unpiled raft (short term)

An SP was jacked into the ground at a constant rate of 1 mm/s until the pile tip reached a depth of 135 mm below the ground surface. After 1 hour following the completion of pile penetration, SLTSP was conducted at a relatively low loading rate of 0.1 mm/s until the pile head had settled by 12.5 mm. It should be noted that the rest period of 1 hour is not sufficient to excess pore pressures, which generate during the jacking process, to dissipate totally.

However, the purpose of this test is just to roughly estimate the bearing capacity of an SP to determine the magnitude of load steps applied to PRFs. Therefore, it is acceptable.

For the UR short term load test, the raft was first set at the center location on the ground surface, whereupon static loading SLTUR* was conducted at a constant rate of 0.1 mm/s until the raft resistance reached a peak (ultimate capacity). The load steps applied to the pile foundations were determined from the results of the SLTSP and SLTUR*; the details are described later.

3.2.4.2 Load test of unpiled raft

For the long term load test of unpiled raft SLTUR, the position of the raft was firstly drawn on the ground surface, at the center location of the model ground. The pore water pressure cells and the earth pressure cell were then installed into the ground at a depth of around 5 mm beneath the raft base (the ground surface). The raft was then set at the predetermined location on the ground surface. The DG1-DG4 and ENC were set to measure the foundation settlement, whereupon SLTUR was conducted. The applied load was increased by multiple steps by the air cylinder in a load-controlled manner. Each load step was maintained for a sufficient duration to obtained the long term behavior of the foundation. The details are described later.

3.2.4.3 Load test of pile foundations

The procedure for the load test of each pile foundation was as follows. First, piles were jacked into the ground one by one with a center-to-center pile spacing $s = 6D$ or $3D$ until the penetration depth reached 135 mm. The penetration rate was 1 mm/s, which was the same as that used for the penetration process of the SP. Fig. 3.16 (a) shows a photo taken during penetration process of 1 pile.

After the penetration process (PPT) of the piles, a rest period was given before conducting SLTIPs. This rest period was for the excess pore water pressure, which was generated during jacking processes, to dissipate. To determine the rest period, the best method is to install pore water pressure cells into the ground before the piles are jacked. However, the installation of the pore water pressure cells will disturb the model ground. Therefore, in this study, the rest period was determined simply by invoking the one-dimensional consolidation theory. The time duration t required for 90 % of PWP on average to dissipate is calculated using the following equation (Terzaghi, 1960):

$$t = \frac{T_v \times H^2}{c_v} \tag{3-5}$$

where T_v is the time factor, taken as 0.848 for 90% of PWP to dissipate; H is the drainage distance, taken as 293 mm (thickness of the clay layer); c_v is the consolidation coefficient, estimated as 3325 mm^2/h from the oedometer test at a consolidation pressure of 100 kPa that is the same as the consolidation pressure for the model ground.

It is noticed that T_v = 0.848 is used for the uniform initial excess pore pressure. The initial excess pore pressure just after the pile jacking is not uniform. However, uniform excess pore pressure was assumed, because the initial excess pore pressure was not measured in the experiments.

A time duration t = 21 hrs (calculated using Eq. (3-5)) is required for 90% of PWP to dissipate. Based on this result, the SLTIPs in the pile foundation was carried out 1 day (24 hrs) after the completion of PPT.

The SLTIPs were conducted on each pile at a displacement rate of 0.1 mm/s until the pile head settled by around 10 mm. Fig. 3.16(b) shows a photo taken during the SLTIP process. After that, the raft was placed on the heads of the piles with a gap of around 5 mm between the raft base and the ground surface, the settlement-measurement devices were set, and static load test of pile group SLTPG was conducted at a displacement rate of 0.1 mm/s until the raft base touched the ground surface. Fig. 3.16(c) shows a photo taken during the SLTPG process. Whereupon the PG changed to the piled-raft (PR) condition and the PG loading test was terminated. It is noted that SLTPG was carried out as soon as possible after SLTIP because the authors aimed to investigate the (residual) capacity of PG with the same rest period of 1 day after the completion of pile installation. The duration between SLTIPs and SLTPG was about 30 minutes, this waiting time was for checking the flatness of the ground surface and setting raft and measurement devices for SLTPG.

The loading method was then changed from a displacement-controlled manner using the jack to a load-controlled manner using the air cylinder for a long-term load test of the PRF. The raft was removed temporarily, and the PWP transducers and EP cells were installed into the ground at a depth of 5 mm just beneath the raft base at the locations as shown in Fig. 3.17 at this stage. The raft was then set again on the pile heads, and the displacement measuring devices were also set again. In the PR condition, the vertical load was increased in multiple steps, each of which was maintained for a sufficient time to observe the long-term behavior of the foundation. Fig. 3.16(d) shows a photo taken during the SLTPR process.

For each model foundation, the applied load was increased in multiple steps until the foundation settlement exceeded 10% of the raft width B_r. The settlement of 10% of B_r could be regarded as the ultimate state after Cooke (1986). The magnitudes of load steps in order from small to large were decided to be the same for all the long-term load tests, for

comparison purposes. Of course, the total number of load steps for each model foundation varied because the ultimate capacity of each foundation was different.

3.3. Experimental results

3.3.1 Load test of single piles and unpiled raft

Fig. 3.18 shows the results of SLTSP and SLTUR*. The SP reached its ultimate capacity with a pile-head displacement of around 1 mm (0.1*D*), whereas the UR* had a much higher ultimate capacity. Interestingly, however, the initial stiffnesses ($\Delta P/\Delta w$) of the SP and UR were almost equal.

The bearing capacities of the SP and UR were around 108 N and 2130 N, respectively. As suggested by Cooke (1986), the ultimate capacity of the UR* was determined from the load–settlement curve at a settlement of 0.1B_r. The ultimate capacity of the foundation herein was roughly predicted by summing the ultimate capacity of UR* and the ultimate capacity of SPs. The sum of the UR* bearing capacity and four times, nine times, and sixteen times the SP bearing capacity was 2562 N, 3102 N, and 3858 N, respectively. These values were considered as the predicted ultimate capacity of the piled raft for the cases of 4P-6*D*/ 4P-3*D*, 9P-3*D*, and 16P-3*D*, respectively. Table 3.7 shows load steps applied to the foundations and the corresponding factors of safety F_S, based on the predicted ultimate capacity of each foundation.

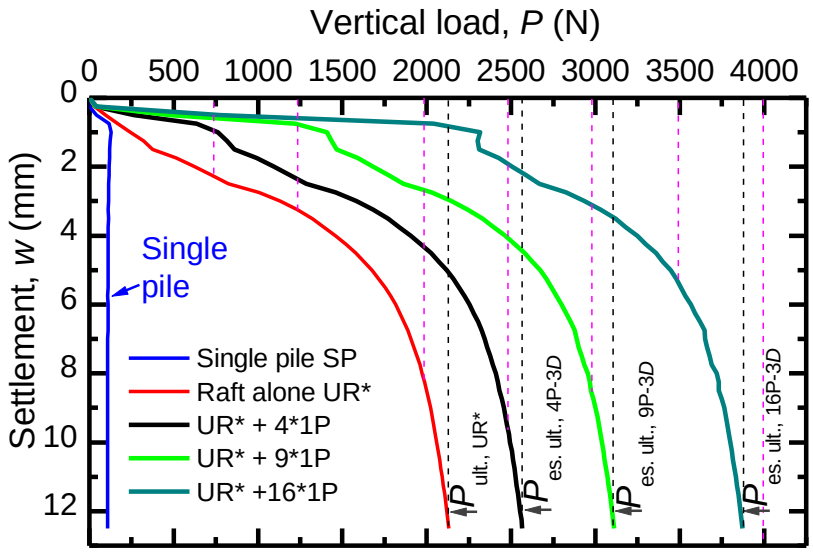

Fig. 3.18. Load tests of single pile and unpiled raft (SP & UR*).

Table 3.8. Magnitude of applied loads on piled rafts and corresponding factors of safety.

Applied loads	Factors of safety F_S			
	UR*	4P-6*D*/ 4P-3*D*	9P-3*D*	16P-3*D*
750 N	2.85	3.42	4.14	5.14
1250 N	1.70	2.04	2.48	3.09
2000 N	1.06	1.28	1.55	1.93
2500 N	0.85	1.02	1.24	1.54
3000 N	-	0.85	1.03	1.29
3500 N	-	-	0.89	1.10
4000 N	-	-	-	0.96
4500 N	-	-	-	0.86

3.3.2 Load test of individual piles in pile foundation

3.3.2.1 Jacking processes

Fig. 3.19 shows the jacking force of each pile of the foundations for (a) 4P-6*D*, (b) 4P-3*D*, (c) 9P-3*D*, and (d) 16P-3*D*. The sequences of pile installation were also shown in these figures. In the cases of (a) 4P-6*D* and (b) 4P-3*D*, pile 1 (P1) was jacked first, followed by piles 2 (P2), 3 (P3), and 4 (P4). As such, P1 behaved as an SP during the jack-in processes. For the cases of (c) 9P-3*D*, and (d) 16P-3*D*, the pile, which was jacked first, was P3 and P7, respectively. As such, P3 and P7 behaved as an SP during the jack-in processes of 9P-3*D* and 16P-3*D*, respectively. It is clear from the figure that, these single piles had similar resistances with a resistance of about 85 N at the settlement of 135 mm (final jacking depth).

In the case of 4P-6*D*, it is interesting that no significant difference was seen in the resistances of the four piles. The four piles had almost equal resistance, which was equal to that of the SP (P1), indicating negligible interaction among the piles.

In the case of (b) 4P-3*D*, (c) 9P-3*D*, and (d) 16P-3*D*, some piles had slightly higher resistances than the SP in the later stages of their installation, such as P7 in the case of 9P-3*D* and P2 and P15 in the case of 16P-3*D*. However, the differences between pile resistances were small. Therefore, it could be said that, during jack-in in saturated clayey ground at a penetration rate of 1 mm/s, the sequences of pile installation, the pile number, and the pile spacing do not affect the pile resistance significantly.

3.3.1.2 Static load test of individual piles in pile foundation

One day after the jacking processes were completed, SLT of each pile (SLTIP) was conducted. Fig. 3.20 shows the results of those tests for (a) 4P-6*D*, (b) 4P-3*D*, (c) 9P-3*D*, and (d) 16P-3*D*. The sequence of the SLT of each pile was also shown on these figures.

Let us consider the cases of (a) 4P-6*D* and (b) 4P-3*D* first, in these cases, the four piles were arranged symmetrically and had similar positions. The SLT was conducted first on P4 followed by P3, P2, and P1. Fig. 3.20(a) and (b) show that P4 behaved very similarly in both cases. Its resistance increased rapidly with the pile displacement and reached a peak of 175 N at a pile-head settlement of around 1 mm (0.1*D*), whereupon it exhibited softening behavior. That is, the pile resistance then decreased with increasing pile-head settlement and reached a residual resistance of 135 N for 4P-6*D* and 140 N for 4P-3*D*. For 4P-6*D*, the other three piles (P1–P3) exhibited almost the same load–settlement response and behaved in a similar manner to P4. Each pile reached a peak of around 140 N and then decreased to a residual resistance of around 120 N. These values were smaller than the corresponding resistances of P4, on which the SLT was conducted first. For 4P-3*D*, P1–P3 also behaved similarly, but they did not exhibit clear softening behavior. The capacity of these piles was around 135 N.

In general, the residual pile resistance for 4P-3*D* in the SLTIP was marginally higher than that of the corresponding pile for PF-6*D*, even though they had almost the same resistance during installation. This difference may have been due to the effect of the pile spacing. The resistance of each pile in both groups was higher than that of the SP (see Fig. 3.18) on which the SLTSP was conducted 1 hour after penetration. It is thought that this result was due to ground consolidation during the rest period before the SLTIP in the pile foundations. It is reasonable to think that the excess PWP generated during pile installation dissipated and that the soil surrounding the piles recovered its strength during the 1-day rest period in the cases of pile foundations.

For the cases of (c) 9P-3*D* and (d) 16P-3*D*. The piles were arranged symmetrically with three types of pile positions (corner piles, edge piles, and center piles). The results show that the corner piles (P7, 1, 5, and 9 for the case of 9P-3*D* and P14, 4, 13, and 1 for the case of 16P-3*D*), of which SLTs were conducted firstly, had higher resistances, in comparison with edge piles and center piles. Oppositely, the center piles (P3 for the case of 9P-3*D* and P10, 6, 11, and 7 for the case of 16P-3*D*), of which SLTs were conducted lastly, had the lowest resistances.

In general, for all 4 pile foundations, the pile, of which SLTIP was carried out later, had lower resistance. One of the possible reasons is that the SLT process of previous piles generated PWP and resulted in reduced lateral stresses of the surrounding soil. Consequently, the resistance of the pile, of which SLT was carried out later, became smaller. The corner piles (SLTIPs were conducted first) exhibited softening behavior.

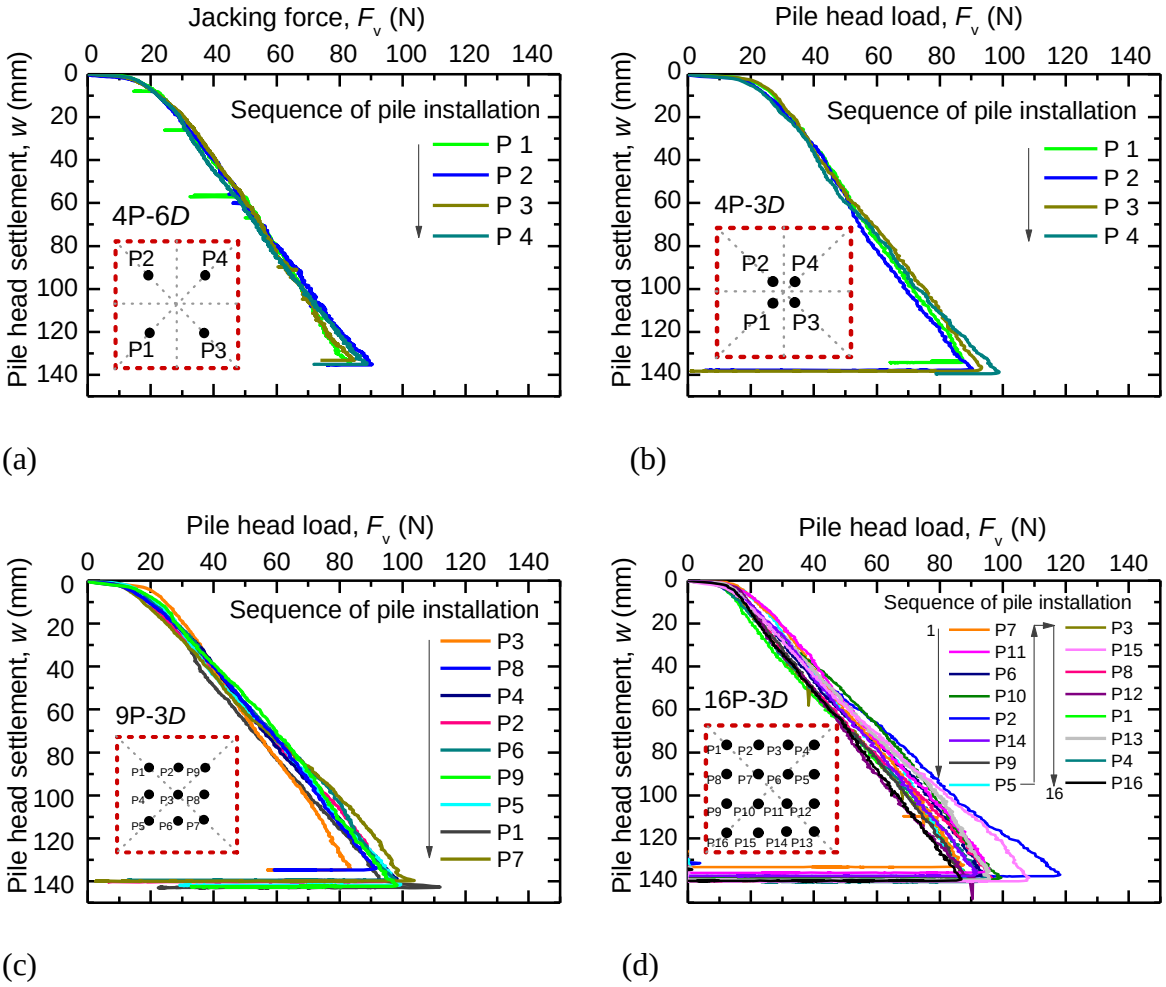

Fig. 3.19. Pile resistance during pile jacking processes in pile foundations: (a) 4P-6*D*; (b) 4P-3*D*; (c) 9P-3*D*; and (d) 16P-3*D*.

3.3.3 Static load test of pile groups

The load–settlement curves from the SLTPGs are presented in Fig. 3.21 for (a) 4P-6*D*, (b) 4P-3*D*, (c) 9P-3*D*, and (d) 16P-3*D*. The load–settlement curve of the PG (for which the load was measured directly via the load cell), that of each pile (for which the load was obtained from strains measured via SGs near the pile top), and the sum of the load–settlement curves of the piles in each group are shown in these figures. The sum of pile loads estimated from the strain measurements was clearly smaller than the total applied load on the raft measured using the load cell. It should be noted that the distance from the SGs at the top level of each pile to the pile head was 20 mm, therefore the total load on the piles measured using the SGs were smaller than that on the raft because part of the applied load was carried by the shaft resistance between the pile head and the top SG level. The difference between the applied load and the sum of pile loads was indicated by one coefficient for each foundation. In the figure, one more curve, which was calculated by multiplying the sum of pile loads by the coefficient, was added for each case of foundation. The coefficient for the cases of (a) 4P-

6*D*, (b) 4P-3*D*, (c) 9P-3*D*, and (d) 16P-3*D* were 1.17, 1.20, 1.16, and 1.15, respectively. It is noticed that, although the pile load obtained at the top SG level was smaller than the actual pile-head load, the axial force at the top SG level is referred to herein as the "pile load."

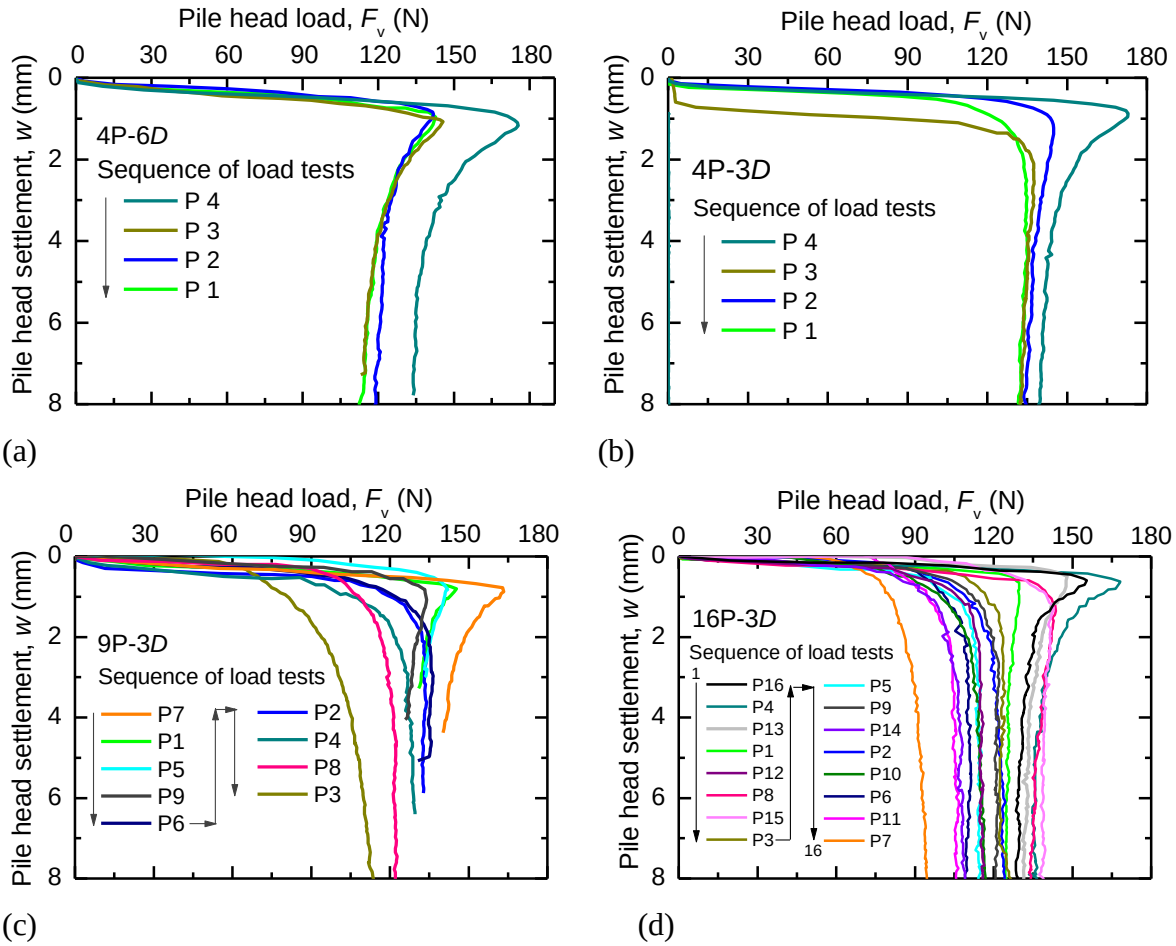

Fig. 3.20. Load vs. settlement during static load test of each pile in pile foundations: (a) 4P-6*D*; (b) 4P-3*D*; (c) 9P-3*D*; and (d) 16P-3*D*.

Table 3.9. Pile capacity and pile group capacity in load tests of each pile and load tests of pile groups.

Description	Foundation cases			
	4P-6*D*	4P-3*D*	9P-3*D*	16P-3*D*
Pile group ultimate capacity $P_{ult,\ PG}$ (N)	516	590	1225	2100
Sum of pile head load in SLTPG $P_{pile\ heads}$ (N) (from strain gages)	440	490	1055	1825
Average load per pile in SLTPG $P_{P,aver.,\ SLTPG}$ (N) ($P_{ult,\ PG}$/ pile number)	129	148	136	131
Average load per pile in SLTIP $P_{P,aver.,\ SLTIP}$ (N)	124	136	127	120

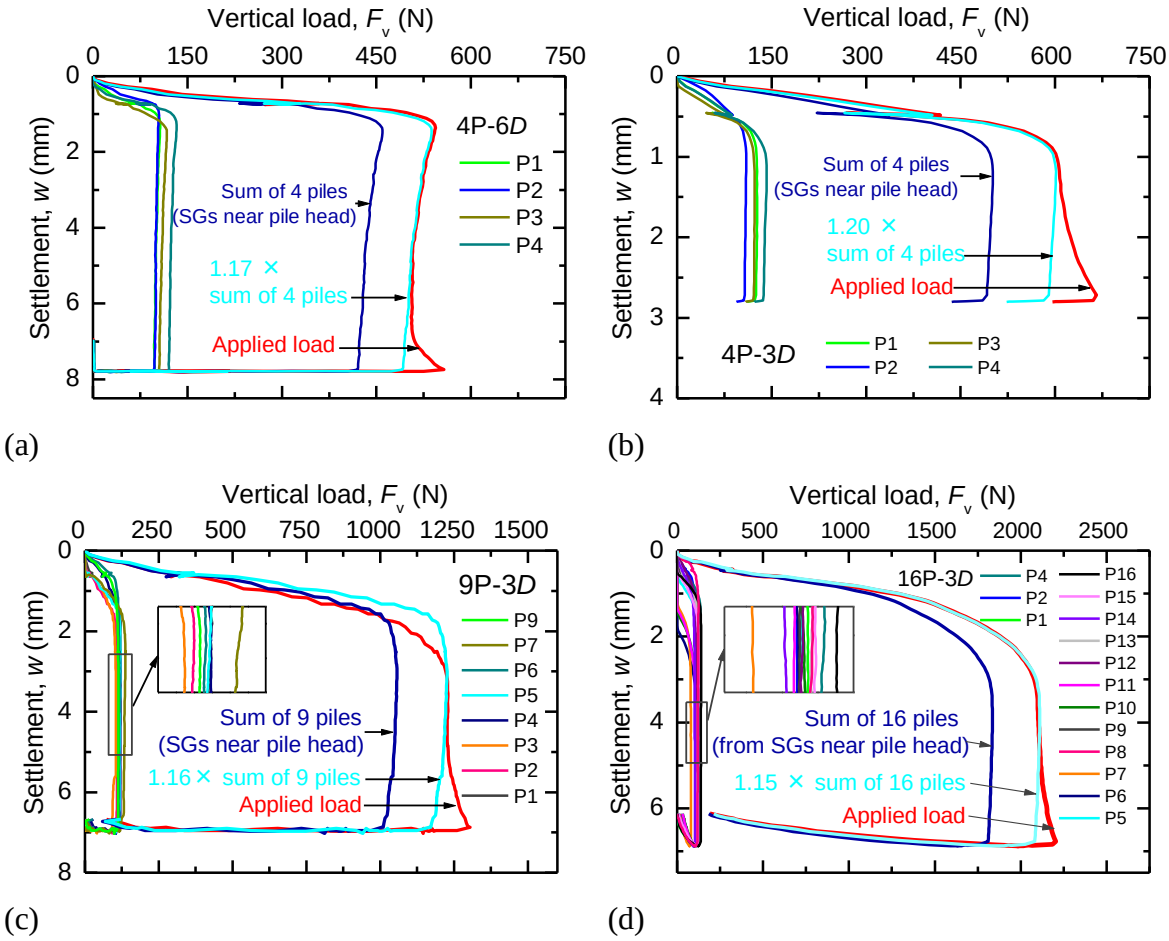

Fig. 3.21. Load vs. settlement during static load test of pile group: (a) 4P-6*D*; (b) 4P-3*D*; (c) 9P-3*D*; and (d) 16P-3*D*.

Table 3.8 presents the ultimate capacity of the pile groups and the corresponding average load carried by a pile at the ultimate condition of the pile groups. In Table 3.8, the average load per pile in static load tests of individual piles SLTIP was also shown for comparison purposes.

Fig. 3.21 (a)-(d) show that the ultimate PG resistance of 4P-6*D*, 4P-3*D*, 9P-3*D*, and 16P-3*D* were 516 N, 590 N, 1225 N, and 2100 N, respectively. The average load per pile for the four groups were 129, 148, 136, and 131 N, respectively.

Firstly, comparing the results of 4P-6*D* to that of 4P-3*D* to know the effect of pile spacing on the behavior of pile groups. Fig. 3.21 (a) and (b) show that the PG with narrower pile spacing s = 3*D* had larger resistance and initial stiffness than those of the PG with larger pile spacing s = 6*D*. The pile loads obtained from the strains, which were measured from strain gages at the top level (20 mm from the pile head), were also higher in the case of 4P-3*D* (490 N), compared to the case of 4P-6*D* (440 N). For the case of 4P-6*D*, from the ratio between the sum of pile loads and the applied load on the raft (1/1.17 or 85 %), It is thought that 15 % of the applied load was carried by the pile shaft resistance on 20 mm from the pile

top to the top strain gage level. Similarly, in the group of 4P-3*D* with the ratio between the sum of pile loads and the applied load on the raft of 1/1.20 (or 83 %), about 17 % of the applied load was carried by the pile shaft resistance on 20 mm from the pile top to the top strain gage level. The load carried by the shaft resistance on the first 20 mm of pile top section for the case of 4P-3*D* was slightly higher than that of 4P-6*D*.

Comparing the results between 4P-3*D*, 9P-3*D*, and 16P-3*D* to investigate the effect of pile number on the behavior of PG. Of course, the PG ultimate capacity increased with the increasing number of piles (Table 3.7). However, it is interesting that the average load per pile decreased with the increasing pile number (Table 3.8). Looking at the zoom-in of the pile load on Fig. 3.21(c) and (d), it is clear that the center piles in the PGs of 9P-3*D* and 16P-3*D* carried smaller load than the corner and edge piles did. This may be the reason for the lower average load per pile when the number of piles in the group increased. The proportion of applied load carried by the 20-mm-pile-top section between the pile head and top strain gage level was also decreased from 17 % to 13 % with the increasing number of piles.

Comparing pile behavior in SLTIP and SLTPG, Table 3.8 shows that, for all 4 pile foundations, the average load carried by each pile in SLTPG was moderately higher than that by the corresponding pile in SLTIP. This indicates that the interaction among the piles when they were loaded at the same time increased the pile resistance.

For the case of 9P-3*D* and 16P-3*D*, the experimental results also show the effect of pile position on the pile behavior. In the zoom-in figures in Fig. 3.21(c) and (d), the results show that in PG condition, the average load carried by a corner pile was highest and that by a center pile was lowest among three types of pile position, this trend is similar to the pile behavior in SLTIP (Fig. 3.20).

3.3.4 Load test of piled rafts

In the PR condition, the load steps were planned to be applied as mentioned earlier in Table 3.7. After completion of the increasing applied load of each load step, the applied load was maintained constant for a sufficient duration to observe the time-dependent behavior of the foundation. The results were divided into three main periods as the load-increasing period, the primary consolidation period, and the secondary consolidation period. The results of each period were discussed in the following sections.

3.3.4.1 Behavior during load-increasing period

a. Behavior during load-increasing period of unpiled raft

Fig. 3.22 shows how the applied load *P* and the settlement *w* of unpiled raft changed over the entire experimental duration as well as zoom-in of load-increasing period of each load

step. A large settlement occurred and foundation settlement exceeded 10 % of raft width when the third load step (P = 2 kN) was applied; consequently, the load test was stopped after the third load step. Also shown in the figure is the uplift force P_w, which was calculated by multiplying the PWP by the raft base area. It is noticed that the pore water pressure was measured at different locations beneath the raft base, and the measured results show that the distribution of pore pressures varied slightly between measurement locations, however, the uplift force herein were calculated from the measured value at the raft base center, assuming the PWP to be distributed uniformly over the raft base. Fig. 3.23(a)–(c) show the increments of the applied load (or raft load, because there is no pile in this experiment, the raft supported all the applied load) and uplift force during the load-increasing periods of the three load steps of UR, respectively.

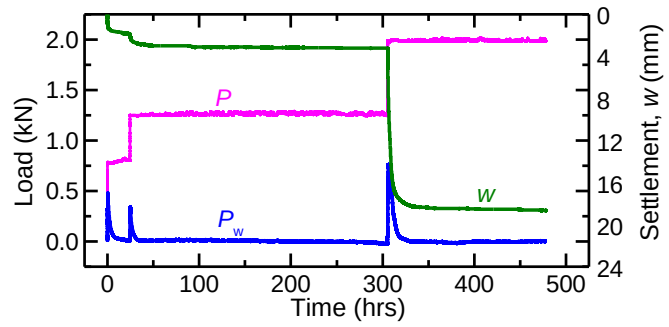

(a)

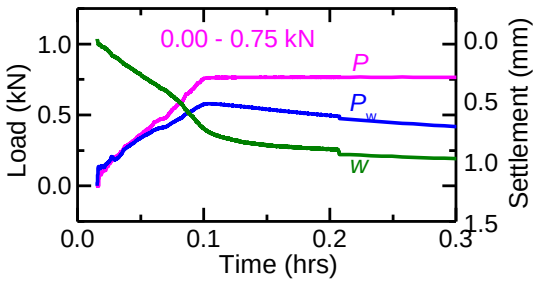

(b)

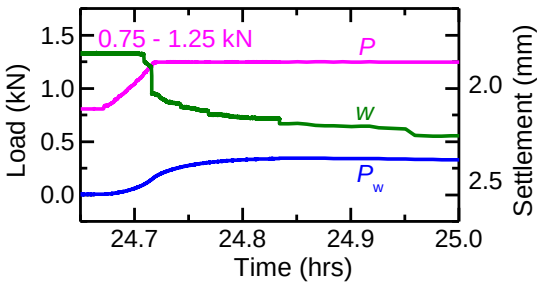

(c)

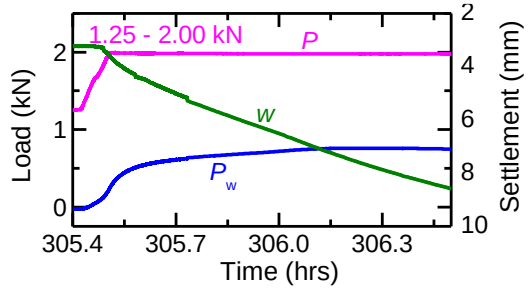

(d)

Fig. 3.22. Changes of load and settlement of UR with time: (a) full-time of loading test; zoom-in of load-increasing period of (b) first load step; (c) second load step; (d) third load step.

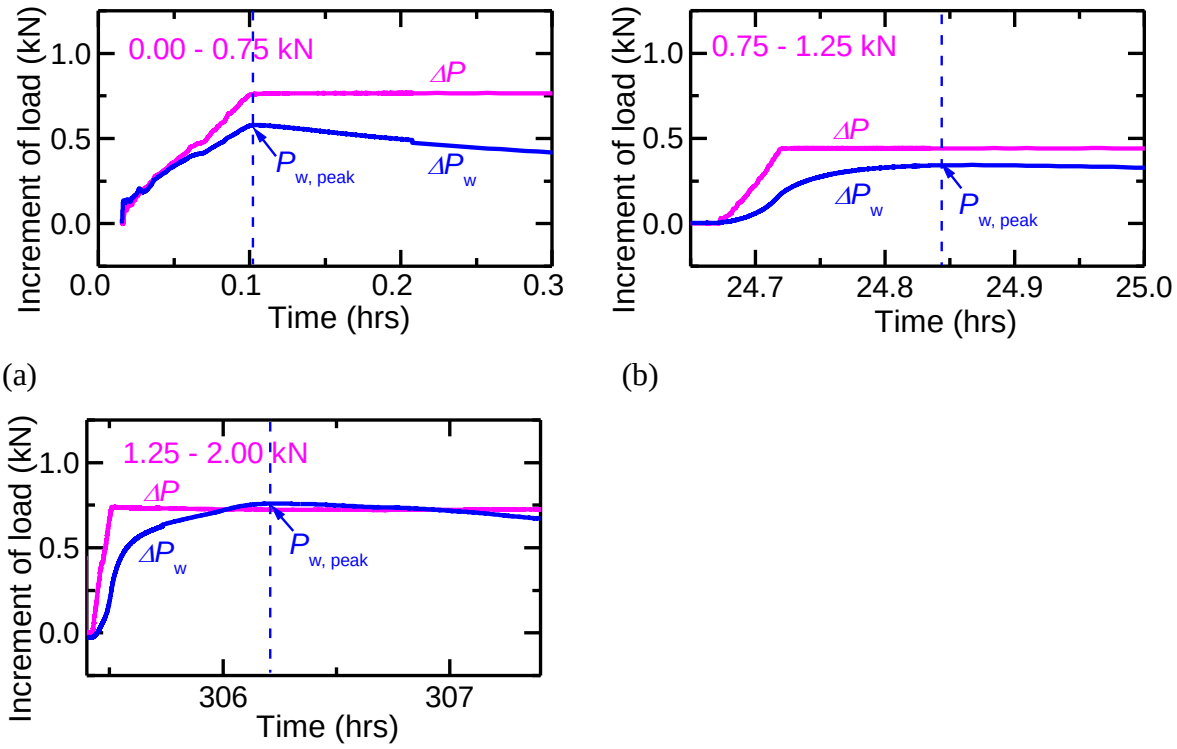

Fig. 3.23. Increments of loads during load-increasing period in loading tests of unpiled raft: (a) first load step; (b) second load step; (c) third load step.

Focusing first on the first load step P = 0.75 kN, it is seen from Fig. 3.22(b) that the uplift force P_w (or pore water pressure PWP) at the raft base started increasing when the applied load P started increasing, and the P_w reached a peak at the same time when the P reached the target value of 0.75 kN. The P_w carried about 80 % of P at the peak. The foundation settlement also increased with increasing applied load. After the applied load reached 0.75 kN, the foundation continued to settle at a lower speed.

For the second and the third load steps, Fig. 3.22(c) and (d) show that when the applied load P began to increase, the uplift force P_w also began to increase but the increment of P_w was small at the early stages of the load-increasing period, compared to the increment of P. The foundation settlement did not increase immediately with increasing P, but did increase after the applied load began to increase for a while. The P_w began to increase quickly when the foundation settlement began to increase. It should be noted that the applied load remained constant after it was increased to the target value of each load step but that the PWP continued to increase for a short while to reach a peak. Consequently, the "load-increasing period" herein refers to the time from when the load began to be increased to the time of peak PWP, the term "immediate settlement" refers to the settlement that occurred in the load-increasing period, and the "primary consolidation period" refers to the time from the end of the load-increasing period to when the PWP returned to almost zero. In the second load step,

Fig. 3.23(b) shows that at peak value, P_w supported a large part (about 80 %) of the applied load. In the last load step, Fig. 3.23(c) shows that P_w supported up to 100 % of the applied load. Note from Fig. 3.23(c) that ΔP_w seemed to slightly exceed ΔP because the P_w was calculated from PWP at the raft base center, where PWP was a little slightly higher than PWP at the other locations.

b. Behavior during load-increasing period of 4P-6D and 4P-3D

Fig. 3.24(a) shows how the applied load P and the settlement w of 4P-6D changed over the entire experimental duration. A large settlement occurred (w > 10% raft width B_r) when the third load step (P = 2 kN) was applied, and some cracks were seen on the ground; consequently, the loading test was completed after the third load step. Also shown in the figure are (i) the load P_p carried by the four piles, (ii) the load P_r carried by the raft, and (iii) the uplift force P_w, which was calculated by multiplying the PWP at the raft base center by the raft base area (assuming the PWP to be distributed uniformly over the raft base). Fig. 3.24(b)–(d) show magnified views of the load-increasing period of the three load steps, and Fig. 3.25(a)–(c) show the increments of the applied load, raft load, pile load, and uplift force during the load-increasing periods of the three load steps of 4P-6D, respectively. The corresponding results for 4P-3D are shown in Figs. 3.26 and 3.27, respectively. Note that all the load steps applied on both the foundations were larger than the corresponding pile group ultimate capacities.

Focusing first on the results for 4P -6D, Fig. 3.24(b) shows that in the early stages of the load-increasing period when the applied load P was less than 0.5 kN, the settlement increase was minor. When an initial small load less than 0.3 kN (about 70 % of ultimate capacity of 4 SPs) was applied, the pile resistance P_p increased rapidly to support the load, and this increase was almost equal to that of the applied load. Consequently, the piles were effective at suppressing the foundation settlement in this stage. The pile resistance continued to increase to a temporary peak $P_{p,\,peak}$ = 0.38 kN in this load-increasing period, whereupon the pile resistance decreased (softening behavior) and the foundation began settling rapidly. The raft resistance P_r increased rapidly to support the increased applied load as well as the part of the load that was transferred from the pile resistance because of the softening behavior of the piles after the peak pile resistance.

Let us look at how the excess PWP (or uplift force P_w in the figures) changed at the raft base. The PWP clearly began to increase when the settlement began to increase, and the PWP and the settlement increased sharply after the pile resistance reached its peak.

The PWP reached 17 kPa at the end of the load-increasing period in the first load step, at which time the raft load was 0.42 kN, which was 56% of the applied load. The value

$P_{w\,=}$ 0.266 kN due to PWP = 17 kPa corresponded to 63% of the raft load or 35% of the applied load of 0.75 kN (Table 3.9). The changes ΔP, ΔP_p, ΔP_r, and P_w (= ΔP_w) with time during the load-increasing period in the first load step are shown in Fig. 3.25(a) and are the same as those in Fig. 3.24(b).

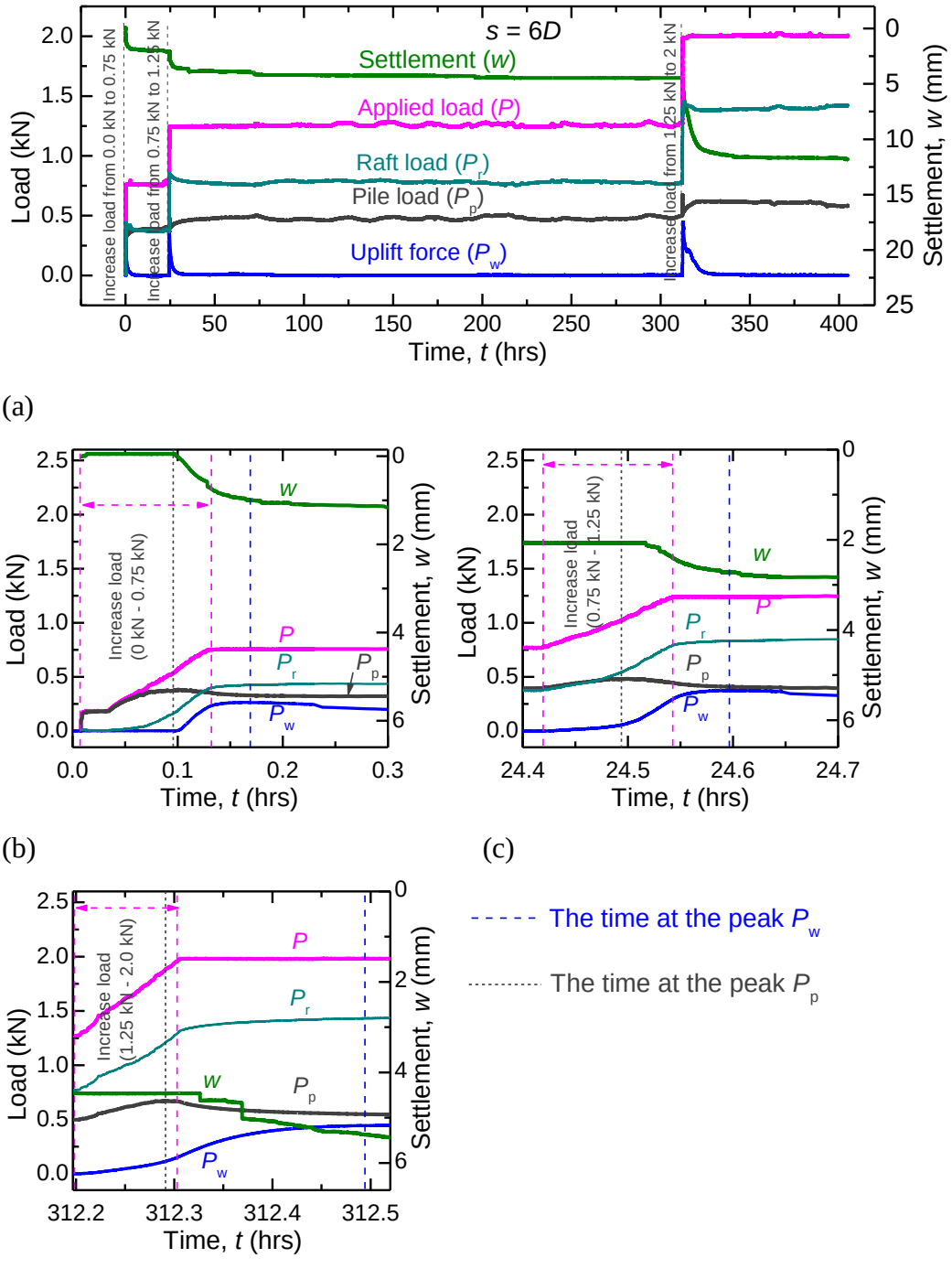

Fig. 3.24. Changes of load and settlement of 4P-6*D* with time: (a) full-time of loading test; zoom-in of load-increasing period of (b) first load step; (c) second load step; (d) third load step.

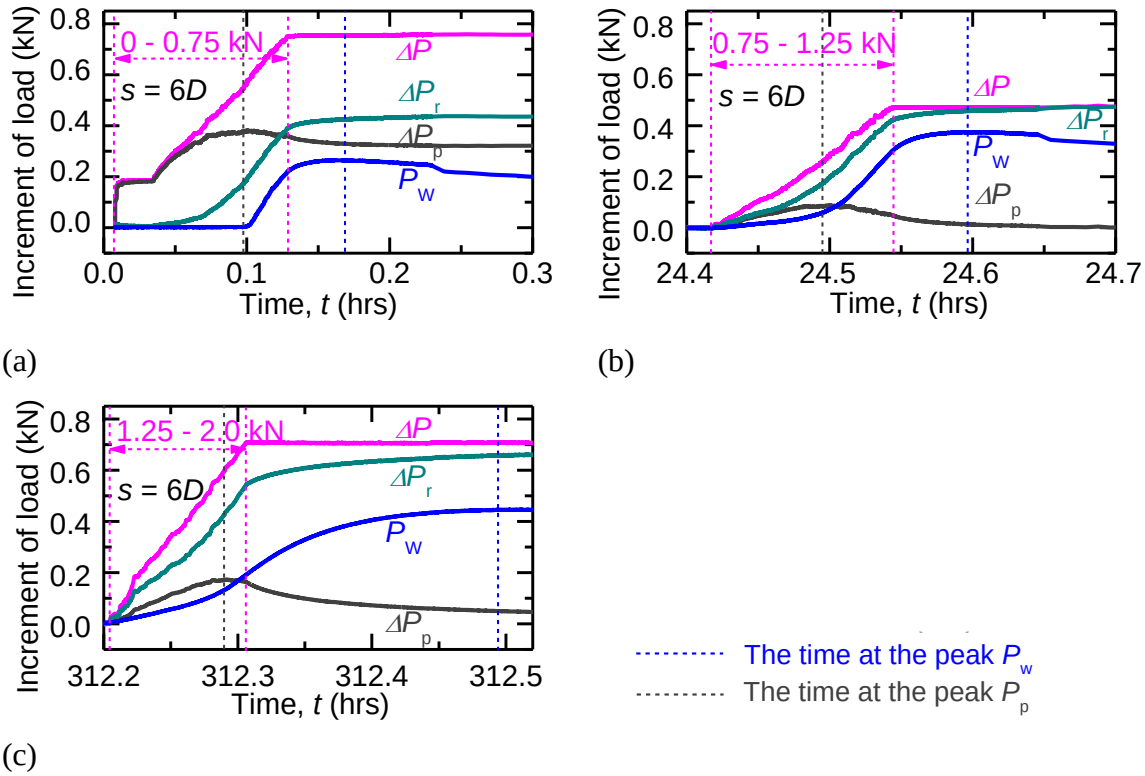

Fig. 3.25. Increments of loads of 4P-6*D* during load-increasing period: (a) first load step; (b) second load step; (c) third load step.

In the second and third load steps (Figs. 3.24(c) and 3.24(d)), in the early stages of the load-increasing period, the settlement increase was minor. Consider Figs. 3.25(b) and 3.25(c), in which the increments of P, P_p, P_r, and P_w from the start of each load step are compared. It is clear from Figs. 3.25(b) and 3.23(c) that both the pile resistance and the raft resistance began to increase from the start of the load-increasing period (early stages). In the later stages of the load-increasing period, the foundation exhibited similar trends to those in the first load step (i.e., the pile resistance increased to a peak and then decreased, and the PWP increased with time and reached a peak in a short duration after the applied load reached its target value). The most important difference between the first load step and the others is the load carried by the raft at the end of the load-increasing period. As mentioned above, the raft carried 56% of the applied load at the end of the load-increasing-period of the first load step. In the second and third load steps, Figs. 3.25(b) and 3.23(c) show that the increment of the raft load was 0.49 kN and 0.67 kN, respectively, equal to 98% and 89%, respectively, of the increment of the applied load in the second and third load steps. The reason for this phenomenon is that the pile reached its ultimate state in the first load step. The ultimate pile resistance increased in the second and third load steps (see Fig. 3.24), but its increment was

relatively small compared with that of the applied load. Therefore, when the second and third load steps were applied, the raft supported most of the increased applied load.

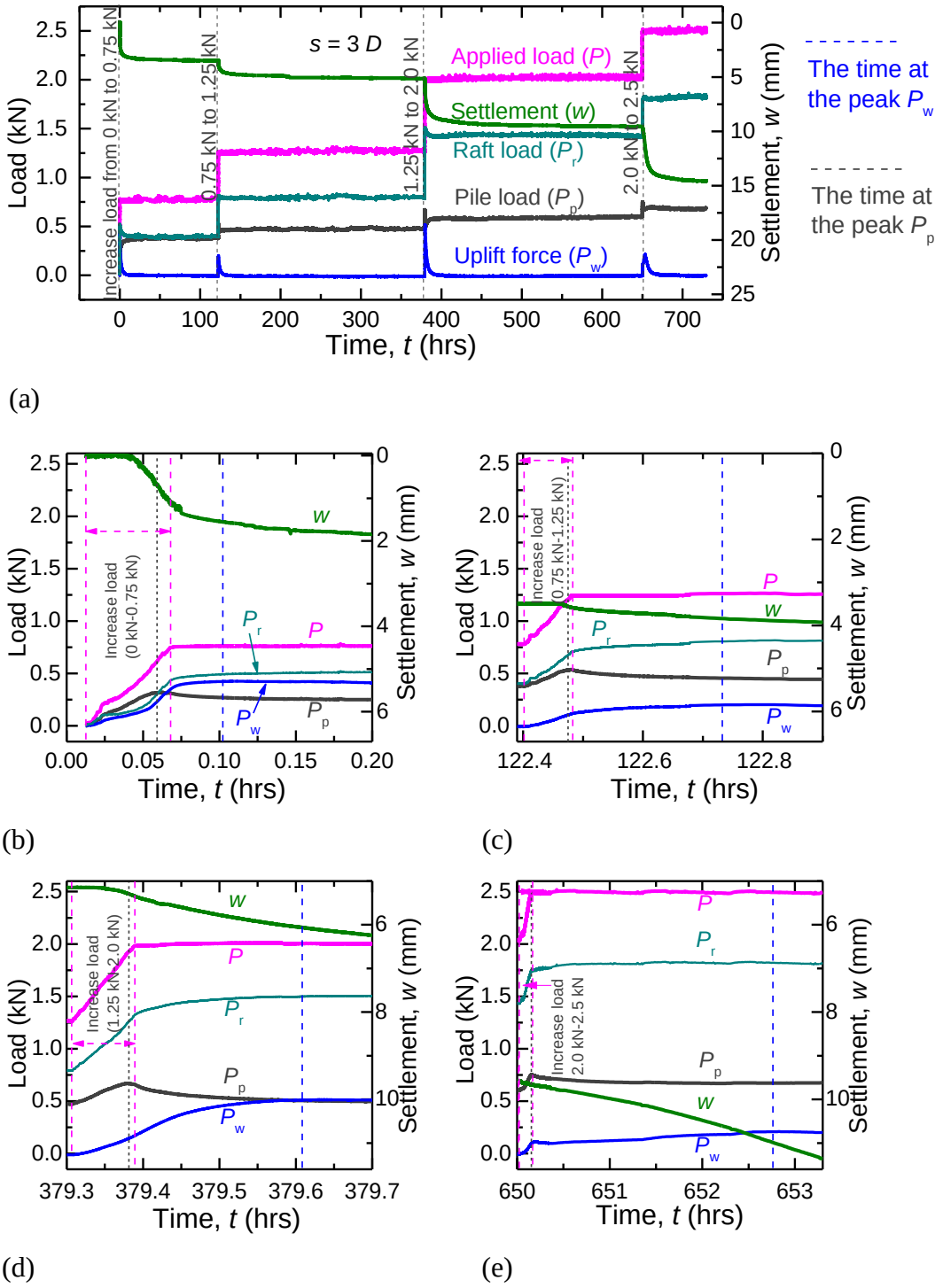

Fig. 3.26. Changes of loads and settlement of 4P-3*D* with time: (a) full-time of loading test; zoom-in of load-increasing period of (b) first load step; (c) second load step; (d) third load step; (e) fourth load step.

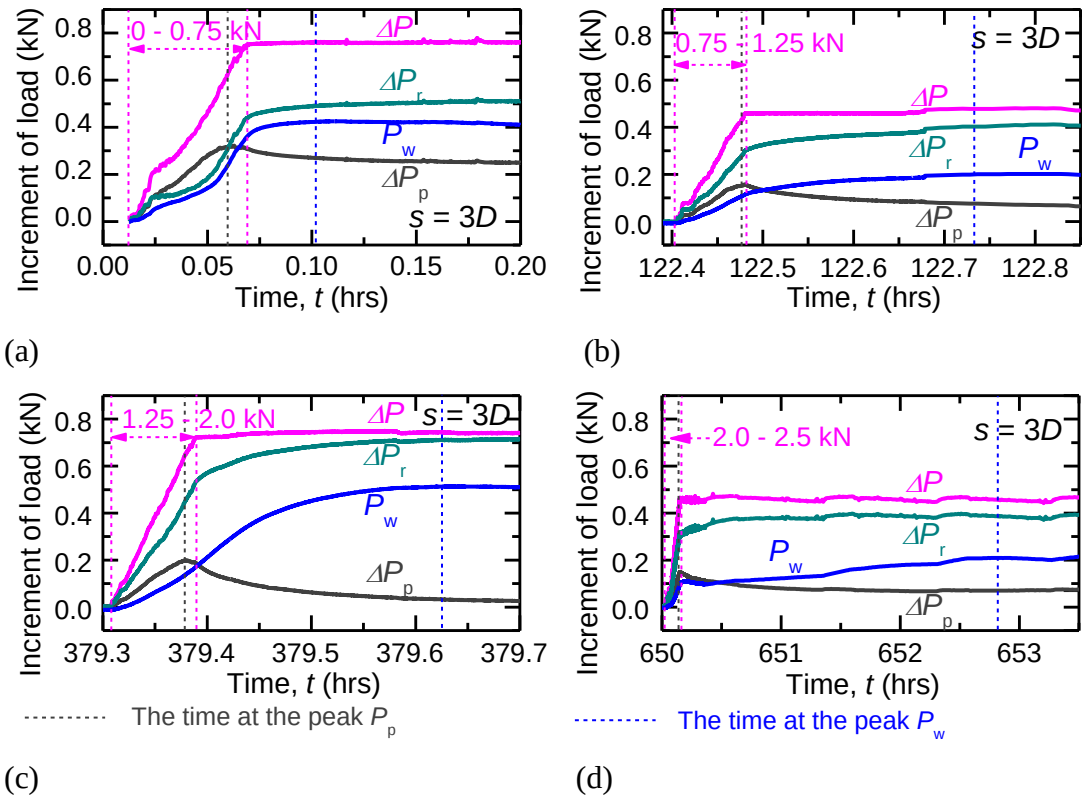

Fig. 3.27. Increments of loads of 4P-3*D* during load-increasing period: (a) first load step; (b) second load step; (c) third load step; (d) fourth load step.

As for 4P-3*D*, Figs. 3.26 and 3.27 show clearly that it behaved very similarly to 4P-6*D* (Figs. 3.24 and 3.25) but with slightly different magnitudes. Let us consider the differences in more detail to investigate how the pile spacing affects the settlement and load transfer in the load-increasing periods. In the load-increasing period of the first load step, the piles in 4P-3*D* (Fig. 3.26(b)) supported less load than did those in 4P-6*D* (Fig. 3.24(b)). Therefore, it is reasonable that the settlement of 4P-6*D* (Fig. 3.24(b)) was less than that of PF-3*D* (Fig. 3.26 (b)). In the load-increasing period of the second load step, the opposite trends were seen: because the increment of the pile resistance of 4P-3*D* (Fig. 3.27(b)) was larger than that of 4P-6*D* (Fig. 3.25(b)), the settlement increment of 4P-3*D* (Fig. 3.26(c)) became smaller than that of 4P-6*D* (Fig. 3.24(c)). In the third load step, the increments of pile resistance and settlement during the load-increasing period were almost equal for both foundations (see Figs. 3.25(c) and 3.27(c), and Figs. 3.24(d) and 3.26(d)).

Next, we compare the PWP between the two foundations. Compared with the corresponding values for 4P-6*D* (Fig. 3.24), the peak PWP for 4P-3*D* (Fig. 3.26) was higher in the first load step, lower in the second load step, and almost equal in the third load step. Interestingly, the PWP trend was similar to the settlement one. The detailed values of the peak PWP are summarized in Table 3.10, as are the percentages of (i) the increment of raft load supported by PWP and (ii) the increment of the applied load supported by PWP at the

end of the load-increasing period. According to Table 3.10, a significant proportion of the increment of raft load was supported by PWP, at least 43% and at most 73%.

Table 3.10. Increment of raft load during load-increasing period.

(a) 4P-6*D* and 4P-3*D*

Applied load *P* (kN)	Increment of applied load Δ*P* (kN)	4P-6*D* Increment of raft load ΔP_r (kN) [% of Δ*P*]	4P-3*D* Increment of raft load ΔP_r (kN) [% of Δ*P*]
0.75	0.75	0.42 [56 %]	0.50 [66 %]
1.25	0.50	0.49 [98 %]	0.44 [88 %]
2.0	0.75	0.67 [89 %]	0.71 [95 %]
2.5	0.50	- -	0.40 [80 %]

(b) 9P-6*D* and 16P-3*D*

Applied load *P* (kN)	Increment of applied load Δ*P* (kN)	9P-3*D* Increment of raft load ΔP_r (kN) [% of Δ*P*]	16P-3*D* Increment of raft load ΔP_r (kN) [% of Δ*P*]
0.75	0.75	0.13 [17 %]	0.10 [13 %]
1.25	0.50	0.12 [24 %]	0.07 [14 %]
2.0	0.75	0.63 [84 %]	0.10 [13 %]
2.5	0.50	0.29 [60 %]	0.11 [22 %]
3.0	0.50	0.44 [88 %]	0.22 [44 %]
3.5	0.50	- -	0.29 [58 %]
4.0	0.50	- -	0.34 [68 %]
4.5	0.50	- -	0.29 [58 %]

Turning next to the load carried by the four piles, the peak pile-head load in each load-increasing period is presented in Table 3.11, according to which at the first load step of 0.75 kN (750 N), the peak loads carried by the four piles of 4P-6*D* and 4P-3*D* were 0.38 kN (an average of 95 N per pile) and 0.32 kN (an average of 80 N per pile), respectively. Let us look back at the results of the PG load tests (Fig. 3.21(a) and 3.21(b)), in which each pile was loaded until its ultimate capacity. At the ultimate PG load, one pile carried either 110 N (4P-6*D*) or 124 N (4P-3*D*), and the total load on the PG was either 516 N (4P-6*D*) or 590 N (4P-3*D*). Although the load applied on the PRF (750 N) exceeded that applied on the PG (516 N or 590 N), the average load on one pile in the PRF was clearly less than that on one pile in the PG because the raft supported part of the applied load. Horikoshi and Randolph (1996) presented similar results; they investigated the behavior of a PRF with nine piles and

a pile spacing of 8*D* in Kaolin clay, and they found that the piles were loaded to around 70% of the single (capped) pile capacity at the final foundation load.

Looking through the whole of Table 3.11, it is interesting that in both foundations, the peak pile resistance increased with the applied load. As will be explained in detail in the next section, this was caused by the increased effective stresses in the ground. However, a notice from Table 3.11 that although the peak pile resistance increased with applied load, the proportion of the applied load carried by the piles at the peak pile resistance decreased. This was because the increments in pile resistance in the second, third, and fourth load steps were small compared with the increment in the applied load, and most of the latter was supported by the raft (Fig. 3.25).

Table 3.11. Peak pore water pressure (PWP) in load-increasing period.

(a) 4P-6*D* and 4P-3*D*

Applied load (kN) [average applied pressure (kPa)]	4P-6*D* Peak PWP (kPa) [$P_{w,\,peak}$ (kN)] {% of increment of raft load; % of increment of applied load}		4P-3*D* Peak PWP (kPa) [$P_{w,\,peak}$ (kN)] {% of increment of raft load; % of increment of applied load}	
0.75 [48]	17 [0.266]	{63 %; 35 %}	27.4 [0.428]	{69 %; 46 %}
1.25 [80]	24 [0.378]	{73 %; 72 %}	13.1 [0.205]	{43 %; 38 %}
2.0 [128]	29 [0.454]	{68 %; 60 %}	32.8 [0.513]	{64 %; 60 %}
2.5 [160]	-	-	13.5 [0.211]	{43 %; 34 %}

(b) 9P-6*D* and 16P-3*D*

Applied load (kN) [average applied pressure (kPa)]	9P-6*D* Peak PWP (kPa) [$P_{w,\,peak}$ (kN)] {% of increment of raft load; % of increment of applied load}		16P-3*D* Peak PWP (kPa) [$P_{w,\,peak}$ (kN)] {% of increment of raft load; % of increment of applied load}	
0.75 [48]	6.4 [0.100]	{77 %; 13 %}	1.0 [0.016]	{16 %; 2.0 %}
1.25 [80]	2.3 [0.036]	{30 %; 07 %}	0.5 [0.008]	{11 %; 1.6 %}
2.0 [128]	27.0 [0.427]	{68 %; 57 %}	0.7 [0.011]	{11 %; 1.5 %}
2.5 [160]	7.6 [0.119]	{41 %; 24 %}	0.6 [0.010]	{09 %; 2.0 %}
3.0 [192]	22.0 [0.349]	{79 %; 70 %}	14.1 [0.038]	{17 %; 7.6 %}
3.5 [224]			3.3 [0.052]	{18 %; 10 %}
4.0 [256]			8.6 [0.135]	{40 %; 27 %}
4.5 [288]	-	-	4.8 [0.075]	{26 %; 15 %}

Table 3.12. Peak pile resistance in load-increasing period in each load step.

Applied load P (kN)	4P-6D (kN)	[% of P]	4P-3D (kN)	[% of P]	9P-3D (kN)	[% of P]	16P-3D (kN)	[% of P]
0.75	0.38	[51 %]	0.32	[43 %]	0.66	[88 %]	0.65	[87 %]
1.25	0.48	[38 %]	0.53	[42 %]	1.03	[82 %]	1.11	[89 %]
2.0	0.68	[34 %]	0.68	[34 %]	1.40	[70 %]	1.82	[91 %]
2.5	-	-	0.75	[30 %]	1.57	[63 %]	2.21	[88 %]
3.0	-	-	-	-	1.83	[61 %]	2.46	[82 %]
3.5	-	-	-	-	-	-	2.77	[79 %]
4.0	-	-	-	-	-	-	3.06	[77 %]
4.5	-	-	-	-	-	-	3.36	[75 %]

After the full applied load of each load step was achieved, the applied load was held constant for long enough to observe the time-dependent behavior of the foundations during both the primary and secondary consolidation periods.

c. Behavior during load-increasing period of 9P-3D and 16P-3D

Fig. 3.28 shows the changes of the applied load P and the settlement w of the foundation for the whole experimental duration. The load carried by the 9 piles P_p, the load carried by the raft P_r, and the uplift force P_w are also shown in the figure. The P_w here is also calculated by multiplying the PWP by the raft base center area (assuming that the PWP distributed uniformly over the raft base). Fig. 3.28(b)-(f) are zoom-ins of the load-increasing periods of the 5 load steps, respectively. Fig. 3.29(a)-(e) compare the increments of ΔP, ΔP_p, ΔP_r, ΔP_w (= P_w) and Δw from the start of the load-increasing period of the 5 load steps. The corresponding results for 16P-3D are shown in Figs. 3.30 and 3.31, respectively.

It is noted that the ultimate pile group capacity $P_{PG,\,ult.}$ of 9P-3D and 16P-3D were 1225 N and 2100 N, respectively. Therefore, for the case of 9P-3D, the applied load P = 750 N in the 1st loading step was less than the corresponding $P_{PG,\,ult.}$ and the applied load P = 1250 N in the 2nd loading step was just above the corresponding $P_{PG,\,ult.}$ In the last three load step P = 2000, 2500, and 3000 N, the applied loads exceeded the ultimate pile group capacity (same as the applied load for 4P-6D and 4P-3D). For the case of 16P-3D, the applied loads P = 750, 1250, and 2000 N of the first 3 load steps were smaller than the corresponding $P_{PG,\,ult.}$ and the applied load of the last 5 load steps were larger than the corresponding $P_{PG,\,ult}$.

Let us focus first on the results of the 9P-3D first, for the first load step, Fig. 3.28(b) (or Fig. 3.29(a)) shows that, when the load was increased, the resistance of the piles increased rapidly, and the increase of pile resistance was almost equal to the increase of the applied

load. Hence, the piles mainly supported the load and suppressed the settlement of the foundation in this load step. At the end of this period, 87 % of the load was carried by the piles.

The settlement of the foundation was minor when the applied load was smaller than 300 N. After the load exceeded 300 N, the settlement of the foundation increased more rapidly and reached 0.77 mm until the end of this load-increasing period.

The PWP at the raft base started to increase when the settlement started to increase, and the PWP increased sharply when the settlement increased rapidly. The uplift force P_w supported a large part of the raft load (77%).

The behaviors of the foundation in the 2nd load step (see Fig. 3.28(c) and Fig. 3.29(b)) were quite similar to those in the 1st load step. The piles still carried over 80 % of the applied load, the foundation settlement, the raft load, and the PWP at the raft base were minor.

The results of the 3rd load step are shown in Figs. 3.28(d) and 3.29(c). In general, when the applied load exceeded the $P_{PG,\ ult.}$, the behavior of 9P-3*D* became similar to the behavior of 4P-3*D* and 4P-6*D*. At the early stages of the load-increasing period, when the increment of the applied load was small (ΔP < 0.3 kN in Fig. 3.29(c)), the increase of the settlement was minor. Both the pile resistance and the raft resistance increased to support the increment of the load. The pile resistance increased until reaching a temporary peak $P_{p,\ peak}$ = 1.4 kN (Fig. 3.28(d)). After reaching the peak, the pile resistance reduced (softening behavior) and the foundation started to settle rapidly. The raft resistance P_r then increased to support the increment of the applied load as well as the part of load transferred from the pile resistance due to the softening behavior of the piles after the peak pile resistance. Until the end of the load-increasing period of the 3rd load step, the raft supported 84 % of the increment of the applied load ($\Delta P_r = 0.84\Delta P$, see Fig. 3.29(c)). The P_w at the raft base increased and supported up to 68 % of the raft load at the end of the load-increasing period (Fig. 3.29(c)).

The behaviors of the foundation in the 4th and the 5th load steps were similar to those of the 3rd load step (Fig. 3.28(e) and (f); Fig. 3.29(d) and (e)).

The increment of the raft load and the proportion of increment of applied load, which was supported by the raft load, were indicated in Table 3.9(b). Looking through Table 3.8(b), when the applied load on 9P-3*D* was smaller (1st load step) or almost equal (2nd load step) to the $P_{PG,\ ult.}$ of 9P-3*D*, the pile was effectively at supporting the applied load (over 80 %). When the applied load exceeded the $P_{PG,\ ult.}$, the raft carried a major part of the increment of applied load (ranging from 60 % to 88 %, see Table 3.8(b)).

The peak PWP/ P_w and their corresponding proportions of increment of the raft load and increment of the applied load were presented in Table 3.10(b). In general, PWP supported a noticeable part of the increment of the raft load, at least 30 % and at most 79%.

The peak pile resistance in the load-increasing period in each load step and its corresponding proportion of the applied load was shown in Table 3.11. It is clear from Table 3.11 that the peak pile resistance increased with increasing load. It is thought that when the applied load was smaller than the $P_{PG,\ ult.}$, the increment of peak pile resistance was mainly due to continuing mobilizing the pile resistance because the pile still did not fully mobilize (or did not reach their ultimate capacity) in previous load step. Of course, the increment of peak pile resistance was also partly caused by the ground consolidation process of the previous load step. When the applied load was larger than the $P_{PG,\ ult.}$, the increment of peak pile resistance was mainly due to the ground consolidation process of the previous load step because the pile already reached it ultimate condition (softening behavior, see Fig. 3.28 or 3.29) in the load-increasing period of the previous load step. At the ultimate condition of PR (final load step), the piles in 9P-3*D* carried over 60% of the total applied load, which was a double of the corresponding value of the piles in 4P-3*D*/ 4P-6*D*.

Turning next to the results of 16P-3*D*, Figs. 3.30 and 3.31 show clearly that 16P-3*D* behaved very similarly to 9P-3*D* (Figs. 3.28 and 3.29) but with different magnitudes, due to different pile number. For the first 3 load step, Figs. 3.30, 3.31(a)-(c), and Table 3.11 show that the piles carried around 90 % of the applied load in these load steps and the foundation settlement was small. This indicates that when the applied load was smaller than the corresponding pile group ultimate capacity, the applied load was mainly supported by the piles. As such, the piles were also effective at suppressing foundation settlement in these steps. This trend was similar to the case of 9P-3*D*.

For the 4th load step (Fig. 3.31(d)), although the applied load exceeded $P_{PG,\ ult.}$ (P = 2.5 kN > $P_{PG,\ ult.}$ = 2.1 kN), the foundation still behaved similarly to the first three load steps, as described above. The possible reason for this behavior is that the pile resistances increased during the consolidation processes of the first three load steps. Therefore the pile resistances after the increment were able to carry the applied load.

For the last 4 load steps (P = 3.0, 3.5, 4.0, and 4.5 kN), Fig. 3.31(e)-(h) show that the 16P-3*D* foundation exhibited similar trends to 9P-3*D* (also similar to 4P-6*D* and 4P-3*D*) when $P > P_{PG,\ ult.}$ (i.e., the pile resistance increased to a temporary peak and then decreased, and the PWP increased with time and reached a peak in a short duration after the applied load reached its target value, both the piles and raft increased to support the applied load from the start of the load-increasing period, the raft supported the increment of applied load after the piles reached the peak and exhibited softening behavior and also supported the part of the load transferred from the pile loads due to the softening behavior). The magnitudes of increments of the raft load ΔP_r and PWP (P_w) and the peak pile resistance $P_{p,\ peak}$ in each load step were shown in Tables 3.8(b), 3.9(b), and 3.10, respectively. Also shown in these

tables are the corresponding proportions of the increment of the applied load ΔP or total applied load P supported by ΔP_r, P_w, and $P_{p,\,peak}$.

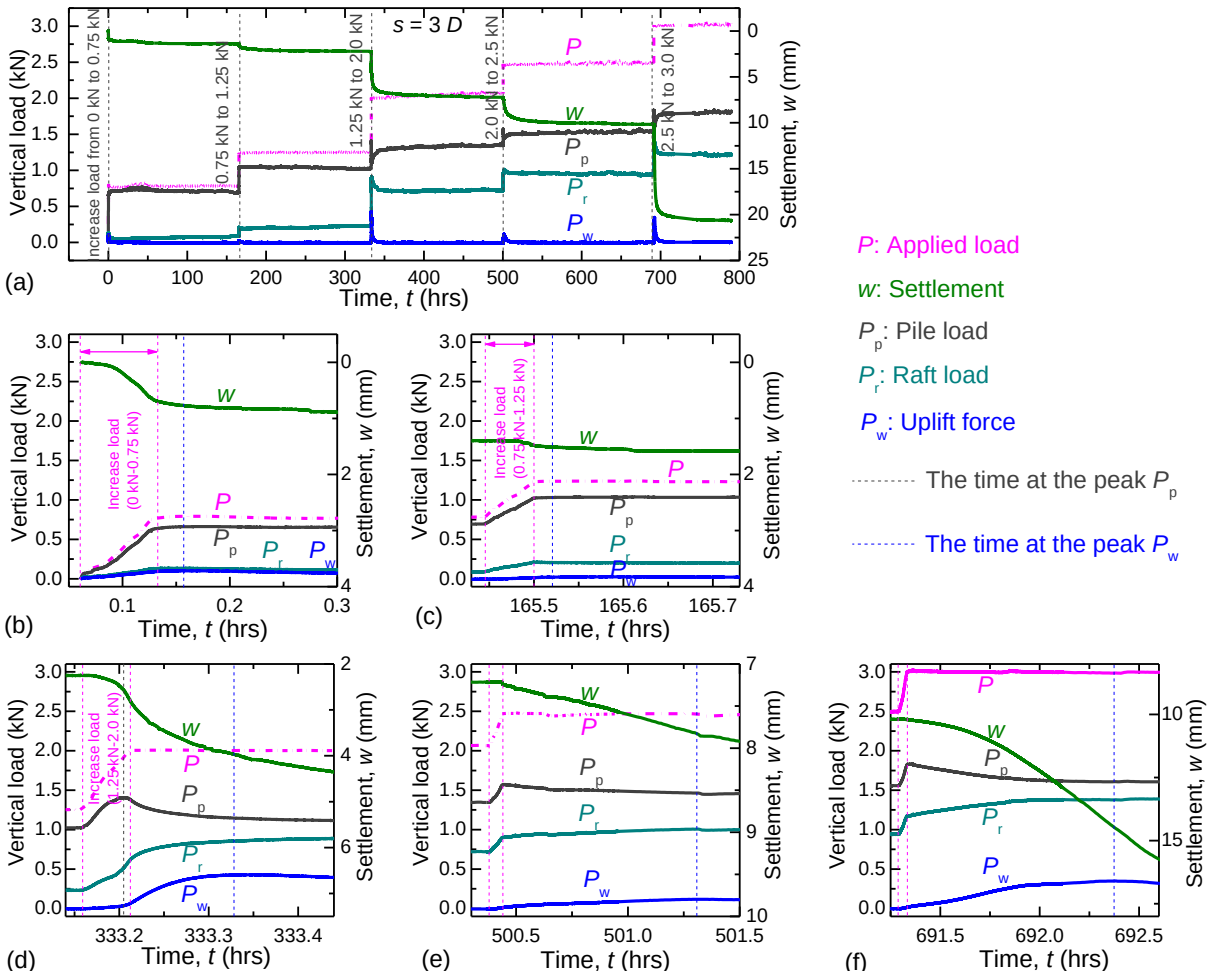

Fig. 3.28. Changes of loads and settlement with time of 9P-3*D*: (a) All load steps; (b) zoom-in of load-increasing period of 1st load step; (c) zoom-in of load-increasing period of 2nd load step; (d) zoom-in of load-increasing period of 3rd load step; (e) zoom-in of load-increasing period of 4th load step; (f) zoom-in of load-increasing period of 5th load step.

Compare 16P-3*D* to the 9P-3*D* and 4P-3*D*, the most significant difference is the load carried by the piles at the peak pile resistance (Table 3.11). Until the ultimate condition of the foundation (the final load step applied on each foundation), the piles of 16P-3*D* still carried up to 75% of the total applied load, meanwhile, that of 9P-3*D* and 4P-3*D* were 60 % and 30% respectively. It is interesting that if we consider the average load per pile at peak resistance, the load carried by each pile in PR condition in cases of 16P-3*D*, 9P-3*D*, and 4P-3*D* were 0.21, 0.203, and 0.188 kN, respectively. It should be noted again that the load carried by each pile in PG ultimate condition in cases of 16P-3*D*, 9P-3*D*, and 4P-3*D* were 0.131, 0.138, and 0.146 kN (Table 3.8), respectively. The piles in 16P-3*D* had the lowest

average pile resistance in PG ultimate condition but the highest average pile resistance in PR ultimate condition, and the opposite was seen for the case of 4P-3*D*. This phenomenon may due to the piles of 16P-3*D* experienced more load steps, larger applied load, and longer loading time in PR condition. Therefore the peak pile resistance in the case 16P-3*D* became larger than that of 4P-3*D*.

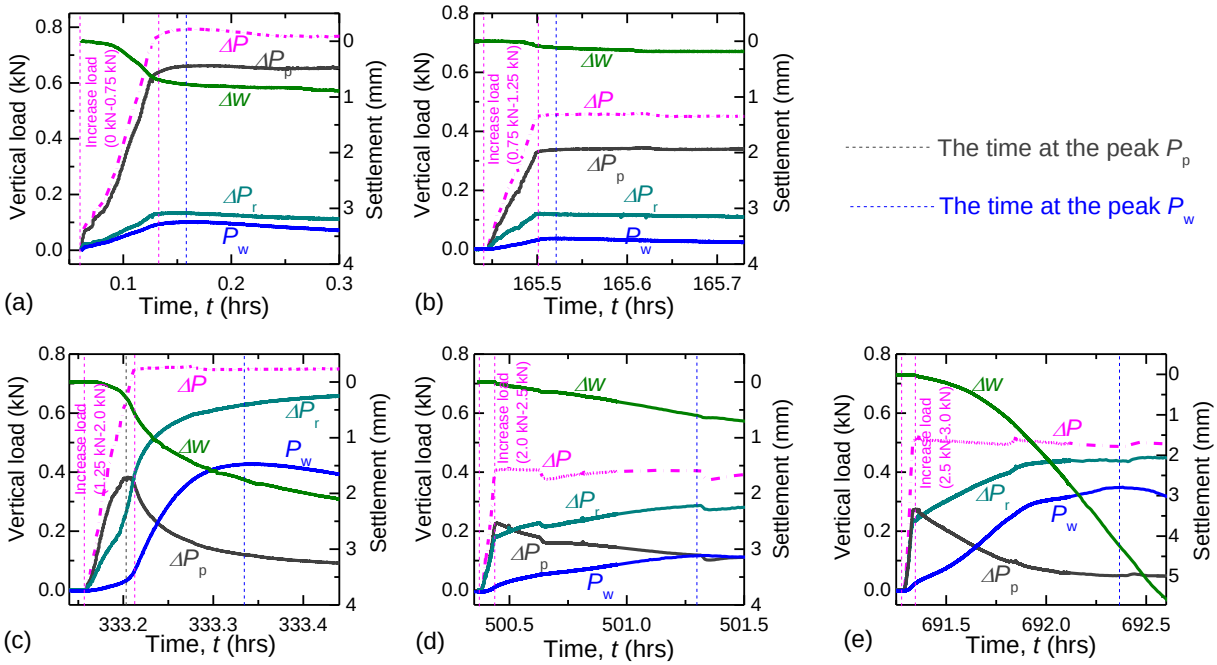

Fig. 3.29. Increments of loads and settlement with time in load-increasing period of 9P-3*D*: (a) 1st load step; (b) 2nd load step; (c) 3rd load step; (d) 4th load step; (e) 5th load step.

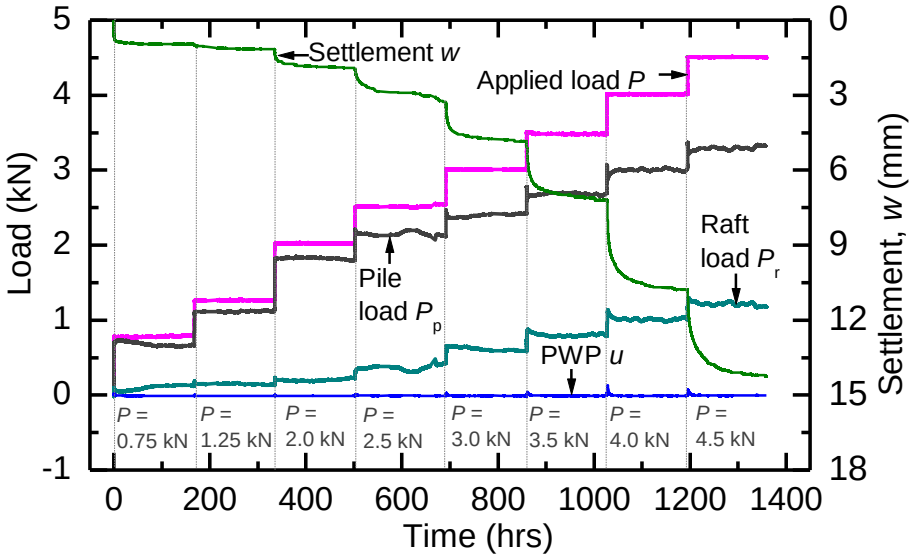

Fig. 3.30. Changes of loads and settlement with time of 16P-3*D*.

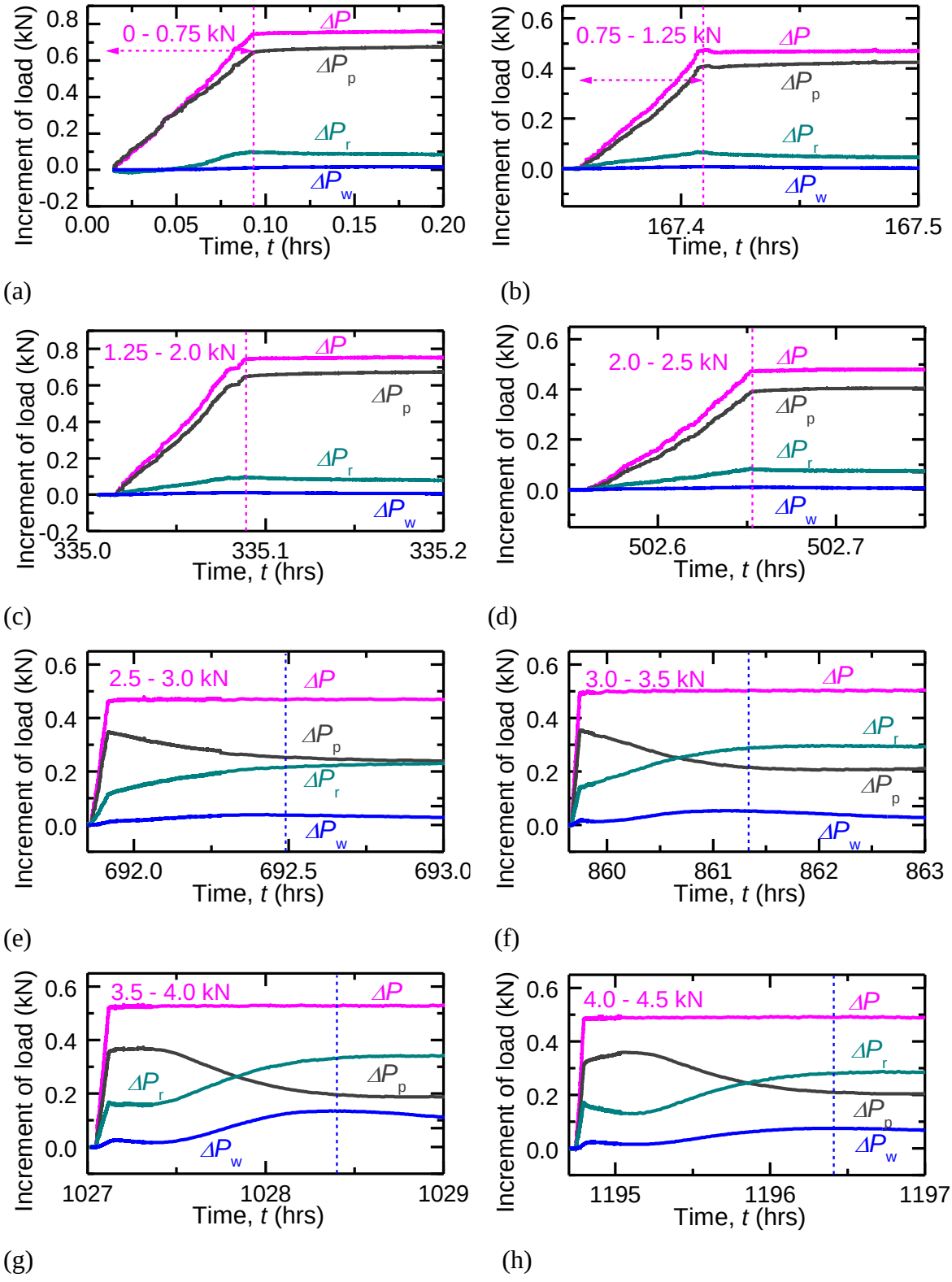

Fig. 3.31. Increments of loads and settlement with time in load-increasing period of 16P-3*D*: (a) 1st load step; (b) 2nd load step; (c) 3rd load step; (d) 4th load step; (e) 5th load step; (f) 6th load step; (g) 7th load step; (h) 8th load step.

3.3.4.2 Behavior during primary consolidation period

After the load-increasing period, the PWP began to dissipate and then returned to the steady state (PWP ≈ 0), and this period could be regarded as the primary consolidation period.

a. Settlement behavior during primary consolidation period of unpiled raft

Fig. 3.32(a) shows how the PWP and settlement of UR changed over the entire experimental duration, in which the highlighted areas can be regarded as the primary consolidation period. Figs. 3.32(b)–3.32(d) are magnified views of the primary consolidation period in each load step of UR.

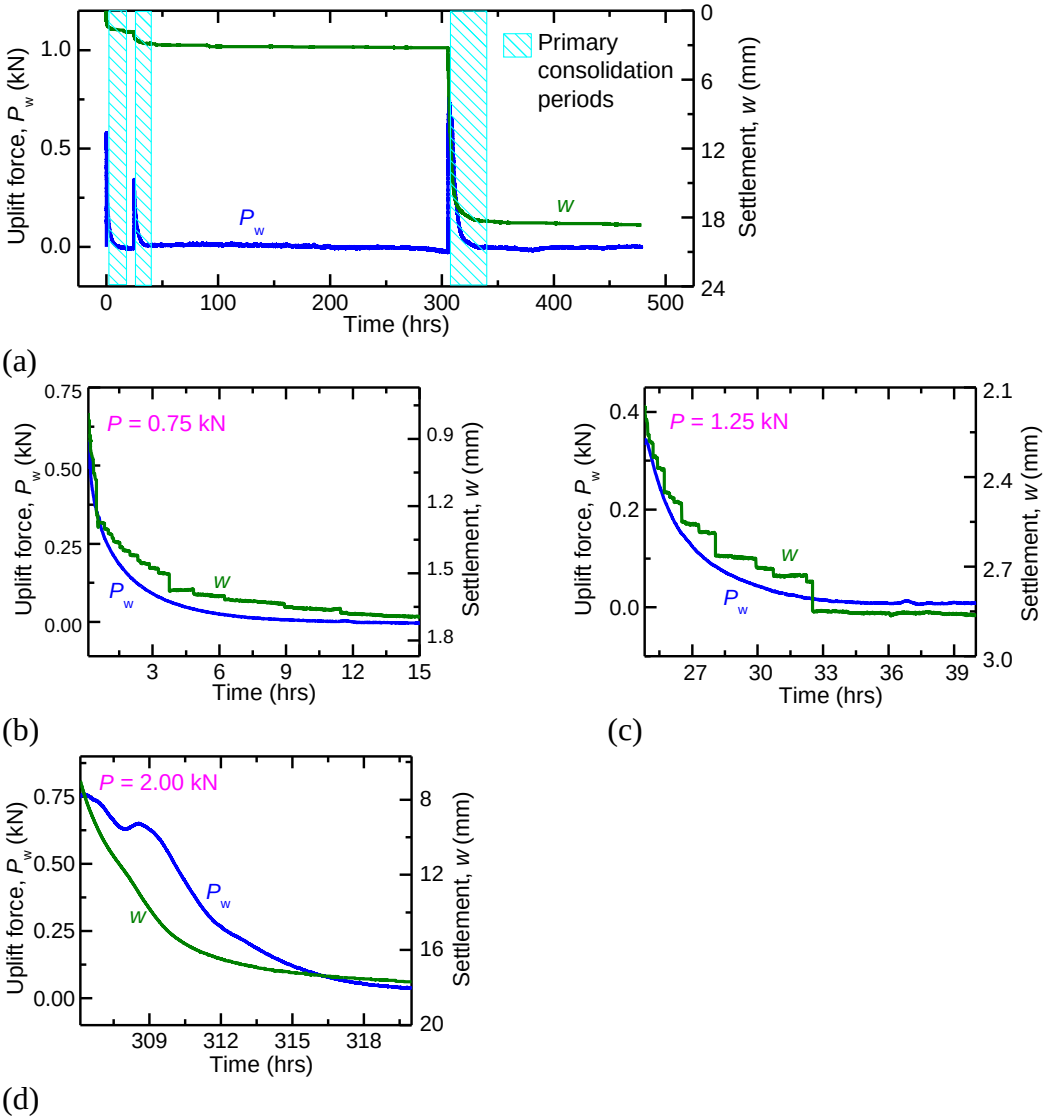

Fig. 3.32. Changes of pore water pressure (PWP) and settlement with time of unpiled raft: (a) all load steps; zoom-in of primary consolidation period of (b) first load step; (c) second load step; (d) third load step.

During the primary consolidation periods of the first and second load steps, Figs. 3.32(b) and 3.32(c) show clearly that the settlement rate was basically proportional to the PWP dissipation rate and that notable amounts of settlement occurred in these primary consolidation periods. For the third load step of P = 2.0 kN, Fig. 3.32(d) shows that the foundation settlement increased sharply in the early stage of the primary consolidation period (i.e., w < 16 mm) and that the settlement rate was not proportional to the PWP dissipation rate at this stage. This behavior may be relevant to some ground failures that occurred when a relatively large load was applied. The long-term load test on the unpiled raft was stopped after the third load step because the failure and large settlement occurred when the third load step was applied.

b. Settlement behavior during primary consolidation period of 4P-6D and 4P-3D

Fig. 3.33(a) shows how the PWP and settlement of 4P-6*D* changed over the entire experimental duration, in which the highlighted areas can be regarded as the primary consolidation period. Figs. 3.33(b)–3.33(d) are magnified views of the primary consolidation period of 4P-6*D*, and Fig. 3.34 shows the corresponding results for 4P-3*D*.

We begin by considering the results for 4P-6*D* in Fig.3.33. During the primary consolidation periods of the first and second load steps, Figs. 3.33(b) and 3.33(c) show clearly that the settlement rate was basically proportional to the PWP dissipation rate and that notable amounts of settlement occurred in these primary consolidation periods. For the third load step of P = 2.0 kN, Fig. 3.33(d) shows that the PWP decreased sharply in the early stage of the primary consolidation period (i.e., w < 9 mm) and that the settlement rate was not proportional to the PWP dissipation rate at this stage. may be relevant to some ground failures that occurred when a relatively large load was applied. The behavior of 4P-6*D* in primary consolidation periods was very similar to the behavior of unpiled raft. In the later stage of the primary consolidation period (i.e., w > 9 mm), the PWP dissipation rate decreased and became proportional to the PRF settlement rate.

As for the 4P-3*D* results, Figs. 3.34(b)– 3.34(e) show that during the primary consolidation periods of all four load steps, the PRF settlement rate was basically proportional to the PWP dissipation rate at the raft base.

It should be noted that after the primary consolidation period of the third load step, the 4P-6*D* settlement became significantly larger than the 4P-3*D* one, whereas in the first and second load steps the 4P-6*D* settlements were smaller than the corresponding 4P-3*D* ones. Compare to the behavior of unpiled raft UR, although the final loads of UR and 4P-6*D* (could be regarded as the ultimate capacity of the foundations) were the same (2.0 kN), the

settlement of UR at the end of the primary consolidation period of the last load step was about 1.5 times that of 4P-6*D*. The settlement of 4P-3D at the end of the primary consolidation period of the applied load of 2.0 kN was only a half of that of UR. These results indicate that the piles reduced foundation settlement effectively, even though only 4 piles were used. In another point of view, when a small number of piles were used, the pile was effective at reducing total foundation settlement rather than increasing the foundation ultimate capacity.

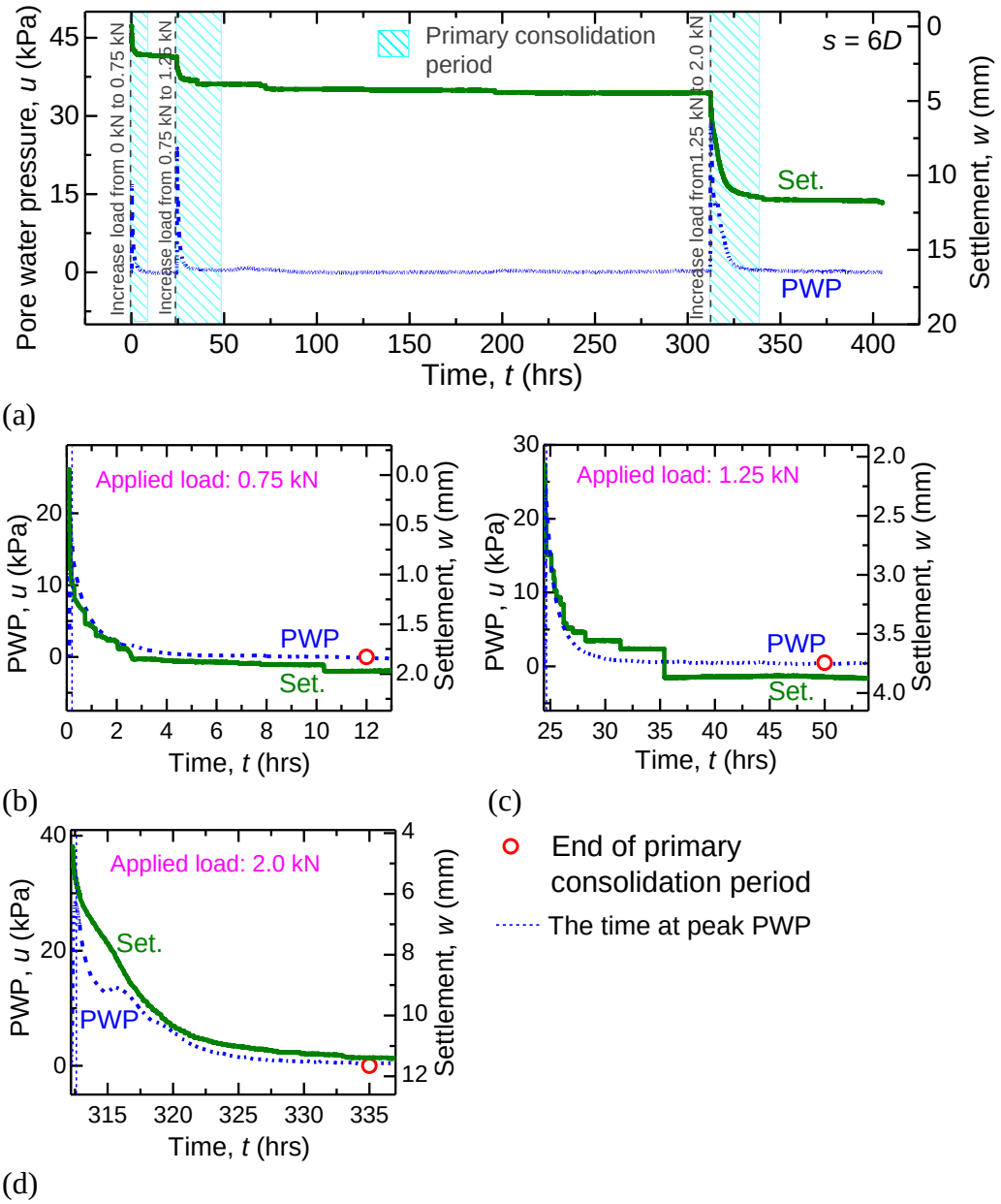

Fig. 3.33. Changes of pore water pressure (PWP) and settlement with time of 4P-6*D*: (a) all load steps; zoom-in of primary consolidation period of (b) first load step; (c) second load step; (d) third load step.

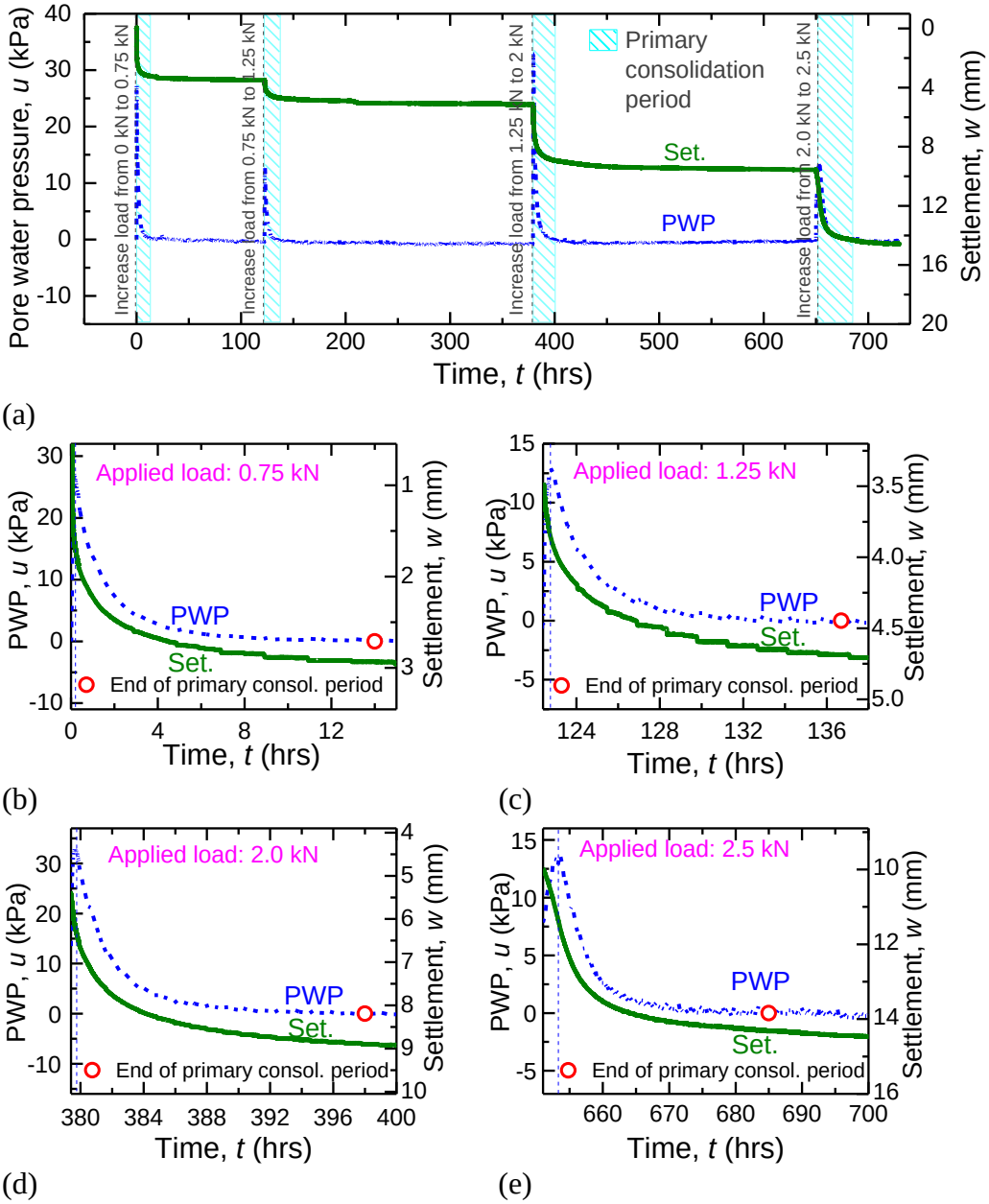

Fig. 3.34. Changes of pore water pressure (PWP) and settlement with time of 4P-3*D*: (a) all load steps; zoom-in of primary consolidation period of (b) first load step; (c) second load step; (d) third load step; (e) fourth load step.

c. Settlement behavior during primary consolidation period of 9P-3D and 16P-3D

Fig. 3.35(a) shows the changes of PWP and settlement of 9P-3*D* over the entire experimental duration. Figs. 3.35(b)–(f) are magnified views of the primary consolidation period of 5 load steps applied on 9P-3*D*. Fig. 3.36 shows the corresponding results for 16P-3*D*.

For the results of 9P-3*D* (Fig. 3.35), the foundation behaved similarly to 4P-3*D* or 4P-6*D*, of which the PRF settlement rate was proportional to the PWP dissipation rate.

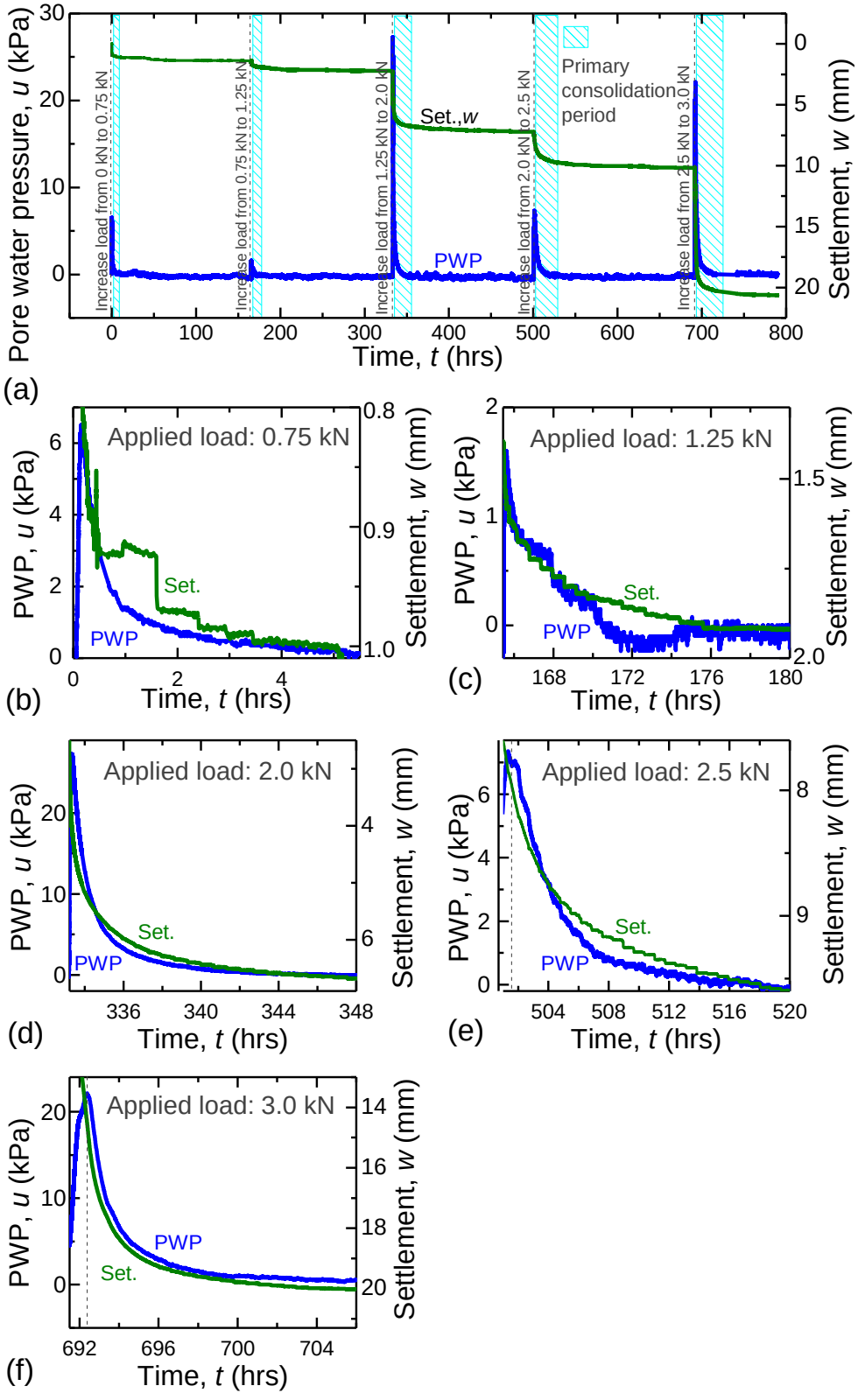

Fig. 3.35. Changes of pore water pressure and settlement with time of 9P-3*D*: (a) all load steps; zoom-in of primary consolidation period of (b) 1st load step; (c) 2nd load step; (d) 3rd load step; (e) 4th load step; (f) 5th load step.

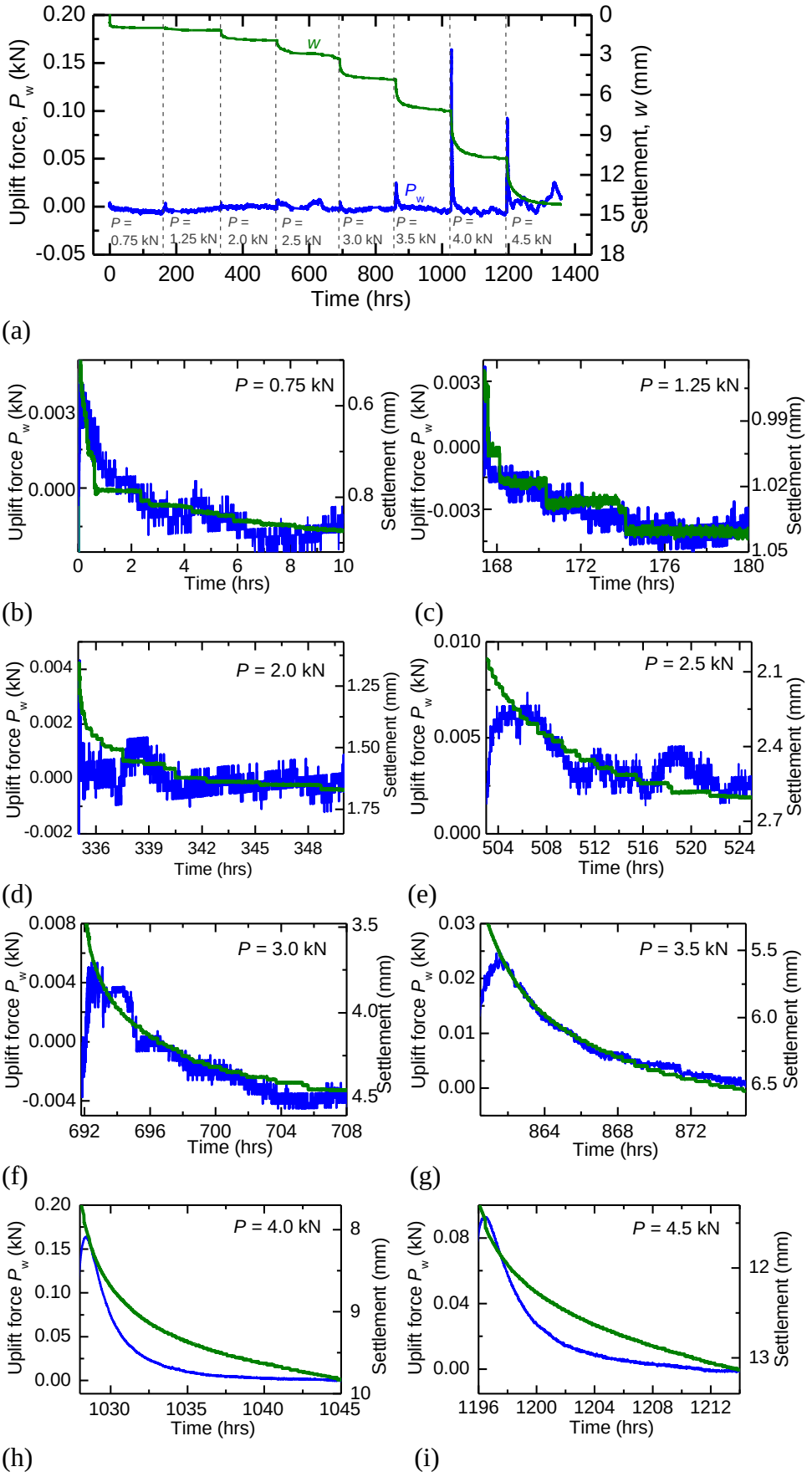

Fig. 3.36. Changes of pore water pressure and settlement with time of 16P-3*D*: (a) all load steps; zoom-in of primary consolidation period of (b) 1st load step; (c) 2nd load step; (d) 3rd load step; (e) 4th load step; (f) 5th load step

(g) 6th load step; (h) 7th load step; (i) 8th load step.

For the results of 16P-3*D*, it should be noted from Fig. 3.36 that, in the excess pore pressure at the raft base center was very small, in comparison with those of the foundations with 0, 4, or 9 piles. The PWP was not really stable at zero after dissipation, one of possibility is that the PWP cell did not work well in this experiment. Interestingly, the foundation settlement during primary consolidation periods of 16P-3*D* was also small, in comparison with the corresponding settlement of the foundations with 0, 4, or 9 piles under the same applied load magnitude. At larger applied load P = 4.0 and 4.5 kN (Fig. 3.36(h) and (i)), the results show that the dissipation rate of PWP was higher than the PRF settlement rate. This phenomenon will be discussed more with the pile response in the primary consolidation period in the next section.

d. Pile resistance behavior during primary consolidation period

We first consider the results of 4P-6*D* and 4P-3*D*.

How the pile and raft loads of each PRF changed with time is shown in Fig. 3.37(a) for 4P-6*D* and Fig. 3.38(a) for 4P-3*D*. Figs. 3.37(b) and 3.38(b) show expanded views of a short duration at the start of the primary consolidation period of the first load step (P = 0.75 kN) for 4P-6*D* and 4P-3*D*, respectively, and Figs. 3.37(c) and 3.38(c) show expanded views of the entire primary consolidation period of the first load step of 4P-6*D* and 4P-3*D*, respectively.

Figs. 3.37(b) and 3.38(b) show that in a short duration at the start of the primary consolidation period of each foundation, the PWP started to dissipate relatively slowly compared to the PWP dissipation rate around t = 0.23 hours for 4P-6*D* (Fig. 3.37(b)) or t = 0.18 hours for 4P-3*D* (Fig. 3.38(b)). After the start of the primary consolidation period, the pile load continued to decrease, reached its lowest value at the aforementioned time, and then increased. The reduced pile load may be due to the softening response of the piles, the latter being thought to cause the lower PWP dissipation rate because the PWP carried part of the load which was transferred from the reduced pile load. After the pile load reached its lowest value, the PWP dissipation rate increased but thereafter decreased with time. A similar phenomenon occurred in the other load steps of both 4P-6*D* and 4P-3*D*.

Figs. 3.37(c) and 3.38(c) show clearly that after the pile resistance reached its lowest value, the load supported by the four piles increased with elapsed time while that supported by the raft decreased. For example, for 4P-3*D* (Fig. 3.38(c)) the pile load increased to a peak of 0.32 kN in the load-increasing period of the first load step, as mentioned above regarding Fig. 3.26(b), and then decreased to its lowest value of 0.25 kN in an early stage of the primary consolidation period (Fig. 3.38(b)). The pile resistance increased again from

0.25 kN to 0.38 kN with elapsed time at the end of the primary consolidation period. Similarly, this phenomenon occurred in the other load steps of both 4P-3*D* and 4P-6*D*. The increased pile resistance was due to the primary ground consolidation, and the PWP dissipation caused the corresponding increased effective ground stresses, resulting in the increased pile resistances. Table 3.12(a) lists the pile loads at the start and end of the primary consolidation period in each load step of both foundations. Let us compare Table 3.10(a), which presents the peak PWPs in the load-increasing periods, and Table 3.12(a), which presents the increments of pile resistance during primary consolidation. Doing so shows that the magnitude of the pile-load increment during primary consolidation was roughly proportional to the magnitude of P_w at the end of the load-increasing period. Hooper (1973) investigated how the consolidation of clay ground affected the load distribution between raft and piles. He measured the load transfer of a PRF supporting a 90-m-high building on London clay during a 3-year post-construction period and reported that the pile load increased by 3% of the total applied load. Furthermore, he computed the pile load using FEM and indicated that the proportion of the total applied structural load carried by the piles increased by approximately 6% because of consolidation.

Next, we consider in detail how the PRF loading increases the ground strength. Fig. 3.12(d) shows the results of TBTs and UCTs on the model ground for PF-3*D* in the form of the values of the undrained shear strength c_u either with or without the effect of the load test. Note that the foundation had settled by around 15 mm upon completion of the load test. Therefore, the profiles of c_u in the loading area begin at the depth of 15 mm (the level of the raft base after loading; see Fig. 3.12(d)), and the depth in the following discussion is that from the raft base upon completion of the load test. The TBT results show clearly that compared with the original state (T1 and T2), c_u was higher near the raft edges (T4 and T5) and highest at the center of the raft base (T3) after the load test and within a depth of around 190 mm from the raft base ($\simeq$ 1.5 times the raft width B). Furthermore, c_u beneath the center of the raft base (T3) was much greater than that of the original model ground (T1 and T2) within a depth of 75 mm. For greater depths, the difference in c_u between the loading area and the original area decreased with depth. At depths greater than 190 mm, c_u of the loading area became equal to that of the original area. The zone between the raft base and the depth of 190 mm could be regarded as the zone that is affected by the load test. The UCT results exhibit similar trends to those of the TBT results. Overall, the increased ground strength is due to the consolidation during the PRF loading. This is an advantage of a PRF, the stress at whose raft base causes ground consolidation.

We turn to the results of 9P-3*D* and 16P-3*D*.

It is noticed again that in the cases of 9P-3*D* and 16P-3*D*, the piles did not exhibit softening behavior in the load-increasing period when the small load ($P \leq P_{PG,\ ultimate}$) was applied. Therefore, the results of 9P-3*D* and 16P-3*D* herein will be shown for a small-load step and a large-load step.

The changes of the pile and raft loads of each PRF with time is shown in Fig. 3.39(a) for 9P-3*D* and Fig. 3.40(a) for 16P-3*D*. Figs. 3.39(b) and 3.40(b) show the expanded views of the primary consolidation period of the first load step of 9P-3*D* and 16P-3*D*, respectively. Figs. 3.39(c) and 3.40(c) show expanded views of a short duration at the start of the primary consolidation period of the third load step (P = 2.0 kN) for 9P-6*D* and the fifth load step (P = 4.0 kN) for 16P-3*D*, respectively, and Figs. 3.39(d) and 3.40(d) show expanded views of the entire primary consolidation period of the third load step (P = 2.0 kN) for 9P-6*D* and the fifth load step (P = 4.0 kN) for 16P-3*D*, respectively.

When the applied load was small, and the pile resistance did not exhibit softening behavior in the load-increasing period, it is seen from Figs. 3.39(b) and 3.40(b) that the pile resistance continued to increase slightly in primary consolidation periods.

When the large load was applied, and the pile resistance exhibited softening behavior in the load-increasing period, the piles behaved similarly to the piles in the cases of 4P-6*D* or 4P-3*D*. Figs. 3.39(c) and 3.40(c) show that after the start of the primary consolidation period, the pile load continued to decrease, reached its lowest value, and then increased. Figs. 3.39(d) and 3.40(d) show that after the pile resistance reached its lowest value, the load supported by the piles increased with elapsed time while that supported by the raft decreased. The increment of pile load was shown in Table 3.12(b). The increment of pile load at under the applied load P = 2.5 kN was not presented in the table because the applied load was unstable at the middle part of the primary consolidation period of this load step due to the unstable of electricity supply at that time. It is noticed from Table 3.12(b) that also the increment of PWP at the raft base was small, the increment of pile load was still noticeable. This is thought that in the case of PRF with a large number of piles, the ground consolidation also occurred significantly at the deeper depths from the raft base, which cause an increase of pile resistance. And, this is also the reason that the PRF settlement rate at the last two load steps of 16P-3*D* was lower than the dissipation rate of PWP in Fig. 3.36. Similar to the cases of 4P-6*D* or 4P-3*D*, this can be explained by the distributions of c_u after the load test, as shown in Fig. 3.12(e) and (f).

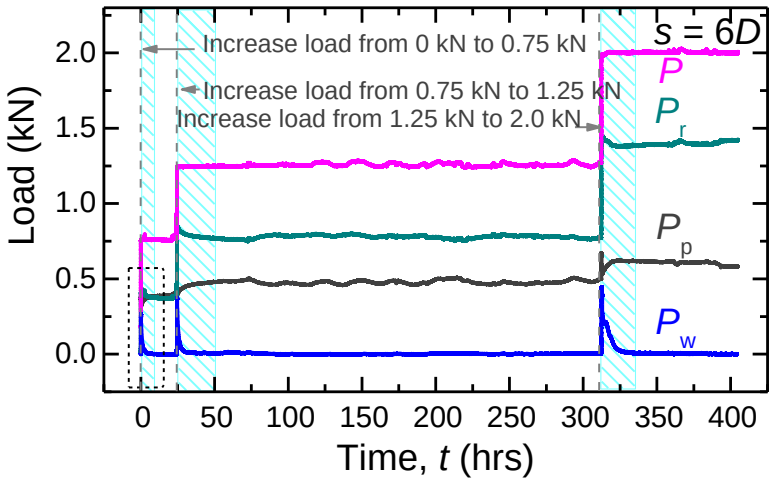

(a)

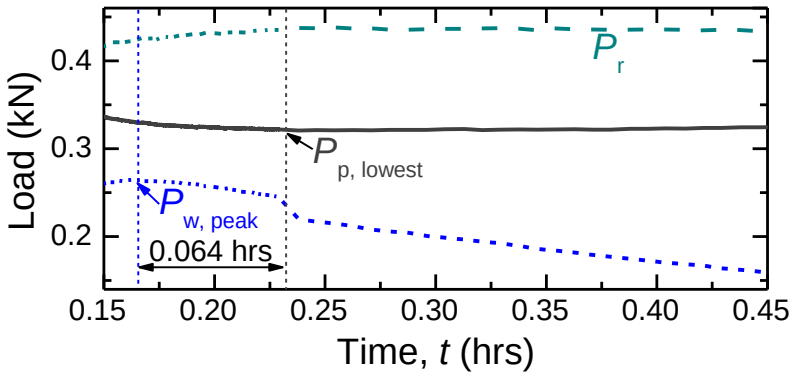

(b)

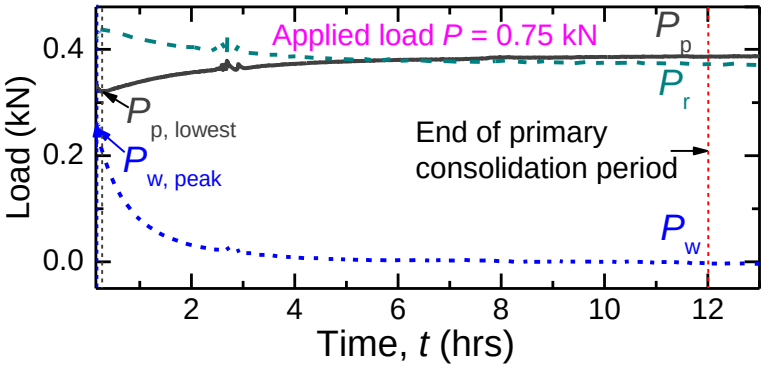

(c)

Fig. 3.37. Load transfer with time of 4P-6*D*: (a) all load steps; (b) zoom-in the early stages of primary consolidation period of the first load step; (c) zoom-in whole primary consolidation period of the first load step.

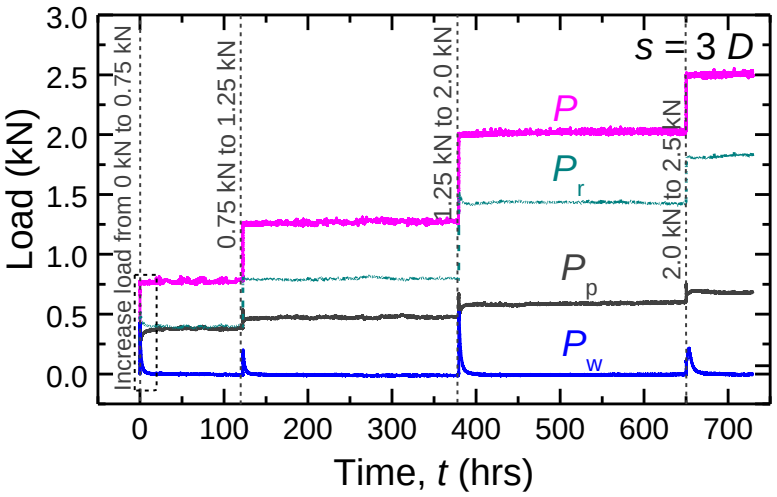

(a)

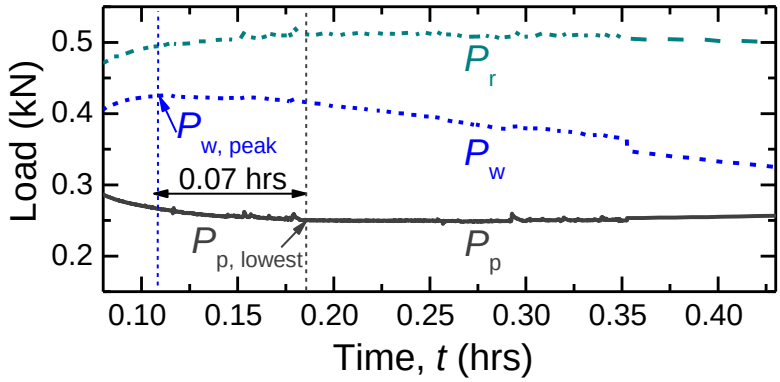

(b)

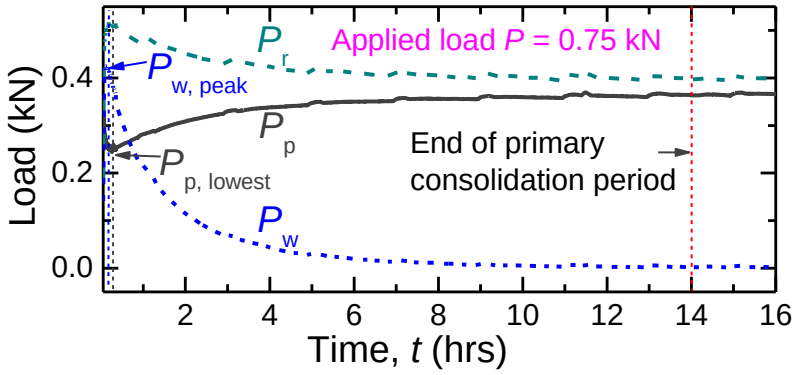

(c)

Fig. 3.38. Load transfer with time of 4P-3*D*: (a) all load steps; (b) zoom-in the early stages of primary consolidation period of the first load step; (c) zoom-in whole primary consolidation period of the first load step.

Table 3.13. Change of pile load during primary consolidation period.

(a) 4P-6*D* and 4P-3*D*

Applied load (kN)	Pile load of PF-6*D* (kN)		Pile load of PF-3*D* (kN)	
	At the start[a]	At the end[b]	At the start[a]	At the end[b]
0.75	0.32	0.39	0.25	0.38
1.25	0.39	0.49	0.44	0.49
2.0	0.53	0.62	0.49	0.58
2.5	-	-	0.66	0.70

Note: [a]Value at lowest point occurred after the peak PWP in each load step

[b]Value when the excess PWP has dissipated totally and backed to zero

(b) 9P-3*D* and 16P-3*D*

Applied load (kN)	Pile load of 9P-3*D* (kN)		Pile load of 16P-3*D* (kN)	
	At the start[a]	At the end[b]	At the start[a]	At the end[b]
0.75	0.64	0.71	0.66	0.72
1.25	1.03	1.05	1.07	1.11
2.0	1.10	1.30	1.78	1.83
2.5	1.45	1.51	-	-
3.0	1.62	1.78	2.35	2.38
3.5	-	-	2.63	2.68
4.0	-	-	2.88	2.98
4.5	-	-	3.21	3.31

Note: [a]Value at lowest point occurred after the peak PWP in each load step

[b]Value when the excess PWP has dissipated totally and backed to zero

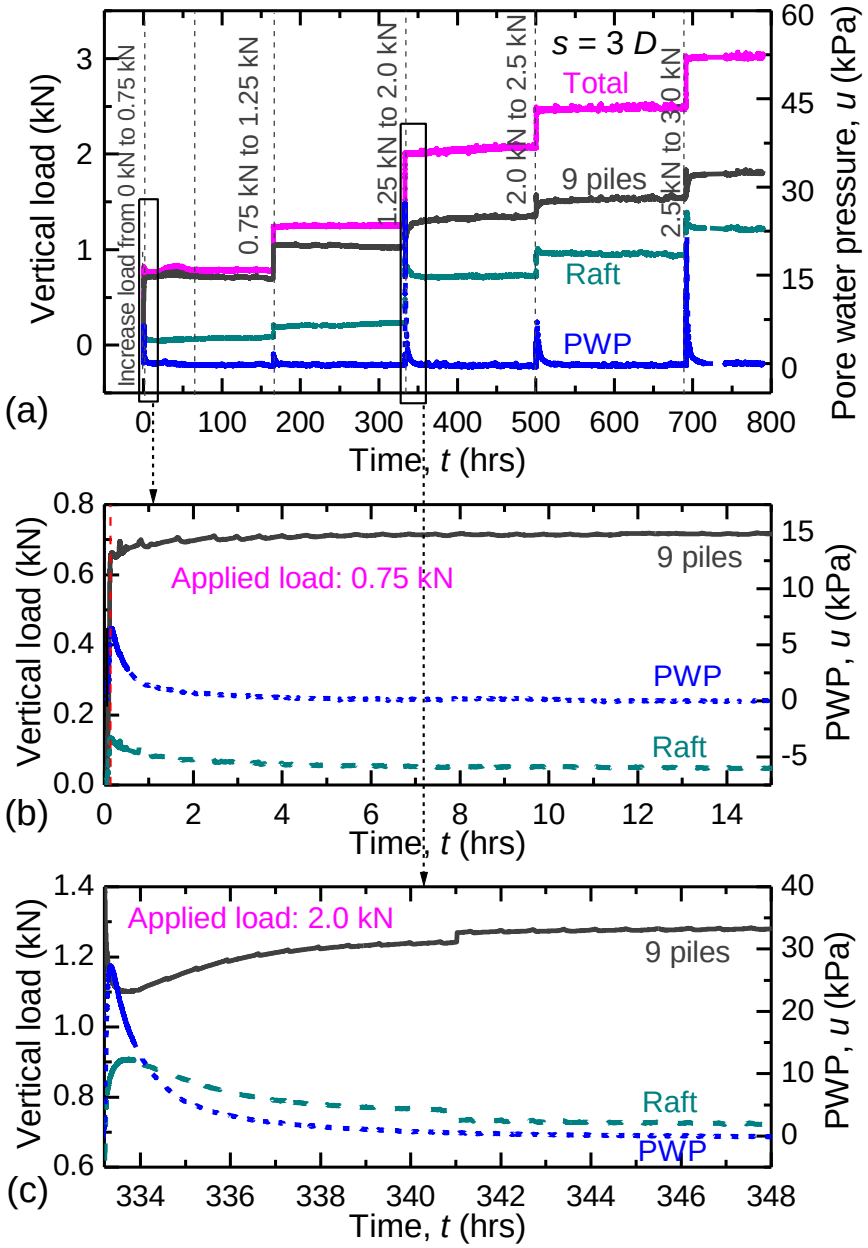

Fig. 3.39. Load transfer with time of 9P-3*D*: (a) all load steps; (b) zoom-in primary consolidation period of the 1st load step; (c) zoom-in the early stages of primary consolidation period of the 3rd load step; (d) zoom-in whole primary consolidation period of the 3rd load step.

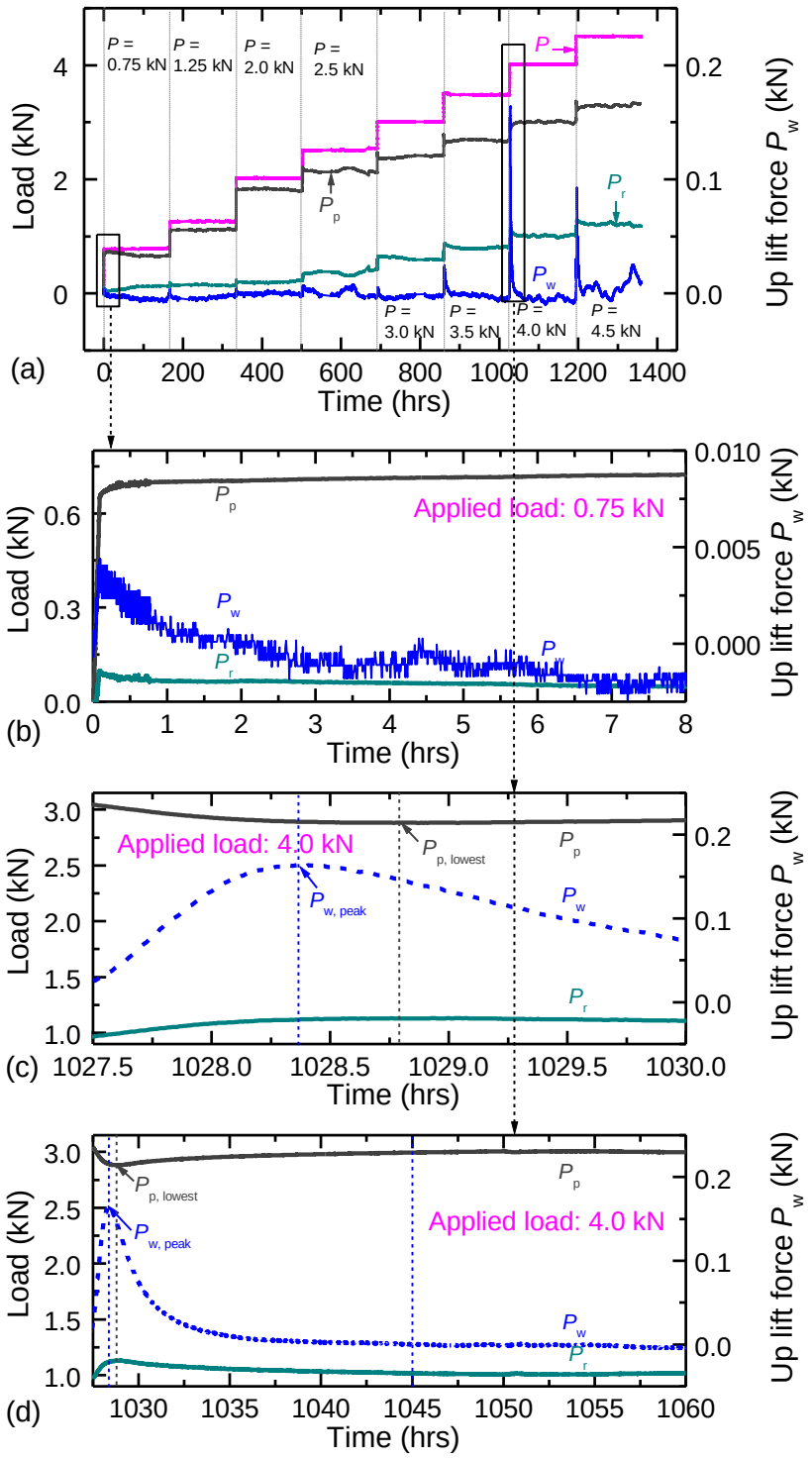

Fig. 3.40. Load transfer with time of 16P-3*D*: (a) all load steps; (b) zoom-in primary consolidation period of the 1st load step; (c) zoom-in the early stages of primary consolidation period of the 7th load step; (d) zoom-in whole primary consolidation period of the 7th load step.

3.3.4.3 Behavior during secondary consolidation period

The secondary consolidation began after completion of the primary consolidation. During secondary consolidation, the foundations continued to settle because of the creep behavior of the ground (see Figs. 3.37(a) for 4P-6*D*, 3.38(a) for 4P-3*D*, 3.39(a) for 9P-3*D*, and 3.40(a) for 16P-3*D*). Here, the creep settlement index C_{cs} is defined as

$$C_{cs} = \mathrm{d}(w/B_r) / \mathrm{d}(\log t) \tag{3-6}$$

For each foundation, Table 3.13 gives C_{cs} as estimated using Eq. (3-6). In Table 3.13, C_{cs} was not estimated for the fourth load step of 16P-3*D* because the technical problem happened with the electricity supply during the consolidation period of this load step, which causes the unstable of the applied load.

Table 3.14. Creep index of the two foundations in each load step.

Applied load P	Creep settlement index, C_{cs} ($\times 10^{-2}$)				
(kN)	UR	4P-6*D*	4P-3*D*	9P-3*D*	16P-3*D*
0.75	0.069	0.1	0.057	0.05	0.032
1.25	0.343	0.15	0.14	0.21	0.108
2.0	0.954	0.18	0.17	1.18	0.449
2.5		-	1.65	0.83	-
3.0		-	-	1.62	1.084
3.5		-	-	-	4.087
4.0		-	-	-	3.247
4.5		-	-	-	5.603

It is interesting to compare the results of 4P-6*D* to those of 4P-3*D*, Table 3.13 shows that the C_{cs} values measured in the second and third load steps of the two foundations were almost equal. For the first load step, the 4P-6*D* C_{cs} was larger than the 4P-3*D* one. For 4P-6*D*, the first load step of 0.75 kN was maintained for only 24 hours, and the PWP at the raft base had dissipated fully by t = 12 hours (see Fig. 17(c)). Therefore, C_{cs} was estimated for an early stage of secondary consolidation of the final 10 hours of this load step. In the other load steps, the measured durations for secondary consolidation exceeded 80 hours, and C_{cs} was estimated from the final 10 hours of each load step. Therefore, the higher C_{cs} in the first load step of 4P-6*D* seems to reflect the secondary compression in an early stage.

It is difficult to compare the effect of pile number on the settlement behavior of the foundations in secondary consolidation periods (comparing UR, 4P-3*D*, 9P-3*D*, and 16P-3*D* together).

In general, C_{cs} was higher when the applied load was larger.

3.3.4.4 Long-term load sharing between raft and piles.

a. Load sharing between raft and piles with time

Fig. 3.41(a) shows the proportions of the applied load shared by the raft and the four piles with elapsed time for 4P-6*D*. In the first load step, the four piles carried up to 51% of the applied load at the end of this period. In the second and third load steps, the load proportions carried by the piles were around 37% and 30%, respectively. Although only four piles were used, they still carried a notable part of the applied load.

Fig. 3.41(b) shows the load proportions shared by the raft and the piles with elapsed time for 4P-3*D*. The load-sharing trend for 4P-3*D* is clearly similar to that for 4P-6*D*. A slight difference between the two foundations is that the load proportion carried by the piles in the case of PF-6*D* was marginally larger than that in the case of PF-3*D*.

Fig. 3.41(c) shows the load proportions shared by the raft and the piles with elapsed time for 9P-3*D*. In comparison to the cases of four-pile piled rafts, the significant difference was the proportion of load carried by the piles. At the small applied loads P = 0.75 kN or 1.25 kN, the piles carried over 80 % of the total applied loads, however, the proportions of pile load were unstable (slightly decreased) with time in secondary consolidation periods. When the large load was applied, similar to 4P-6*D* or 4P-3*D*, the proportion of load decreased with increasing applied load meanwhile the proportion of raft load increased. At the ultimate load of piled raft condition, the piles still carried up to 60 % of the total load.

Fig. 3.41(d) shows the load proportions shared by the raft and the piles with elapsed time for 16P-3*D*. In the first 4 load steps, the piles shared major proportions of the load (just under 90 % in an average), and it is special that the proportion of the pile load was unstable with elapsed time in each load step but did not decrease when the applied load increased. At the larger load steps, the trend of loads shared between the piles and the raft was similar to the PRF with fewer piles. At the ultimate load of piled raft condition, the piles carried up to 73 % of the total load.

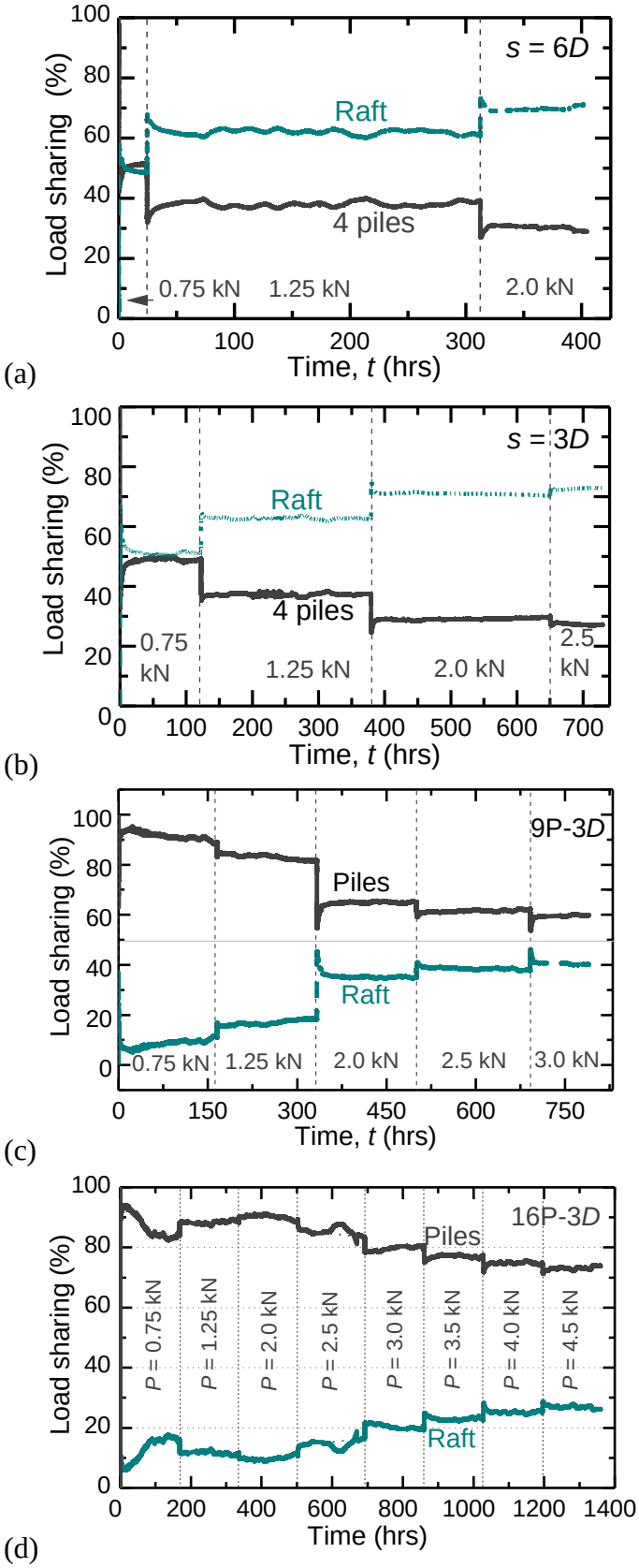

Fig. 3.41. Proportions of load sharing with time: (a) 4P-6*D*; (b) 4P-3*D*; (c) 9P-3*D*; and (d) 16P-3*D*.

In general, the load sharing between piles and raft was depended strongly on the number of piles, the magnitude of applied load, and the time. Tang et al. (2014) observed the behavior of piled raft foundations supported residential buildings in Shanghai. Tang et al. (2014) found no fixed value for the ratio between the pile load and the soil (raft) load and that the ground pressures, pile loads, and settlements varied with the pile arrangement, time, and external loads. This indicates that the experimental results show reasonable trends with the phenomenon obtained by field measurement. The load sharing between raft and piles was stable at the secondary consolidation period when the applied load was sufficiently large, in comparison with the corresponding PG ultimate capacity.

b. Load sharing between raft and piles with settlement

Figs. 3.42(a) and (b) show the load sharing with settlement for 4P-6*D* and 4P-3*D*, respectively.

Focusing first on the load-increasing period for 4P-6*D* (Fig. 3.42(a)), the load carried by the four piles increased rapidly to a peak with a very small settlement in the early stage of the load-increasing period. After the peak pile load, the load carried by the four piles decreased while that carried by the raft increased with increasing settlement during the load-increasing period (called immediate settlement). As mentioned earlier regarding Fig. 3.24, the PWP continued to increase until the end of the load-increasing period (or increased with immediate settlement). That is, the increased raft load in the load-increasing period was due mainly to the increased PWP. After the primary consolidation started, the raft load began to decrease while the pile load began to increase again with the increasing settlement. It is interesting to note that the pile "set-up" (increase in the resistance with elapsed time) occurred during the primary consolidation period. The pile load, raft load, and PWP exhibited similar trends in the second and third load steps. During secondary consolidation, the settlement increments were small and the load sharing between the piles and the raft was stable. Similar behavior to that mentioned above was observed for 4P-3*D* (Fig. 3.42(b)).

For the cases of 9P-3*D* and 16P-3*D* (Fig. 3.42(c) and (d), respectively), when the applied loads were smaller than the corresponding pile group ultimate capacity, the load carried by the piles increased purely with increasing settlement in the load-increasing periods and primary consolidation periods. In the secondary consolidation periods, the load shared by the piles decreased slightly with the increasing settlement. When the larger loads were applied, the behavior observed for 9P-3*D* and 16P-3*D* was similar to the behavior of 4P-6*D* and 4P-3*D*.

It is interesting that the load sharing between raft and piles with long time (in

secondary consolidation periods) in the cases of 9P-3*D* and 16P-3*D* was unstable at the small applied loads but was stable at the large applied loads.

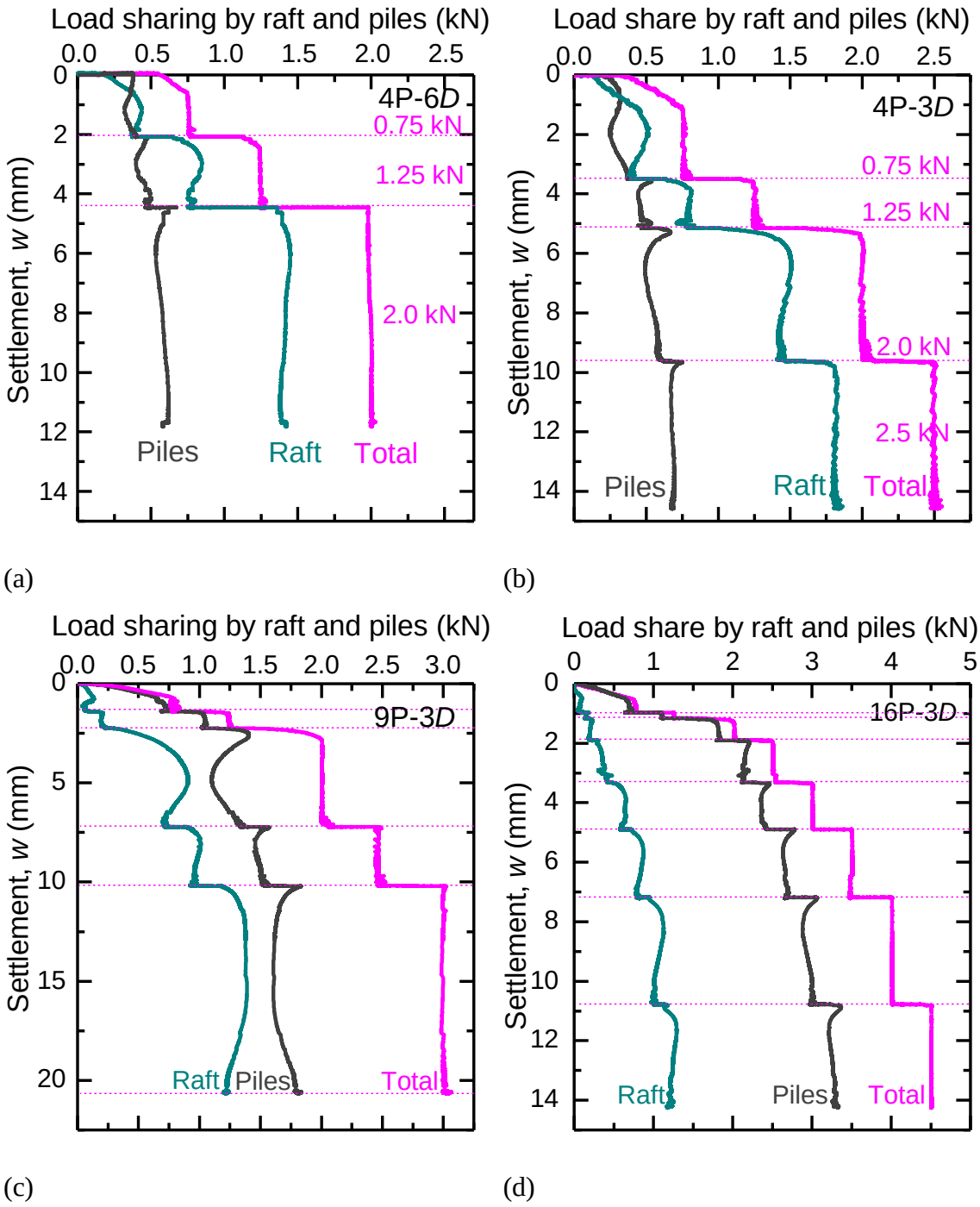

Fig. 3.42. Load sharing with settlement: (a) 4P-6*D*; (b) 4P-3*D*; (c) 9P-3*D*; and (d) 16P-3*D*

3.3.4.6 Axial force along pile

a. Axial force along piles in 4P-6D and 4P-3D

In the cases of 4P-6*D* and 4P-3*D*, all the 4 piles were corner piles, and they were arranged in symmetric positions. In other words, the 4 piles have the same condition. Therefore, in each foundation, the discussions on axial forces along piles were made for only one pile.

Fig. 3.43 shows how the axial force along a pile (P2) in 4P-6*D* changes in the form of the increments in axial force from the start of the first load step. This figure shows how the axial force changes in each load step (Fig. 3.43(a)) as well as for the load-increasing period (Fig. 3.43(b), (e), and (h)), primary consolidation period (Fig. 3.43(c), (f), and (i)), and secondary consolidation period (Fig. 3.43(d), (g), and (j)). Fig. 3.44 shows the corresponding results for the axial force along a pile (P1) in PF-3*D*.

For 4P-6*D*, in the load-increasing period of the first load step, Fig. 3.43(b) shows that both the pile shaft resistance and the pile tip resistance increased to a peak at a normalized displacement *w*/*D* of 0.002. At the peak resistance, the increase in the pile tip resistance was 38 N and that in the pile shaft resistance was 55 N. After the peak resistance, the pile tip resistance was almost unchanged, whereas the pile shaft resistance decreased by around 15 N until the end of this load-increasing period. The decrease in the pile shaft resistance was larger at the pile top sections and smaller at the bottom sections. In the primary consolidation period (Fig. 3.43(c)), the pile shaft resistance increased again, especially at the pile top sections. The increase in the pile tip resistance during primary consolidation was minor. Similar trends with different magnitudes were observed in the second load step (see Fig. 3.43(e)–(g)) and in the third load step (see Fig. 3.43(h)–3.43(j)). During secondary consolidation (Fig. 3.43(d), (g), and (j)), both the shaft and tip resistances were almost unchanged, although the foundations continued to settle.

The axial force along the 4P-3*D* pile behaved similarly to that along the 4P-6*D* pile. Comparing the pile resistance of the two foundations (Figs. 3.43 and 3.44), the pile shaft resistance of each foundation increased by different amounts in the load-increasing period and the primary consolidation period. Note again that the PWP increases during the load-increasing periods of the two foundations were different in each load step (Table 3.10), and this difference in PWP caused the different increases in ground strength, thereby resulting in the different increases in pile resistance between the two foundations during primary consolidation.

During secondary consolidation, the pile shaft resistance of each foundation was similar, with only marginally higher resistance in the case of 4P-6*D*.

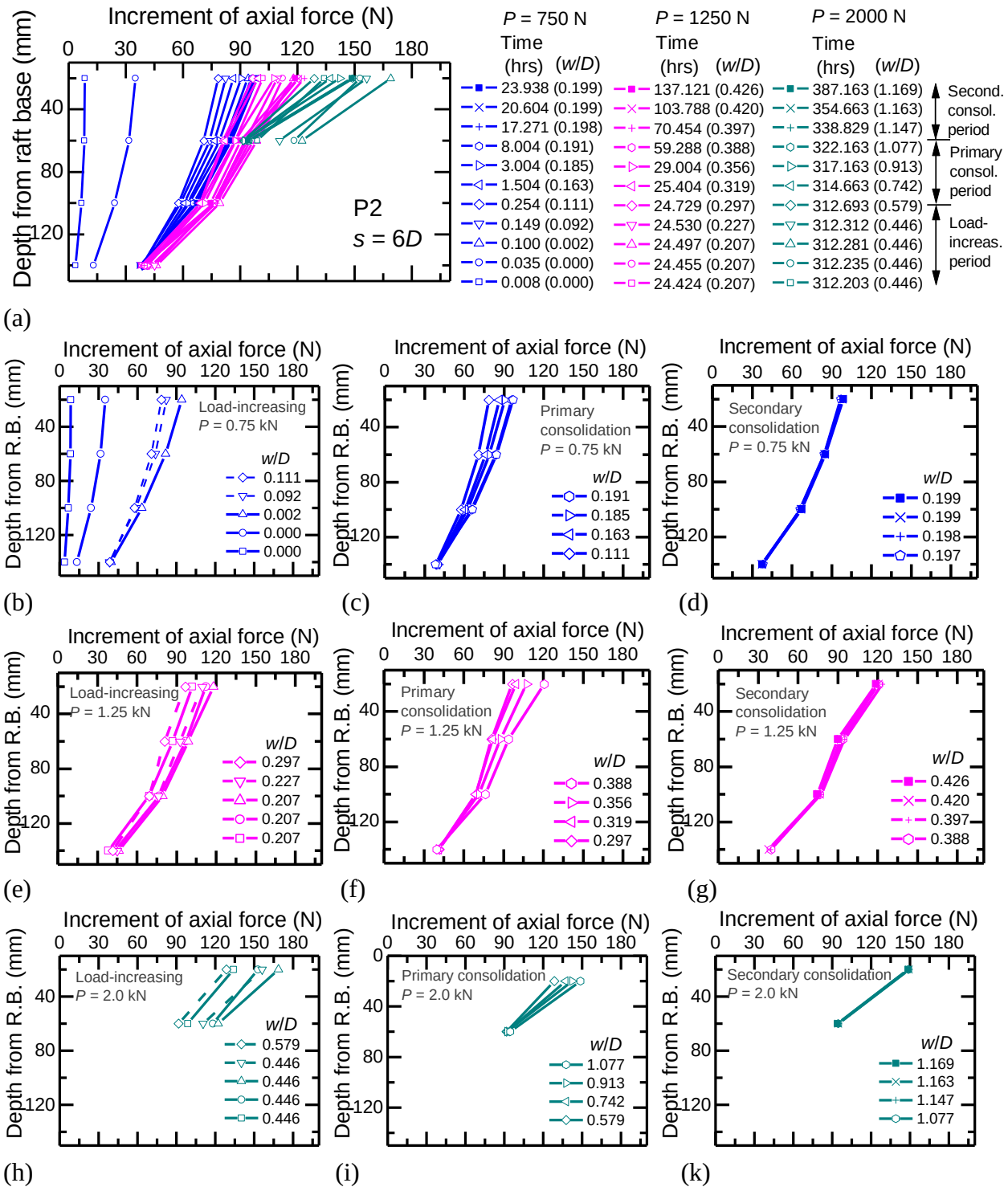

Fig. 3.43. Axial forces along a pile of PF-6*D*: (a) all load steps; (b) load-increasing period of first load step; (c) primary consolidation period of first load step; (d) secondary consolidation period of first load step; (e) load-increasing period of second load step; (f) primary consolidation period of second load step; (g) secondary consolidation period of second load step; (h) load-increasing period of third load step; (i) primary consolidation period of third load step; (j) secondary consolidation period of third load step.

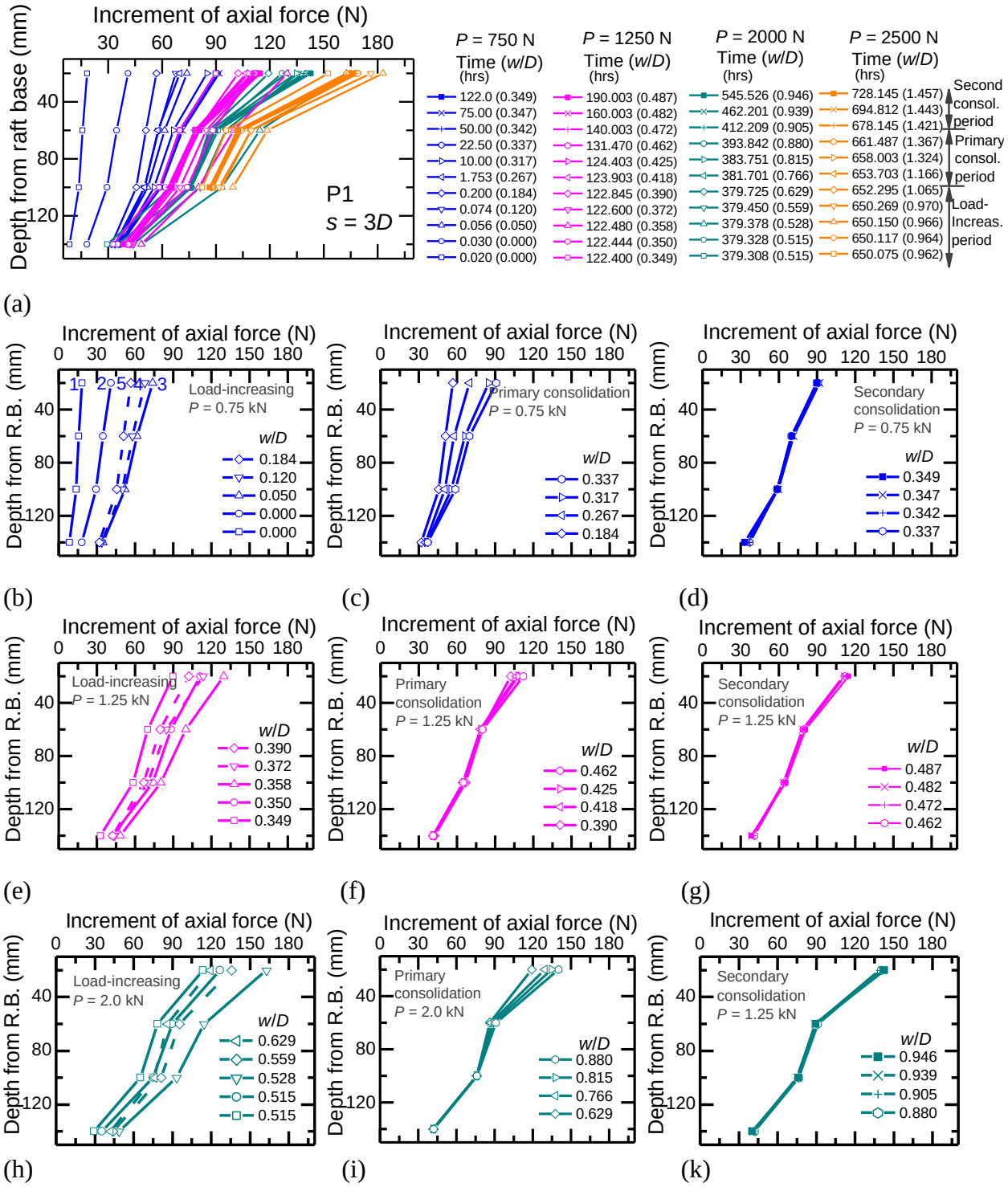

Fig. 3.44. Axial forces along a pile of PF-3*D*: (a) all load steps; (b) load-increasing period of first load step; (c) primary consolidation period of first load step; (d) secondary consolidation period of first load step; (e) load-increasing period of second load step; (f) primary consolidation period of second load step; (g) secondary consolidation period of second load step; (h) load-increasing period of third load step; (i) primary consolidation period of third load step; (j) secondary consolidation period of third load step.

Looking back at Fig. 3.12(c), which shows the undrained shear strength in the loading area of the ground after the load test, the increase in c_u beneath the raft base was greatest within a depth of 75 mm from the raft base. For greater depths, the increase in c_u decreased with depth, and at the depth of 150 mm from the raft base (pile tip level), the increase in c_u was small. These results indicate that the increased pile resistance was due mainly to the increased strength of the ground surrounding the pile shaft. It is reasonable that during the primary consolidation periods, the pile shaft resistance increased significantly along the top sections but modestly along the bottom sections.

b. Axial force along piles in 9P-3D and 16P-3D

In the cases of 9P-3*D* and 16P-3*D*, the piles were arranged in symmetric conditions with three different types of positions (corner pile, edge pile, and center pile). Therefore, the discussion on axial forces along piles in each foundation mentioned three piles representing three pile types, and the effect of pile positions on the changes of axial forces along piles was made also.

We firstly consider the changes of pile head loads.

Fig. 3.45 shows the increment of pile head load with time for 9P-3*D*. In the figure, three piles with three types of position are shown. The load on corner pile (P1) is smaller than that of the center pile (P3) and edge pile (P4) until the later stage of the primary consolidation period in the 1st load step. Thereafter, among three piles, the center pile had the smallest load in the 1st and the 2nd load steps, however, the load of the center pile increased rapidly and became the highest in the last 3 load steps. In contrast, the load of the corner pile (P1) was basically the highest in the 1st and 2nd load steps, however, it was the smallest at the final load step. This is due to the different increments of ground strength in the primary consolidation periods at locations of the center pile and corner pile. As shown in Fig. 3.12(e), after load test on PR, the ground strength was higher at the raft edge and was the highest at the center area. Therefore, it is reasonable that the resistance of the center pile increased most significantly and became the highest at the end of the load test.

Fig. 3.46 shows the increment of pile head load with time for 16P-3*D*. In the figure, the average pile head load of the three types of pile position are shown. The general trends for the increments of pile head loads in the case of 16P-3*D* were very similar to those of 9P-3*D*. Among 3 pile positions, the pile head load of the center pile was basically the lowest in the first 3 load steps. The center pile head load then increased significantly during the last 5 load steps and became the highest in the final 4 load steps. In contrast, the corner pile carried the

highest load until the 4th load step (except for the 1st load step), thereafter, the increment of the corner pile head load became smaller than that of the center pile and the load carried by the corner pile became below that of the center pile at the final load step. The behavior of the edge pile was similar to that of the center pile at the first 4 load steps but was similar to the behavior of the corner pile at the last 4 load steps. Similar to the 9P-3*D*, It is thought that this result was caused by the different increments of ground strength at the different pile locations in the primary consolidation processes.

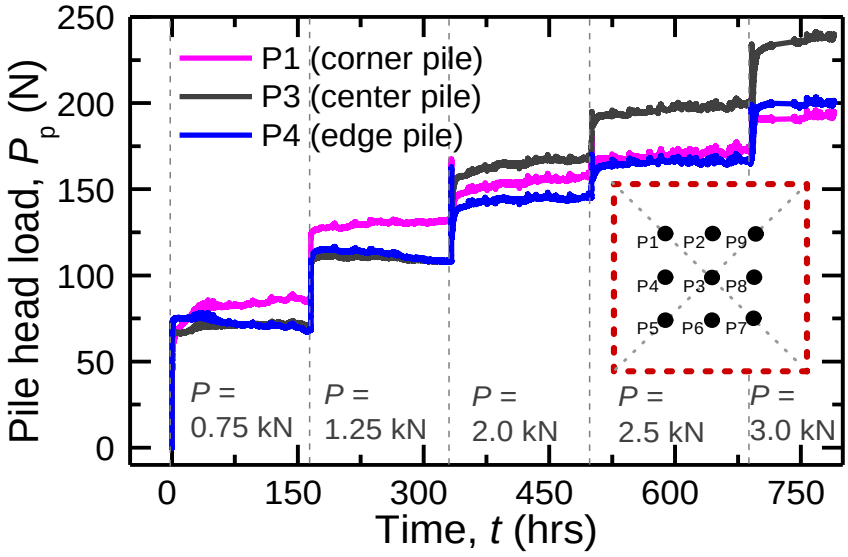

Fig. 3.45. Change of pile head load with applied load in 9P-3*D*.

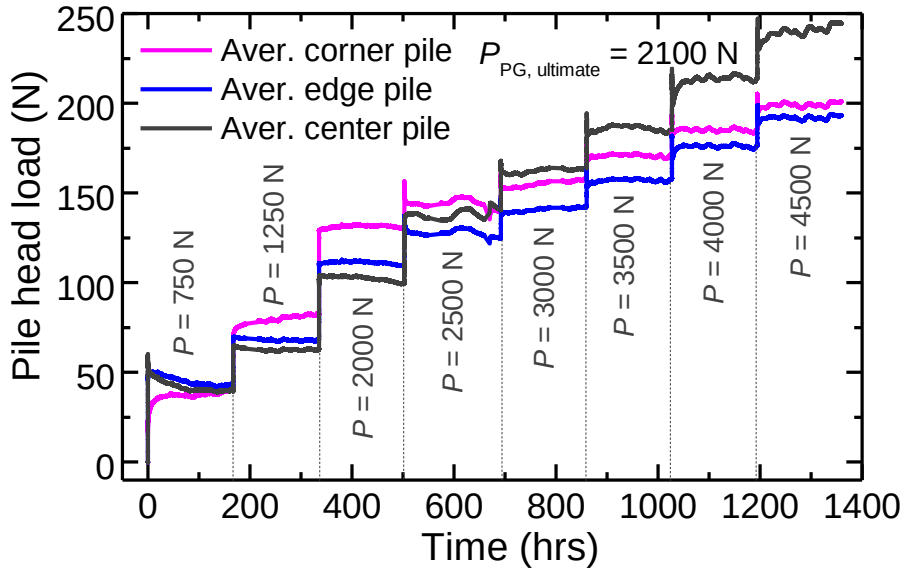

Fig. 3.46. Change of pile head load with applied load in 16P-3*D*.

Next, the changes of axial forces along three type piles with time were considered.

For the case of 9P-3*D*, Fig. 3.47 shows the changes of axial forces along piles with the normalized settlement, *w*/*D*, in cases: (a) corner pile, (b) center pile, and (c) edge pile.

Focusing first on the corner pile (P1, see Fig. 3.47(a)), in the 1st and 2nd load steps, both the shaft and tip resistances increased to support load on this pile, and the shaft resistance supported about a haft of the pile load. In the last 3 load steps, the shaft resistance increased significantly while the tip resistance increased slightly. The increment of pile load, therefore, mainly was supported by the shaft resistance in these load steps. Until the end of the load test, the shaft resistance supported up to 2/3 (125/200 N) of the total pile load.

For the center pile (P3, see Fig. 3.47(b)), in the 1st and 2nd load steps, the load was supported by both the shaft and the tip resistances. The tip resistance of P3 in these steps was almost equal to that of P1, however, the shaft resistance of P3 was smaller than that of P1. The load supported by P3 in the first 2 load steps, therefore, smaller than that by P1. In the last three load steps, the pile shaft resistance increased more sharply. At the end of the load test, the shaft resistance of the center pile was almost equal to the shaft resistance of the corner pile P1. If the pile shaft resistance was extended linearly to the pile tip direction (the strain gages at pile tip was damaged), the tip resistance would also increase significantly during the last 3 load steps, and about a haft of the load (125 N) on P3 would be carried by the pile tip at the end of load test. The tip resistance of P3 would be almost double the tip resistance of P1 at that time.

Looking back at Fig. 3.12(e), c_u beneath the raft center was also greatest at the depth of 150 mm (pile tip level) from the raft base, and was noticeably larger than the c_u beneath the raft edge at the same depth. Therefore, it is reasonable that the tip resistance of the center pile is higher than the tip resistance of the corner pile.

For the edge pile (P4, see Fig. 3.47(c)), the axial forces of the edge pile were almost equal to those of the center pile in the first two load steps. From the 3rd to the 5th load step, the increment of axial forces of P4 was smaller than that of the center pile. From the 4th to the 5th load step, the axial forces of the edge pile became similar to those of the corner pile. It should be noted again that, in the last 3 load steps, the excess pore water pressure generated in the load-increasing period was noticeably higher than that in the first two load steps, therefore, the consolidation of the ground occurred significantly in these load steps, in comparison with the first two load steps. This indicates that the ground consolidation increased the tip resistance of the center pile most significantly, as mentioned earlier.

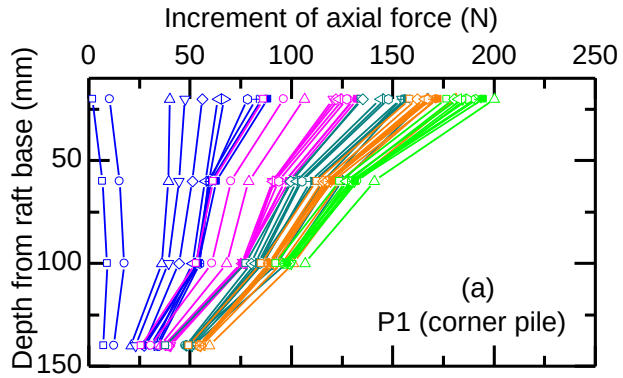

(a)

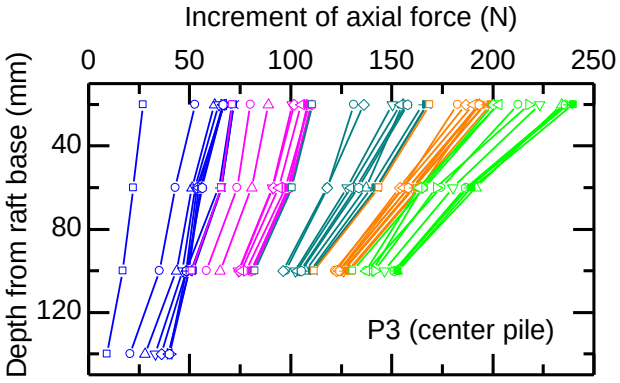

(b)

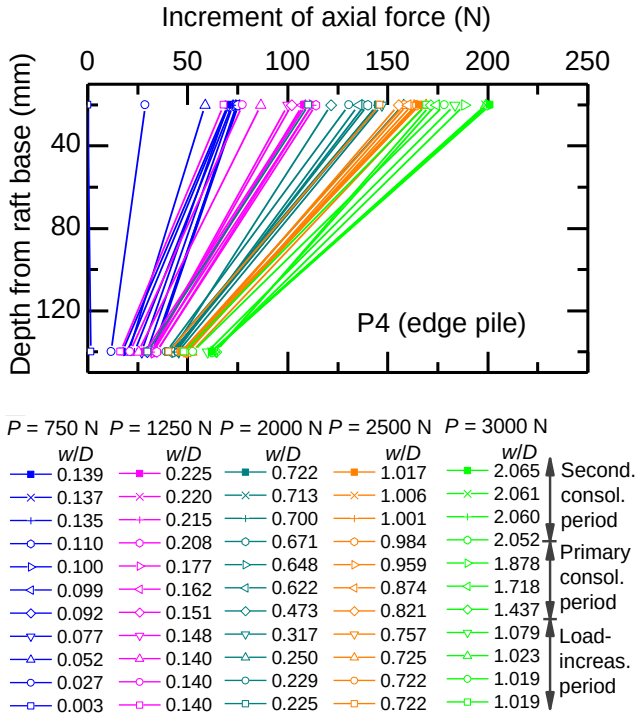

(c)

Fig. 3.47. Axial forces along piles of 9P-3*D*: (a) corner pile; (b) center pile; (c) edge pile

For the case of 16P-3*D*, the increments of axial forces along a corner pile (P16, Fig. 3.48(a)), an edge pile (P15, Fig. 3.48(b)), and a center pile (P6, Fig. 3.48(c)) with normalized settlement *w*/*D* are shown in Fig. 3.48. The axial forces herein were obtained at the end of each load step.

Focusing first on the corner pile, for the first 3 load steps, the shaft resistance increased sharply meanwhile the tip resistance increased slightly. The shaft resistance supported up to 75% of the total pile load at the end of the 3rd load step. For the last 5 load steps, the tip resistance increased more considerably than the shaft resistance and finally supported about 1/3 of the pile load.

In contrast to the corner pile, the center pile had very small shaft resistance for the first 3 load steps, the pile load, therefore, was mainly carried by the bottom section of the pile. However, the shaft resistance of the center pile increased significantly in the last 5 load steps and supported a noticeable part of the pile load at the final step (extrapolated as around 50%: the SGs at the pile tip of the center pile were damaged). Among the 3 piles, the load carried by the center pile was the largest at the final load step because of the large pile tip resistance, although the shaft resistance of the 3 piles was similar.

Interestingly, the tip resistance of the edge pile was almost equal to that of the corner pile. In the first 3 load steps, the shaft resistance of the edge pile was smaller than that of the corner pile but larger than that of the center pile. In the last 5 load steps, the increment of shaft resistance of the edge pile was slightly higher than that of the corner pile. The shaft resistance of the edge pile supported about 60% of the pile load at the final load step.

The increments of undrained shear strength c_u (estimated from T-bar tests, see Fig. 3.12(f)) beneath the raft base show a good agreement with the increments of the resistances of the 3 piles. After the load test, at the depth of 150 mm from the raft base (the pile tip level), the c_u at the center of the loading area (T5, area of the center piles) was larger than the c_u at the edge of the loading area (T3 and T4). The noticeable increases of the center pile load in the last 5 load steps indicate that the ground consolidation occurred significantly in the center area during these load steps.

In general, the experimental results of the 4 pile foundations show that:

1. The corner piles carried the larger load at the small applied loads, in comparison with center piles and edge piles. In contrast, the center piles carried the smallest load at the small

load steps but carried the largest load at the final load steps.

2. The corner piles mobilized the shaft resistance significantly during primary consolidation periods, in comparison with the tip resistance. The shaft resistance carried about 70% of the pile load at the final load of the piled raft foundation.

3. The center pile carried load mainly by tip resistance at the small applied loads. During the consolidation period, both the pile tip and pile shaft resistances increased significantly. The pile tip resistance carried about a haft of the pile load at the final load of piled raft foundation.

4. The shaft resistances of peripheral piles were mobilized from the low level of applied load ($P < P_{PG,\ ultimate}$), but that of the center piles were mobilized at the higher level of applied load ($P > P_{PG,\ ultimate}$).

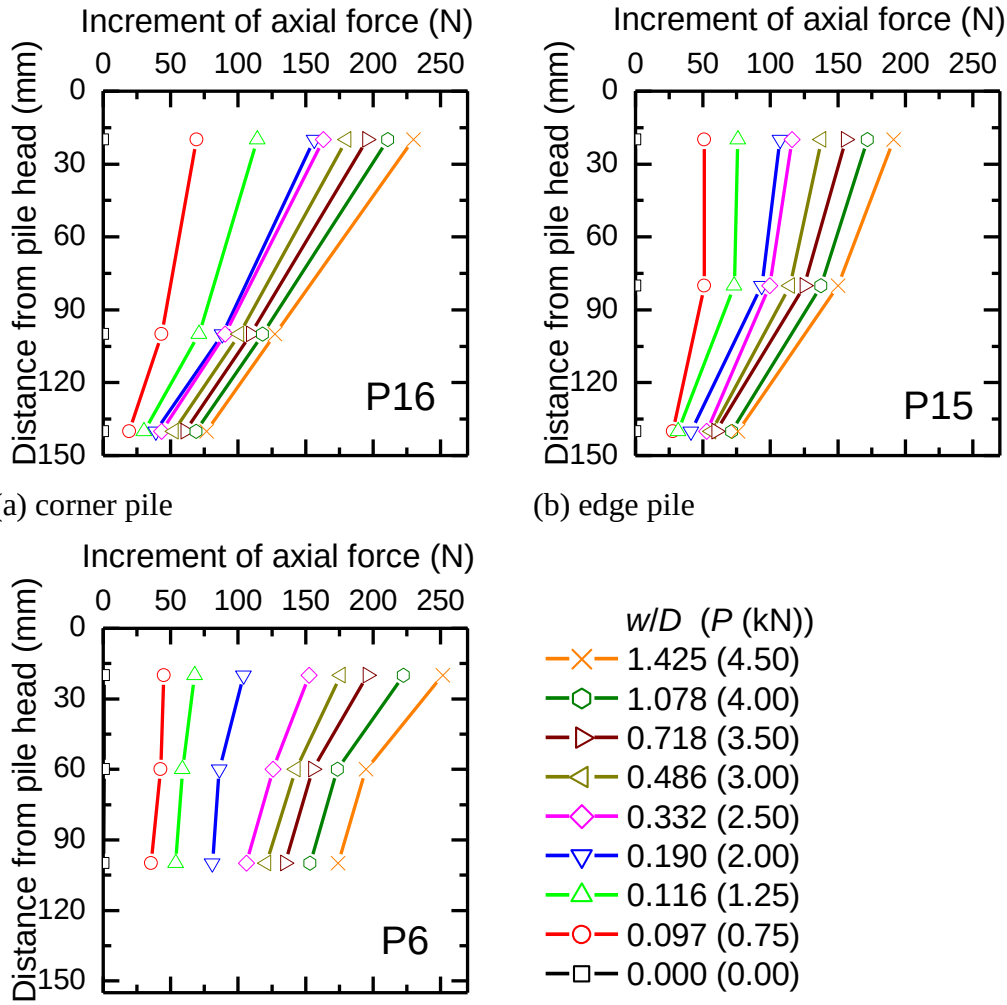

(a) corner pile

(b) edge pile

(c) center pile

Fig. 3.48. Changes of axial forces along piles during SLT of PR.

Interestingly, the average load carried by each pile exceeded 150 N for the cases of 4P-6*D* and 4P-3*D*, and 200 N for the cases of 9P-3*D* and 16P-3*D* at the final load step, which was much larger than the ultimate capacity of each pile in the corresponding PG. This advantage was also caused by the increase of ground strength in consolidation processes in PR conditions.

3.3.4.7 Effect of long-term load tests of piled rafts with different pile arrangement on ground strength

As discussed in the above sections, the PWP generated during the load-increasing periods dissipated with time during the primary consolidation periods. The dissipation of PWP caused increases in ground stresses, resulting in increases of ground strength.

In this section, the increase of undrained shear strength after the load tests of PRFs will be discussed. The effect of pile number and magnitude of final load steps are also discussed.

The distributions of undrained shear strengths c_u with depth beneath the raft base edge (loading area) are shown in Fig. 3.14. In the figure, the results are shown for the short-term load test of unpiled raft UR*, long-term load tests of three PRFs (4P-3*D*, 9P-3*D*, and 16P-3*D*) with the same pile spacing but different pile number. The distribution of average undrained shear strength of the original model ground (without the effect of load test) is also shown in the figure by Eq. (3-4), for comparison purpose. It should be noted again that the foundation had settled by around 15-18 mm upon completion of the load test. Therefore, the profiles of c_u in the loading area begin at the depth of 15-18 mm (the level of the raft base after loading). Fig. 3.14 show that, for the case of the unpiled raft (short-term behavior), the distribution of soil strength beneath the raft base edge after loading was quite consistent with the soil strength of the original model ground (presented by Eq. (3-4)). This indicates that the loading of the unpiled raft in the short-term condition did not have a significant effect on the undrained shear strength of the model ground. This is a reasonable result because the loading time is too short for excess PWP to fully dissipate. For the cases of long-term load tests (4P-3*D*, 9P-3*D*, and 16P-3*D*), the soil strengths beneath the raft base edge after loading became larger than that of the original model ground or that of model ground for the case of UR*. Fig. 3.14 shows clearly that at the shallow depths from the raft base, the increments of c_u of the three PRFs were quite similar. At the deeper depths, Fig. 3.14 shows that the model ground of the PRF with larger pile number and also larger magnitude of the final applied load had larger c_u beneath the raft base edge. Furthermore, compared to the original ground

c_u, Fig. 3.14 shows that the increments of c_u at the depths deeper than 150 mm (from the raft base level after loading) became smaller with increasing depth. The c_u beneath the raft base edge of the 4P-3*D* case became equal to the c_u of the original model ground at the depth of around 240 mm (or around 220 mm from the raft base level after loading); however, the corresponding depth for the 9P-3*D* case was around 270 mm (or around 250 mm from the raft base level after loading), and a deeper depth (about 320 mm from the original ground surface, in extrapolation) is required for the c_u of the 16P-3*D* case to be equal with the c_u of the original model ground. This indicates that the pile arrangement and the level of applied load in long-term load tests affected the ground strength in both the magnitude of c_u increment and the depth of the zone affected by the load test.

The distributions of undrained shear strengths c_u with depth beneath the raft base center (loading area) are shown in Fig. 3.15. In the figure, the results are shown for the short-term load test of unpiled raft UR*, long-term load tests of the unpiled raft UR and three PRFs (4P-3*D*, 9P-3*D*, and 16P-3*D*) with the same pile spacing but different pile number. The distribution of average undrained shear strength of the original model ground (without the effect of load test) is also shown in the figure by Eq. (3-4), for comparison purpose. The trends of the effect of the load tests on ground strength beneath the raft base center were quite similar to those beneath the raft base edge. For the case of short-term load test of unpiled raft UR*, Fig. 3.15 show that the ground strength c_u beneath the raft base center was almost equal to the c_u of the original model ground, indicating the negligible effect of short-term load test on ground strength. For the case of long-term load test of unpiled raft UR, Fig. 3.15 shows that the ground strength c_u beneath the center of the raft base after the load test became much greater than that of the original model ground within a depth of 150 mm from the raft base level. The peak increment occurred at the depth of around 81 mm from the original ground level (or around 63 mm from the raft base level after loading, which was about a haft of the raft width), and after the peak increment, the increment of c_u beneath the raft base center became smaller with increasing depth. At the depths deeper than 270 mm from the original ground model, the c_u beneath the raft center was equal to the original ground c_u. Similar to the long-term load test of UR, the c_u beneath the raft center of 4P-3*D*, 9P-3*D*, and 16P-3*D* was much greater than the original ground c_u, and also larger than the c_u beneath raft base center in the case of UR. Fig. 3.15 shows that the peak c_u for 4P-3*D*, 9P-3*D*, and 16P-3*D* was around 30.6, 32.6, and 38.5 kPa, respectively. The corresponding referenced depths at the peak c_u increment for the three foundations were 90, 180, and 180

mm, respectively. These results indicate that the more piles were used, the deeper zone was affected by the load tests, and the larger load was applied, the larger increment of ground c_u had occurred.

Compare the cu beneath the raft base center to cu beneath the raft base edge, the increment of cu beneath the raft base center was larger than that beneath the raft base edge. About the depth of the zone affected by load test, for the 4P-3*D* case, it is interesting that the affected depths beneath the raft edge and raft center were equal. For the 9P-3*D* and 16P-3*D* cases, unfortunately, the profiles of c_u (or testing depths of T-bar tests and CPTs) were not enough to compare the depth of the zone affected by load tests.

The changes of ground strengths present good agreements with the increments of pile head loads as well as the increment of axial forces along piles as discussed above in the sections 3.3.4.2(d) and 3.3.4.6.

In general, the experimental results of the 4 pile foundations show that:

1. The effect of the short-term load test on the undrained shear strength of the original model ground was negligible.

2. The pile arrangement and the magnitude of applied load in long-term load tests affected the distributions of ground strength in both the magnitude of c_u increment and the depth of the zone affected by load test.

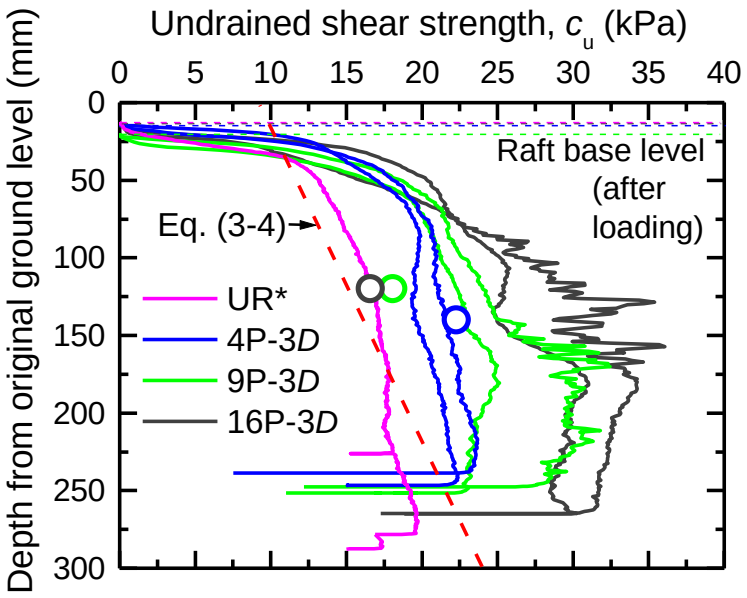

Fig. 3.14. Distributions of undrained shear strength with depth beneath raft edge after loading (shown again).

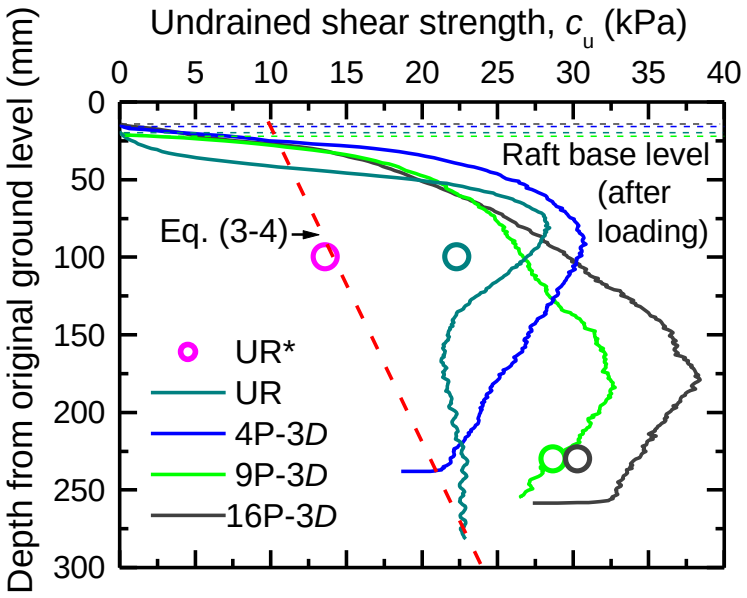

Fig. 3.15. Distributions of undrained shear strength with depth beneath raft center after loading (shown again).

3.3.4.8 Effect of pile arrangement on long-term foundation settlement

The settlements of the 2 PRFs (4P-6*D* and 4P-3*D*) with different pile spacings and the 3 PRFs (4P-3*D*, 9P-3*D*, and 16P-3*D*) with different pile numbers were compared in Figs. 3.49 and 3.50.

Fig. 3.49 compares the load-settlement relationships of the 4 PRFs.

Compare the behaviors of 4P-6*D* and 4P-3*D* first, Fig. 3.49 clearly shows that when the applied loads were small ($P \leq 1.25$ kN or 50 % of the PRF predicted capacity), the foundation with wider pile spacing 4P-6*D* suppressed settlement better than the foundation with narrower pile spacing 4P-3*D*. In contrast, when the applied load was larger than 50 % of the PRF predicted capacity, the PRF with narrower pile spacing suppressed settlement better than did the one with wider pile spacing. At the settlement of 10 % of raft width (w = 0.1 B_r), the foundation with narrower pile spacing supported larger load (regarded as PRF ultimate capacity) than the foundation with wider pile spacing.

Compare behaviors of 3 PRF (4P-3*D*, 9P-3*D*, and 16P-3*D*) with the same pile spacing but different in the number of piles. Fig. 3.49 shows that at the same magnitude of applied loads, the foundation with a larger number of piles had a smaller settlement. The ultimate capacity of PRF was larger with a larger pile number. However, it is interesting that also the pile number of 9P-3*D* was 2.25 times the pile number of 4P-3*D*, the ultimate capacity of 9P-3*D* was 1.2 times the ultimate capacity of 4P-3*D*. Similarly, the pile number of 16P-3*D* was

4 times the pile number of 4P-3*D*, the ultimate capacity of 16P-3*D* was 1.8 times the ultimate capacity of 4P-3*D*.

The effect of pile number on short-term load-settlement behavior of PRFs was investigated in many previous researches as summarized in chapter 2. In short-term behavior, similar settlement and capacity trends were obtained.

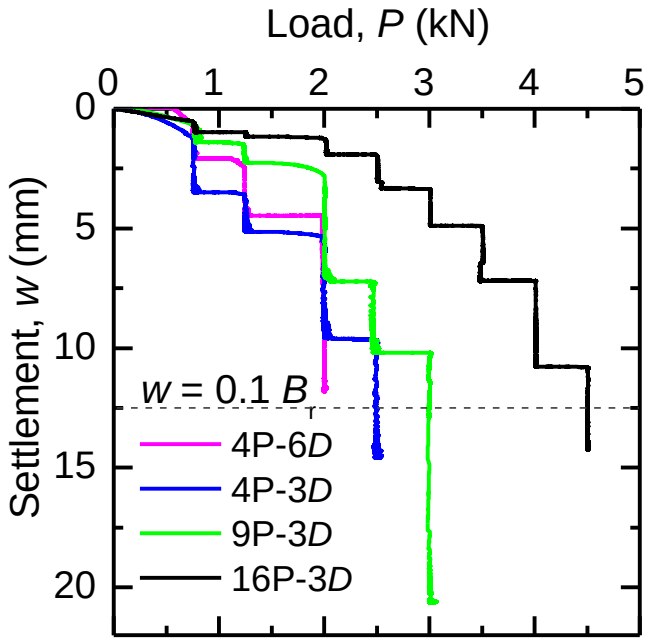

Fig. 3.49. Changes of settlement with load during long-term load tests of piled rafts.

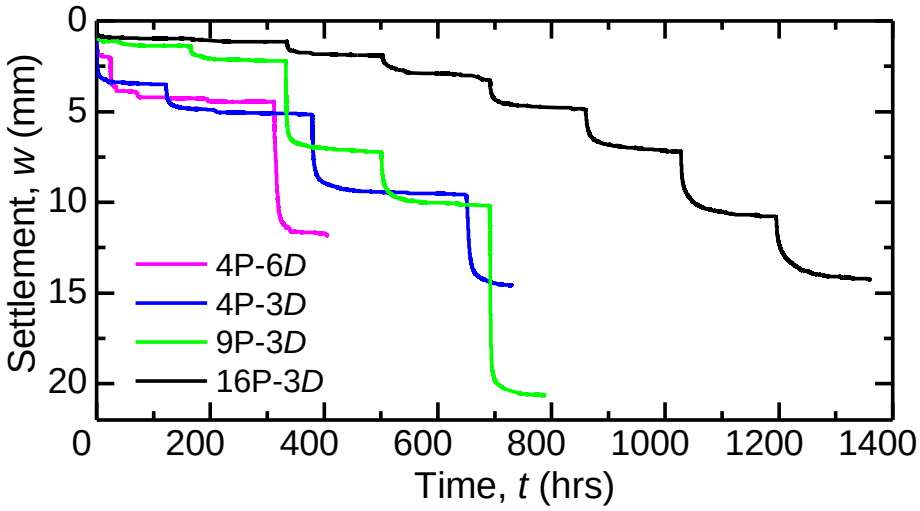

Fig. 3.50. Changes of settlement with time during long-term load tests of piled rafts.

Fig. 3.50 compares the time-dependent settlements of the 4 PRFs. The comparisons of performances the 4 PRFs with different pile arrangements were discussed above, regarding

Fig. 3.49, in aspects of final settlement and capacity. The notable point from Fig. 3.50 is that all the 4 PRFs with different pile arrangements behaved similarly with time. In each load step, the settlement occurred quickly when the load was increased, thereafter the foundation continued to settle noticeably in the early stage (primary consolidation period) after the load-increasing period, and settle slightly for a long time after the primary consolidation period (secondary consolidation period). This phenomenon emphasized the need for attention to the time-dependent settlement when designing PRFs on clayey ground.

3.4 Conclusions of chapter 3

In this chapter, the long-term behavior of PRF models on saturated clay was investigated through small-scale physical modeling. The main findings and suggestions from the experiments within the experimental conditions presented in this study are as follows.

1) During the load-increasing period of small load steps ($P \leq P_{PG,\,ult.}$), the piles were effective at supporting the applied load and suppressing the settlement of the foundation. During the load-increasing period of large load steps ($P > P_{PG,\,ult.}$), the pile resistance increased to a temporary peak and then decreased (softening behavior). The softening behavior of the piles continued for a short duration after the load-increasing period, although the PWP started to dissipate (early stage of primary consolidation period).
2) Stresses from the raft base caused ground consolidation. Consequently, the effective ground stresses increased, thereby increasing the ground strength and stiffness during primary consolidation and increasing the pile resistance.
3) During secondary consolidation, the foundations continued to settle because of ground creep, and the creep settlement index [Eq. (3-6)] was higher when the applied load was larger.
4) During secondary consolidation period, the load sharing between raft and piles was unstable at the relatively small applied load ($P \leq P_{PG,\,ult.}$), however, at the larger applied load, the loads supported by both the raft and the piles were stable, despite the creep settlement continued.
5) The level of applied load P affected the load sharing between the raft and the piles, and also affected the load sharing between piles. The proportion of load supported by piles decreased with the increasing applied load. The corner pile carried larger load at small load steps but smaller load at larger load steps, in comparison with the center pile. The piles carried a notable part of the applied load, even though in cases of only 4 piles.

6) The shaft resistances of peripheral piles were mobilized from the low level of applied load ($P < P_{PG,\ ultimate}$), but that of the center piles were mobilized at the higher level of applied load ($P > P_{PG,\ ultimate}$). The pile shaft resistance of corner piles increased during primary consolidation, especially at the top sections near the raft base.
7) For smaller applied loads, the PRF (4P-6*D*) with the wider pile spacing ($s = 6D$) was better at suppressing the settlement than was the one (4P-3*D*) with the narrower pile spacing ($s = 3D$). For larger applied loads, the opposite was the case.
8) The PRF bearing capacity increased and the PRF settlement decreased with the increasing number of piles in the foundation.

Although the present study involved small-scale experiments, it emphasized the importance of considering the interaction among the piles, the raft, the ground, and the PWP. The results can also be used to validate analytical methods in the design of piled raft foundations on saturated clay ground.

References for chapter 3

Brown, P.T., 1975. Strip footing with concentrated loads on deep elastic foundation. Geotechnical Engineering 6(2), 1-13.

Cooke, R.W., 1986. Piled raft foundations on stiff clays—a contribution to design philosophy. Géotechnique 36(2), 169–203. https://doi.org/10.1680/geot.1986.36.2.169

Hoang, L., Matsumoto, T., 2020. Time-dependent behavior of piled raft foundations on saturated clay: Experimental investigations, International Journal of GEOMATE, 18(66), pp.1-8. DOI: https://doi.org/10.21660/2020.66.9150.

Hoang, L., Matsumoto, T., 2020. Long-term behavior of piled raft foundation models supported by jacked-in piles on saturated clay, Soils and Foundations, 20pp., Online, DOI: https://doi.org/10.1016/j.sandf.2020.02.005.

Hoang, L., Matsumoto, T., Dao, K., 2020. Settlement and pile response in a long-term vertically loaded piled raft foundation model on saturated clay - Experimental study. In: Duc Long P., Dung N. (eds) Geotechnics for Sustainable Infrastructure Development. Lecture Notes in Civil Engineering, vol 62, pp.33-40. Springer, Singapore. DOI: https://doi.org/10.1007/978-981-15-2184-3_3.

Hoang, L., Matsumoto, T., 2019. Effect of pile spacing on the behavior of pile, pile group, and piled raft models supported by jack-in piles under vertical loads in dry sand, Proc. of 16th Asian Regional Conference of Soil Mechanics and Geotechnical Engineering, 4pp., October, Taipei, Taiwan.

Hoang, L., Matsumoto, T., Dao, K., Shimono, S., 2019. Experimental study on time-dependent behaviour of a vertically-loaded piled raft foundation model in soft clay, Proc. of 16th Asian Regional Conference of Soil Mechanics and Geotechnical Engineering, 4pp., October, Taipei, Taiwan.

Hoang, L., Matsumoto, T., 2019. Experimental study on behaviour of vertically loaded piled rafts resting on saturated clayey ground, Proc. of 9th Int. Conf. on Geotechnique, Construction Materials and Environment, November, Tokyo, Japan. ISBN: 978-4-909106025 C3051, 86-91.

Horikoshi, K., Randolph, M.F., 1996. Centrifuge modelling of piled raft foundations on clay. Géotechnique 46(4), 741–752. https://doi.org/10.1680/geot.1996.46.4.741

Low, H.E., Lunne, T., Andersen, K.H., Sjursen, M.A., Li, X., Randolph, M.F., 2010. Estimation of intact and remoulded undrained shear strengths from penetration tests in soft clays. Géotechnique 60(11), 843–859. https://doi.org/10.1680/geot.9.P.017

Terzaghi, K., 1960. From Theory to Practice in Soil Mechanics, John Wiley and Sons, New

York.

The Japanese Geotechnical Society, 2015. Laboratory testing standards of Geomaterials. Maruzen Publishing Co., Ltd., Japan.

Chapter 4

Numerical study on the behavior of piled raft foundations supported by jacked-in piles on saturated clayey ground

4.1 Introduction

In Chapter 3, the long-term behavior of unpiled raft and piled rafts were investigated through a series of physical model tests.

It is important to validate the experimental results, by comparing them with those from numerical approaches, to confirm the mechanisms of PRFs. Therefore, in this chapter, the numerical analyses were conducted. Emphasis is placed on two key points of piled raft design: the time-dependent settlement and the time-dependent effect on the load sharing. It is noticed that the main aim of numerical analysis is to clarify the time-dependent behavior of PRFs rather than the perfect quantitative match between experimental results and numerical results.

The numerical analyses were performed using the three-dimensional finite element program PLAXIS 3D. This software has been developed specifically for the analysis of deformation, stability, and flow in geotechnical engineering projects by the Plaxis bv company. The constitutive soil model called "soft soil creep (SSC) model" was used to model the soil. The parameters for the soil model were mainly obtained from laboratory element tests such as CU triaxial test and Oedometer test. The analysis results are presented and discussed in detail in this chapter, and the comparisons between calculated results and experimental results are made. The suggestions from the analyzed results are given.

4.2 FEM simulation of laboratory soil tests

The simulations of the CU triaxial test and the Oedometer test are conducted in this section, before the analyses of the load tests on pile foundations, to validate the soil model and to estimate the appropriate input parameters for the soil model.

4.2.1 Constitutive model and soil parameters

Constitutive soil model: In the commercial version of PLAXIS 3D 2018, the behavior of compressible soft soils can be modeled by Hardening Soil model, Soft Soil model, Soft Soil Creep model, Cam clay model, and Sekiguchi-Ohta model (PLAXIS 2018, Material Models Manual). Among these models, the time-dependent behavior is introduced in (i) the Soft Soil Creep model and (ii) Sekiguchi-Ohta model. However, the Sekiguchi-Ohta model is for the normally consolidated clays only. In this study, the over-consolidated ground was used, therefore, the constitutive model "Soft Soil Creep model" was selected to model the soil with consideration of time effect. The detail of the Soft Soil Creep (SSC) model was described detailed in Material Models Manual of PLAXIS. Some basic characteristics of the SSC model are:

- Stress-dependent stiffness
- Distinction between primary loading and unloading-reloading
- Secondary compression
- Aging of pre-consolidation stress
- Failure behavior according to the Mohr-Coulomb criterion.

Soil properties: The input parameters for the SSC, which were first used to simulate the CU triaxial test and the Oedometer test, were the parameters obtained from the results of laboratory element tests. These parameters include compression index C_c, swelling index C_s, secondary compression index C_α, internal friction angle ϕ', permeability k, and void ratio e. The remaining other parameters such as effective cohesion c', tensile strength σ_t, and Poisson's ratio for unloading/reloading ν_{ur} were either assumed or set as default. The parameters for the SSC model of the first simulation of the CU triaxial test are shown in Table 4.1. For the simulation of Oedometer test, input parameters are also obtained from laboratory element tests, however, some parameters such as permeability, void ratio, or compression index are taken at the specific load step (for example, the input parameters for the simulation of the last load step are taken from the last load step of the oedometer test), instead of the general/ average values from Table 4.1.

Table 4.1. Parameters for the soft soil creep model.

No.	Basic parameter (Drained/Undrained A material)	Symbol	value	Unit	Source & equation, and notice
1	Compression index	C_c	0.291		Oedormeter test
2	Swelling index	C_s	0.055		Oedormeter test
3	Secondary compression index (Creep index)	C_α	0.00125		Oedormeter test, at σ_v = 1257.2 kPa;
4	Effective cohesion	c'	0.005	N/mm^2	(assumed)
5	Friction angle	ϕ'	34.8	degrees	CU triaxial test
6	Tensile strength	σ_t	0		(default)
	Advanced parameters				
7	Poisson's ratio for unloading/reloading	ν_{ur}	0.17 (assumed)		From E_{ur} and G_{ur} in CD test: $\upsilon' = \frac{E'}{2G} - 1$
8	Pre Overburden pressure	POP	0.1	N/mm^2	Equivalence of 100 kPa
9	Initial void ratio	e_0	0.703		Before load test on the foundation
10	Permeability	k	0.00038	mm/min	Oedometer test (at consolidatiion pressure, p = 113 kPa)
11	Change of permeability	c_k	0.425 (or 0.113)		when σ_v < 150 kPa and e > 0.6 (or when σ_v > 150 kPa and e < 0.6) Obtained from e - log k relationship: $C_k = \frac{e - e_0}{\log \frac{k}{k_0}}$
12	Unsaturated unit weight	γ_{unsat}	0. 000019	N/mm^3	
13	Saturated unit weight	γ_{sat}	0. 0000197	N/mm^3	Taken as 0 when analyzing CU triaxial test
14	Unit weight of water	γ_{water}	0.00001	N/mm^3	

4.2.2 FEM simulation of triaxial test

Fig. 4.1 shows the finite element mesh for the simulation of the CU triaxial test. Only a quarter of the soil specimen was modeled, based on the symmetric conditions of the model. The simulation of the CU triaxial test includes consolidation stages and axial compression stage.

The boundary conditions assigned to boundary surfaces of this model include prescribed displacement boundary and flow boundary conditions.

For the prescribed boundary displacements, horizontal displacements on the symmetrical surfaces were fixed, and the vertical displacements at the bottom surface were fixed.

For the flow boundary conditions, impermeable condition was set on the symmetrical surfaces due to the axisymmetric conditions, and at the top surface. The permeable condition was set at the lateral surface and the bottom end of the soil specimen according to the test conditions (note that the lateral surface of the specimen was surrounded by a drain paper which was connected to drainage line at the bottom end).

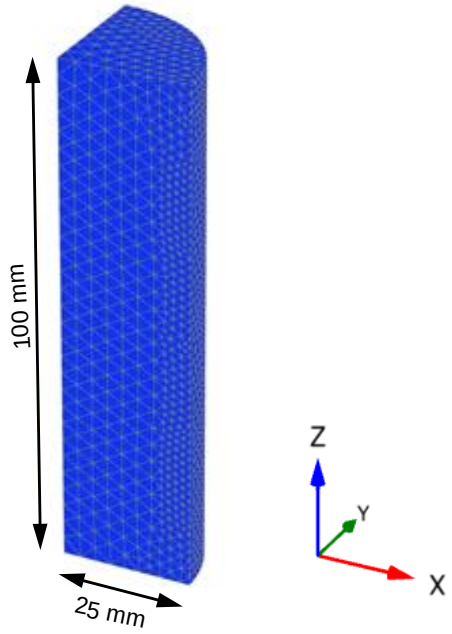

Fig. 4.1. Finite element mesh for the CU triaxial test.

The comparison of the laboratory test result and the numerical result in the consolidation stage is shown in Fig. 4.2. In the figure, the change of volume strain ε_v with elapsed time is shown. It is seen that the calculated results showed a reasonable matching with the measured results in both tendency and quantity. The calculated compression rate is slightly higher than

the measured one at the early stages of the consolidation process. At the end of the consolidation process, the calculated volume strain reaches about 90% of the measured value.

Fig. 4.3 shows the comparisons of total stress paths and effective stress paths between simulation and measurement in the undrained shearing stage. The relationship between effective mean normal stress p' and deviatoric stress q was simulated well from the start of the shearing stage until the failure state was nearly reached. In the CU test, phase shift behavior was measured at q/p = 1.11. Although the numerical results did not simulate this phenomenon, the numerical results simulated the measured results reasonably.

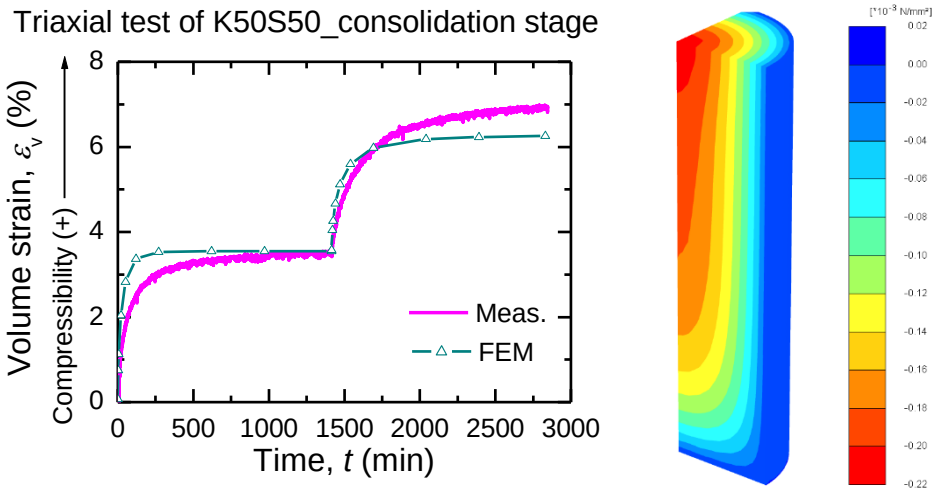

Fig. 4.2. Change of volume strain during consolidation stage of CU triaxial test.

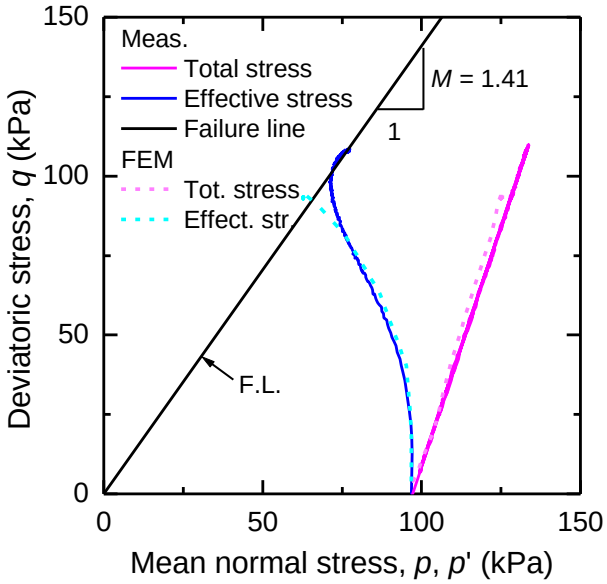

Fig. 4.3. Normal stress versus deviatoric stress during axial compression stage of CU test.

Fig. 4.4 shows the relationship between deviatoric stress q and PWP during the shearing stage. The FEM result shows a good agreement with the result of the laboratory soil test until the commencement of the phase shift.

Figs. 4.5 and 4.6 compare simulation results and measured results in terms of the relationship between deviatoric stress q and axial strain ε_a, and the relationship between pore water pressure and axial strain during the shearing stage.

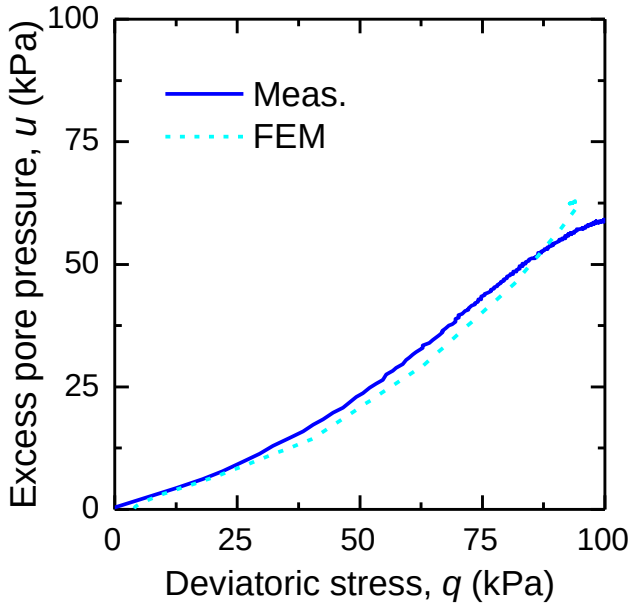

Fig. 4.4. Deviatoric stress versus excess pore pressure during axial compression stage of CU triaxial test.

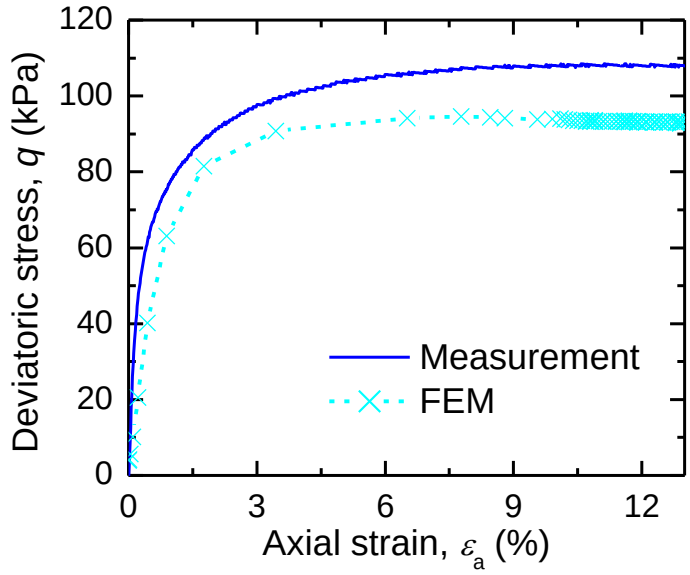

Fig. 4.5. Deviatoric stress versus axial strain during shearing stage of CU triaxial test.

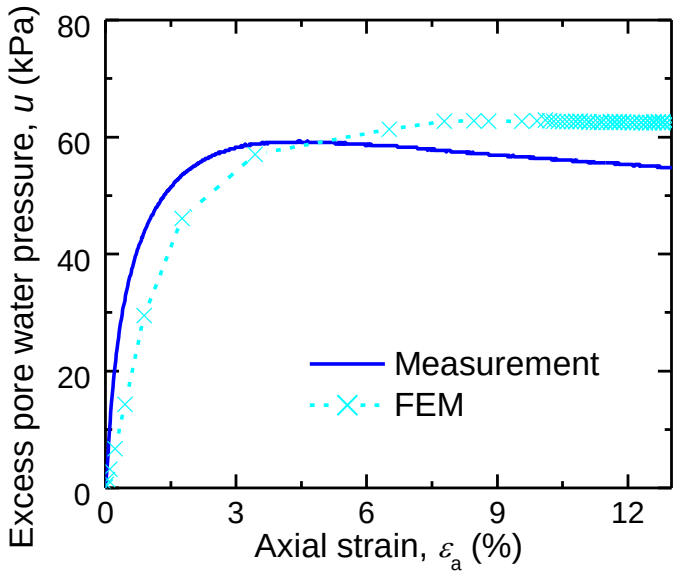

Fig. 4.6. Excess pore water pressure versus axial strain during axial compression stage of CU triaxial test.

In general, the tendencies of the measured results of stresses, strain, and pore water pressure were simulated well with the Soft Soil Creep model and the input parameters obtained from laboratory soil tests.

4.2.3 FEM simulation of oedometer test

The oedometer test was also simulated to validate the above-mentioned soil model and the soil parameters for long-term behavior (secondary compression) of the soil. Fig. 4.5 shows the simulation results. The laboratory test results are also shown in the figure for comparison purposes. It is noticed that the pressure applied in the oedometer test was increased by multiple steps as mentioned in Section 3.2.2.2. The results in Fig. 4.7 are of the last load step, of which the applied pressure was kept for a long time to observe creep settlement. The input parameters for the simulation of the oedometer test were obtained from the oedometer test at the corresponding load step as shown in the figure.

Fig. 4.7 shows that the simulation results had a similar trend to the measured results. The simulation settlement at the early stage was slightly higher than the measured one, however, at the later stage, the simulation result fits with the measured time-settlement curve.

The conclusion from the simulations is that the behavior of the soil used in the experiments is simulated well with the Soft Soil Creep model, of which most of the input parameters were obtained from the laboratory soil tests. Therefore, in the next step of this

study, the simulations of load tests on model foundations will be carried out, using the same soil model and input parameters.

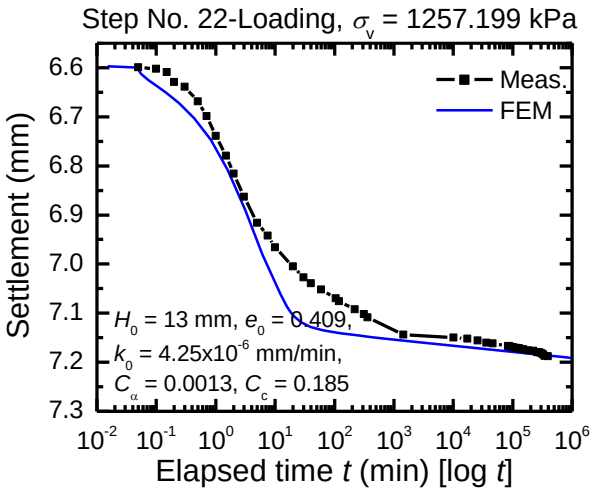

(a) Settlement versus elapsed log time

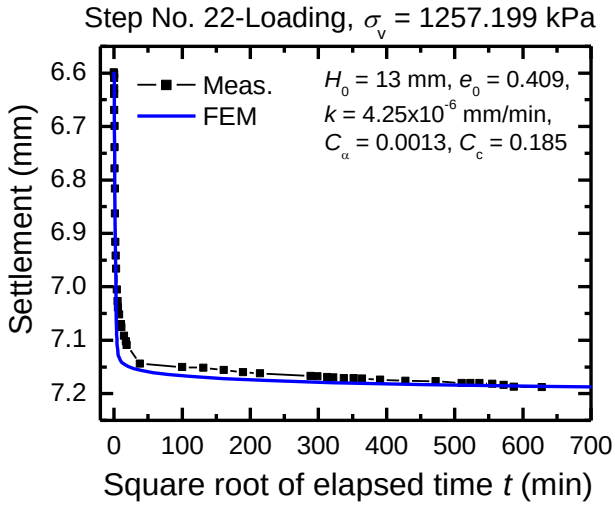

(b) Settlement versus elapsed square root time

Fig. 4.7. Change of settlement with time at final load step of oedometer test.

4.3. FEM simulation of load tests on model foundations

4.3.1 Modeling of raft and pile

The raft was modeled by a linear elastic materials, and the properties of the raft are shown in Table 4.2.

To model the piles, volume elements with a linear elastic material was used. In this study, a hybrid model in which beam elements surrounded by solid volume elements was

employed, according to Kimura and Zhang (2000). A big advantage of the hybrid pile is to easily obtain axial forces, bending moments, and shear forces along pile from those in the beam elements by considering stiffness ratios of the hybrid pile over the beam. Fig. 4.8 shows the mechanism of the hybrid model. In the hybrid model of this research, the beam element carried a large proportion (90%) of the bending stiffness *EI* and axial stiffness *EA* of the pile. Therefore, the stiffness of the surrounding volume elements is reduced to 10% of the actual value. However, it is noticed that the reduced stiffness of the surrounding elements of the hybrid pile is still much higher than that of the surrounding soil. In such a condition, Kimura and Zhang (2000) showed the validity of the hybrid pile by comparison with experimental results. A verification study on the validity of the hybrid pile model was again conducted by Vu (2017). The properties of the beam and the solid pile are summarized in Table 4.2.

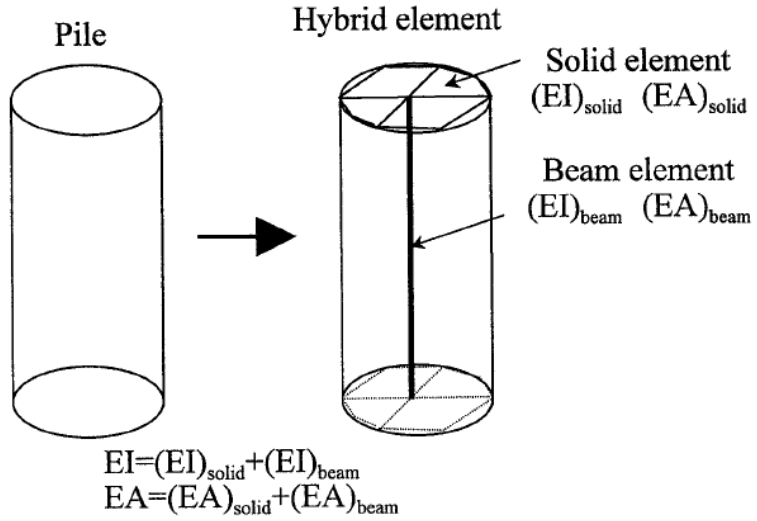

Fig. 4.8. Mechanism of the hybrid model (after Kimura and Zhang, 2000).

Table 4.2. Properties of the elastic elements

Description	Beam	Solid pile	Raft
Material model		linear elastic	linear elastic
Unit weight, γ (N/mm^3)	10.52×10^{-6}	1.169×10^{-6}	78.8×10^{-6}
Young's modulus, E (N/mm^2)	2628	292	200×10^{3}
Poisson's ratio, ν	-	0.406	0.3

Interface elements were assigned at the raft base, on the pile shafts and pile tips (Fig. 4.9). The material properties of the interface were estimated from the properties of adjacent

soil (K50S50). The strength properties of the interface (cohesion c_{int} and friction angle ϕ_{int}) were set by assigning a value for the strength reduction factor R_{inter}. To roughly estimate the value of R_{inter}, a series of simple tests were conducted, of which the pile or raft was allowed to slip on the dry K50S50 surface (for the details, see in Appendix A). Based on the results of the tests, in the following calculations, a value of R_{inter} = 0.9 is assigned for the pile-soil interface. To avoid the errors occurring at the corner points of the pile tip (singular points), the interface elements between pile and soil were extended in both horizontal and vertical directions. Fig. 4.9 shows the interface elements between raft-soil and pile-soil.

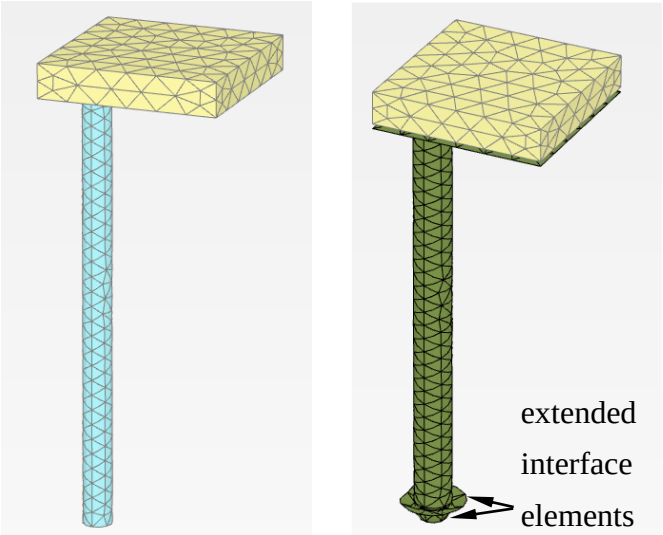

(a) Non-activate (b) Activate

Fig. 4.9. Interface elements between raft base – soil and pile-soil.

4.3.2 Mesh and boundary conditions

The numerical simulations were performed using PlAXIS 3D (Brinkgreve and Broere, 2018). The dimensions of the numerical models are the same as the physical modeling. Fig. 4.10 shows the dimensions of the numerical simulation, in which only 1/4 of the physical model was modeled due to axisymmetric conditions.

Two types of boundary conditions are assigned to boundary surfaces of this model: displacement boundary and flow boundary conditions.

For the prescribed boundary displacements, horizontal displacements on the symmetrical surfaces and the lateral surface of the ground were fixed. And, vertical displacements on the bottom surface of the ground were fixed.

For the flow boundary conditions, due to the axisymmetric conditions, the impermeable condition was set on the axisymmetrical planes. Impermeable conditions were also set on the lateral surface and the bottom surface of the ground according to the experimental conditions.

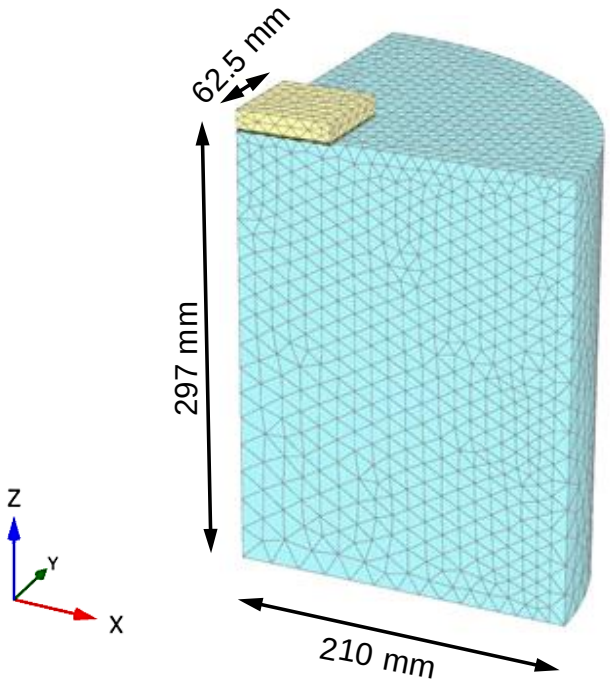

Fig. 4.10. FEM mesh and boundary conditions.

4.3.3 Constitutive model and soil parameters

As mentioned earlier, the Soft Soil Creep (SSC) model will be used to model soil behavior in the simulations of piled raft behavior. The soil parameters estimated directly from the laboratory element tests and the numerical simulations of the CU triaxial test and the oedometer test are used. The detailed soil parameters for SSC are presented in Table 4.1.

4.3.4 Simulation of pile installation effect

4.3.4.1 Effect of pile jacking process on pile resistance and ground stresses

It is widely known that the pile installation process makes a difference in bearing capacity between pre-embedded piles and jacked piles.

When a pile is jacked into the ground, the soil will be displaced outwards from the pile. Fu and Xiaoyu (2011) state that the soil within a radial distance of 2 times pile diameters from the pile shaft is completely remodeled, and heaving may occur in the upper part of the

ground. A plastic zone is developed around the pile where the mobilized shear stress exceeds the undrained shear strength of the soil. The excess pore water pressures are generated during the pile installation process, primarily due to the increase in total stress as the soil is compressed outwards by the pile. The magnitude of the pore pressures induced by the installation process decreases rapidly with distance from the pile shaft, and becomes negligible at a distance of 5-10 pile diameters (Dong, 2000). Consequently, the consolidation process occurs as the pore water pressure dissipates, soil particles will move inwards towards the pile shaft and most of the soil will be unloading in shear. At the zone near the pile shaft, the shear strength of the soil recovers to an even higher value in magnitude than the initial value before piling (which is termed "side shear setup"). The consolidated soft clay remains tightly adhered to the pile shaft. In general, the installation process changes the effective stresses and density of the soil surrounding the pile, hence modifies the strength and stiffness of the soil and, consequently changes the pile resistance.

4.3.4.2 Previous simulations on effect of jacking process with PLAXIS software

The installation effect of a single jacked pile was simulated with the PLAXIS program by several ways in previous researches. The following are a summary of methods used to simulate the effect of pile installation.

Prescribing volume expansion method: This method was introduced by Broere and van Tol (2006), where the installation effect of a single pile on sand ground is taken into account by applying a certain amount of volumetric strains on the soil volume elements which present pile volume. The sand behavior was modeled by Hardening soil model or Morh-Coloumb model. They noticed from the study that the interface element between the soil and the pile has a strong influence on the pile capacity and may lead to numerical inaccuracies. To avoid this pitfall, it is possible to first perform the expansion of the volume elements, which will later present the pile, and the interface elements are activated after the volume expansion stage. The value of initial pile expansion yet affected the resistance of the pile. They pointed out from several trial simulations that the case of a volumetric strain of 50% achieved a pile capacity close to the load capacity observed in the centrifuge test. About the load distribution along pile, the shaft friction was invariably too high, and the base resistance was still too low. This is caused by the high prestressing around the shaft as compared with the amount of prestressing near the pile tip. This result was studied and confirmed again by Nguyen (2017)

Prescribing horizontal displacement method: This method was introduced by Broere and van Tol (2006). In their analyses, the installation effect was considered by applying prescribed displacements at the pile-soil boundary. The horizontal prescribed displacement is applied at the pile shaft while the vertical prescribed displacement is applied at the pile tip. Broere and van Tol (2006) showed that in this way, the bearing capacity of the pile found from the FEM fits relatively well with the experimental results. The base resistance is influenced mainly by the amount of vertical prestressing and the shaft friction by the horizontal prestressing. The sensitivity of the total load capacity to variations in horizontal prestressing is far higher than to variation in vertical prestressing. Pham (2009) used this method again to model the installation effect of a driven pile with the Hypoplasticity soil model. Some special treatment was applied for pile tip corner points to get more compatible results. Nguyen (2017) simulated the pile load test in sand with this method again and pointed out that the shaft resistance is very sensitive with the horizontal prescribed displacement, while the tip resistance was influenced slightly or even reduced. One of the limitations of this technique is the magnitude of the applied vertical displacement to avoid severe distortion under the pile tip.

Adaption for material properties along the pile shaft and under the pile tip: This method was indicated by Nguyen (2017) for a single pile installed in sand. To model the pile load test of a displacement pile with a pre-embedded pile, stiffness and strength parameters such as Young's modulus, friction angle, and dilation angle of the soil zones surrounding the piles were modified (Fig. 4.11.). Park, Park, and Lee (2016) also used a similar technique when analyzing load response and load sharing behavior of piled rafts installed with driven piles in sands. In the research, the influence of the installation process of the driven piles in sands was simulated by increasing relative density and lateral stress of the soil influence zone around piles (Fig. 4.12.).

Press-replace method (PRM): This method was first introduced by Andersen et al. (2004) for modeling the set-up of suction anchors.

Fig. 4.13 shows the procedure of PRM. In PRM, the initial finite element mesh is preserved while the pile material at the corresponding pile volume will be updated at the beginning of each pile pressed-in stage (pile installation period). The technique was successfully used by Engin (2013) for undrained cone penetration test and refined for the installation of piles in sand. The method was validated by Tehrani et al. (2016) to compare the efficient simulation of the installation of jacked piles between PRM and the material

point method. Recently, the method was used by Tan et al. (2019) for considering the effects of interface roughness on the mobilized shear strength and radial stresses.

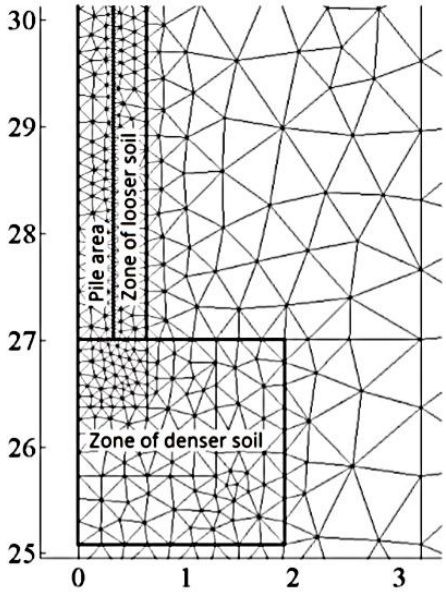

Fig. 4.11. Simulation of pile installation effect by adapting material properties. (Nguyen 2017).

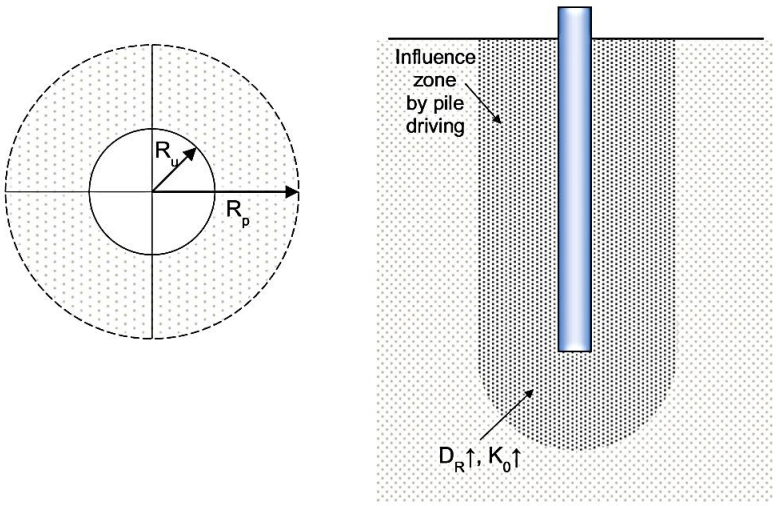

Fig. 4.12. Influence soil zone by pile driving: (a) cavity expansion model and (b) soil condition in within influence zone. (Park, Park and Lee, 2016).

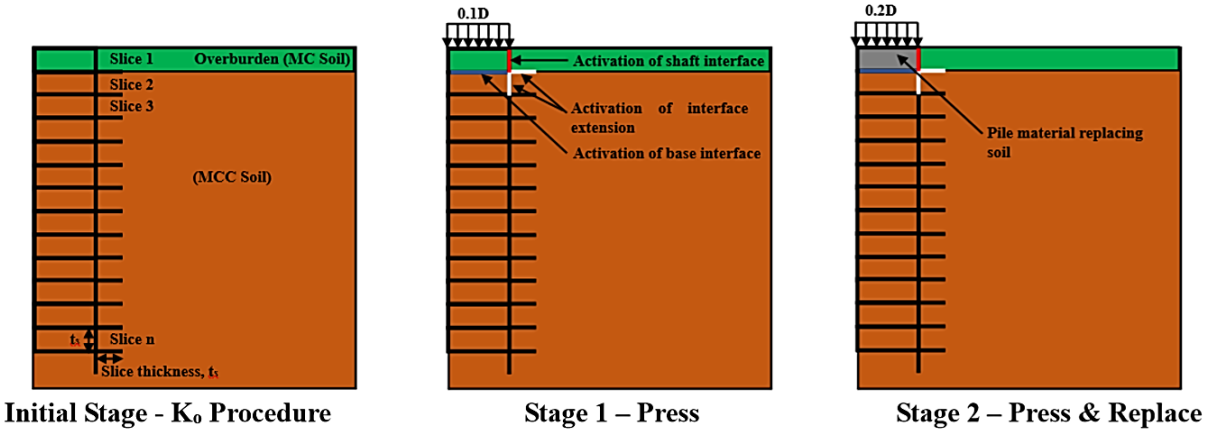

Fig. 4.13. Press-Replace procedure. (Tan et al. 2019).

4.3.4.3 Selection of an appropriate method for simulation of jacking process in this study

From the literature review, each method has its advantages and disadvantages, and most of the previous researches studied with sand ground.

The PRM method reasonably simulated the jacking process of a pile in sandy, and more recently, was used to predict the behavior of soil subjected to undrained pile installation as mentioned above. However, it is seen from the method that, the pile needs to be divided into multiple thin slices and pressed into the ground by multiple steps (the installation process of a pile with 150 mm long and 10 mm diameter could be imposed in 150 calculation steps, if the slice thickness t_s and the prescribed displacement u_z of each step are kept at 0.1D, following Tan et al. (2019)). If this method was applied for the cases of piled raft foundation, of which a large number of piles can be used, and the long-term load test including consolidation periods is applied by multiple-steps, significant work will be required.

For the method of adaption material properties along the pile shaft and under the pile tip, it is difficult to use this method when a pile is jacked into saturated clay with consideration of consolidation processes because (i) it is difficult to know the properties of the soil after jacking process, (ii) soil properties will change with time and distance from the pile shaft because the consolidation processes occur after the jacking process, and (iii) effect of the overlapping zone when more than one pile is installed.

The volume expansion method is simple. This method could give reasonable load capacity if a suitable value of volume strain is applied. However, the problem of this method is that the stress acting on the pile shaft is high, but that on the pile tip is low.

Prescribed displacement is also a simple method. This method could give reasonable load capacity by suitably combining both the horizontal and vertical displacements. One of

the limitations of this technique is the magnitude of the applied vertical displacement to avoid severe distortion under the pile tip.

From the literature review, simulation of the installation process of pile(s) is still a complicated topic and needs significant work. Most of the studies generally studied on a single pile in the sand and there is no rule/ equation to define the value of strain/ displacement/ modification soil parameter to simulate the installation process. However, the main aim of this study is not the perfect simulation for the installation process. The main purpose of this study is to investigate the time-dependent tendencies of settlement and load distribution between raft and piles and load distribution between piles. Therefore, in this study, the simple technique of volume expansion will be first employed. It is also interesting to validate the performance of this method when a pile is jacked in saturated clay.

To select an appropriate value of volume strain which will be applied to calculate the behavior of piled raft foundations, several trial simulations of single piles with different magnitudes of volume strains were conducted. The calculated results of single piles were compared with the measured results. The value of volume strain which gives good agreement with the measured result will be selected to simulate the behavior of pile groups and long-term behavior of piled raft foundation. The simulations of single piles with different values of volume strain are shown in Appendix B. In the following calculations, the lateral strains of pile volumes applied for the calculations of the four foundation models (4P-6*D*, 4P-3*D*, 9P-3*D*, and 16P-3*D*) are $\varepsilon_{xx} = \varepsilon_{yy} = 12.5$ %. Note that vertical strain ε_{zz} was set to be 0, which means that pile installation was modeled by pure cylindrical cavity expansion.

4.3.5 Cases and calculation phases

Cases: In this study, the 4 model piled raft foundations are analyzes including 4P-6*D*, 4P-3*D*, 9P-3*D*, and 16P-3*D*. As mentioned in Section 4.3.2, only 1/4 of each model foundation and the ground will be modeled, owing to symmetric conditions, to reduce the calculation time (Fig. 4.14). In the case of 9P-3*D* (Fig. 4.14(c)), 1/4 volume of center pile and 1/2 volume of edge piles are modeled, and the input strength parameters for the beam elements (cross-sectional areas of the beams) of the center pile and edge piles were also reduced proportionally.

Calculation phases: The analysis procedure is as same as the experiment procedure. The calculation procedure for each foundation is as follows:

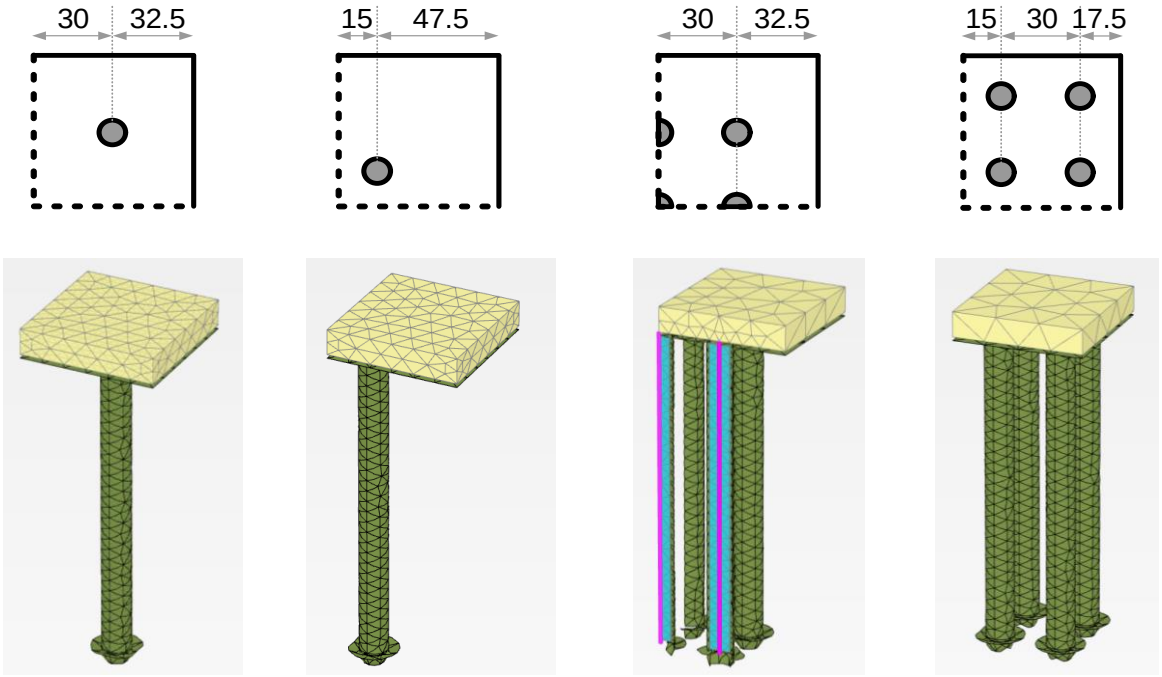

(a) 4P-6*D* (b) 4P-3*D* (c) 9P-3*D* (d) 16P-3*D*

Fig. 4.14. Model piled raft foundations.

Step 1: Self-weight analysis of the model ground: Initial material of the whole calculation domain is soil. The vertical soil stress is calculated from the self-weight with the groundwater table set at the ground surface level. The horizontal soil stress is generated by K_0-procedure. The pre-consolidation pressure was taken into account by the pre-overburden pressure *POP* value.

Step 2: Set the piles in the ground: The pile is located by changing the material properties of the soil at the pile location from soil to pile. The interface elements between at the pile shaft and pile tip, and soil are set (activated).

Step 3: Apply volume expansion to simulate the effect of pile installation on the ground stresses: The volume strains in horizontal directions are applied to elements presenting pile volume.

Step 4: Consolidation analysis of the model ground with piles after volume expansion stage: One day was set for the consolidation stage after completion of the volume expansion stage, according to the experimental procedure.

Step 5: Apply static load test on piles (pile group): Downward prescribed displacements are applied at the heads of all piles at the same time.

Step 6: Unload the applied load on piles: The downward prescribed displacement in step 5 is released (deactivated).

Step 7: Consolidation analysis of the model ground with piles after applying static load: Four hours are set for the consolidation stage after unloading the static load test on the pile group, according to the experiment procedure (step 6).

Step 8: Set raft: The raft is set on the piles (the cluster at the raft location is activated).

Step 9: Apply the first load step on piled raft foundation in consolidation condition: Uniform pressure is applied (activated) on the raft surface, and consolidation analysis is set for this phase.

Step 10: Consolidation for long-term observation of the first load step: Pressure on the raft surface is maintained during consolidation time.

Steps 9 and 10 are repeated for further load steps, increasing pressure on the raft according to the experimental conditions.

It is noticed that the time sequence used in the analyses followed the experimental time sequence. For the experimental time sequence, refer to the section of the test procedure in Chapter 3.

4.3.6 FEM results of load tests on pile foundations

4.3.6.1 Simulation results of pile group

Fig. 4.15 shows the measured and calculated load-settlement relationships during static load tests of the 4 pile groups ((a) 4P-6*D*; (b) 4P-3*D*; (c) 9P-3*D*; (d) 16P-3*D*). It is seen from the figure that the trends of measured load-settlement curves are simulated reasonably.

Considering the tendency of initial stiffness first, Fig. 4.15 shows that the calculated results are in good agreement with the measured results. Both the measured and simulated results show that the pile group resistance almost reaches the peak at a settlement of 1.2 mm for the case of 4P-6*D*; around 1.6 mm for the case of 4P-3*D*; around 2.3 mm for the case of 9P-3*D*; and around 3.3 mm for the case of 16P-3*D*.

Regarding the ultimate bearing capacity of the pile group, Fig. 4.15(a) shows that the calculated result for the case of 4P-6*D* is larger than the measured one. For the results of 3 pile groups with the same pile spacing of 3*D* (Fig. 4.15(b), (c), and (d)), the measured result of 4P-3*D* is simulated well, however, for the cases of 9P-3*D* and 16P-3*D*, the FEM results show that when the pile number increases, the calculated results become smaller than the corresponding measured ones.

The detail values of pile group ultimate capacity and pile ultimate capacity are presented in Table 4.3. It is seen from the Table that the calculated average pile resistance decreases with increasing pile number. Comparing the calculated results between 4P-6*D* and 4P-3*D*,

the pile resistance in pile group with narrower pile spacing (3*D*) is smaller than that in the pile group with larger pile spacing (6*D*). In general, although there are differences in magnitudes between the measured and simulated results, the simulated trend is reasonable.

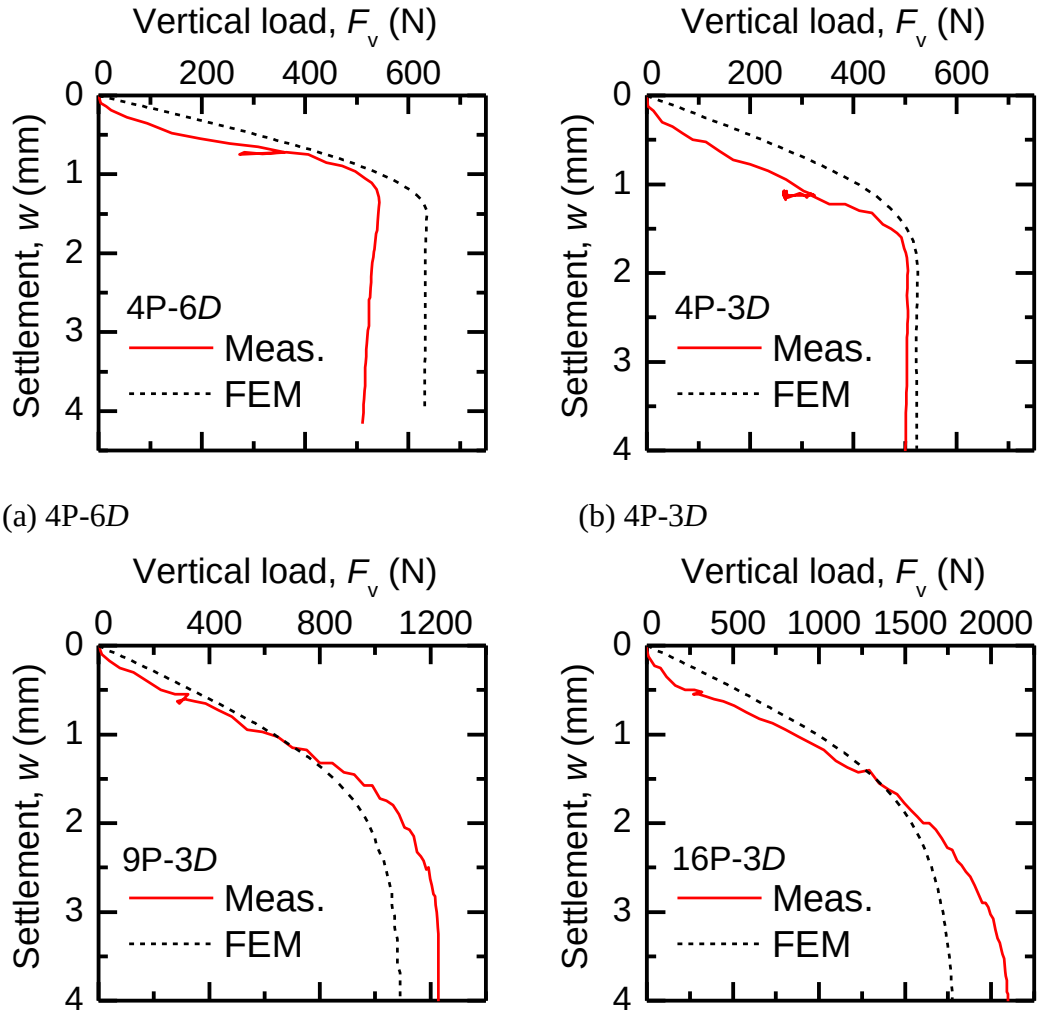

(a) 4P-6*D* (b) 4P-3*D*

(c) 9P-3*D* (d) 16P-3*D*

Fig. 4.15. Measured and calculated results during static load test of pile groups.

Table 4.3. Experimental and numerical results of pile capacity and pile group capacity in SLTPG.

Description		Foundation cases			
		4P-6*D*	4P-3*D*	9P-3*D*	16P-3*D*
Pile group ultimate capacity $P_{ult,\,PG}$ (N)	Measured	516	503	1225	2100
	FEM	608	525	1090	1772
Average load per pile in SLTPG $P_{P,aver.,\,SLTPG}$ (N) ($P_{ult,\,PG}$/ pile number)	Measured	129	126	136	131
	FEM	152	131	121	111

4.3.6.2 Simulation results of piled raft

a. Time-settlement and time-pore water pressure relationships

Fig. 4.16 shows the FEM results of the change of foundation settlements and the change of PWPs with the elapsed time of the four piled raft foundations. In the figure, the periods when the applied load is increasing and the periods when the applied load is kept constant are shown by solid lines and line-symbol lines, respectively.

Fig. 4.17(a)-(d) compare the changes of calculated and measured settlements with elapsed time of the four foundations. Fig. 4.18(a)-(d) compare the changes of calculated and measured pore water pressure with time at the raft base center of the four foundations.

Firstly, we consider the simulation results of 4P-6*D* and 4P-3*D* shown on Fig. 4.16(a)-(b) and Fig. 4.17(a)-(b). Fig. 4.16(a)-(b) shows that the foundation settlements occur significantly during the load-increasing period, the settlements then continue increasing noticeably in the early stage of the consolidation period (primary consolidation) and increasing slightly in the later stage of the consolidation period (secondary consolidation). In general, the trends of the measured settlements are simulated well. In terms of magnitude, Fig. 4.17(a)-(b) show that the simulated settlements of both the foundations are smaller than the measured ones. However, if considering the increment of the settlements, the differences between the measured results and the calculated results mainly happen in the first load step. The increments of foundation settlements in other load steps are simulated reasonably.

Comparing the trend of calculated settlements between 4P-6*D* and 4P-3*D*, the calculated settlement of 4P-6*D* is smaller than that of 4P-3*D* in the first and second load steps, this trend is similar to the measured results. In the third load step, the calculated settlements of the two foundations are almost equal, however, the measured results show that the 4P-6*D* settlement was noticeably larger than that of 4P-3*D*.

The load-settlement curves of 9P-3*D* and 16P-3*D* are shown in Fig. 4.16(c)-(d) and Fig. 4.17(c)-(d). For both the cases, the simulations are successful until the 4th load step. When the applied load of the 5th load step is increasing, the failure occurs in the simulations. The settlements of both 9P-3*D* and 16P-3*D* are simulated well in the first two load steps in terms of both tendency and magnitude. From the third load step, the calculated results of 9P-3*D* are slightly smaller than the measured results, meanwhile, the opposite trend is seen in the case of 16P-3*D*.

Comparing the calculated settlements between 4P-3*D*, 9P-3*D*, and 16P-3*D* (foundations with the same pile spacing), at the same magnitude of the applied load, the settlement is reduced with increasing pile number.

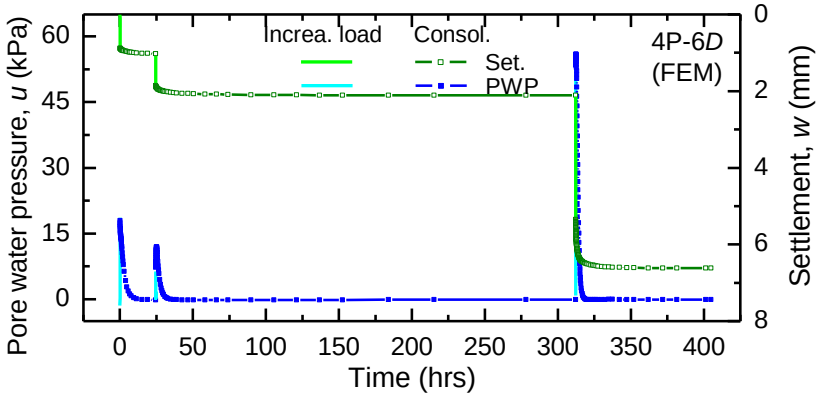

(a) 4P-6*D*

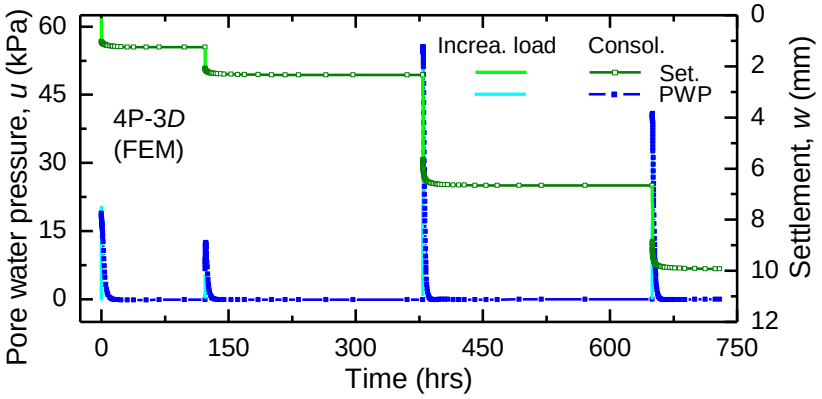

(b) 4P-3*D*

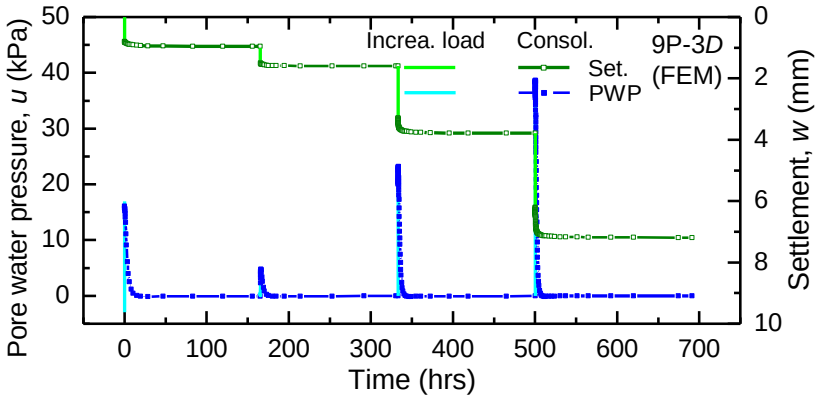

(c) 9P-3*D*

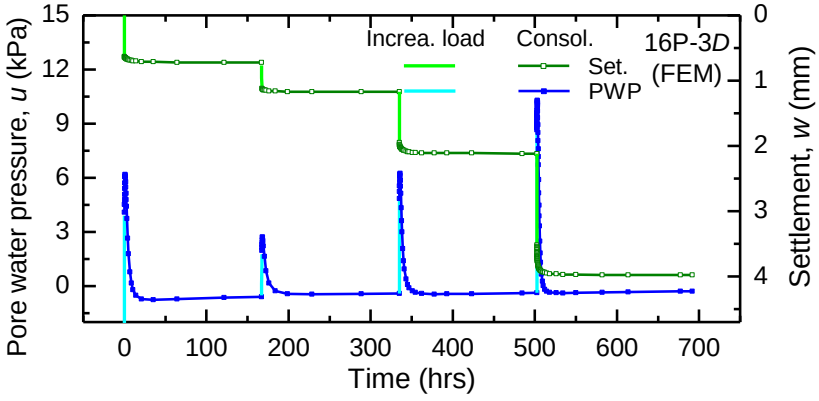

(d) 16P-3*D*

Fig. 4.16. Calculated results of time-dependent settlements and pore water pressures.

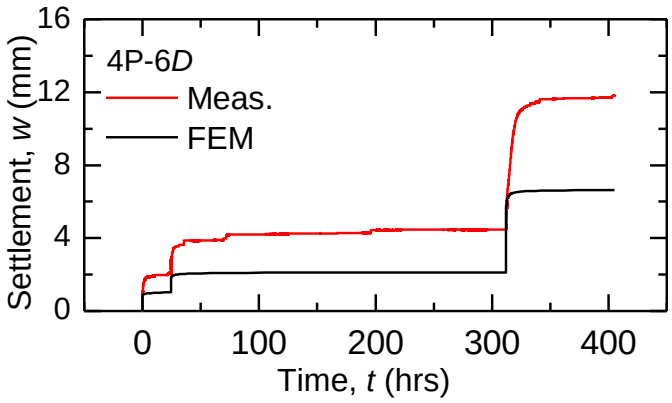

(a) 4P-6*D*

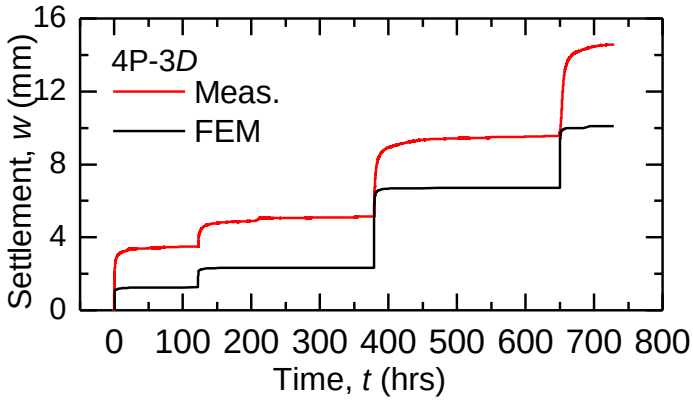

(b) 4P-3*D*

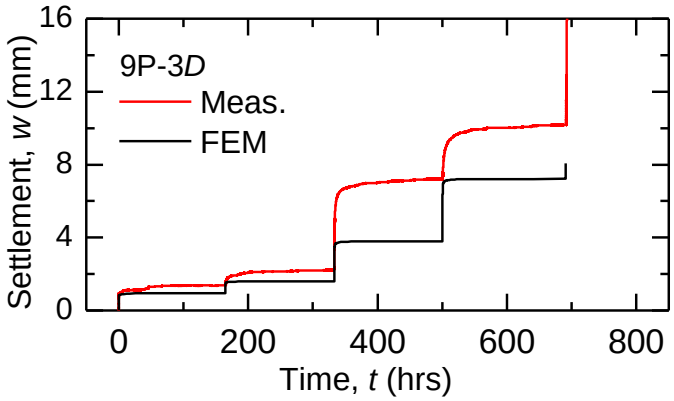

(c) 9P-3*D*

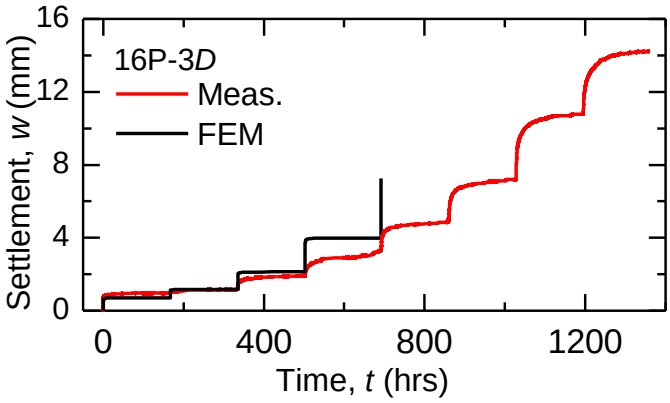

(d) 16P-3*D*

Fig. 4.17. Calculated and measured results of time-dependent settlements.

Let us consider the changes of calculated pore water pressures with the elapsed time, Fig. 4.16 shows that the PWPs start to increase with increasing settlement when the applied load is increasing. After reaching the target value, the applied load is kept constant; interestingly, both the measured and calculated results indicate that the PWP continued to increase in short duration to reach a temporary peak (except for the first load steps of which the calculated PWPs reach the peak when the applied load just reaches its target value). After reaching the peak, the PWPs dissipate with time and return to the steady-state. This phenomenon is similar to the measured trend. Fig. 4.18 compares the measured results and simulated results. It is noted again that, the function of the PWP cell in the case of 16P-3*D* did not work well. Fig. 4.18 shows that as the applied load is larger, the calculated PWP dissipation rate becomes faster than the measured one. This may be caused by the change of permeability with the applied pressure in the experiment; and the adjustment in the input of permeability k and the change of permeability c_k for clay could give more suitable results. In general, the trends of measured results are simulated reasonably.

Next, we consider the change of PWP and settlement of the four foundations with the elapsed time during the primary consolidation periods. Fig. 4.19(a) shows how the PWP and settlement of 4P-6*D* changed over the entire experimental duration, in which the highlighted areas can be regarded as the primary consolidation period. Figs. 4.19(b)–4.19(d) are magnified views of the primary consolidation periods of 3 load steps. Figs. 4.20–4.22 show the corresponding results for 4P-3*D*; 9P-3*D*; and 16P-3*D*, respectively.

We begin by considering the results for 4P-6*D* in Fig. 4.19. During the primary consolidation periods of the first and third load steps, Figs. 4.19(b) and 4.19(d) show that the settlement rates are basically proportional to the PWP dissipation rates. For the second load step, the settlement rate is lower than the PWP dissipation (Fig. 4.19(c)). It is noted that the calculated PWP of the second load step is smaller than the calculated PWP of the first load step, meanwhile, the measured results show the opposite trend; this phenomenon will be explained by load transferred to the piles in the next section. Comparing to the measurement, the calculated settlement rates are lower than the measured ones in the first and second load steps but higher than the measured rate in the third load step. However, the important point in common between the calculated results and the measured results is that notable amounts of settlement occurred in these primary consolidation periods; and after the PWPs at the raft base center dissipate totally, the increments of both calculated and measured PRF settlements become much slower and smaller.

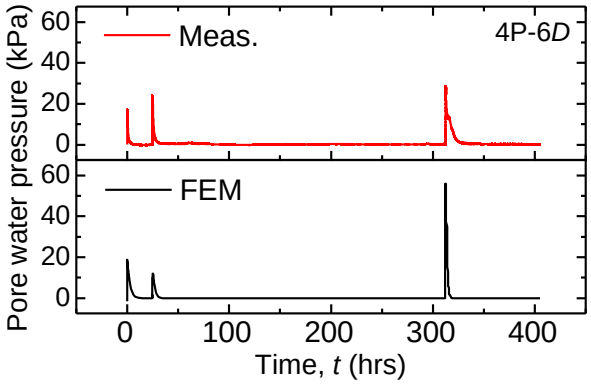

(a) 4P-6*D*

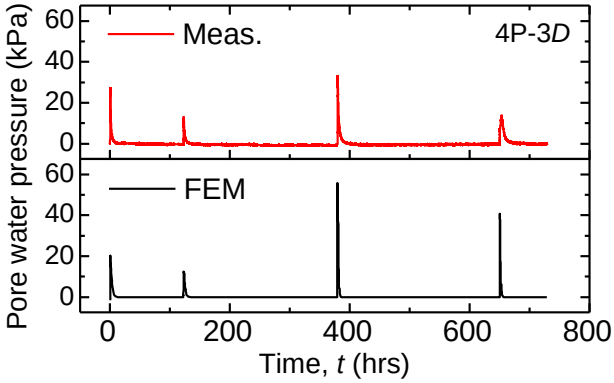

(b) 4P-3*D*

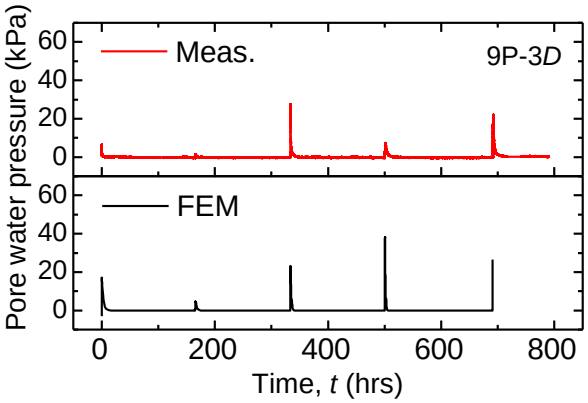

(c) 9P-3*D*

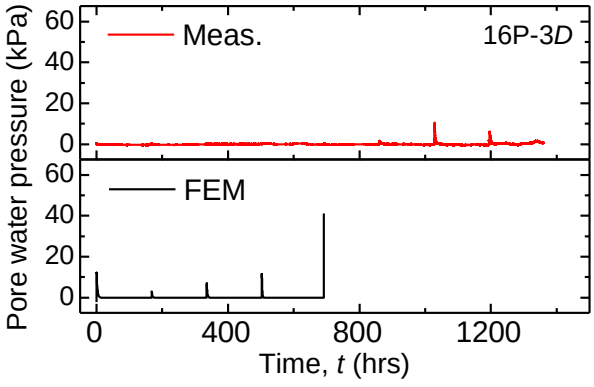

(d) 16P-3*D*

Fig. 4.18. Calculated and measured results of time-dependent excess pore water pressure.

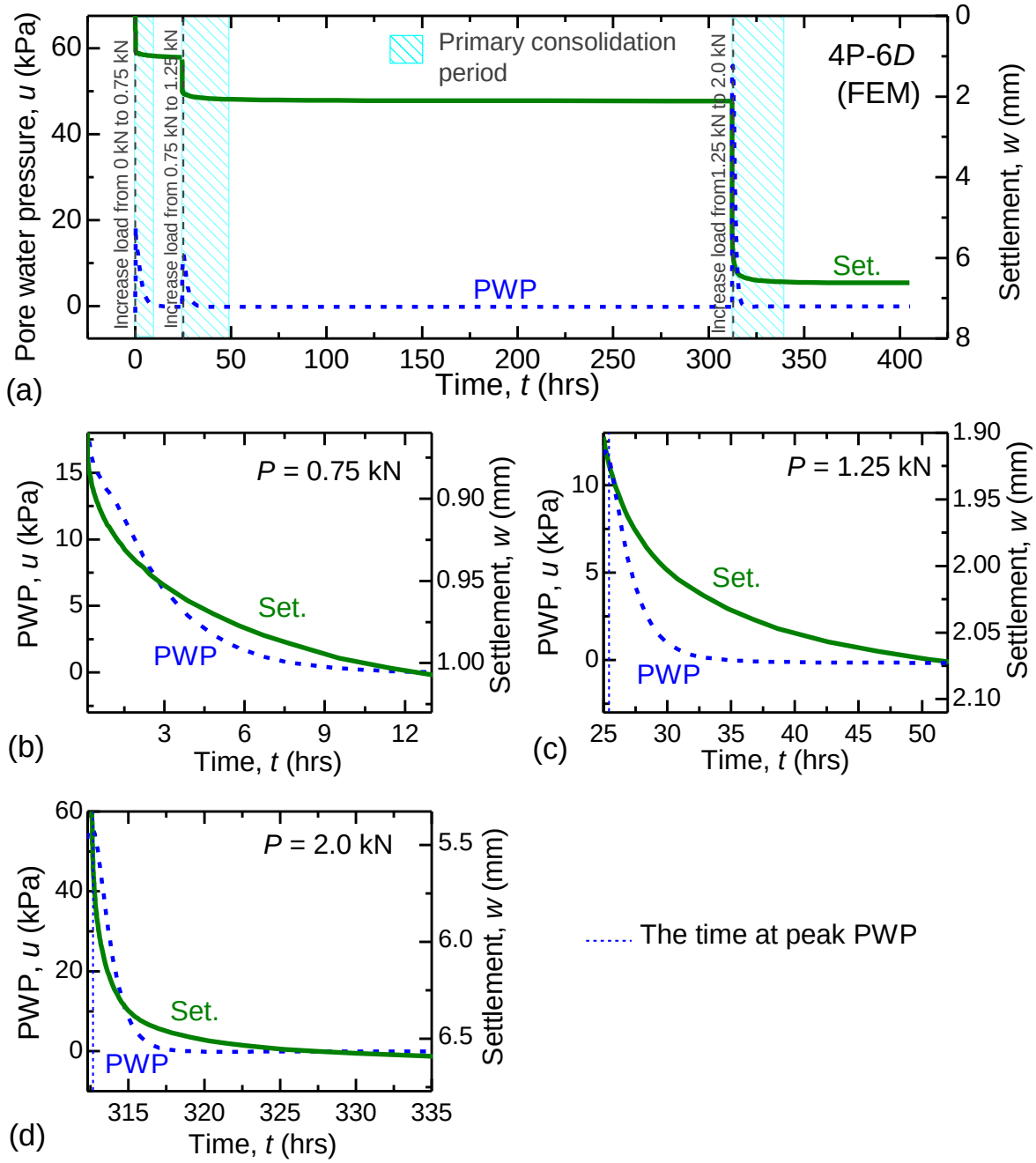

Fig. 4.19. FEM results of changes of pore water pressure (PWP) and settlement with time of 4P-6*D*: (a) all load steps; zoom-in of primary consolidation period of (b) first load step; (c) second load step; (d) third load step.

As for the results of 4P-3*D*, 9P-3*D*, and 16P-3*D*, Figs. 4.20– 4.22 show that during the primary consolidation periods of all four load steps, the PRF settlement rate was basically proportional to the PWP dissipation rate at the raft base. It is suggested from both the measured and calculated results that for the PRF configurations in this study, the settlement rate could be roughly obtained if we know the PWP dissipation rate at the raft base center.

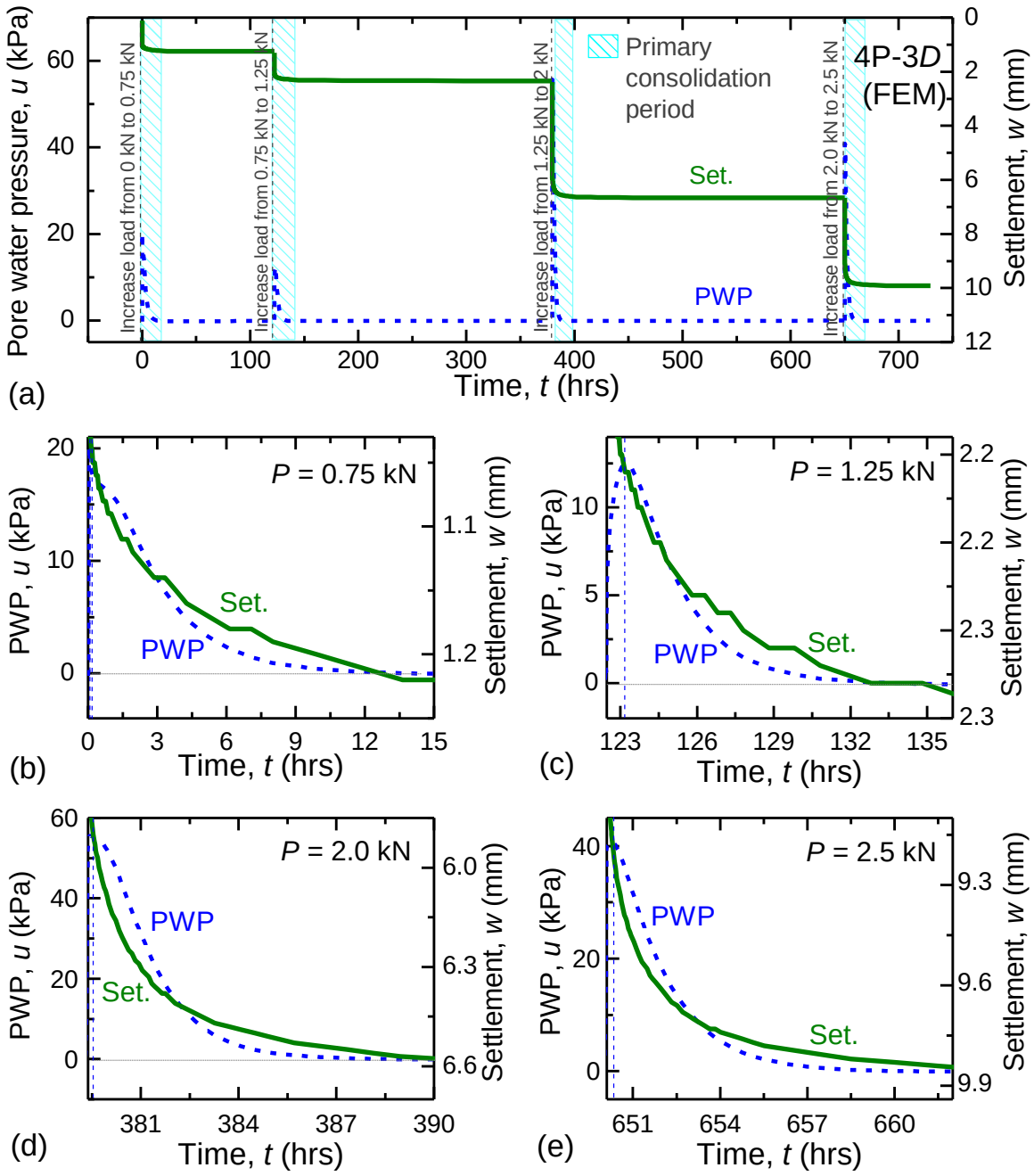

Fig. 4.20. FEM results of changes of pore water pressure (PWP) and settlement with time of 4P-3*D*: (a) all load steps; zoom-in of primary consolidation period of (b) first load step; (c) second load step; (d) third load step; (e) fourth load step.

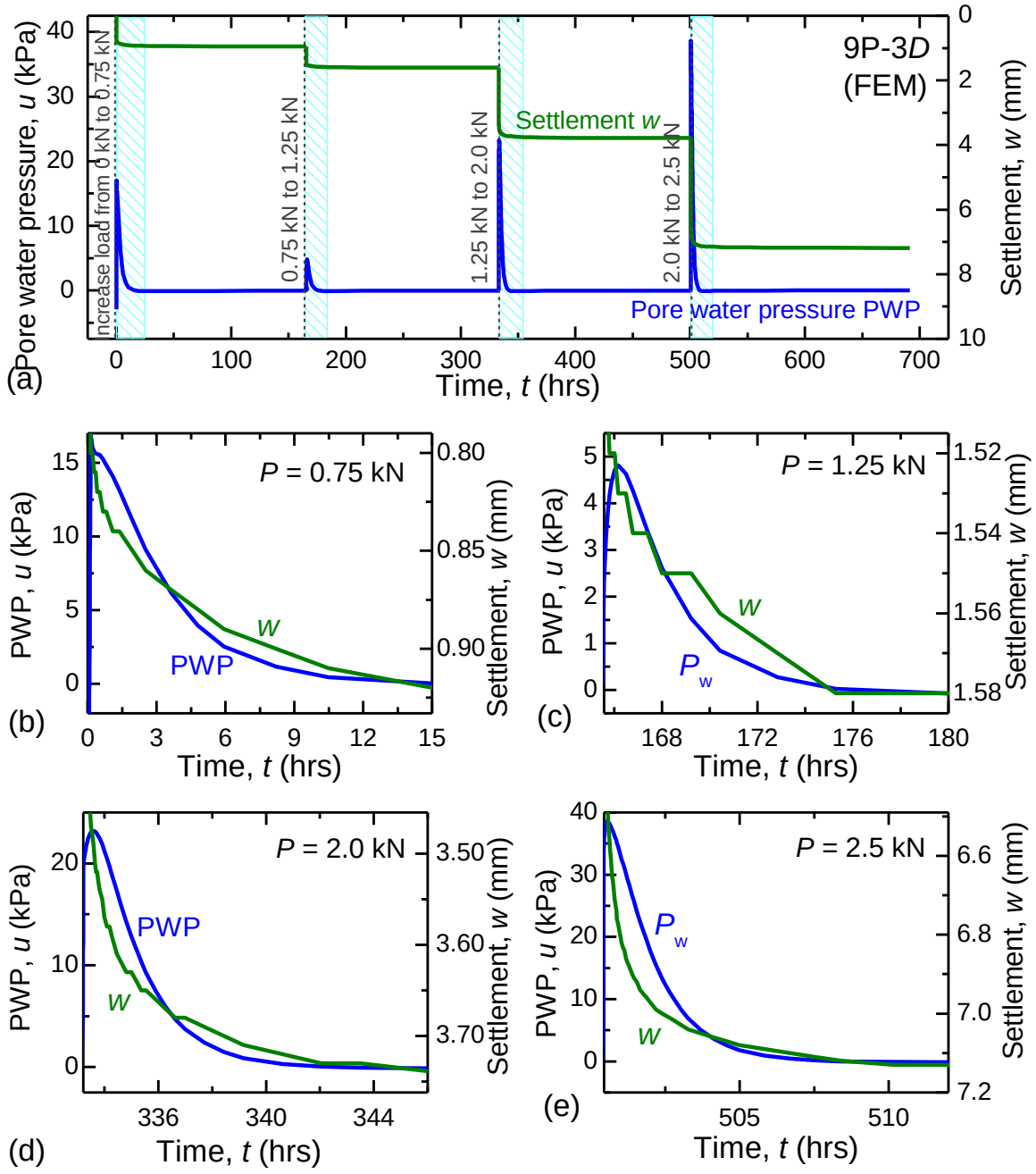

Fig. 4.21. FEM results of changes of pore water pressure (PWP) and settlement with time of 9P-3*D*: (a) all load steps; zoom-in of primary consolidation period of (b) first load step; (c) second load step; (d) third load step; (e) fourth load step.

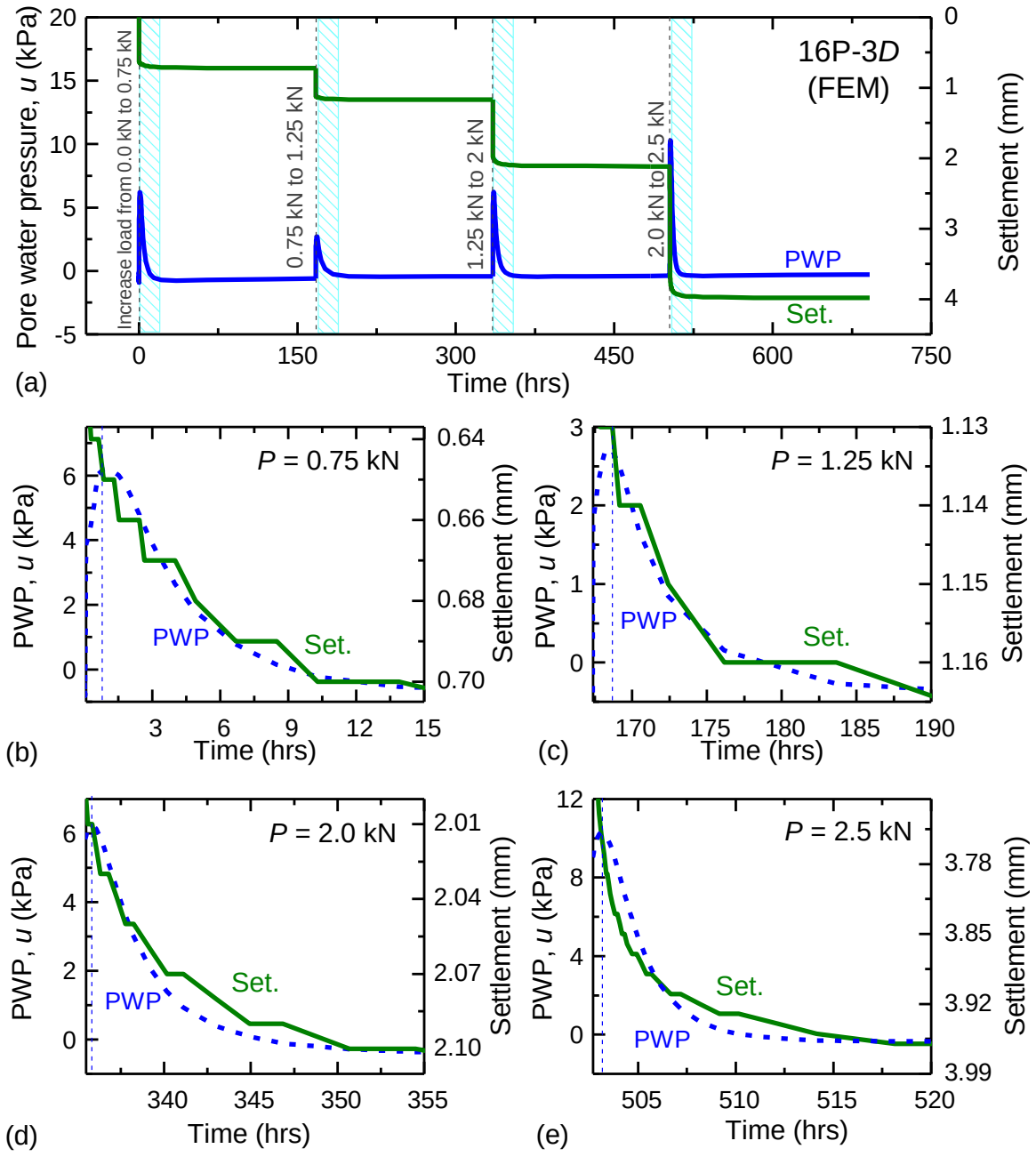

Fig. 4.22. FEM results of changes of pore water pressure (PWP) and settlement with time of 16P-3*D*: (a) all load steps; zoom-in of primary consolidation period of (b) first load step; (c) second load step; (d) third load step; (e) fourth load step.

b. Change of pile head load with time

How the pile load of each PRF changed with time is shown in Fig. 4.23(a) for 4P-6*D*; Fig. 4.23(b) for 4P-3*D*; Fig. 4.23(c) for 9P-3*D*; and Fig.4.23(d) for 16P-3*D*. It is noticed in each figure that the magnified view of the early stage of the load-increasing period of the last load step is shown.

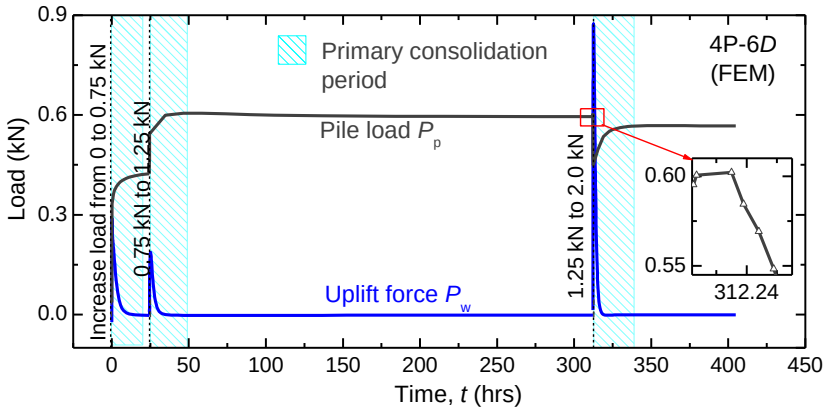

(a) 4P-6*D*

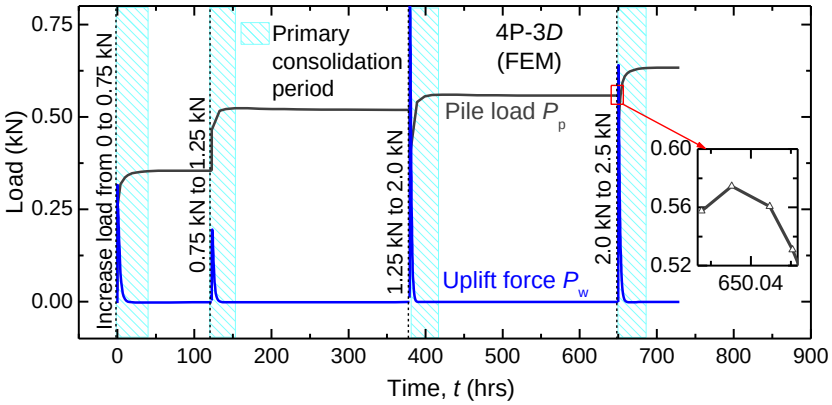

(b) 4P-3*D*

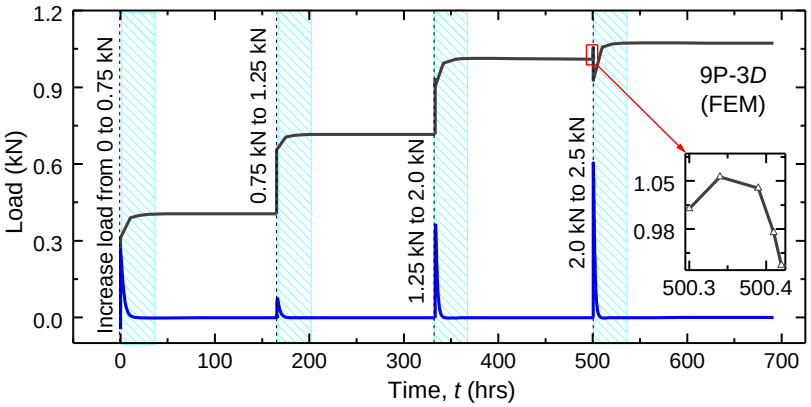

(c) 9P-3*D*

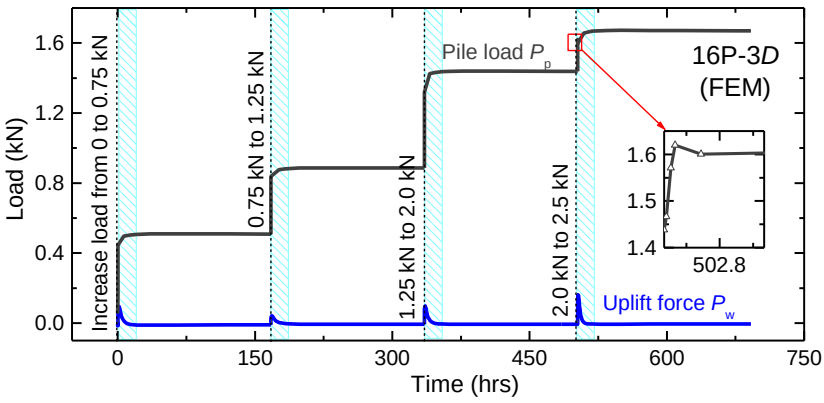

(d) 16P-3*D*

Fig. 4.23. Change of calculated pile load with time: (a) 4P-6*D*; (b) 4P-3*D*; (c) 9P-3*D*; (d) 16P-3*D*

We consider the pile behavior when the applied load is increasing first. For the cases of 4P-6*D* and 4P-3*D*, in the first and second load steps, the pile resistances increase purely when the applied load is increasing. In the third load step of 4P-6*D* and the third and fourth load steps of 4P-3*D*, the pile resistances firstly increase slightly and then reduce dramatically (softening behavior occurs) when the applied load is increasing (see the magnified view in each figure). Compare to the measurements, the measured results of both the foundations show that the softening behavior of the pile occurred from the first load step. For the case of 9P-3*D*, both the calculated and measured results show that the softening behavior occurs from the third load step when the applied load *P* is increasing from 1.25 kN to 2.0 kN. For the case of 16P-3*D*, the calculated results show that the softening behavior occurs from the fouth load step when the applied load is increasing to 2.5 kN, meanwhile the measured results show that the softening behavior occurs from the fifth load step when the applied load is increasing to 3.0 kN. Regarding the magnitude of the increment or reduction of pile resistance when the applied load is increasing, the calculated results show smaller increments but larger reductions, in comparison with the corresponding measured ones.

Overall, during the load-increasing periods, although there are differences between the measurement and the simulations in the magnitudes and the load stages of which the softening behavior occurs, the phenomena are similar.

Let us look at the change of pile resistances during primary consolidation periods. On Fig. 4.23, the highlighted areas could be regarded as the primary consolidation periods. It is clearly seen from the figure that the pile resistances of all four foundations increase noticeably with elapsed time during primary consolidation periods. This phenomenon was also obtained in the experiments and was explained by the increase of effective stresses in the ground due to the dissipation of excess pore water pressures in the primary consolidation period.

During secondary consolidation periods, interestingly, similar to the measured results (except for the first two load steps of 9P-3*D* and 16P-3*D*), the calculated pile resistances are also stable with time.

In general, the measured trends are simulated reasonably although there are differences in magnitudes.

c. Change of axial force along piles with applied load

The changes of axial forces along piles with increase in the applied load of the four foundations are shown in Figs. 4.24-4.27 in the form of the increments in axial force from the start of the first load step. Both the measured and calculated results are shown for comparison. It is noted that, on each figure, the axial forces before and after the consolidation stage of each load step are shown by the dashed line and line-symbol line, respectively.

In the cases of 4P-6*D* and 4P-3*D*, the 4 piles have the same condition, therefore, the discussions on axial forces along piles were made for only one pile in each foundation. In the cases of 9P-3*D* and 16P-3*D*, the piles were arranged in symmetric conditions with 3 different types of positions (corner pile, edge pile, and center pile). Therefore, the discussion in each foundation is made on three piles representing three pile types, and the effect of pile positions on the changes of axial forces along piles are compared with the measured results.

Let us consider the cases of 4P-6*D* first. It is seen from Fig. 4.24 that in the first load step, the calculated results are almost fit to the measured results quantitatively. Both measured and calculated results indicate that the load carries by each pile before and after the consolidation period is about 80 N and 100 N, respectively; of which the pile tip carries about 25N. So, the pile shaft carries a large part of the pile load. The increment of pile tip resistances during the consolidation period is small in this load step. In the second load step, the calculated results show a larger increment of axial force, in comparison with the measured one. Because the piles support a larger load, the calculated raft load, as well as the pore water pressure at the raft base, are smaller than the corresponding measured results, as mentioned in the previous sections. For the third load step, the measured results are simulated well.

Fig. 4.25 compares the calculated axial forces and measured axial forces for 4P-3*D*. It is seen from the figure that the calculated results are almost fit to the measured results quantitatively.

Fig. 4.26 shows the axial forces along a corner pile, an edge pile, and the center pile in 9P-3*D*. In general, the calculated results of axial forces along all three piles are underestimated. The measured results are significantly higher than the calculated results. However, it is interesting that the tendencies of all three piles are predicted well by the simulation. Similar to the measured results, the calculated results show that the load on the center pile is smaller than those on the corner pile and edge pile in the first and the second load steps. Thereafter, among three piles, the load of the center pile increases most

significantly and becomes the highest among 3 piles in the last 2 load steps. In contrast, the load on the corner pile is the highest in the first load step, however, it was the smallest at the final load step. The load on edge pile is the largest in the 2nd load step, and is between the load on the center pile and the load on the corner pile in the other load steps.

Interestingly, among three piles, the increment of tip resistance is the most significant in the center pile and is the least in the corner pile in both the measurement and simulation. The tip of the center pile supports about half of the center pile load at the last load step while the tip of the corner pile supports only one-fourth of the corner pile load. At the final load step, both measured and calculated results show that the center pile carries the largest load among three piles. This is mainly due to the significant larger tip resistance.

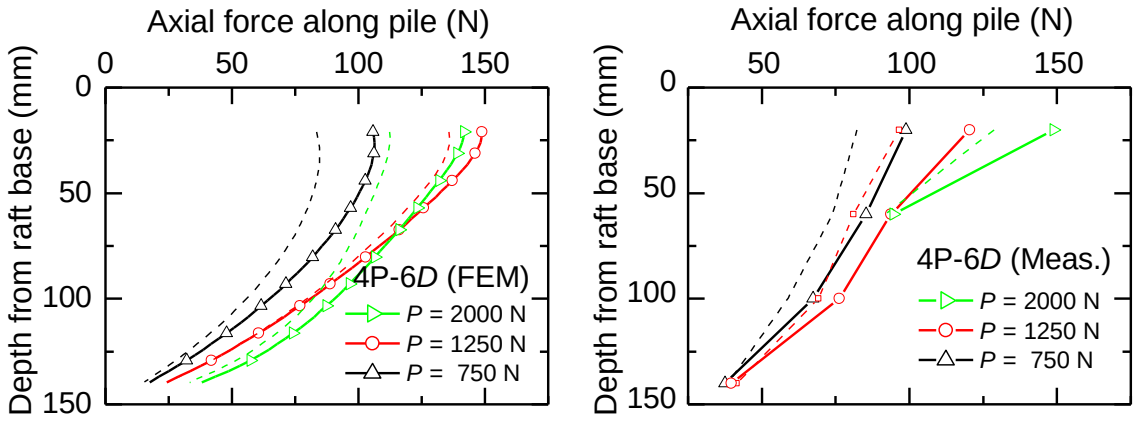

(a) Calculated (b) Measured

Fig. 4.24. Axial force along a pile in 4P-6*D*.

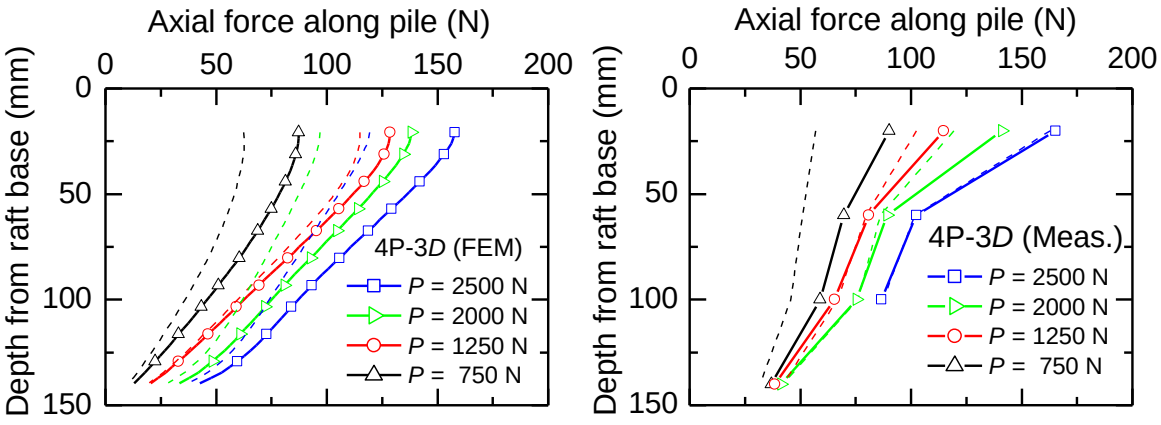

(a) Calculated (b) Measured

Fig. 4.25. Axial force along a pile in 4P-3*D*.

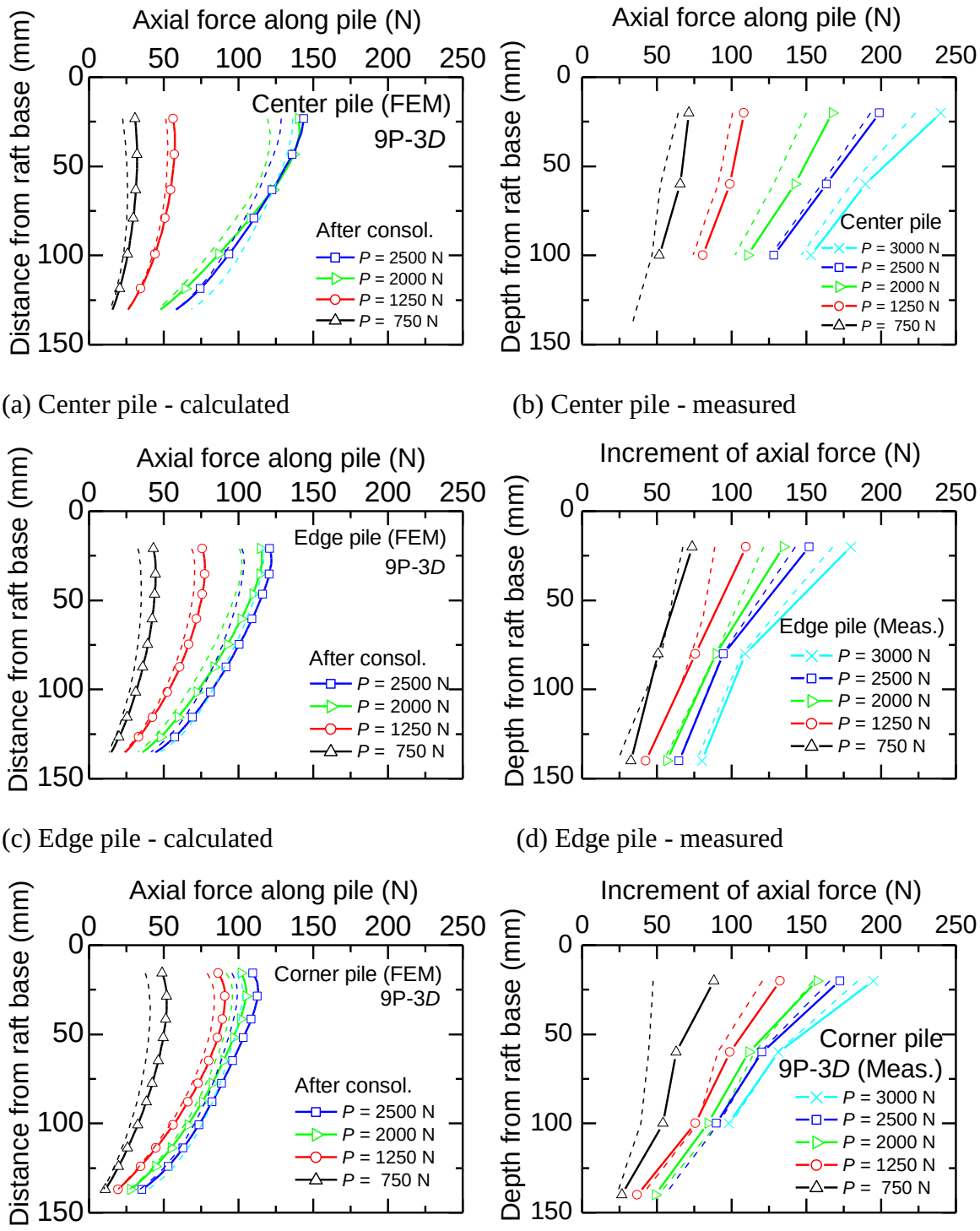

(a) Center pile - calculated

(b) Center pile - measured

(c) Edge pile - calculated

(d) Edge pile - measured

(e) Corner pile - calculated

(f) Corner pile - measured

Fig. 4.26. Axial force along a pile in 9P-3*D*.

Fig. 4.27 shows both the calculated and measured axial forces along a corner pile, an edge pile, and the center pile in 16P-3*D*. The measured change of axial forces for the case of 16P-3*D* are similar to those for the case of 9P-3*D*. The calculated results are in good

agreement with the measured results in terms of the tendency of loads carried by three pile types and loads sharing between the shaft and the tip resistances.

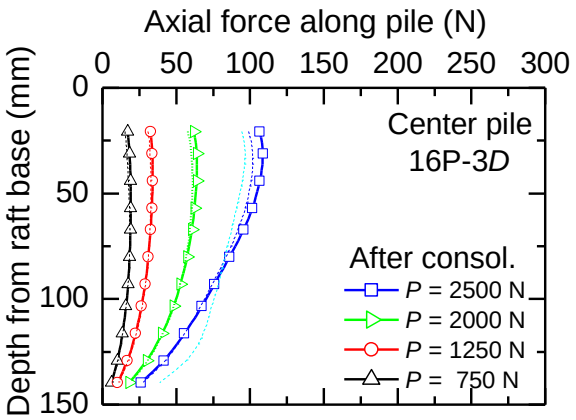

(a) Center pile - calculated

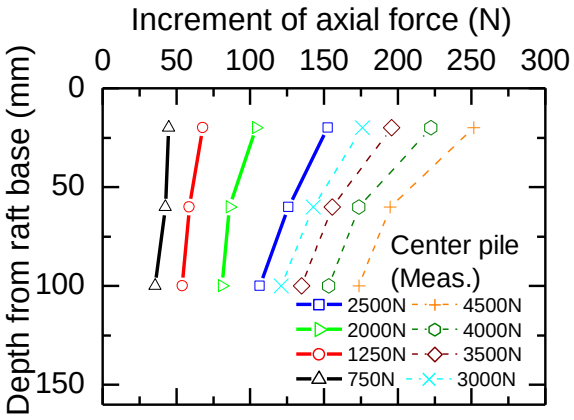

(b) Center pile - measured

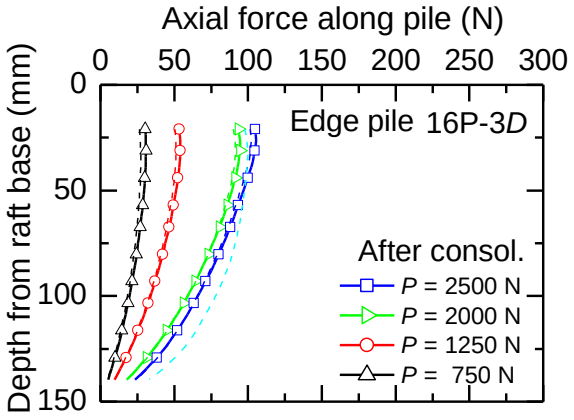

(c) Edge pile - calculated

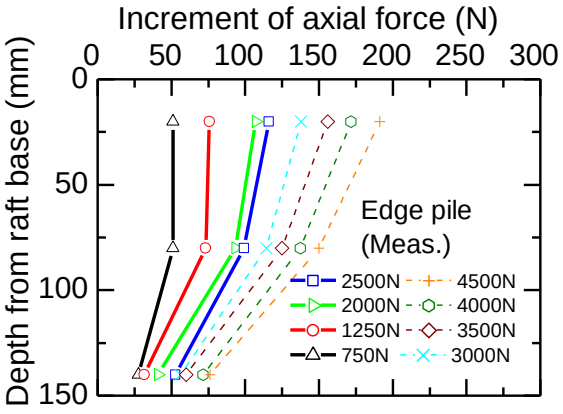

(d) Edge pile - measured

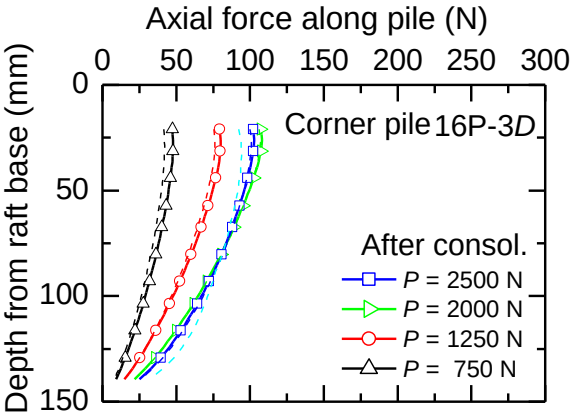

(e) Corner pile - calculated

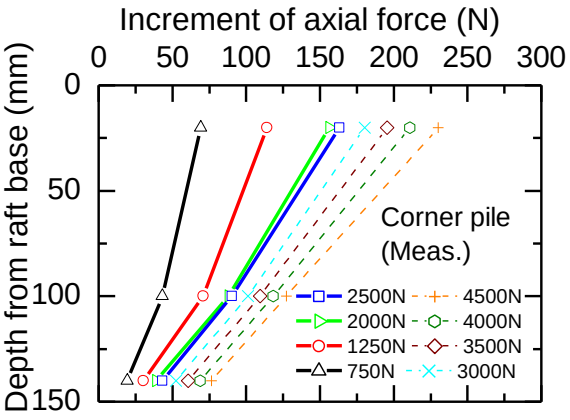

(f) Corner pile - measured

Fig. 4.27. Axial force along a pile in 16P-3*D*.

d. Load sharing between raft and piles

The changes in load sharing between raft and piles are shown in Fig. 4.28 for 4P-6*D* foundation, Fig. 4.29 for 4P-3*D* foundation, Fig. 4.30 for 9P-3*D* foundation, and Fig. 4.31 for the 16P-3*D* foundation.

Looking at Fig. 4.28 for the 4P-6*D* foundation, the measured trend of load sharing is simulated reasonably. Both the measured and calculated results show that the proportion of load supported by the raft increases with increasing applied load, meanwhile, the opposite is observed for the proportion of load supported by the piles. Comparing the measured and calculated results quantitively, the calculated proportion of pile load in the second load step is higher than the corresponding measured value because the FEM result of the second load step shows a larger pile load, as mentioned before. The pile load proportions of the two other load steps are simulated well.

Fig. 4.29 shows the load sharing between raft and piles for the 4P-3*D* foundation. As mentioned in the previous section, the pile loads are simulated well in all three load steps, the load sharing between the raft and the piles is also simulated well quantitatively.

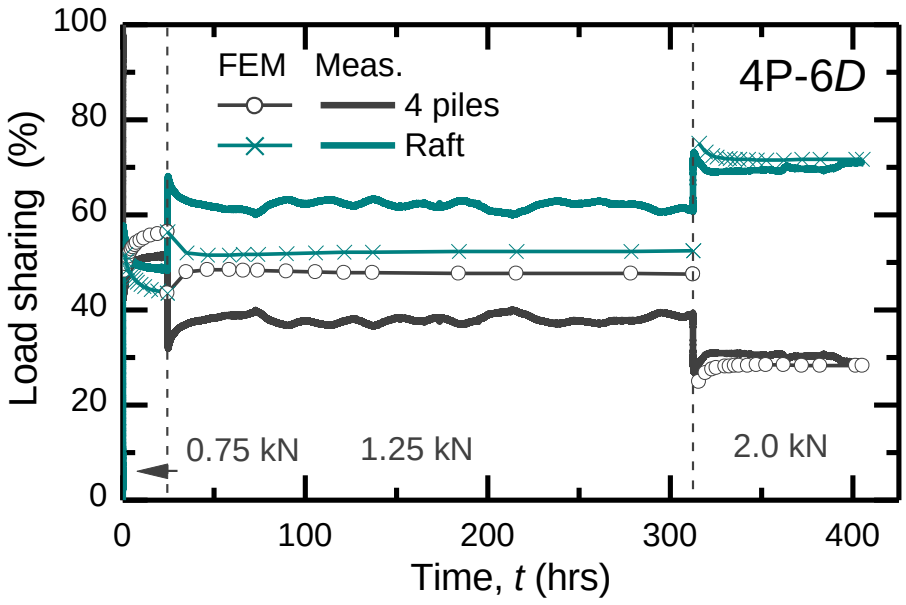

Fig. 4.28. Load sharing between raft and pile in 4P-6*D* foundation

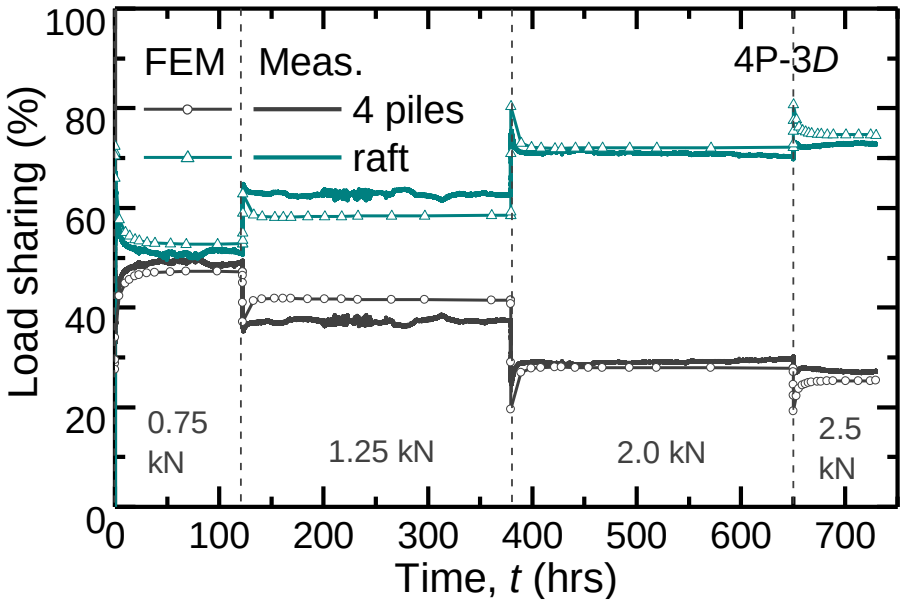

Fig. 4.29. Load sharing between raft and pile in 4P-3*D* foundation.

Fig. 4.30 and Fig. 4.31 show the load sharing between the raft and the piles for 9P-3*D* and 16P-3*D* respectively. The figures show that the calculated proportion of load carried pile is smaller than the measured value in all load steps. This result is obvious because in the section of axial force along pile, FEM results show that the calculated pile loads are underestimated the measured pile load. However, the calculated trend is reasonable, in comparison with the measured trend.

In conclusion, both the measured and calculated results indicated that the applied load affected the load sharing between the raft and the piles. As the applied load is larger, the proportion of pile load is smaller. When the applied load exceeds the pile group's ultimate capacity, the proportion of pile load decreases in load-increasing time because of the softening behavior of the pile, and increases in primary consolidation period because of the increments of effective ground stresses. The load sharing between the raft and the piles is stable in the secondary consolidation period.

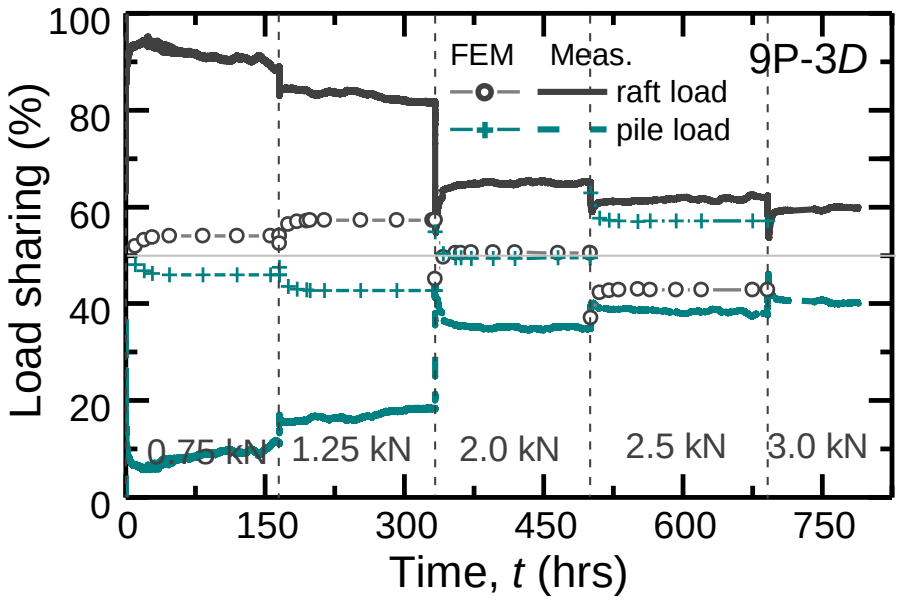

Fig. 4.30. Load sharing between raft and pile in 9P-3*D* foundation.

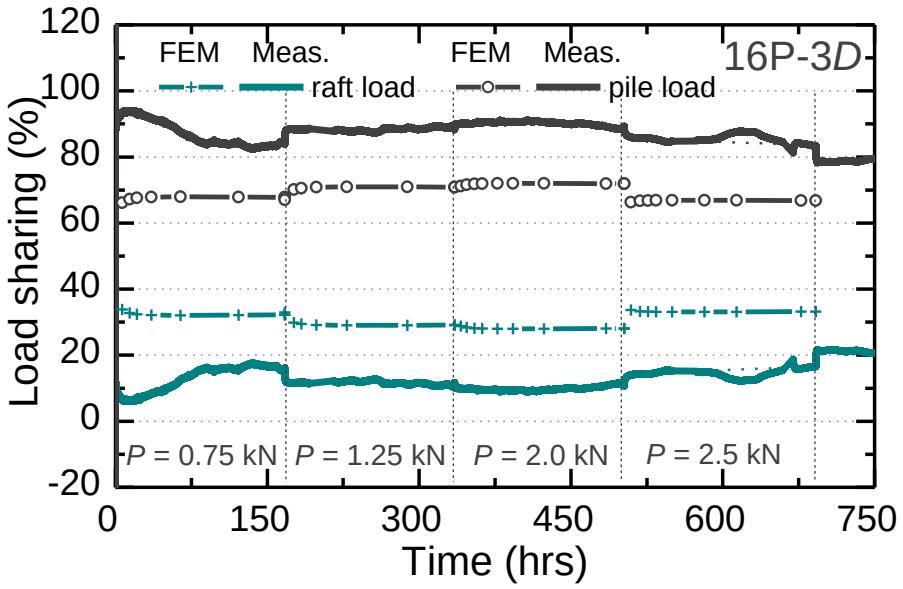

Fig. 4.31. Load sharing between raft and pile in 16P-3*D* foundation.

4.4 Conclusions of Chapter 4

In this chapter, a series of FEM analyses of long-term vertical load tests of PRF models on saturated clay were conducted to investigate the behavior of piled raft foundations on saturated clay ground, and to confirm the experimental results. The main findings and conclusions from the FEM analyses within the above conditions are as follows:

1) The tendency of measured settlements was simulated reasonably. The foundations settle significantly during the load-increasing period. The settlements then continues increasing noticeably in the early stage of the consolidation period (primary consolidation) and increasing slightly in the later stage of the consolidation period (secondary consolidation).
2) The softening behavior of piles (reduction of pile resistance) may occur when the load is increasing. The PWP continues increasing in a short duration after the load is kept constant.
3) The arrangement of piles in the piled raft foundation affected the axial forces along piles. For the cases of 4P-6*D* and 4P-3*D*, the piles in PRF with larger pile spacing have slightly larger shaft resistance at the same applied load. For the cases of 9P-3*D* and 16P-3*D*, the location of the pile affects the change of pile axial forces with the applied load.
4) The level of applied load *P* affects the total load carried by the piles, and also affects the proportions of load sharing between piles. FEM results of both the cases of 9P-3*D* and 16P-3*D* indicated that the corner piles carry the largest load at small applied load but carry the smallest load at larger applied load, in comparison with the center piles and edge piles. The opposite trend was obtained for the center piles.
5) Similar to the measured results, FEM results of both the cases of 9P-3*D* and 16P-3*D* showed that the shaft resistances of peripheral piles (corner and edge piles) are mobilized more significantly from the low level of applied load, in comparison with center piles. Oppositely, the shaft resistances of the center piles increase more significantly at the higher level of applied load, compared to those of peripheral piles. The center piles have significantly large tip resistance at the large applied loads, compared to peripheral piles.
6) FEM results showed that at the small applied loads, the settlements of the 4P-6*D* foundation are slightly smaller than those of the 4P-3*D* foundation. At the large applied loads, the settlements of the two foundations are almost equal.
7) At the same magnitude of applied load, the PRF settlement decreases with the increasing number of piles in the foundation.

References for chapter 4

Andersen, K.H., Andresen, L., Jostad, H.P., Clukey, E.C., 2004. Effect of Skirt-Tip Geometry on Set-Up Outside Suction Anchors in Soft Clay. ASME 2004 23rd International Conference on Offshore Mechanics and Arctic Engineering, Vancouver, British Columbia, Canada, 1035-1044. doi:10.1115/OMAE2004-51564

Broere, W., van Tol, A. F., 2006. Modelling the bearing capacity of displacement piles in sand. In Proc. of the Institution of Civil Engineers, Geotechnical Engineering 159(ICE, GE3), 1-13.

Doherty, P., Gavin, K., 2013. Pile aging in cohesive soils. Journal of Geotechnical and Geoenvironmental Engineering 139(9), 1620. https://doi.org/10.1061/(ASCE)GT.1943-5606.0000884

Dong, G. W., 2000. Visco-elastic consolidation subsequent to pile installation. Computers and Geotechnics 26(2), 113–144. https://doi.org/10.1016/S0266-352X(99)00028-2

Engin H. K., Brinkgreve, R. B. J, van Tol, A. F., 2013. On the numerical modelling and incorporation of installation effects of jacked piles: a practical approach. In: Hick M, editor. Installation Effects in Geotechnical Engineering, 104-110.

Engin, H.K., 2013. Modelling Pile Installation Effects – A Numerical Approach. Ph. D. thesis, Geo-Engineering Section Delft University of Technology, The Netherlands. DOI: 10.4233/uuid:3e8cc9e2-b70c-403a-b800-f68d65e6ea85

Engin, H.K., Brinkgreve, R.B.J., van Tol, A.F., 2015. Simplified numerical modelling of pile penetration – the Press-Replace technique. International Journal for Numerical and Analytical Methods in Geomechanics 39(15), 1713-1734. https://doi.org/10.1002/nag.2376

Fu, H., Xiaoyu, L., 2011. Analysis of Settlement Induced by Dissipation of the Excess Pore Water Pressure Due to Piling in Soft Clay. Proceeding of GeoHunan International Conference 2011, 90–99. https://doi.org/10.1061/47631(410)11

Kimura, M. and Zhang, F., 2000. Seismic evaluations of pile foundations with three different methods based on three-dimensional elasto-plastic finite element analysis. Soils and Foundations 40(5), 113-132.

Nguyen, T., 2017. Modelling of pile load tests in granular soils: Loading rate effects. PhD thesis of Delft University of Technology, DOI: 10.4233/uuid:07dc4081-2436-4b6b-8f6d-b36d6a588047

Park, D., Park, D., Lee, J., 2016. Analyzing load response and load sharing behavior of piled rafts installed with driven piles in sands. Computers and Geotechnics, 78, 62-71. http://dx.doi.org/10.1016/j.compgeo.2016.05.008q

Pham, H.D., 2009. Modelling of Installation Effect of Driven Piles by Hypoplasticity. Master thesis of Delft Univeristy of Technology.

PLAXIS 3D 2018 - Material Models Manual, PLAXIS, https://www.plaxis.com/support/manuals/plaxis-3d-manuals/

Tan, P. S., Tan, S. A., Goh, S. H., 2019. Numerical study of pile soil interface using Press-Replace method in undrained soil. Proc. of 16th Asian Regional Conference of Soil Mechanics and Geotechnical Engineering, 4pp., October, Taipei, Taiwan.

Tehrani, F. S., Nguyen, P., Brinkgreve, R. B. J., van Tol, A. F., 2016, Comparison of press-replace method and material point method for analysis of jacked piles. Computers and Geotechnics 78, 38-53, https://dx.doi.org/10.1016/j.compgeo.2016.04.017

Vu, A.T., 2017. Experimental and Numerical Study on Behaviours of Pile Group and Piled Raft Foundations Having Batter Piles Subjected to Combination of Vertical and Cyclic Horizontal Loading. PhD thesis of Kanazawa Univeristy.

Chapter 5

Summary, conclusions and recommendations

5.1 Introduction

In this thesis, the time-dependent behavior of vertically loaded piled raft foundation models supported by jacking piles is studied by experimental and numerical method. A series of experiments on the foundations with 0, 4, 9, and 16 piles were conducted on saturated clay. Numerical simulations of the experiments were conducted using finite element method through a three-dimensional program Plaxis 3D 2018. The Soft Soil Creep model was used to describe clay ground, of which the soil parameters were basically obtained from laboratory element tests. The installation effect of pile was simulated by the volume expansion method.

In this chapter, the main contents and merits of each chapter are summarized again, and the recommendations for further studies as well as for the design of piled raft foundation on clay are made.

5.2 Summary of each chapter

The contents of each chapter are summarized as follows:

Chapter 1: The background and motivation of the research, the objectives of the research, and the structure of the thesis were presented.

Chapter 2: The literature review of previous researches related to piled raft on clay was briefly summarized.

Chapter 3: The long-term behavior of 5 PRF models on saturated clay was investigated through small-scale physical modeling in this chapter. The detailed descriptions of model foundations, model grounds, test devices, instrumentation, and tests procedure were presented in this chapter. The soil investigation technique and the laboratory soil test were shown in this chapter. The undrained shear strength of ground was obtained from cone penetration tests, T-bar tests, and unconfined compression tests. The main findings and suggestions from the experimental results within the experimental conditions presented in this study are as follows.

1) During the load-increasing period of small load steps ($P \leq P_{PG,\ ult.}$), the piles were effective at supporting the applied load and suppressing the settlement of the foundation. During the load-increasing period of large load steps ($P > P_{PG,\ ult.}$), the pile resistance increased to a temporary peak and then decreased (softening behavior). The softening behavior of the piles continued for a short duration after the load-increasing period, although the PWP started to dissipate (early stage of the primary consolidation period).

2) Stresses from the raft base caused ground consolidation. Consequently, the effective ground stresses increased, thereby increasing the ground strength and stiffness during primary consolidation and increasing the pile resistance.

3) During secondary consolidation, the foundations continued to settle because of ground creep, and the creep settlement index [Eq. (3-6)] was higher when the applied load was larger.

4) During the secondary consolidation period, the load sharing between raft and piles was unstable at the relatively small applied load ($P \leq P_{PG,\ ult.}$), however, at the larger applied load, the loads supported by both the raft and the piles were stable, despite the creep settlement continued.

5) The level of applied load P affected the load sharing between the raft and the piles, and also affected the load sharing between piles. The proportion of load supported by piles decreased with the increasing applied load. The corner pile carried larger load at small load steps but smaller load at larger load steps, in comparison with the center pile. The piles carried a notable part of the applied load, even though in cases of only 4 piles.

6) The shaft resistances of peripheral piles were mobilized from the low level of applied load ($P < P_{PG,\ ultimate}$), but that of the center piles were mobilized at the higher level of applied load ($P > P_{PG,\ ultimate}$). The pile shaft resistance of corner piles increased during primary consolidation, especially at the top sections near the raft base.

7) For smaller applied loads, the PRF (4P-6D) with the wider pile spacing (s = 6D) was better at suppressing the settlement than was the one (4P-3D) with the narrower pile spacing (s = 3D). For larger applied loads, the opposite was the case.

8) The PRF bearing capacity increased and the PRF settlement decreased with the increasing number of piles in the foundation.

Although the present study involved small-scale experiments, it emphasized the importance of considering the interaction among the piles, the raft, the ground, and the PWP. The results can also be used to validate analytical methods in the design of piled raft foundations on saturated clay ground.

Chapter 4: A series of FEM analyses of long-term vertical load tests of PRF models on saturated clay were conducted to confirm the experimental results and to investigate deeper insight into the foundation behavior. The simulations of laboratory element tests such as CU triaxial test and oedometer test were conducted before the analyses of piled foundations to select an appropriate constitutive soil model and examine the input parameters for the soil model. The simulations of element tests showed that both the CU triaxial test and oedometer test were calculated well with the constitutive model called "Soft Soil Creep model" and the input soil parameters were basically obtained from the laboratory element tests without modifications. Therefore the same soil model and the same soil parameters were used for further calculations. The effects of pile installation was simulated by cylindrical expansion of pile using volume expansion of pile volume elements. This method is simple and could give some reasonable results on the pile resistance. Several simulations of pile groups with different values of volume expansion were conducted to find an appropriate value of volume strain which is used to analyze the time-dependent behavior of piled raft foundations. The analyses of 4 piled raft foundations were finally conducted. The main findings and conclusions from the FEM analyses of piled raft foundations within the above conditions are as follows:

8) The tendency of measured settlements was simulated reasonably. The foundations settle significantly during the load-increasing period. The settlements then continues increasing noticeably in the early stage of the consolidation period (primary consolidation) and increasing slightly in the later stage of the consolidation period (secondary consolidation).
9) The softening behavior of piles (reduction of pile resistance) may occur when the load is increasing. The PWP continues increasing in a short duration after the load is kept constant.
10) The arrangement of piles in the piled raft foundation affected the axial forces along piles. For the cases of 4P-6*D* and 4P-3*D*, the piles in PRF with larger pile spacing have slightly larger shaft resistance at the same applied load. For the cases of 9P-3*D* and 16P-3*D*, the location of the pile affects the change of pile axial forces with the applied load.
11) The level of applied load *P* affects the total load carried by the piles, and also affects the proportions of load sharing between piles. FEM results of both the cases of 9P-3*D* and 16P-3*D* indicated that the corner piles carry the largest load at small applied load but carry the smallest load at larger applied load, in comparison with the center piles and edge piles. The opposite trend was obtained for the center piles.

12) Similar to the measured results, FEM results of both the cases of 9P-3*D* and 16P-3*D* showed that the shaft resistances of peripheral piles (corner and edge piles) are mobilized more significantly from the low level of applied load, in comparison with center piles. Oppositely, the shaft resistances of the center piles increase more significantly at the higher level of applied load, compared to those of peripheral piles. The center piles have significantly large tip resistance at the large applied loads, compared to peripheral piles.
13) FEM results showed that at the small applied loads, the settlements of the 4P-6*D* foundation are slightly smaller than those of the 4P-3*D* foundation. At the large applied loads, the settlements of the two foundations are almost equal.
14) At the same magnitude of applied load, the PRF settlement decreases with the increasing number of piles in the foundation.

5.3 Recommendations

In this research, the behavior of piled raft foundation models under only vertical centered static loads was investigated. However, in practice, the architecture of large and modern buildings is usually eccentric, and the horizontal or dynamic loads also can appear. The investigation of piled raft foundation behavior under different load conditions is one of the interests in future research.

Finding the effective pile length to optimize the design of piled raft foundation by conducting similar experimental procedures with different pile arrangements is also one of the objectives for further research. In practice, the raft is not usually completely rigid. The bending of the raft will affect the load distributed to beneath soil and piles, therefore another objective for further research is to investigate PRF behavior with a flexible raft.

FEM study with further adjustments for the current method or with a more appropriate simulation of installation effect is useful for the design of PRF supported by jacking piles. Therefore, this is also one target for further research.

The findings of this research are only within the small-scale experimental conditions, large-scale experiments or centrifuge tests or field tests are useful to validate the results and to adopt the results to the practical design.

APPENDIX A

Estimation of strength reduction factor R_{inter} between pile and soil, and raft and soil

1. Introduction

In this section, a series of simple tests were conducted to estimate the strength reduction factor between pile and soil, and between raft and soil.

2. Estimation of strength reduction factor R_{inter} between pile and soil

These experiments were conducted as follows:

- The dry mixture of K50S50 was poured and compacted on a rough surface.
- The pile was placed on the prepared surface, the direction of the pile axis is perpendicular to bottom edge of the surface (see Fig. A1).
- The the top edge of the surface is raised gradually until the pile start to slide down on the surface.
- Measure the height *h* (Fig. A1) at the time the pile starts to slide, and calculate the tilt angle of the surface at that time. This tilt angle is regarded as friction angle between pile and soil $\phi_{p\text{-}s}$.

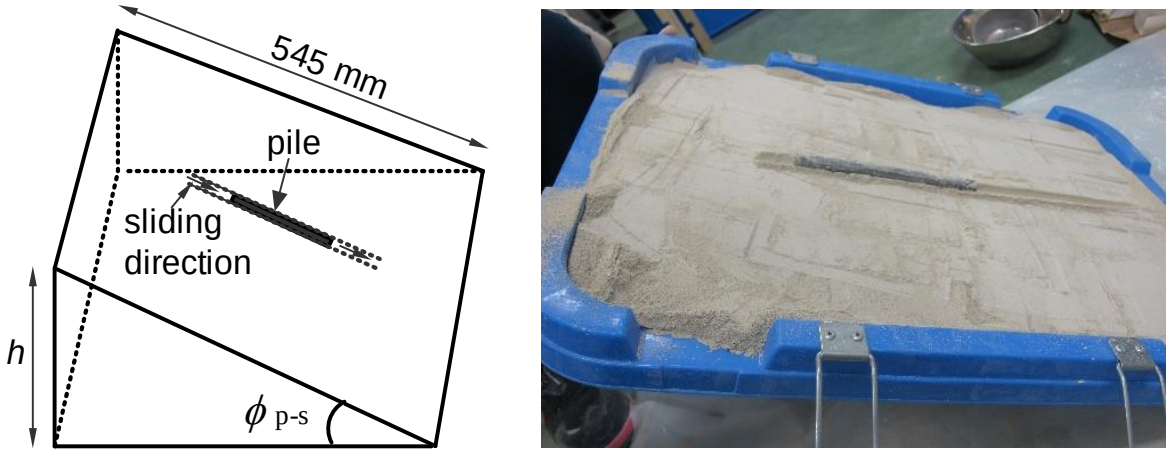

(a) (b)

Fig. A1. Set-up of experiments for estimation of strength reduction factor R_{inter} between pile and soil: (a) model of experiments; (b) a photo taken during experimental procedure.

Results of tests:

h_{average} = 294 mm

$\phi_{\text{p-s}} = 32.6^0$

$\phi_{\text{soil}} = 34.8^0$

$R_{\text{inter p-s}} = \tan(\phi_{\text{p-s}}) / \tan(\phi_{\text{soil}}) = 0.92$

3. Estimation of strength reduction factor R_{inter} between raft and soil

The procedure of these experiments are similar to the procedure of experiments which used for estimation of strength reduction factor R_{inter} between pile and soil. The set-up of experiments are shown in Fig. A2.

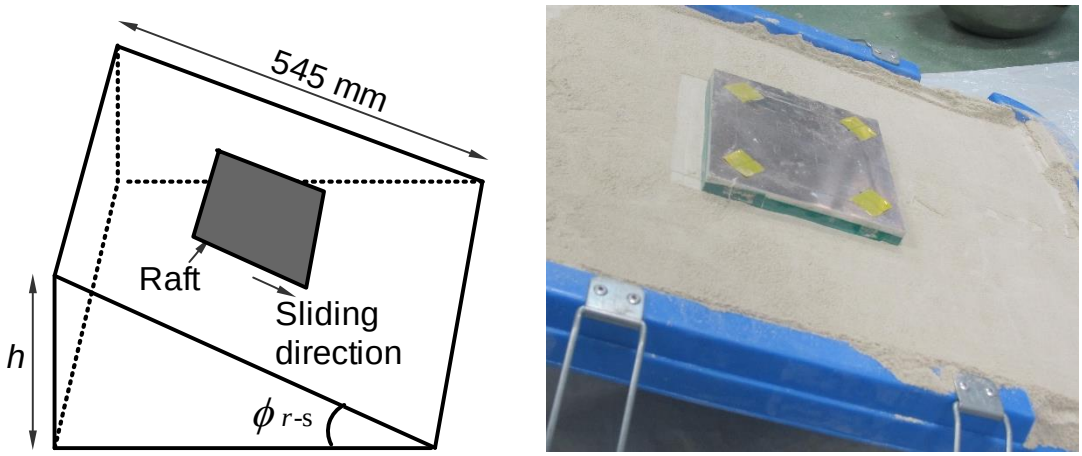

(a) (b)

Fig. A2. Set-up of experiments for estimation of strength reduction factor R_{inter} between raft and soil: (a) model of experiments; (b) a photo taken during experimental procedure.

Results of tests:

h_{average} = 257 mm

$\phi_{\text{r-s}} = 28^0$

$R_{\text{inter r-s}} = \tan(\phi_{\text{r-s}}) / \tan(\phi_{\text{soil}}) = 0.765$

APPENDIX B

Simulations of single jacked-in piles

B1. Model 1: Symmetric condition

Fig. B1 shows the model of a single pile in symmetric condition analyses.

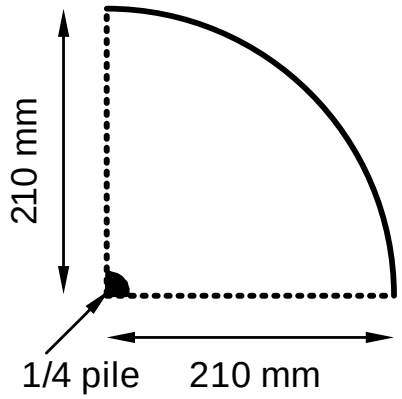

Fig. B1. Symmetric model of a single pile.

I. Static load tests of single piles were conducted immediately after the installation

a/ Simulate installation effect by expansion method

Calculation stages: Self-weight analysis → Set the piles in the ground → Apply volume expansion (lateral strains) to pile volume elements → Vertical static load test.

Results:

Load- settlement curve during SLT: Fig. B2 shows load - settlement relations during SLT of a single pile. Both the measured and calculated results are shown. When SLT was conducted with no expansion ($\varepsilon_{xx} = \varepsilon_{yy} = 0$ %), the pile resistance is small and far below the measured result. When a small lateral strain was applied to the pile volume elements ($\varepsilon_{xx} = \varepsilon_{yy} = 2.5$ or 5 %), the pile resistance increased significantly. Interestingly, when the lateral strains were larger ($\varepsilon_{xx} = \varepsilon_{yy} = 7.5$; 10; 12.5; 15 %), the pile resistance was almost similar to that of the case $\varepsilon_{xx} = \varepsilon_{yy} = 5$ %. This indicates that when using the volume expansion method to simulate the simulation of SLT of a single pile in clay of which the SLT was conducted

immediately after the installation (without consolidation), a small amount of lateral strain could maximize pile resistance.

Compare between calculated and measured results, the calculated results are smaller than the measured result.

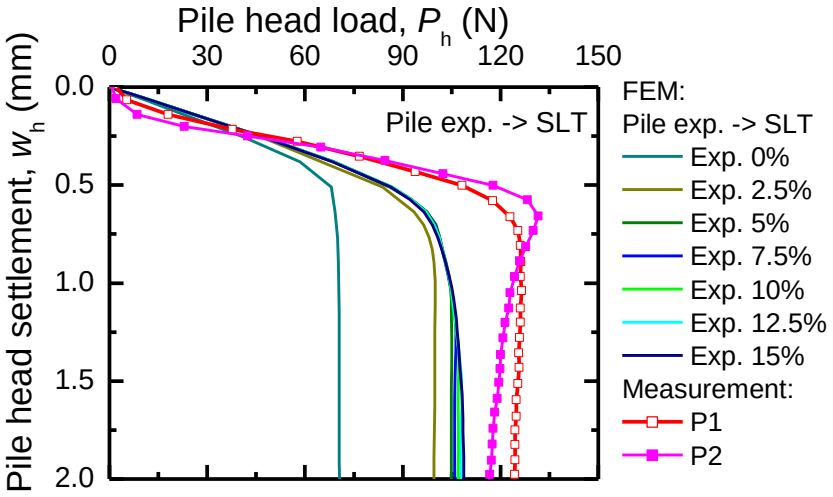

Fig. B2: Load- settlement curve during SLT of single piles without consolidation process.

Axial force along pile: Fig. B3 compares the calculated axial forces (with different lateral strains) to the measured axial force. The FEM results show that the volume expansion method increases pile shaft resistance significantly meanwhile the pile tip resistance was almost unchanged with changing of lateral strains. The calculated tip resistance was quite small, in comparison with the measured result. In general, the pile shaft resistance was simulated very well, except for the top section.

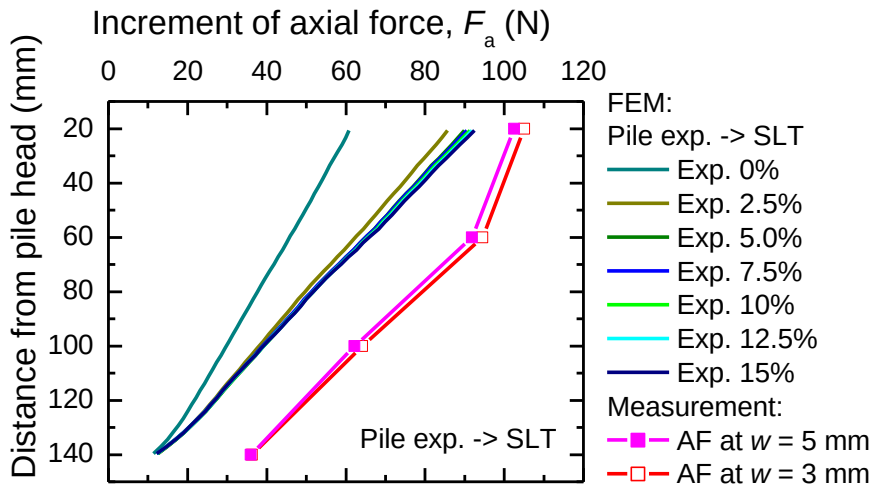

Fig. B3: Axial force along pile during SLT of single piles without consolidation process.

b/ Combine expansion and vertical displacement method

Calculation stages: Self-weight analysis → Set the piles in the ground → Apply volume expansion (lateral strains) to pile volume elements and vertical displacement (displacement of 0.1 pile diameter) → Vertical static load test.

Fig. B4 shows the load- settlement curve during SLT of SPs, of which the combination lateral expansion and vertical displacement method was employed to simulate the pile installation effect.

It is seen from Fig. B4 that the pile resistance increases but is not significant compared to the corresponding pile resistance when only the lateral expansion method was employed (Fig. B2). This indicates that the vertical displacement is not effective in the increase of pile resistance when modeling the behavior of the jacked-in pile subjected to static load immediately after the installation process.

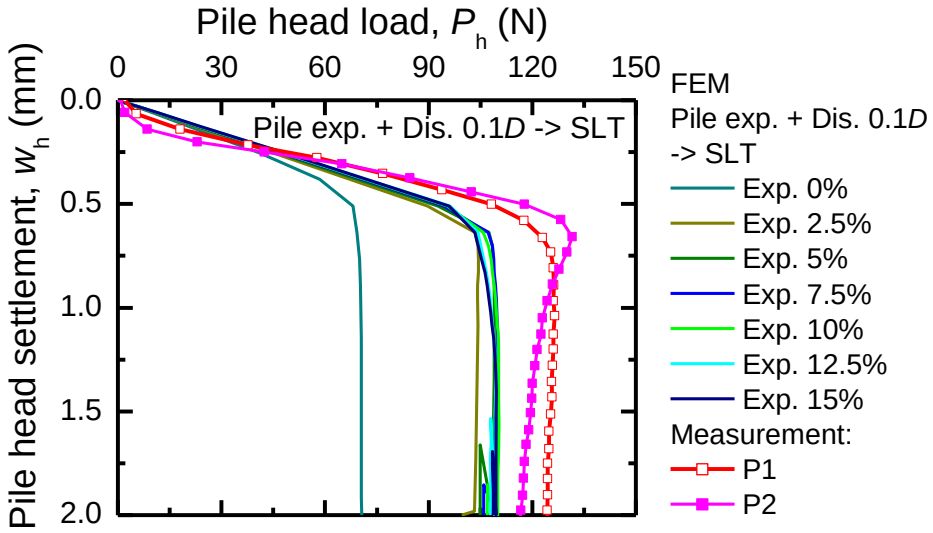

Fig. B4: Load- settlement curve during SLT of single piles without consolidation process.

Axial force along pile: Fig. B5 compares the calculated distributions of axial forces along the pile (with different lateral strains) to the measurement one. Similar to the results of load-settlement relations, the distributions of axial forces when using the combination of expansion and vertical displacement method are quite similar to the distributions of axial forces when using the volume expansion only.

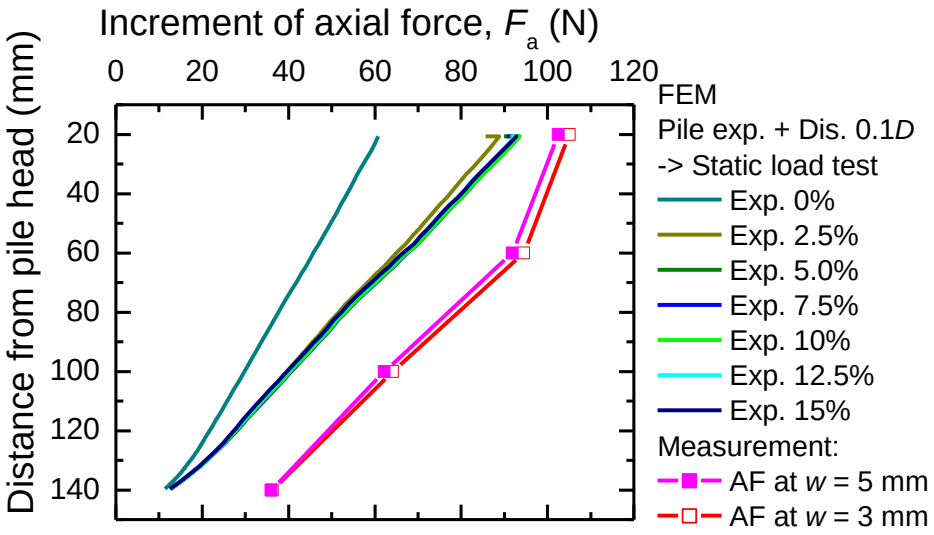

Fig. B5: Axial force along pile during SLT of single piles without consolidation process.

II. Static load test of single pile was conducted 1 day after the installation

a/ Expansion method

Calculation stages: Self-weight analysis → Set the piles in the ground → Apply volume expansion (lateral strains) to pile volume elements → Consolidation in one day → Vertical static load test.

Results:

Load- settlement curve during SLT: Fig. B6 shows load - settlement relations during SLT of a single pile. Both the measured and calculated results are shown. It is seen that when the 1 day consolidation period was set before the SLT was conducted, both the measured and calculated results indicate that the pile resistance increase significantly. Fig. B6 shows that the larger lateral expansion was applied, the higher pile resistance was achieved. The value of the lateral strain of $\varepsilon_{xx} = \varepsilon_{yy}$ = 7.5% - 12.5% gives good agreements with the measured result.

Axial force along pile: Fig. B7 compares the calculated axial forces (with different lateral strains) to the measured axial force. The FEM results show that the volume expansion method increases pile shaft resistance significantly meanwhile the pile tip resistance was almost unchanged with changing of lateral strains. The pile shaft resistance became larger when the lateral strains were larger.

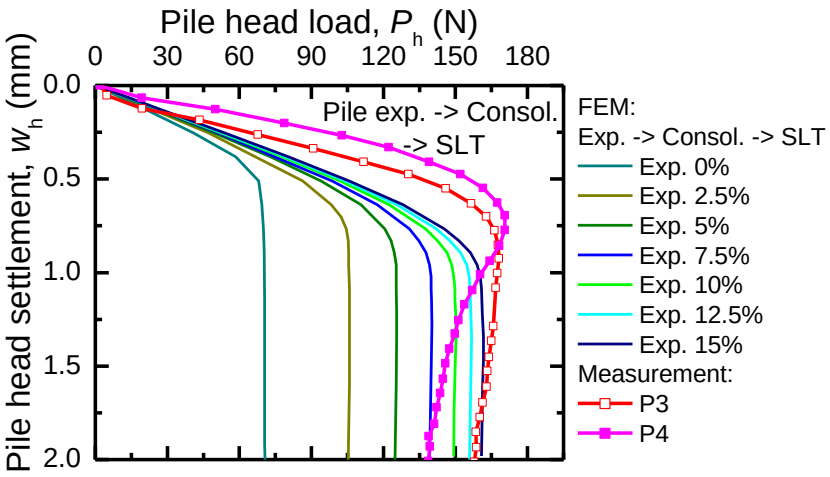

Fig. B6: Load- settlement curve during SLT of single piles with consolidation process.

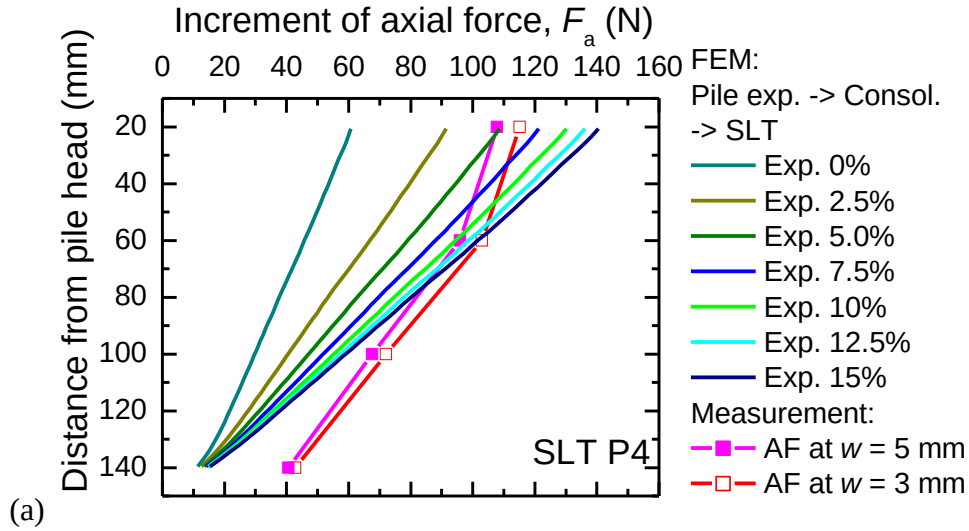

(a)

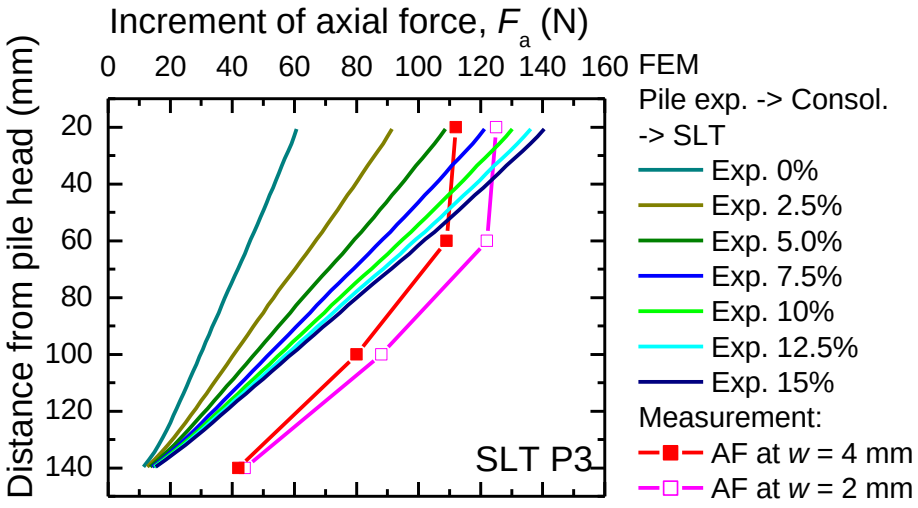

(b)

Fig. B7: Axial force along pile during SLT of single piles with consolidation process.

b/ Combine expansion and vertical displacement method

Calculation stages: Self-weight analysis → Set the piles in the ground → Apply volume expansion (lateral strains) to pile volume elements and vertical displacement of 0.1D for pile head at the same time→ Consolidation in one day → Vertical static load test.

Results:

Load- settlement curve during SLT: Fig. B8 shows load - settlement relations during SLT of a single pile. Both the measured and calculated results are shown. It is seen that when the 1 day consolidation period was set before the SLT was conducted, both the measured and calculated results indicate that the pile resistance increase significantly. Fig. B6 shows that the larger lateral expansion was applied, the higher pile resistance was achieved. The value of the lateral strain of $\varepsilon_{xx} = \varepsilon_{yy}$ = 7.5% - 10% gives good agreements with the measured result.

Compare to the results of part a, where only lateral volume expansions were applied, the similar trends were obtained, however, the pile resistance was larger when the vertical displacement was applied.

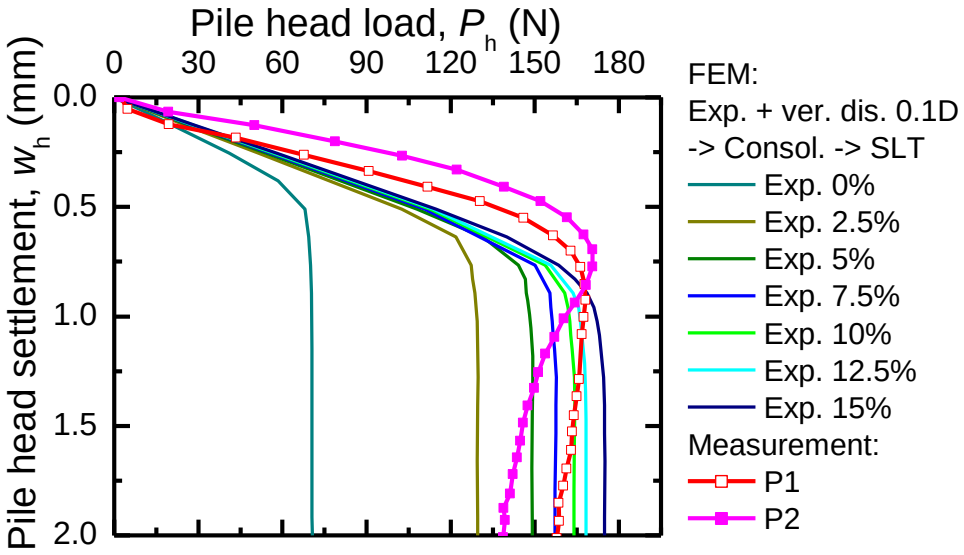

Fig. B8: Load- settlement curve during SLT of single piles with consolidation process.

Axial force along pile: Fig. B9 compares the calculated axial forces (with different lateral strains) to the measured axial force. The FEM results show that the combination of volume expansion and vertical displacement increases both the pile shaft and pile tip

resistances; however, the increment of pile shaft resistance is much more significantly, compared to that of the pile tip resistance.

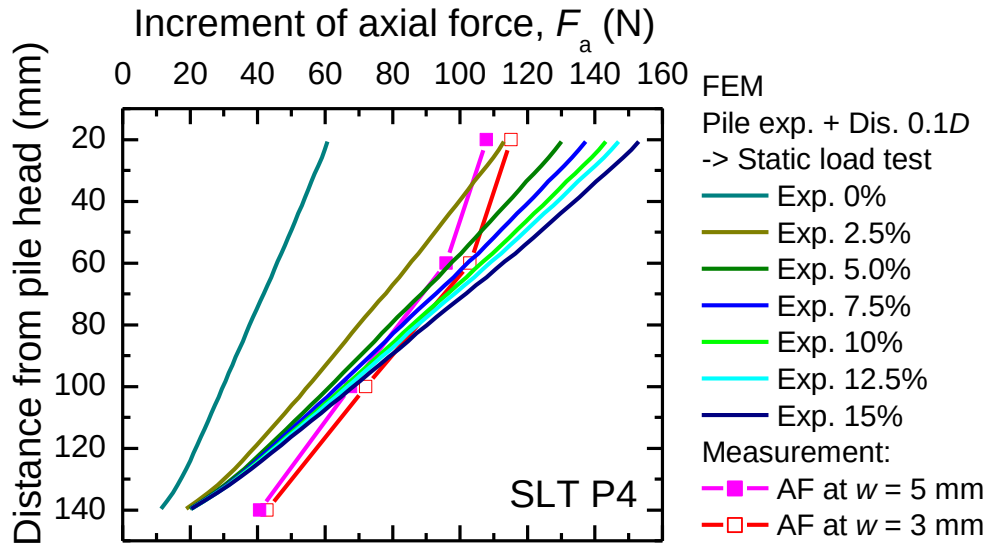

(a)

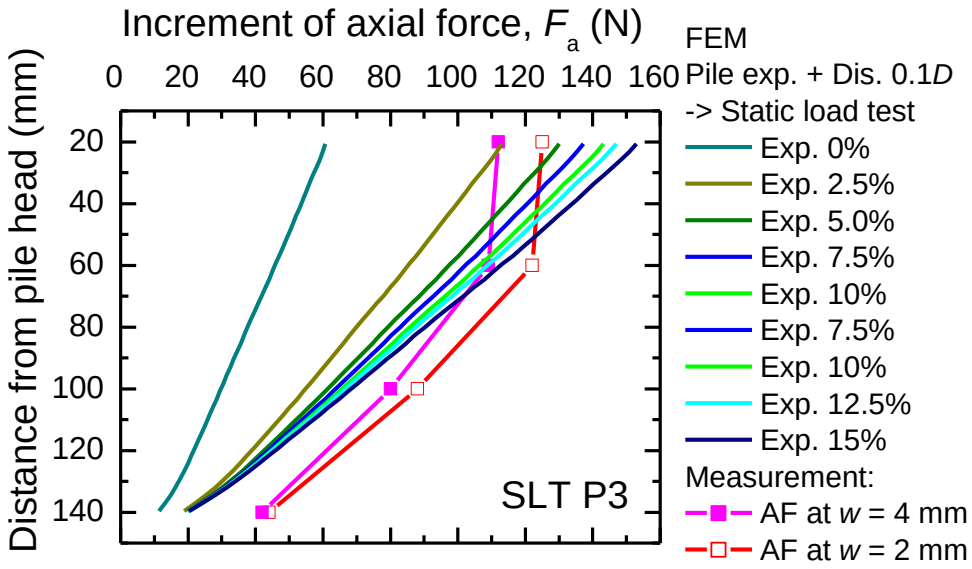

(b)

Fig. B9: Axial force along pile during SLT of single piles with consolidation process.

c/ Conclusions

+ For SLT of SP which was conducted immediately after the installation process:

- Calculated pile resistance could be maximized by applying a small value of lateral strains ($\varepsilon_{xx} = \varepsilon_{yy} = 5$ %). Larger lateral strains are not effective in increase pile resistance.

- The volume expansion method (applying lateral strains) increases only pile shaft resistance. The combination of lateral strain with vertical displacement does not have much influence on pile resistance as well as the distribution of axial force along the pile.

+ For SLT of SP which was conducted 1 day after the installation process:

- Calculated pile resistance increases with increasing lateral strains.

- The volume expansion method (applying lateral strains) increases only pile shaft resistance. The pile tip resistance is unchanged. The combination of lateral strain with vertical displacement has a moderate influence on both pile tip and pile shaft resistances.

- When only lateral strain is applied to simulate the influence of the installation process, at $\varepsilon_{xx} = \varepsilon_{yy} = 12.5$ %, the FEM gives reasonable results with the measurement. When the combination of different lateral strains with vertical displacement of 0.1*D*, the FEM gives reasonable results with the measurements at $\varepsilon_{xx} = \varepsilon_{yy} = 7.5\%$-10 %.

B2. Model 2: Full pile

Fig. B10 shows the model of a full single pile (non-symmetric condition) analyses.

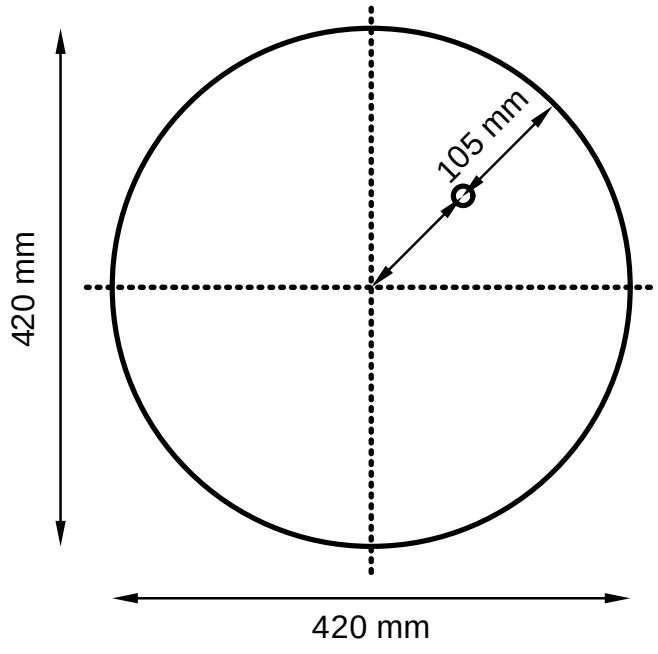

Fig. B10. Model of a single pile.

I. Static load test of single pile was conducted immediately after the installation

a/ Expansion method

Calculation stages: Self-weight analysis → Set the piles in the ground → Apply volume expansion (lateral strains) to pile volume elements → Vertical static load test.

Results:

Load- settlement curve during SLT: Fig. B11 shows load - settlement relations during SLT of the SP. Both the measured and calculated results are shown. When SLT was conducted with no expansion ($\varepsilon_{xx} = \varepsilon_{yy} = 0$ %), the pile resistance is small and far below the measured result. When a small lateral strain was applied to the pile volume elements ($\varepsilon_{xx} = \varepsilon_{yy} = 2.5$ or 5 %), the pile resistance increased significantly. Interestingly, when the lateral strains were larger ($\varepsilon_{xx} = \varepsilon_{yy} = 7.5$; 10; 12.5; 15 %), the pile resistance does not increase much, but is almost equal to that of the case $\varepsilon_{xx} = \varepsilon_{yy} = 5$ %. This indicates that when using the volume expansion method to simulate the simulation of SLT of a single pile in clay of which the SLT was conducted immediately after the installation (without consolidation), the pile resistance could be maximized by applying a small amount of lateral strain.

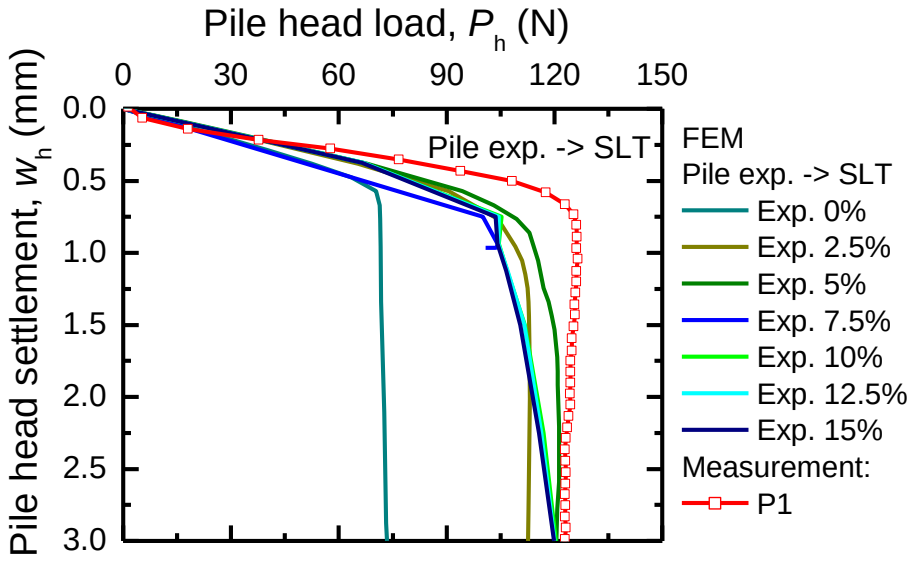

Fig. B11: Load- settlement curve during SLT of SP without consolidation process.

Axial force along pile: Fig. B12 compares the calculated axial forces (with different lateral strains) to the measured axial force. The FEM results show that the volume expansion method increases pile shaft resistance significantly meanwhile the pile tip resistance was almost unchanged with changing of lateral volume expansions. The calculated tip resistance

was quite small, in comparison with the measured result. In general, the pile shaft resistance was simulated well, except for the top section.

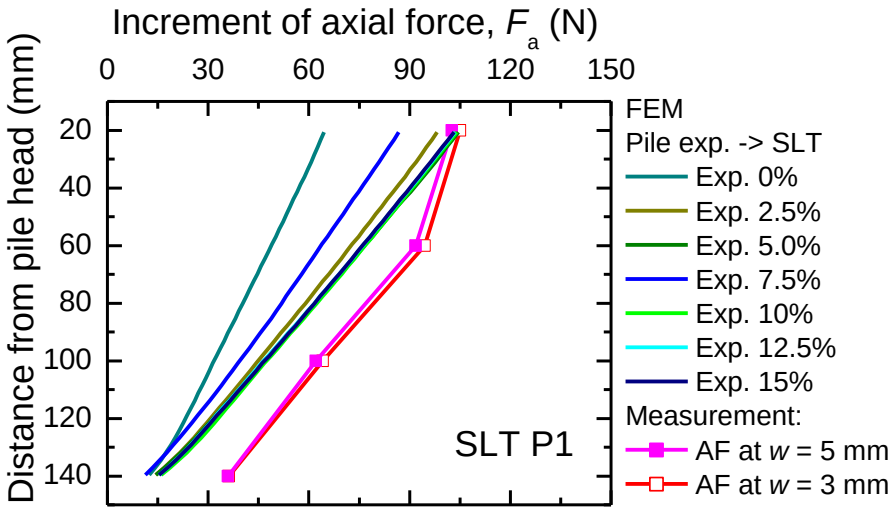

Fig. B12: Axial force along pile during SLT of SP without consolidation process.

II. Static load test of single pile was conducted 1 day after the installation

a/ Expansion method

Calculation stages: Self-weight analysis → Set the piles in the ground → Apply volume expansion (lateral strains) to pile volume elements → Consolidation in one day → Vertical static load test.

Results:

Load- settlement curve during SLT: Fig. B13 shows the calculated load-settlement relations of the SP with different lateral strains. The measured result is shown to compare. Similar to the results of the model 1 (symmetric geometry), the pile resistance increases with increasing lateral strains. The initial stiffness also increases with increasing volume expansion. The calculated pile resistance is reasonable when $\varepsilon_{xx} = \varepsilon_{yy} = 12.5$ %, compared to the measured result.

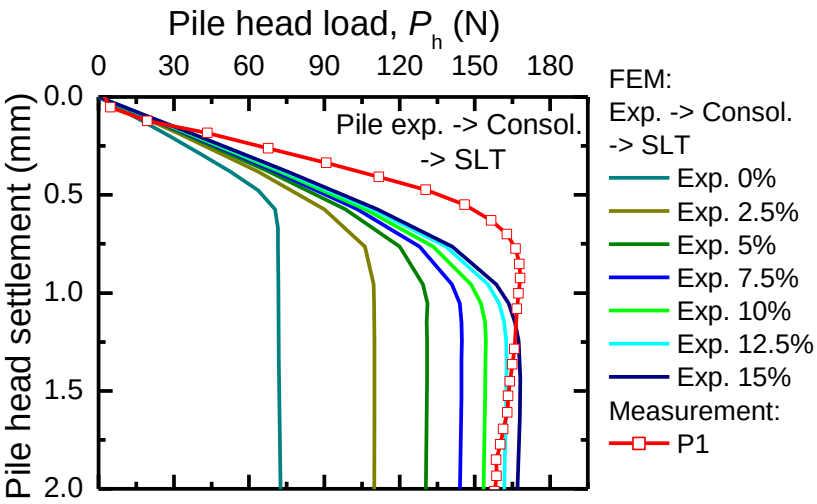

Fig. B13: Load- settlement curve during SLT of SP with consolidation process.

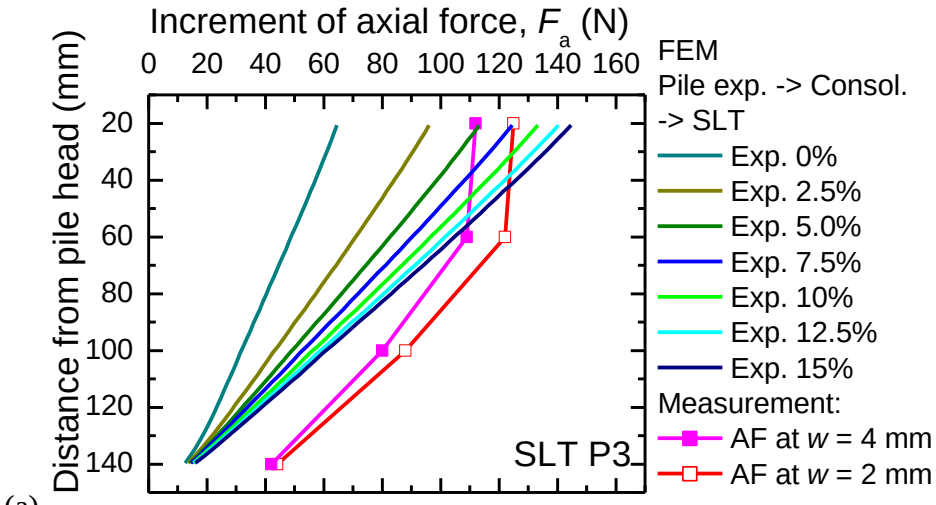

(a)

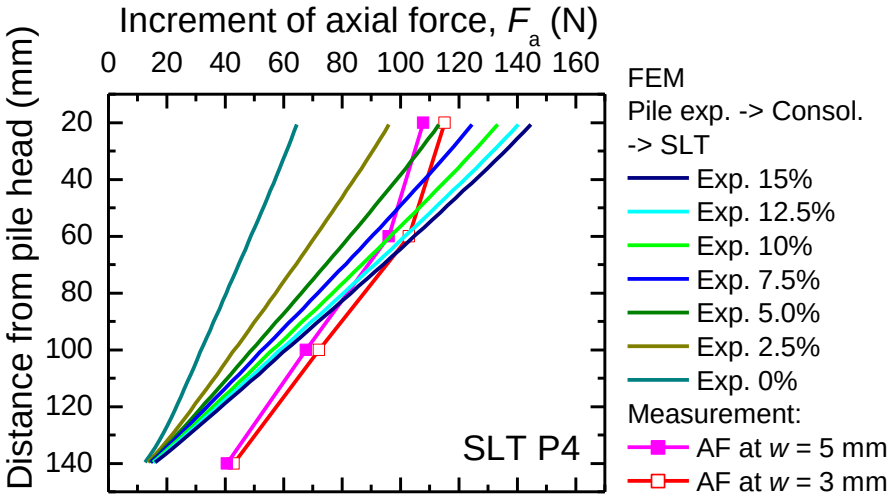

(b)

Fig. B14: Axial force along pile during SLT of SP with consolidation process.

Axial force along pile: Fig. B14 shows axial forces distributed along the pile when different lateral strains are applied. Basically, the pile shaft resistance increases with increasing lateral strains meanwhile the pile tip resistance is almost unchanged.

b/ Combine expansion and vertical displacement method

Calculation stages: Self-weight analysis → Set the piles in the ground → Apply volume expansion (lateral strains) to pile volume elements and vertical displacement of 0.1*D* for pile head at the same time→ Consolidation in one day → Vertical static load test.

Load- settlement curve during SLT: Fig. B15 shows the calculated load - settlement relations of the SP when the combination of different lateral strains and vertical displacement of 0.1*D* is applied to simulate the effect of the pile installation process on pile resistance. The measured result is shown to compare. It is seen from the figure that the pile resistance as well as the initial stiffness of load-settlement curves increase with increasing lateral strains. The calculated result gives reasonable agreement with the measured result when the combination of vertical displacement of 0.1*D* and lateral strains $\varepsilon_{xx} = \varepsilon_{yy} = 7.5$ % is used to simulate the pile installation effect. Compare to the scheme of only volume expansion, the pile resistance increases moderately when the vertical displacement is combined.

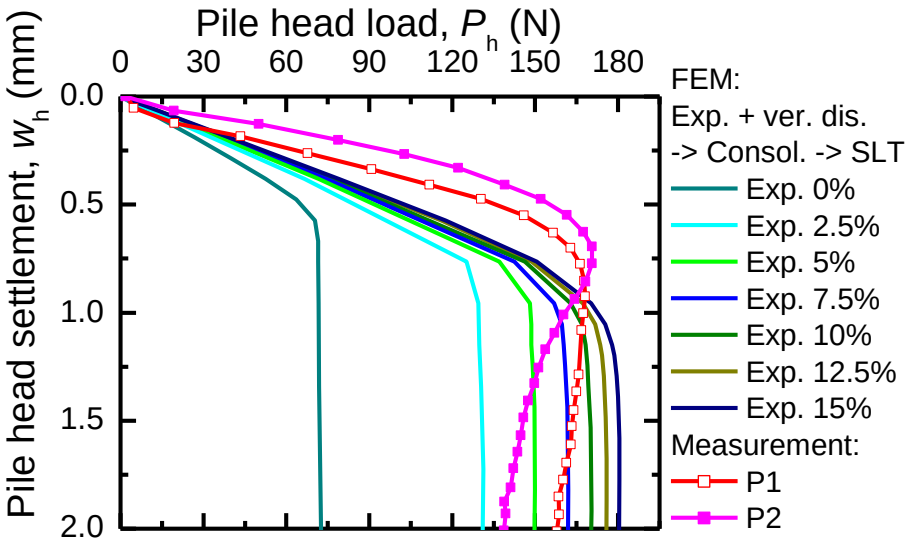

Fig. B15: Load- settlement curve during SLT of SP with consolidation process.

Axial force along pile: Fig. B14 shows axial forces distributed along the pile when different lateral strains are applied. Basically, when the combination of lateral strains and vertical displacement is applied, both the pile shaft and pile tip resistances increase, compared to the case of application of only lateral strains. Although the calculated tip

resistance is still smaller than the measured one, the tip resistance increases by about 30% when the pile installation effect is simulated by combining vertical displacement with lateral strains.

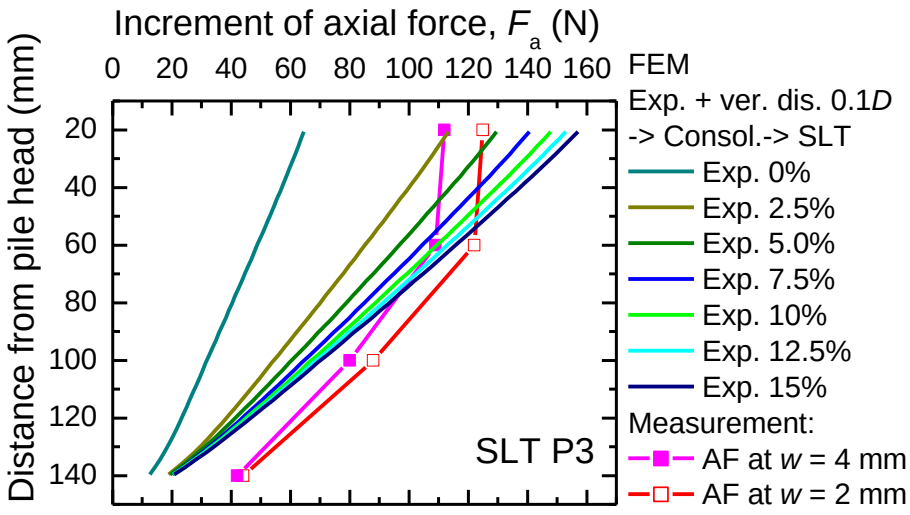

(a)

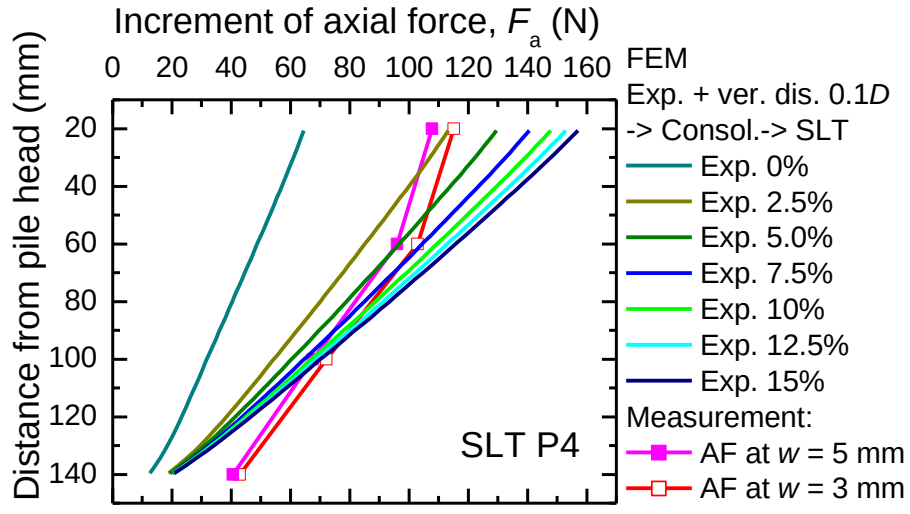

(b)

Fig. B16: Axial force along pile during SLT of SP with consolidation process.

c/ Conclusions

+ For SLT of SP which was conducted immediately after the installation process:

- Calculated pile resistance could be maximized by applying a small value of lateral strains ($\varepsilon_{xx} = \varepsilon_{yy} = 5$ %). Larger lateral strains are not effective in increase pile resistance.

- When only lateral strain is applied, only pile shaft resistance increases. The combination of lateral strain with vertical displacement does not have much influence on pile resistance as well as the distributions of axial force along the pile.

+ For SLT of SP which was conducted 1 day after the installation process:

- Calculated pile resistance increases with increasing lateral strains.

- The volume expansion method (applying lateral strains) increases only pile shaft resistance, the pile tip resistance is unchanged. The combination of lateral strain with vertical displacement has a moderate influence on both pile tip and pile shaft resistances.

- When only lateral strain is applied to simulate the influence of the installation process, at $\varepsilon_{xx} = \varepsilon_{yy} = 12.5$ %, the FEM gives reasonable results with the measurement. When the combination of different lateral strains with vertical displacement of $0.1D$, the FEM gives reasonable results with the measurement at $\varepsilon_{xx} = \varepsilon_{yy} = 7.5\%$.